Tsunami Damage Prediction for Buildings: Development of Methods for Empirical and Analytical Fragility Function Derivation

Joshua Macabuag

A thesis presented for the degree of
Doctor of Engineering

Department of Civil, Environmental and Geomatic Engineering
University College London
University of London

October 2017

Supervised by:
Prof Tiziana Rossetto
Prof Ian Eames

Declaration

I, Joshua Macabuag confirm that the work presented in this thesis is my own. Where information has been derived from other sources, I confirm that this has been indicated in the thesis.

Abstract

Over the past two decades, tsunami have been the cause of 33% of total deaths and 35% of total economic losses due to natural disasters globally, and currently 6 out of 10 of the most populous megacities in the world are at risk of being severely affected by tsunami. Quantifying tsunami risk is therefore centrally important for land use and emergency planning in the DRR sector, for human and financial loss estimation in the insurance sector, and for performance-based design in the engineering sector. Tsunami fragility functions are statistical models that relate a measure of tsunami intensity (e.g. inundation depth) to probabilities of damage exceedance for a number of damage states, and form a key component of tsunami risk models. This thesis presents improved derivation methods for empirical fragility functions (those derived from observed damage data from past tsunami), and research towards methodologies for deriving analytical fragility functions (those constructed from structural analysis in the absence of past damage data).

First, a critical review of the literature related to the prediction of building damage due to tsunami is presented. This review highlights that it is unclear which of the many available statistical methods available provide optimal empirical fragility functions. It is also seen that analytical methods are required for damage prediction in the vast majority of at-risk areas, however few such functions exist. Hence tsunami loads on buildings and methods of structural analysis under tsunami loading are critically reviewed so as to identify and justify the loading and analysis assumptions to be employed throughout this thesis.

A methodology for deriving optimal empirical tsunami fragility functions for a given dataset is then developed and demonstrated using a unique, disaggregated building damage dataset from the 2011 Japan Tsunami. The proposed methodology identifies the key Tsunami Intensity Measures (TIMs) and improved statistical methods to be used for fragility function derivation. A number of techniques novel in the field of empirical fragility function derivation are introduced: Multiple Imputation, K-fold Cross-Validation, and semi-parametric models. Furthermore, a preliminary methodology is also presented for quantifying debris-related effects on fragility functions.

Methods for structural analysis for the derivation of analytical fragility functions are then developed. First an investigation is carried out on how time-dependent effects, ductility and overstrength (a structure's ability to maintain a load greater than its yield value) affect structural damage analysis. This is then extended to develop a simplified method for estimating tsunami-induced structural damage under tsunami loading, suitable for use in the large number of analyses required to derive analytical fragility functions of populations of buildings.

By introducing advanced methods for selecting optimal TIMs and statistical models, and by furthering the field of structural analysis under tsunami loading, this research has the potential to influence how both empirical and analytical tsunami fragility curves are constructed in the future.

Acknowledgements

The author was funded as part of the Willis Research Network (WRN) and the EPSRC Engineering Doctorate Programme. Travel to conduct this collaborative work was kindly funded by the Sasakawa Foundation and the Earthquake Engineering Field Investigation Team travel grant.

I would like to thank Shigeko Tabuchi, Simon Edwards, Paul Jones and Marc Lehmann of Willis Towers Watson for allowing me to gain exposure to the catastrophe modelling sector and the opportunity to support the work of Willis Towers Watson through several placements. I would like to thank Dr Ioanna Ioannou of EPICentre, UCL, for her patient tutelage on all things related to R and statistics, and would also like to thank Dr Ioannis Kosmidis and Prof Richard Chandler of the Department of Statistical Science, UCL, for advising on the statistical analysis conducted in this thesis. I would like to acknowledge the many years of successful collaboration between EPICentre, UCL (UK) and IRIDeS, Tohoku University (Japan) which has made this work possible, with particular thanks to Dr Anawat Suppasri and Prof Fumihiko Imamura for hosting me in Japan for several months.

And my main thanks goes, of course, to my supervisor Professor Tiziana Rossetto, who has been not only a mentor but a role-model in all things.

Finally, I would like to dedicate this thesis to my beautiful wife Natsuko for her endless support, and to my perfect daughter Maya who entered this world half-way through Chapter 4!

Contents

Table of Figures

Table of Tables

Terminology

Terminology used through this thesis is summarized below.

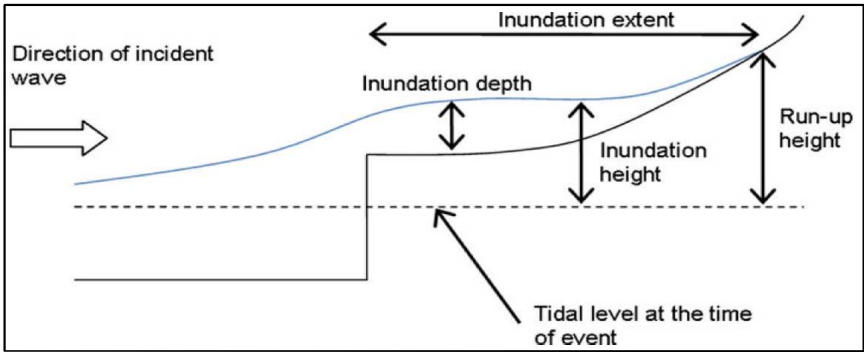

Schematic diagram defining tsunami terminology used in this paper (adapted from Fraser et al., 2012).

ρ	Density
μ	Mean
a	Tsunami loading coefficient (Japanese design standards
B	Building Width
BA	Building Attribute
C_D	Drag coefficient
CHPO	Constant-height pushover
CoV	Coefficient of Variance
DM	Damage Mechanism
DS	Damage State
F	Force
F_{drag}	Hydrodynamic drag force
FE	Finite Element
$F_{hydrostatic}$	Hydrostatic force
F_{qs}	Quasi-steady force (referring to the load estimation defined by Foster et al 2017)
Fr	Froude Number
g	Acceleration due to gravity
GAM	General Additive Model
GEJE	Great East Japan Earthquake and Tsunami
GLA	Energy Grade-Line Analysis
GLM	Generalized Linear Model
h	Inundation depth
IM	Intensity Measure
LC	Load case
MF	Moment-flux
MLIT	Ministry of Land Infrastructure Tourism and Transport (Japan)
MMF	Moment of momentum-flux
OLS	Ordinary Least Squares
PO	Pushover analysis
PTVA	Papathoma Tsunami Vulnerability Assessment
THA	Time-History Analysis
TIM	Tsunami Intensity Measure
v	Velocity
VHPO	Variable-height pushover

Accronyms and symbols used throughout the thesis.

1 Introduction

1.1 Background

Tsunami are long propagating waves that travel at high speeds across large bodies of water (e.g. oceans), typically generated by large scale seafloor displacements (e.g. earthquakes or landslides) or underwater explosions (NOAA n.d.). When they reach coastal areas, they can inundate up to several kilometres inland. As a result, large tsunami often cause many deaths and costly damage or destruction to infrastructure in the coastal region (Table 1-1).

Table 1-1: The selection of major historic tsunami and their impact. (Armijo, Lacassin, & Delorme, 2010; Camfield, 1980; EEFIT, 2011a; Lynett, Borrero, Liu, & Synolakis, 2003; Rabinovich & Thomson, 2007; Satake, 1995; Siripong, 2006; Wilson, Dengler, Legg, Long, & Miller, 2010).

Year	Location	Cause	Max. wave height (m)	Runup (m)	Number of deaths or missing	Cost (USD)
1755	Lisbon, Portugal	Earthquake	6	30 (Algarve)	20000	No information
1883	Java & Sumatra, Indonesia	Volcanic eruption	37	35 (Merak, Java)	36000+	No information
1896	Sanriku, Japan	Earthquake	9.1 (Shira-hama)	24.4 (Hawaii)	27000+	No information
1958	Lituya Bay, Alaska	Landslide (aerial)	51	516	2	No information
1992	Nicaragua	Earthquake	1.17 (Puerto Sandino)	9.9	170	25 M
1998	Papua New Guinea	Submarine landslide	10	4.2	3000+	No information
2004	Indian Ocean	Earthquake	3+ (Sri Lanka)	15+ (Cape Coral)	275000	> 15 B
2010	Chile	Earthquake	2.5	27 (Constituçion)	400+	> 15 B
2011	Japan	Earthquake	15	40.5	20000+	122-235B

Tsunami are responsible for 33% of total deaths and 35% of total economic losses due to natural catastrophes globally over the past two decades (Guha-Sapir, Below, & Hoyois, 2015), and currently threaten 6 out of 10 of the world's most populous megacities (Government Office for Science, 2012). Following recent large events (i.e. Indian Ocean

2004, Chile 2010 and Japan 2011) significant resources have been dedicated worldwide to improve tsunami hazard models. This has resulted in significant advances being made in the identification of tsunamigenic earthquake sources and their activity, and in the modelling of tsunami propagation and inundation both numerically and experimentally (Ingrid Charvet, 2012; Tiziana Rossetto, Allsop, Charvet, & Robinson, 2011). However, quantification of tsunami risk to the urban environment also requires estimation of building damage for a given inundation.

The most widely accepted definition of risk to natural hazard in the built environment is the one provided by Cricthon (1999), which can be applied to tsunami risk as shown in Figure 1-1.

Tsunami Risk = Tsunami Hazard X **Vulnerability** x Exposure

Tsunami hazard =	The probability of a potentially damaging tsunami occurring at a site within a given period of time.
Vulnerability =	The likelihood of losses (financial and casualty) given a tsunami of a particular intensity.
Exposure =	Quantification of the number of people and buildings at risk.

Figure 1-1: The components of tsunami risk. Vulnerability is highlighted as it encompasses building damage estimation, the focus of this thesis.

The tsunami hazard in Figure 1-1 cannot be reduced, as it is determined by Nature, and may even potentially increase due to rising sea levels linked with climate change. Global exposure in Figure 1-1 is increasing as a result of global trends such as growing coastal populations due to rapid urbanization of coastal cities and higher urban densities causing people to settle in marginal “at risk” locations (Tiziana Rossetto, 2013).

Therefore from Figure 1-1 it is clear that reducing vulnerability is key to reducing tsunami risk to a site. Building vulnerability assessments form the basis for any plan of risk mitigation and transfer by governments, insurers, developers etc, and have important applications for future tsunami risk mitigation through engineering design, human and financial loss estimation, and land use and emergency planning.

Vulnerability assessments relate losses (financial and casualty) to a measure of tsunami intensity. Note that, similar to earthquake terminology, “intensity” describes a tsunami’s effect at a particular location (where as “magnitude” describes the total energy released by a tsunami), and an “intensity measure” (TIM) refers to the parameter used to quantify

the intensity (e.g. inundation depth or flow velocity). Whilst some vulnerability assessment methods directly relate probable losses to tsunami intensity, more detailed assessments separate the assessment of likely building damage (fragility assessment) from the estimation of losses due to that damage (the loss model), as shown in Figure 1-2. The fragility (sometimes referred to as “physical vulnerability”) in this case can be expressed either as a damage matrix, damage function or fragility curve, each of which relate an indicator of building damage versus a measure of the tsunami intensity at the location of each building considered.

Vulnerability = **FRAGILITY** X LOSS Model

Fragility =	The probability of building damage given a tsunami of a particular intensity.
Loss Model =	Probable losses (financial and casualty) for a given level of building damage.

Figure 1-2: The components of vulnerability. Fragility is highlighted as it is the focus of this thesis.

Damage matrices (Table 1-2) state the expected Damage State (DS) to be experienced above a TIM threshold (e.g. collapse where inundation depth > 2m). Damage functions give the average expected DS for a particular building type for a given TIM. Fragility curves (Figure 1-4) are a family of cumulative distribution functions that provide the probability of a given type of building exceeding specified damage states (each individual curve represents a specific DS) for a given TIM. Vulnerability curves (Figure 1-5) are cumulative distribution functions that relate expected human or financial losses to a TIM.

Damage matrices and damage functions provide a deterministic framework for determining damage (i.e. for a given intensity they specify a level of damage). Therefore, they do not represent aleatoric uncertainty (statistical or random error) in the building DS. I.e. they do not model the realistic situation that for a given TIM there are a range of damage states that a building could occupy, each with a given probability of occurring.

Fragility functions quantify the probability of falling within each DS and so go some way to represent the aleatoric uncertainty. They are therefore the preferred method for fragility analysis for the purpose of quantitative risk or loss analysis. Financial and casualty loss modelling is outside of the scope of this thesis and so vulnerability functions will not be considered, and the remainder of this thesis will focus on presenting improved methods for derivation of fragility functions.

Tsunami intensity	0	1	2	3	4	5
Tsunami height (m)	1	2	4	8	16	32
Damage : wooden house	partly damaged	completely destroyed				
Damage : masonry house	withstand		no data	completely destroyed		
Damage : reinforced concrete building	withstand			no data	completely destroyed	
Damage : fishing boats		damage	50% damage	completely damaged		

Table 1-2: Damage Matrix, defining the expected DS for a given TIM ("tsunami height" indicates "tsunami inundation depth" according to the terminology of this thesis).

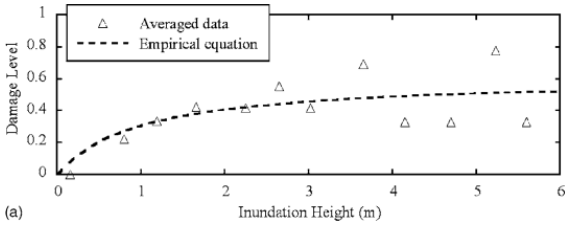

Damage level (D)	Value
No damage	0
Damage to secondary members	0.33
Damage to primary members	0.67
Collapse	1.00

Figure 1-3: Damage function (Ruangrassamee, Yanagusawa, Foytong, & Al., 2006), graphically defining the expected DS for a given TIM ("tsunami height" indicates "tsunami inundation depth" according to the terminology of this thesis).

Proportion of buildings damaged to each DS

at 2m inundation depth:

- 5% buildings at Damage State 1 (100%-95%)
- 20% buildings at Damage State 2 (95%-75%)
- 25% buildings at Damage State 3 (75%-50%)
- 20% buildings at Damage State 4 (50%-30%)
- 30% buildings at Damage State 5

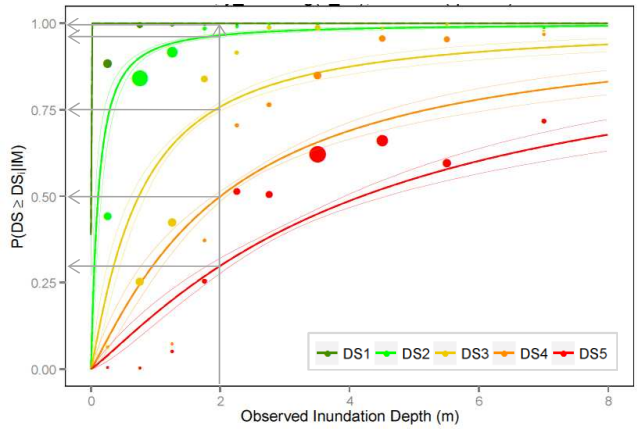

Figure 1-4: Fragility functions (Joshua Macabuag, Rossetto, & LLoyd, 2014b), graphically defining the probability of buildings falling within a number of damage states for a given TIM.

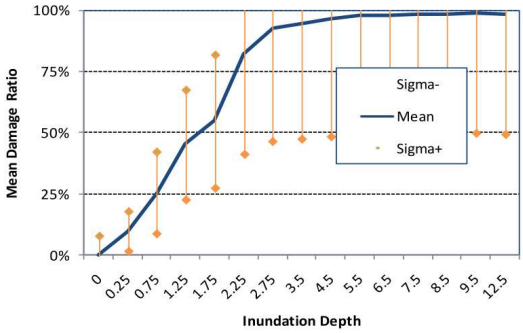

Figure 1-5: Vulnerability function (Masuda, Williams, Shahkarami, Rafique, & Bryngelson, 2012), graphically defining the expected damage ratio (cost of repair/cost of replacement) for a given TIM.

Tsunami fragility relationships are derived from inundation and damage data. Consistent with the terminology used by the Global Earthquake Model, regardless of how tsunami

inundation information (x-axis) is gathered fragility functions can be classified based on how the building damage data has been sourced: empirical (through studies of damaged buildings), judgment-based (through expert elicitation), analytical (through numerical simulations) or hybrid (a combination of the above).

Compared to seismic studies, few fragility functions for buildings affected by tsunami exist, and the vast majority have all been based solely on empirical data. However, the applicability of empirical tsunami fragility functions for buildings is limited by the availability and quality of data from past events. Similar construction types from different countries or regions can perform very differently under the same tsunami conditions (Anawat Suppasri et al., 2013), and so the correct application of empirical fragility functions is therefore very specific to the locations from where damage data was taken. Analytical techniques are therefore required to generate tsunami fragility functions for the majority of at-risk locations around the world where tsunami damage data is not available, and so analytical fragility functions will be addressed in this thesis.

1.2 Aim

This thesis presents research into improved methods for of empirical and analytical tsunami fragility function derivation for buildings. The over-arching aims of this research are as follows:

1. Critically evaluate the existing literature related to the prediction of building damage due to tsunami.
    a. Evaluate the existing suite of tsunami fragility functions.
    b. Assess existing relationships for estimating tsunami-induced loading on onshore structures.
    c. Review building damage mechanisms and methods of structural analysis under tsunami loading.
2. Define the preferred statistical methods and optimum intensity measure (TIM) for use in tsunami fragility function analysis.
    a. Investigate improvements to fragility function accuracy that can be gained from using advanced statistical methods.
    b. Test different estimations of force and other TIMs for their ability to correlate with observed damage statistics from past tsunami.
    c. Investigate methods for evaluating and treating the effect of debris on fragility function derivation.
3. Develop methods for analytical fragility function derivation.
    a. Examine structural behaviour under tsunami loading.
    b. Investigate optimal structural analysis methods suitable for analytical fragility function derivation.

1.3 Structure of Report

Chapter 2 presents a critical review of the literature related to the prediction of building damage due to tsunami. Types of building damage observed due to tsunami are categorized (section 2.2) and the current state of the art on probabilistic damage prediction is reviewed (section 2.3), highlighting that methods are required to generate fragility functions by structural analysis. Therefore, definitions of tsunami loading are critically reviewed and quantitatively compared, and methods of structural analysis under tsunami loading are examined (section 2.4). Finally, a summary is made of highlighted research needs (section 2.5).

Chapter 3 frames the research question and sub-questions that will enable the step-wise investigation of improved methods for developing empirical fragility functions, and methods for deriving analytical fragility functions in the absence of past damage data.

Chapter 4 identifies the key Tsunami Intensity Measures (TIMs) and improved statistical methods to be used for fragility function derivation, and derives empirical fragility functions using a detailed, disaggregated building damage dataset. Firstly, exploratory analysis of the dataset is conducted (section 4.2), and then regression analysis is conducted to demonstrate improved statistical methods proposed to define the optimal fragility functions (section 4.3). The analysis is then repeated using numerical tsunami inundation model results to identify the TIM which most successfully describes the observed damage (section 4.4). Finally, a preliminary methodology for quantifying debris-related effects on fragility functions is presented (section 4.5).

Chapter 5 presents research towards the development of analytical tsunami fragility functions. It is first shown analytically that an Elastic-Perfectly-Plastic Single Degree of Freedom structure can maintain a load greater than its yield load for a duration of time (section 5.2), i.e. if overstrength influences structural capacity. A sensitivity analysis is then conducted (section 5.3) to determine the effect of damping, strain-hardening and load-duration on overstrength. The chapter concludes (section 5.4) by investigating a simplified method of estimating structural capacity under tsunami loading on the basis of the above analyses, suitable for use in the large number of analyses required to derive analytical fragility functions of populations of buildings.

Chapter 6 summarizes the study and outlines key conclusions.

1.4 Research Outputs

The work presented in this thesis builds upon research published or submitted in the following publications.

Journal Papers

- Macabuag J., Raby A., Pomonis A., Nistor I., Rossetto T., Wilkinson S. (2017). *Tsunami Design Procedures for Engineered Buildings: A Critical Review*. **Proceedings of the Institution of Civil Engineers: Structures and Buildings** (submitted).
- Rossetto T., Macabuag J., Petrone C., Eames I. (2017). Investigation of New Relationships for Considering Ductility in the Assessment of Structures Under Tsunami Loading. **Earthquake Spectra** (submitted).
- Macabuag J., Rossetto T., Ioannou I. (2017). Investigation of the Effect of Debris-Induced Damage for Constructing Tsunami Fragility Curves for Buildings, **Geosciences** (submitted).
- Charvet I., Macabuag J., Rossetto T. (2017). *Estimating Tsunami-Induced Building Damage Through Fragility Functions: Critical Review and Research Needs*. **Frontiers in Built Environment - Earthquake Engineering**, Aug 2017.
- Macabuag J., Rossetto T., Ioannou I., Suppasri A, Sugawara D., Adriano B., Imamura F., Eames I., Koshimura S., (2016). Investigation of Optimum Intensity Measures and Advanced Statistical Methods for Constructing Tsunami Fragility Curves for Buildings. **Natural Hazards**, Aug 2016.
- Raby A., Macabuag J., Pomonis A., Wilkinson S., Rossetto T. (2015). *Implications of the 2011 Great East Japan Tsunami on sea defence design*. **International Journal of Disaster Risk Reduction**, 14, 332–346.

Conferences

- Macabuag J., Rossetto T., Ioannou I., Suppasri A, Sugawara D., Adriano B., Imamura F., Eames I., Koshimura S., Proposed Methodology for Defining Optimal Intensity Measures for Empirical Tsunaml Fraglllty Functions, **Proc. 16th World Conference on Earthquake**, Santiago, Jan 2017.
- Macabuag J., Rossetto T., Ioannou I., (2016), Investigation of the Effect of Debris-Induced Damage for Constructing Tsunami Fragility Curves for Buildings, **Proc. 1st International Conference on Natural Hazards & Infrastructure**, 28-30 June, 2016,Chania, Greece.

- Macabuag J., Rossetto T., (2014). Towards the Development of a Method for Generating Analytical Tsunami Fragility Functions, **Proc. 2nd European Conference on Earthquake Engineering and Seismology**, Istanbul, Aug 2014.
- Macabuag J., Rossetto T., (2014). Sensitivity Analysis of a Framed Structure Under Several Tsunami Design-Guidance Loading Regimes, **Proc. 2nd European Conference on Earthquake Engineering and Seismology**. Istanbul, Aug 2014.
- Macabuag J., Rossetto T., Lloyd T., Structural Analysis for the Generation of Analytical Tsunami Fragility Functions, **Proc. 10th US National Conference on Earthquake Engineering**, Alaska, USA, Jul 2014.

Books

- Suppasri A., Macabuag J., et al. (2015). *Building Damage Assessment and Implications for Future Tsunami Fragility Estimations*. In, **Handbook of Coastal Disaster Mitigation for Engineers and Planners** (p. 147–178), Jul 2015.

Reports

- *EEFIT Japan Team, Recovery Two Years After the 2011 Tohoku Earthquake and Tsunami*, **Institution of Structural Engineers (online)**, www.istructe.org/resources-centre/technical-topic-areas/eefit/eefit-reports, Dec 2013.
- *EEFIT Japan Team, The Mw9.0 Tōhoku Earthquake and Tsunami of 11th March 2011*, **Institution of Structural Engineers (online)**, www.istructe.org/resources-centre/technical-topic-areas/eefit/eefit-reports, Dec 2011.

2 Literature Review

2.1 Introduction

This chapter presents a critical review of the literature related to the prediction of building damage due to tsunami.

The chapter begins by categorizing the types of building damage observed due to tsunami (section 2.2). The current state of the art on probabilistic damage prediction is then reviewed (section 2.3). Section 2.3.1 categorizes various methods for tsunami damage prediction highlighting fragility functions as the preferred method, and then summarizes the currently available tsunami fragility functions. Methods for quantifying, measuring and estimating building damage (the response variable being predicted by fragility functions) and tsunami intensity (the explanatory variable used to predict damage) are presented in sections 2.3.2, and 2.3.3, respectively. Section 2.3.4 summarizes the statistical methods for deriving fragility functions. This review highlights that existing methods are primarily empirical, many based on data in Japan, and therefore, that alternative methods are required for damage prediction in areas without empirical data.

A proposed methodology for addressing the current gap in tsunami building damage prediction is to generate fragility functions by structural analysis. Hence, various aspects of fluid-structure interaction are investigated in section 2.4. Methods of estimating inundation parameters are briefly discussed in section 2.4.1, and definitions of tsunami loads on structures are critically reviewed and quantitatively compared in section 2.4.2. Section 2.4.3 outlines structural analysis methodologies under tsunami loading. A high degree of variability in the resulting load-estimates is found, demonstrating high uncertainty not only in determining the tsunami inundation parameters, but also in understanding their effects on buildings.

Finally, section 2.5 presents a summary of identified research needs to be addressed in the remainder of this thesis.

This thesis focuses on the prediction of building damage subjected to tsunami onshore flow, and so source, propagation and inundation modelling approaches will not be discussed in detail. This thesis specifically focuses on damage prediction applications in catastrophe modelling (i.e. concerning the assessment of existing buildings). Hence, engineering applications (e.g. fragility functions used for performance-based design) and

prescriptive code-based design will not be considered. Building codes will however be discussed in the context of their presentation of tsunami loading definitions.

2.2 Observed Building Damage and Failure Mechanisms Under Tsunami Loading

Tsunami fragility functions link probabilities of building damage with a measure of tsunami inundation. Therefore, in order to investigate fragility functions it is necessary to first consider the types of loading that tsunami impose on buildings, and the types and mechanisms of damage that can occur as a result.

The 2011 Great East Japan Earthquake and tsunami (2011 GEJE) lead to the investigation of tsunami-induced effects on engineered structures (G. Y. K. Chock, Robertson, Kriebel, Francis, & Nistor, 2013; EEFIT, 2011b, 2013). In addition to preceding seismic damage (Figure 2-1) this event exhibited tsunami-induced building damage and failure due to several tsunami effects as well as from the combination of these effects. Figure 2-2 shows a categorization of tsunami loads and effects on buildings. This thesis focuses specifically on the effects of fluid loading.

There are several methods for grouping building damage (G. Y. K. Chock, Robertson, Kriebel, et al., 2013; Fukuyama, Kato, & Ishihara, 2013) considering global lateral deflection, out-of-plane failure of walls, disproportionate collapse (from the failure of load-bearing elements) and foundation effects (e.g. scour, sliding and overturning) (EEFIT, 2013). Figure 2-3 shows a categorization of observed damage mechanisms (DMs) which will be referred to throughout this thesis.

Figure 2-1: Preceding seismic damage. Indicated by conjugate shear cracking of facade in Kamaishi. (photo: EEFIT)

Fluid Loading	• Hydrostatic forces (of the form ~$k\rho gh$):
	  ○ Lateral fluid pressure;
	  ○ Vertical buoyancy effects;
	• Hydrodynamic forces (of the form ~$k\rho hu^2$):
	  ○ Drag;
	  ○ Bore impact (i.e. the impulse applied by the leading edge of the incoming flood).
		 **(a)**  **(b)**

Debris	• Impact from large water-borne objects (e.g. cars, ships, shipping containers, trees, building fragments etc.) (a function of the debris mass and velocity and the time taken to bring the debris to rest); • Increase in flow viscosity/density due to entrained smaller debris/sediment; • Damming (filling of openings with debris, increasing the effective area experiencing lateral load).	 **(c)**  **(d)**
Foundation Effects	• Scour: loss of material about foundations • Reduced bearing capacity due to increased pore pressure	 (e)  (f)

Figure 2-2: Tsunami Loads and Effects observed during the 2011 Great East Japan Earthquake and Tsunami (all images: EEFIT (2011), characterization consistent with ASCE 7-16).

a) Minami Gamou Wastewater Treatment Plant): RC walls in deformed by primarily hydrostatic pressure (analysed by G. Chock & Robertson (2013)).

b) Residual deformation to an RC building.

c) Evidence of a large debris impact on the top floor of overturned RC-framed building in Onagawa (collapse likely due to combination of drag, buoyancy, debris and seismic damage).

d) Openings dammed in Shichigahama by debris.

e) and f) Scour undermining foundations (left: Arahama, Sendai) (right: Onagawa).

	Damage Mechanisms		
Non-structural Damage	 DM1.1: Flood Damage to Contents	 DM1.2: Damage to Cladding/Finishes	
Local Structural Damage	 DM2.1: Member Failure	 DM2.2: Load-Bearing Wall Failure	
Global Superstructure Failure	 DM3.1: Global Lateral Deflection/Failure	 DM3.2: Progressive Collapse	
Foundation Failure	 DM4.1: Overturning	 DM4.2: Sliding	 DM4.3: Bearing Failure

Figure 2-3: Tsunami-induced damage and failure mechanisms (EEFIT, 2011b). Note that all of these failures may have been caused by a combination of several tsunami effects (lateral fluid forces, buoyancy, debris impact and foundation effects) and ground shaking. The given Damage Mechanism references are used throughout this thesis. Note that DM4.2 shows sliding damage of a seawall rather than a building, as there are few images of buildings sliding which have not also failed due to additional mechanisms such as overturning.

2.3 Tsunami Fragility Functions

This section provides a critical review of the existing literature on tsunami fragility functions to be addressed in this study. As this thesis looks to improve both empirical and analytical fragility techniques, section 2.3.1 summarizes existing fragility studies in both categories separately. So as to identify research gaps present in the literature as a whole, the key components of fragility functions are expanded on in subsequent sections, namely the response variable (building damage, section 2.3.2), explanatory variable (the Tsunami Intensity Measure, TIM, section 2.3.3) and the statistical model which links the two (section 2.3.4).

2.3.1 Existing Fragility Assessment Methods

Tarbotton et al. (2015) presents a review of existing empirical tsunami fragility functions, comparing 17 studies and providing basic suggestions on improvements. However, some of these comparisons are not very qualified in the text (e.g. damage state definition comparisons are useful but subjective), and Tarbotton's discussion of statistical methods is basic, stating only past precedent with no discussion of the advantages and disadvantages of the various statistical approaches employed with no discussion of parameter estimation methods. The literature review presented in this thesis considers a larger number of empirical fragility studies than Tarbotton et al. (2015), includes analytical tsunami fragility functions and goes into much greater depth regarding each component of the fragility functions, particularly the statistical analysis used to define the model parameters.

Alongside the published studies reviewed in the following sections, there are also substantial proprietary investigations carried out by commercial catastrophe risk modelling companies using confidential insurance loss information. Whilst these cannot be included in this thesis, the comprehensive review and recommendations presented here are of significance to modellers and model developers interrogating or developing these proprietary functions.

2.3.1.1 Qualitative Fragility/Vulnerability Assessments

An alternative method to fragility function analysis for assessing the potential for building damage and loss is the Papathoma Tsunami Vulnerability Assessment (PTVA) Model (Dominey-Howes, D Papathoma, 2006; Papathoma, Dominey-Howes, Zong, & Smith, 2003) which assigns a relative "Building Vulnerability" score to buildings, which are then used to highlight areas that are most at risk.

The PTVA assessments are based on visual screening of buildings (on the ground or remotely). They assign scores to structural characteristics thought to contribute to the building vulnerability as well as additional factors such as the presence of seaward obstacles. The final score is obtained by weighting each component score with weights calibrated through observations from past tsunami. Note that according to the GEM terminology being used in this thesis (T Rossetto, Ioannou, Grant, & Maqsood, 2014), the Building Vulnerability score is actually a measure of fragility, as it reflects the likelihood of buildings experiencing physical damage. Human vulnerability is a function of the building vulnerability and the population exposed.

The relative vulnerability scores provide a qualitative assessment of fragility, which is useful in identifying individual buildings with a high potential for damage. However, these methods cannot be directly used for quantitative loss assessment and fragility functions are the preferred method for application to quantitative risk analyses (Figure 1-1). Therefore, PTVA will not be considered further in this thesis.

2.3.1.2 Empirical Fragility Functions

Empirical fragility functions are based on observed damage data from tsunami events. Table 2-1 shows existing empirical tsunami fragility functions for the 1993 Japan tsunami, 2004 Indian Ocean tsunami, 2009 Samoa Tsunami, and 2010 Chilean Tsunami. Table 2-2 shows existing empirical tsunami fragility functions for the 2011 Japan tsunami.

In Table 2-1 and Table 2-2, TIM indicates the Tsunami Intensity Measure assigned to each building, discussed in detail in section 2.3.3 (h = inundation depth, v = velocity, F = drag force, MF = momentum flux, MMF = moment of momentum flux, F_{QS} = a new proposed quasi-steady force estimate). The explanatory variable data-source describes how the TIM was determined for each building (sim. = numerical inundation simulation). The response-variable data-points indicate the number of buildings in the study (- = data not given in the reference, Aggr. = aggregated, note that all data is aggregated when used in OLS models, see below and section 2.3.4). Response variable data-source indicates how damage data was collected (remote = satellite or aerial imagery, survey = visual inspection in the field). #DS indicates number of damage states (including DS0, so that #DS=2 indicates 1 fragility curve, generally collapse). The model column indicates the statistical model describing the fragility function (OLS = standard linear model with parameters estimated via ordinary least squares, GLM = generalized linear model using maximum likelihood parameter estimation with various link functions, see section 2.3.4).

It can be seen that there are many more fragility functions derived from data for the 2011 Japan tsunami (19 fragility functions) than for all previous tsunami combined (11 fragility functions). This is indicative of the unprecedented quantity and quality of data that became available following the 2011 Japan tsunami, where an unprecedented number of detailed damage surveys were carried out by authorities such as Japan's Ministry of Land Infrastructure Tourism and Transport (MLIT) which provided a database of all of the houses (over 200,00) within the tsunami inundation zone.

Existing fragility functions cover several construction types, including engineered structures in Japan (RC, steel, masonry and timber), and primarily non-engineered structures in Thailand, Indonesia and Samoa. Some studies consider construction year (Amakuni & Terazono, 2011; Anawat Suppasri, Charvet, Imai, & Imamura, 2014) and number of stories (Anawat Suppasri et al., 2013, 2014) in defining their building classes, though most do not make this distinction. The majority of studies use normal or lognormal models with Ordinary Least Squares (OLS) parameter estimation, with improved models (e.g. Generalised Linear Model, see section 2.3.4) becoming more widely used in more recent studies.

Until the 2011 Great East Japan Earthquake and Tsunami (2011 GEJE), no fragility curves existed for engineered buildings. Furthermore, tsunami fragility curves were based on aggregated empirical datasets where building damage statistics for a number of different geographical areas (of small or large size) are combined, with each such area assumed to be associated with a single TIM value. For example, Peiris (2006) constructs curves using data from the entire SW and SE coasts of Sri Lanka. Even in cases where disaggregated data is available researchers have at times aggregated the damage observations over areas with similar TIM values, e.g. Suppasri et al. (2012). The vast majority of existing fragility curves are determined from aggregated empirical data using linear regression models and Ordinary Least Squares (OLS) parameter estimation. However, Charvet et al (2014) and Rossetto et al. (2014) show that OLS regression in these cases is not theoretically correct as several of the linear model assumptions are violated by the data. For example, OLS regression assumes that errors are normally distributed, when in fact damage data is binary (damaged/not damaged), or ordinal (falling into one of several damage state categories). Charvet, et al. (2014) postulate that Generalized Linear Models (GLMs) should provide an improvement over OLS for deriving fragility curves, as they allow for a relaxation of some of the assumptions, but do not compare the results of using this statistical model fitting approach to more complex non-parametric alternatives. Furthermore, no existing study has quantifiably assessed the effects of data aggregation and OLS linear model assumption violation on model predictive power.

Table 2-1: Published empirical fragility functions for the 1993 Japan tsunami, 2004 Indian Ocean tsunami, 2009 Samoa Tsunami, and 2010 Chilean Tsunami.

Reference		Explanatory Variable			Response Variable			Model	Comments
		Tsunami Event	TIM	Data-Source	Data-points	#DS	Data-Source		
EF1	(Koshimura & Kayaba, 2010)	Japan 1993	h,v,F	sim.	769	2	Remote	OLS	In Japanese. Curves for Hokkaido, Japan
EF2	(Pomonis & Peiris, 2005)	Indian Ocean 2004	h	Survey	45,714	4	Survey	OLS	Curves for SW and SE coast of Sri Lanka
EF3	(W. P. S. Dias, Yapa, & Peiris, 2009)				33,900				Curves for Sri Lanka, compared with analytically derived curves
EF4	(Koshimura, Oie, Yanagisawa, & Imamura, 2009)		h,v,F	sim.	48,910	2			Curves for Banda Aceh, Indonesia
EF5	(Anawat Suppasri, Koshimura, & Imamura, 2009)				-		Remote		Curves for Phang Nga, Thailand
EF6	(Murao & Nakazato, 2010)		h		1,535	4	Survey		Compares curves with other authors'
EF7	(A. Suppasri, Koshimura, & Imamura, 2011)		h,v,F		4,596	2	Remote		Compares curves for Phang Nga and Phuket, Thailand
EF8	(Valencia, Gardi, Gauraz, Leone, & Guillande, 2011)		h	Survey	2,576	6	Survey, Remote		Error about datapoints and mean curve indicated (Banda Aceh, Indonesia)
EF9	(Gokon, Koshimura, & Matsuoka, 2009)	Samoa 2009	h,v	sim.	902	2	Remote	OLS	Curves for Tutuila Island, American Samoa
EF10	(Reese et al., 2011)		h, debris	Survey	201	5	Survey	GLM	First use of GLM (American Samoa). Considers curves w/wo debris and sheltering.
EF11	(Mas et al., 2012)	Chile 2010	h	sim.	915	2	Remote	OLS	Curves for Dichato, Chile. Visually compares curves from various countries

Table 2-2: Published empirical fragility functions derived from data for the 2011 Great East Japan Earthquake and Tsunami.

Reference		Explanatory Variable		Response Variable			Model	Comments
		TIM	Data-Source	Data-points	#DS	Data-Source		
EF12	(Amakuni & Terazono, 2011)	h,v,F	Survey	8,653	2	Remote	OLS	Compares multiple locations (Miyagi, Japan) and multiple construction years
EF13	(Nihei, Maekawa, Ohshima, & Yanagisawa, 2012)	h		~5,000		Survey, Remote		Curves for Natori, Japan (in Japanese)
EF14	(Koshimura & Gokon, 2012)			157,640				Compares curves for various locations across Japan (in Japanese)
EF15	(Yanagisawa & Yanagisawa, 2012)			202		Survey		Curves for Sendai, Japan (in Japanese)
EF16	(Anawat Suppasri, Mas, Koshimura, et al., 2012a)			189	5			Visually compares curves from Sri Lanka and Miyagi (Sendai and Ishinomaki), Japan
EF17	(Anawat Suppasri, Mas, Charvet, et al., 2012)			251,301 (aggr.)	6			Uses aggregated government survey data
EF18	(Maruyama, Kitamura, & Yamazaki, 2013)	h,v,F		>335	2			Curves using data for Chiba prefecture, Japan. Does not specify number of non-collapsed buildings in survey.
EF19	(Hayashi, Narita, & Koshimura, 2013)			8,244				Flow velocities validated against observations
EF20	(Anawat Suppasri et al., 2014)	h		63,605	6			Compares topography, number of floors, building use, construction year, material (Ishinomaki, Japan), using disaggregated data.
EF21	(Charvet, Ioannou, Rossetto, a. Suppasri, et al. 2014)			178,448 (aggr.)			GLM	Compares ordered and partially ordered models, various link functions, and quantifies inclusion of building class, for aggregated data.
EF22	(Charvet, Suppasri, et al. 2014)			56,950				Separates data by terrain type: plain, narrow coast (backed up by high topography), and river, for Ishinomaki, Japan, for disaggregated data.
EF23	(Narita & Koshimura, 2015)			64,860	2		OLS	Damage data for each curve collated according to topographic features, building distribution, sea defences, ground elevation and slope.
EF24	(I Charvet, Suppasri, Kimura, Sugawara, & Imamura, 2015)	h, v, debris	sim.	19,815	6		GLM	Kesennuma, Japan (disaggregated data). Concludes that debris has significant effect on fragility functions. Fragility surfaces also presented.
EF25	(Tanaka & Kondo, 2015)	MF, MMF		-	2		OLS	Recommends switching between fragility functions for high and low Froude cases. Does not specify the number of buildings surveyed.
EF26	(Tanaka, Onai, & Kondo, 2015)	h, MF, MMF						
EF27	(Macabuag et al. 2016a)	h, v, MF, F, Fr, F_{QS}	Survey sim.	67,125	6		OLS GLM GAM	Treatment of missing data. Proposed TIM and model optimisation method. First use of GAMs for tsunami fragility.
EF28	(Macabuag et al. 2016b)	h, v, MF, F, Fr, F_{QS}, debris					GLM GAM	Inclusion of debris has large effect on fragility, which can be quantified.
EF29	(De Risi, Goda, Mori, & Yasuda, 2016)	h	Survey	147,668			OLS GLM	First use of Bayesian Methods to investigate the effect of uncertainty in inundation observations. Effect on loss estimates also considered.
EF30	(De Risi, Goda, Yasuda, & Mori, 2017)	h,v	sim.	>200,000			GLM	Fragility surfaces. Show velocity important in coastal plains.

The intensity measure (independent variable) represented in a fragility curve should provide the best possible representation of the damage potential of the tsunami inundation. Tsunami-induced building damage can arise due to hydrostatic forces (including buoyancy), hydrodynamic effects (drag and bore impact) and debris (impact and damming). The severity of these effects is determined by a number of flow parameters, yet the majority of existing tsunami fragility curves adopt the local maximum inundation depth as the TIM, often because it can be estimated from post-tsunami reconnaissance of buildings and also from numerical modelling of tsunami inundation. Other parameters of the flow can also be derived from inundation modelling, with more or less reliability, (depending on the numerical code used, its validation and the refinement in grid size). Velocity and hydrodynamic force (approximated by the standard form-drag equation) have been used as TIMs in some recent studies (e.g. Koshimura et al. 2009 and Charvet et al. 2014). Tanaka and Kondo (2015) consider momentum flux (an indicator of drag force) and moment of momentum flux (the product of momentum flux and inundation depth, thought to be a proxy for the overturning moment induced by the flow) in deriving their fragility curves. They further recommend using different fragility curves for flow conditions characterised by high and low Froude numbers (a measure of flow velocity non-dimensionalised by the gravity wave velocity, indicating the flow regime such that Fr<1 indicates sub-critical flow and Fr>1 indicates choked flow). Overall these studies do not show a consensus as to which flow parameter is the most appropriate TIM to estimate fragility (discussed in section 2.3.3).

2.3.1.3 Analytical Fragility Functions

Analytical tsunami fragility functions are based on synthetic damage data derived from structural analyses, and allow for quantification of risk even in the absence of empirical building damage data. The use of analytical fragility functions is well established in seismic risk assessment (Baker, 2013; Meslem & Ayala, 2012; Tiziana Rossetto & Elnashai, 2005). However, few analytical tsunami fragility functions have been published. This section evaluates the literature and highlights gaps that will be addressed in Chapter 5.

The current analytical fragility function literature (Table 2-3) The structural analysis methods are discussed in more detail in section 2.4.3, but introduced here to enable the discussion of the analytical fragility function literature which follows. Time-History Analysis (THA) is a stepwise analysis of a structure's dynamic response to a specific load which may vary with time. PushOver analysis (PO) is a nonlinear static analysis whereby a structure is loaded (generally into the post-yield region) by an incrementally increasing lateral force. Constant-Height Pushover (CHPO) is a variable of the traditional

PO, where force is incrementally increased whilst a fixed inundation depth is maintained. Variable Height Pushover (VHPO) instead increases force by incrementally increasing inundation depth.

Table 2-3 summarizes existing analytical tsunami fragility functions. Inundation parameters are generally determined as per FEMA 646 (denoted as <*variable*>=*FEMA*¸ discussed in section 2.4.1.2), or as random variables with either uniform distributions (denoted *uni(a,b)*, where *a* and *b* denote the lower and upper limits of the distribution) or lognormal distributions (denoted *Lognormal(μ,CoV)*, where *μ* and *CoV* denote the mean and Coefficient of Variance of the distribution). Force estimation methods are denoted either hydrostatic, drag, or quasi-steady (see section 2.4.2.4). The 'pressure distribution' column describes the vertical distribution of lateral pressure (see section 2.4.2.2). Under 'structural model', *FE* denotes Finite Element, and *mechanistic* denotes empirical calculation of specific failure mechanisms.

Table 2-3a: Published analytical tsunami fragility functions.

Reference		Explanatory Variable				Response Variable				Statistical Model	Comments
		TIM	Determination of Inundation Parameters	Force Estimation Method	Pressure Distribution	Structural Model	Data-points	#DS	DS Estimation Method		
AF1	Dias et al. (2009)	h	h≈unif(0,H_{max})	hydrostatic + drag	triangular, uniform	mechanistic (masonry)	33,900	2	F > $F_{capacity}$	OLS	Compares empirical and analytical curves for the SW and SE coast of Sri Lanka
AF2	Park et al. (2012)	h	$h \approx Lognormal(\bar{h}, CoV)$ … $\bar{h}$≈unif(0,H_{max}) u=FEMA	hydrostatic + drag	triangular, uniform	SDoF (2-storey timber)	-	2	THA	OLS	Considers combined effect of earthquake + tsunami for single case-study building
AF3	S. Park et al. (2013)	h	$h \approx Lognormal(\bar{h}, CoV)$ … $\bar{h}$≈unif(0,H_{max}) u=FEMA	hydrostatic + drag	triangular, uniform	SDoFs (timber population)	1,422	2	THA	OLS	Extends Park et al. (2012) to consider population of buildings (Cannon Beach, Oregon, USA)
AF4	Kircher & Bouabid (2014)	h	-	drag	uniform	seismic PO curves	-	3	seismic ISD thresholds	OLS	Compares tsunami load with HAZUS seismic capacity curves for USA
AF5	Nanayakkara & Dias, (2016)	h	h≈unif(0,H_{max})	drag	bilinear triangular	mechanistic (masonry, RC)	1,000,000	2	F > $F_{capacity}$	OLS	Monte Carlo simulation for masonry and RC structures typical of Srilankan construction types. Collapse load capacities are calculated for simplified structural models

Table 2-3b: Published analytical tsunami fragility functions (cont.).

Reference		Explanatory Variable				Response Variable				Statistical Model	Comments
		TIM	Determination of Inundation Parameters	Force Estimation Method	Pressure Distribution	Structural Model	Data-points	#DS	DS Estimation Method		
AF6	(Attary, van de Lindt, Unnikrishnan, Barbosa, & Cox, 2016)	h MF MMF	h≈unif(0,H_{max}) u≈unif(0,$v_{Fr<2}$)	drag	uniform	FE (multistorey steel)	10,000	5	CHPO (seismic ISD thresholds)	Non-parametric cumulative distribution	Monte Carlo simulation varying tsunami and structural properties, to generate fragility surfaces.
AF7	(Alam, Barbosa, Scott, Cox, & van de Lindt, 2017)	h MF MMF	h≈unif(0,H_{max}) u≈unif(0,$v_{Fr<2}$)	drag	uniform	FE (multistorey RC)	960	2	CHPO	GLM	Uses First-Order Second-Moment Method to develop multiple structural models. Considers changes in opening sizes, and individual member failure.
AF8	(Karafaglial, Fotopoulou, & Pitilakis, 2017)	h	h≈unif(0,H_{max}) u=FEMA	drag + bore + debris	uniform	FE (multistorey steel, RC)	-	5	CHPO (element material-strain thresholds)	OLS	Develops curves for Seaport buildings and Warehouses in Greece. Building-specific strain thresholds were defined through pushover analysis.
AF9	(Petrone, Rossetto, & Goda, 2017)	h F_{QS}	inundation simulations	quasi-steady	triangular, trapezoidal	FE (multistorey RC)	803	2	CHPO VHPO THA	GLM	Compares multiple capacity estimation methods and pressure distributions, utilizing inundation simulations of Tohoku, Japan

Seismic analytical fragility functions provide a probabilistic link between a seismic Intensity Measure (IM) and the structural response, represented by an Engineering Demand Parameter (EDP). Multiple damage data points are formed by repeating structural analysis for a range of IMs and a range of building configurations within the constraints of the building type being considered. The expected damage state is assigned to each analysis based on EDP thresholds, and statistical regression methods are then applied to this damage data set to generate fragility functions.

The following studies are discussed further in the Appendix A.

Analytical methods are also considered for flood and windstorm fragility assessments. Nadal et al (2010) models the failure mechanisms of structural components due to fluvial flood damage, using Monte Carlo simulation to account for uncertainty in structure and inundation depth and hydrodynamics (waves, turbulent bores, debris impacts, time dependent local soil scour), presenting 3D damage functions as output. De Risi et al. (2013) and Kelman & Spence (2004) model structural components, incrementing depth and velocity and comparing with a threshold force which defines failure. For engineered structures, the HAZUS hurricane model (FEMA, n.d.) considers multiple non-structural components (roof, cladding, openings), comparing loads due to wind and wind-borne debris to threshold values.

In the case of tsunami, Dias et al. (2009) used Monte Carlo simulation of simple non-engineered structures to verify empirical tsunami fragility functions. They derived the structural fragility by estimating sliding and overturning failures, corresponding to Damage Mechanism DM4.1 and DM4.2 in Figure 2-3. Loading was calculated based on a range of inundation depths, where depth was treated as a random variable with a uniform distribution for values between 1.5m-9.14m, and triangular distribution for values <1.5m. Nanayakkara & Dias, (2016) extend this methodology to consider masonry and reinforced concrete (RC) buildings representative of Sri Lankan construction. Collapse values were calculated for multiple typical building configurations, where sliding was assumed as the masonry failure mechanism. RC collapse was assumed to occurr at the formation of a plastic hinge mechanism calculated for a simplified frame and cross-strut (modelling the in-fill panel) model. Inundation depth was then simulated one million times, and for each time a building was randomly selected, and a force was calculated and compared to the structure's collapse force. As structural capacity for both studies was calculated mechanistically, it is unclear if epistemic uncertainty may arise from unconsidered failure mechanisms. It is also unclear whether comparison of peak load

and statically-derived structural capacity sufficiently captures collapse probability, which will be investigated further in Chapter 5.

Kircher & Bouabid (2014) generate analytical tsunami fragility functions for use in the new proposed HAZUS tsunami model. Non-structural and contents damage is estimated based entirely on inundation depth in relation to floor levels. Structural damage is calculated by equating hydrodynamic loads, calculated according to FEMA (2012), with HAZUS seismic structural capacity curves for the individual building types under investigation. It is argued that fewer damage states are required to calculate tsunami loss than for seismic loss ("slight damage" is excluded, and "moderate" and "extensive" damage states are not included for shorter structures). The structural system is considered undamaged until initial yield, and collapse occurs at the ultimate capacity of the structure. Failure due to individual element failures, progressive collapse and foundation damage is ignored. Note that by using seismic capacity curves Kircher & Bouabid (2014) are assuming that a structure's capacity curve under seismic and tsunami loading regimes are the same (i.e. for the same base shear induced by seismic or tsunami loading, the structural response such as deflection will be the same). However, seismic and tsunami loading are fundamentally different in their distributions, points of application (as well as very different time-dependent effects), and so this assumption will be examined in Chapter 5.

Park et al. (2012) created tsunami fragility functions for a 2-storey timber frame building, by conducting multiple non-linear time-history analyses of an equivalent single-degree-of-freedom (SDoF) system. Loading was calculated as the summation of hydrostatic and drag components as defined by FEMA (2012). Tsunami inundation depths were generated that had mean values from 0.0m to 5.0m in 0.1m increments, a coefficient of variance (CoV) of 13.5%, and an assumed lognormal distribution. The fragility was calculated from the proportion of simulations for which the load (demand) exceeded the capacity of the structure. The fragility equation assumes a lognormal distribution, and parameters were estimated using least-squares regression. The analysis was carried out for the cases of tsunami only, design basis earthquake (DBE) followed by tsunami and maximum credible earthquake (MDE) followed by tsunami, where the preceding earthquake reduced the capacity of the structure (calculated via non-linear time-history analysis) prior to tsunami loading. Park et al. (2013) then combined fragility functions for multiple structures in order to derive a collapse fragility function for a given town. It should be noted that in Park et al. (2012) the derived fragility functions are observed to be sensitive to the CoV chosen. This suggests that the suite of TIM data must be selected

carefully when deriving analytical fragility functions, and it is unclear the criteria for selecting an appropriate suite of tsunami data.

Attary et al. (2016) uses Monte Carlo simulation to generate analytical tsunami fragility functions for a three-storey steel structure. The methodology used is shown in Appendix A. A structure is generated, and for a given depth and velocity, the force is calculated. A constant-height pushover (see section 2.4.3) is carried out for the given inundation depth up to the specified force, assuming a uniform vertical distribution of lateral pressure. Depth and velocity are incremented to try all combinations defined by Fr<2, up to a maximum considered tsunami depth. Inter-storey Drift (ISD) is used as the EDP and compared with seismic ISD-thresholds for each damage state, though it is acknowledged that new tsunami-specific EDP thresholds should be developed. Alam et al (2017) extend the work of Attary et al. (2016), to additionally consider shear and flexural failure of individual members. As an alternative to the very many iterations required by Monte Carlo simulation, First-Order Second-Moment (FOSM) analysis is instead conducted to sample variable material and geometric properties and develop 32 variations of the structural model. Of the variables considered, it was found that openings and breakaway panels were the largest sources of uncertainty in the model. It was also found that member failure (rather than simply global failure) has a significant effect on the fragility functions, with global failures tending to overestimate capacity. It is not clear whether the method chosen for generating input tsunami loadings is optimal. For example, at a given inundation depth the full range of velocities are explored with equal weighting, whereas it might be more accurate to consider that for a given depth some velocities are more likely than others.

It is not clear whether the method of varying depths around a mean for a series of mean depths (Attary et al., 2016; S. Park et al., 2013, 2012) is optimal. This approach dopes not capture aleatoric uncertainty in the loading. It models uncertainty in the inundation model (or depth survey data) but fragility functions should define the probability of damage exceedance at a given TIM value. The aleatoric uncertainty derives from information that is not captured by the TIM. I.e. fragility functions do not represent variation in the hazard, but variation in the response given a TIM (e.g. for a given depth, a range of velocities and debris densities may be experienced, resulting in a range of responses).

Karafaglial et al (2017) develop curves for Seaport buildings and Warehouses in Greece. Damage states were defined based on building-specific material strain thresholds, which were defined through pushover analysis following the methodology set out in macabuag

2014. It is noted that, by limiting the damage definition to use only material strain as the Engineering Demand Parameter (EDP) misses global and storey-level failures. Furthermore, althoough various combinations of drag, bore and debris impacts were applied to the structures, it is not clear how the relative number of iterations for each scenario were defined, making the resulting fragility functions difficult to assess. This again highlights a lack of concensus on the definition of input loadings for which to derive fragility functions.

Petrone et al., (2017) compares several methods of structural analysis under tsunami loading, and their effects on fragility function derivation. Fragility functions are created for a case-study 10-storey RC tsunami evacuation building in Japan. Both triangular and trapezoidal vertical distributions of net lateral pressure are considered. Multiple capacity estimation methods are compared (discussed in detail in section 2.4.3). Inundation simulations of Tohoku, Japan are utilized to derive 803 wave traces (tsunami time-histories, each derived from numerical inundation simulation). Structural capacity obtained from pushover analysis (CHPO and VHPO) is compared with the peak forces applied by each wave trace to define whether the building has collapsed. Regression is then preformed on the collapse/survived datapoints. The same is done for THA of the 803 traces, where collapse is defined when an inter-storey drift ratio (IDR) corresponding to the peak force is reached. Results compare well, indicating capacity curves obtained by the constant-height and variable-height pushovers can be used to derive fragility functions for the collapse damage state, with VHPO being shown to be the preferred methodology.

The above studies show a wide range of structural models and methods for defining damage states from that model (discussed in detail in section 2.3.1.3), as well as of methods for deriving a suitable suite of tsunami inundation parameters, showing that there is no consensus in these areas for the derivation of analytical fragility functions.

2.3.2 The Fragility Function Response Variable: Building Damage

Empirical fragility functions are based on observed damage data and analytical functions on synthetic data. This thesis utilizes both methods, and so issues associated with damage data collection and derivation, as highlighted by the literature, are discussed in this section.

The tsunami damage scales for buildings that can be found in the literature are often not consistent and are seen to have different Damage State (DS) definitions and a varying number of DSs (as shown by the studies presented in Table 2-1 and Table 2-2). The

damage scale used by the Japanese Ministry of Land Infrastructure Tourism and Transport (MLITT) following the 2011 GEJE are shown in Table 2-4. With reference to the Damage Mechanisms categorized in Figure 2-3, only non-structural damage (DM1) is implied by damage states DS1-DS3 and structural damage (DM2-6) is implied by DS4-DS6. This thesis conducts empirical fragility analysis of data from MLITT building damage database for the 2011 GEJE (Chapter 4), and so the damage scale in Table 2-4 will be referred to throughout.

Table 2-4: Damage state definitions used by the Japanese Ministry of Land Infrastructure Tourism and Transport following the 2011 Great East Japan Earthquake and Tsunami. Descriptions from Japan Cabinet Office (2013), usage descriptions from Suppasri et al. (2014). This damage scale will be referred to throughout this thesis.

Damage State		Description	Use	Image
DS1	Minor Damage	Inundation below ground floor The building can be reused by removing mud below the floor boards	Possible to use immediately after minor floor and wall cleanup.	
DS2	Moderate Damage	The building is inundated less than 1m above the floor (can be reused after a repair)	Possible to use after moderate repairs.	
DS3	Major Damage	The building is inundated more than 1m above the floor (below the ceiling)	Possible to use after major repairs.	
DS4	Complete Damage	The building is inundated above the ground floor level.	Major work is required for re-use of the building.	
DS5	Collapsed	The key structure is damaged, and difficult to repair to be used as it was before	Not repairable.	
DS6	Washed Away	The building is completely washed away except for the foundation	Not repairable.	

A number of alternative damage scales (e.g. EEFIT (2011b)) are presented in Appendix B. Mc Cullagh and Nelder (1989) states that damage scales for fragility analysis must follow two rules:

1. Levels of response (DSs) are mutually exclusive,
2. Each new response should correspond to an increase in intensity (i.e. of the hazard IM).

The damage scale in Table 2-4 (and many of the scales presented in the Appendix B) violate the first rule above. For example, buildings with inundation below the ground floor ceiling, DS3, could experience collapse, DS5. Therefore inspectors inspecting a building which falls into multiple DS categories is presented with a subjective choice as to which DS to assign. Charvet, et al (2014) highlight that the descriptions of DS5 and DS6 of the MLITT damage scale (Table 2-4) also violates the second rule. Note also that the MLITT damage scale shows an assumed direct correlation between the hazard intensity (inundation depth in this case) and damage, in that depth is specified directly in the DS descriptions for DS1-DS3, and so structural response is not actually considered by these definitions. These violations have implications for the uncertainty in the observations for empirical studies and for defining damage as a function of structural response for analytical studies, both issues which will be considered when using the damage scale throughout this thesis.

Empirical building damage data is collected either via ground survey (visual inspection), or remotely (aerial or satellite photography). Remote sensing allows for the rapid collection of large amounts of data. However, the limitation on satellite remote sensing damage surveys is that the only detectable damage state is often “total collapse” (and where intermediate damage states are included, their accuracy is low), meaning that accurate fragility functions cannot be formed for partial collapse states (e.g. all studies in Table 2-1 and Table 2-2 utilising remote sensing consider only 2 damage states). Construction material can often not be determined remotely. Ground surveys can determine material and intermediate damage states. However, surveys take much more time than remote sensing, and uncertainty is introduced due to combining data from surveyors of differing experience, segregation of data collected to damaged buildings only, errors in survey forms, or combination of data from different surveys.

Damage/fragility/vulnerability curves derived from empirical damage data are very specific to the location being investigated and cannot typically be generalized or applied to similar structures in a different geographical location (Figure 2-4). E.g. fragility functions derived from data prior to 2011 often represent non-engineered buildings, which limits their application to risk assessment of more highly developed coastlines.

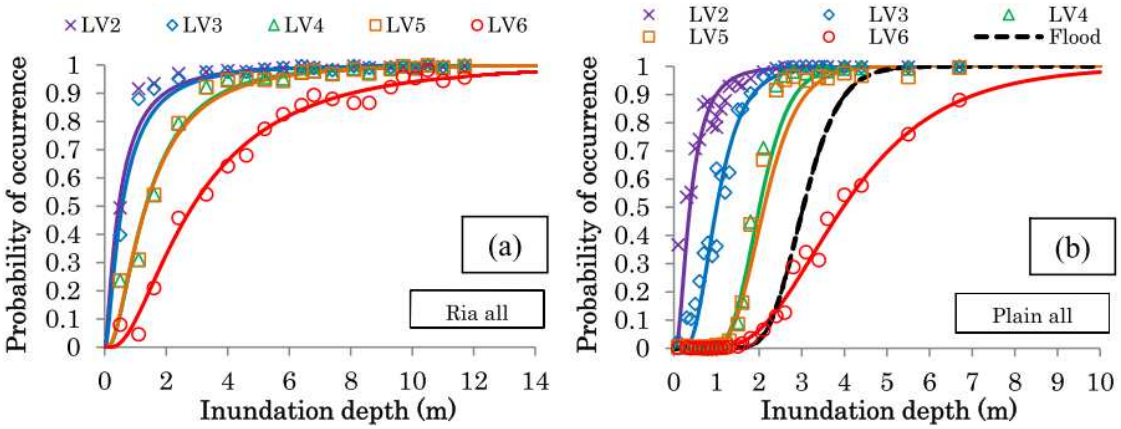

Figure 2-4: Fragility functions for ria coast (left) and plain coast (right), but both from the same city of Ishinomaki, Japan (Anawat Suppasri et al., 2014).

In the case of an earthquake-generated tsunami where damage is surveyed in the near-field regions, it is likely that the earthquake has damaged buildings before the tsunami's arrival (Figure 2-3). If the tsunami-induced damage cannot be separated from the earthquake-induced damage, this creates bias in the data (T Rossetto, Ioannou, & Grant, 2012), which is difficult to remove for empirical studies.

In order for the fragility results to be representative of the different structural responses to tsunami loading, typically buildings are classified according to structural properties and analysis is carried out on each class separately. Building attributes which govern tsunami performance are summarized in Table 2-5. Suppasri et al. (2014) considers structural material, height, occupancy and date of construction (concluding that date of construction did not greatly affect tsunami performance). All other existing studies consider structural material only. However, the building classifications are not consistent between studies. For example, Tinti et al. (2011) divides masonry buildings into 5 sub-classes of structures with varying construction materials and numbers of stories, and Valencia et al. (2011) consider two types of masonry-structures (class B and C). Fragility functions from different studies can often not be compared for this reason.

It has been shown that aggregating damage data by building type (i.e. creating "general" fragility functions) gives less-accurate results for large damage states, but has less effect for lower damage states where damage is non-structural (Reese et al., 2011). Therefore, grouping buildings into non-structural classes (e.g. lines of business used in the insurance industry: commercial, residential, industrial) will give a good representation at lower damage states, but have greater uncertainty at higher damage states, due to a high variation of structural performance within the building class.

Table 2-5: Building attributes which govern tsunami performance (BA1-BA10). Note that material is the only attribute considered in existing studies, with the exception of Suppasri et al. (2014).

Building Attribute		Description	Example
BA1	Material of the Lateral Load-Resisting System	Structural material.	RC
BA2	Lateral Load-Resisting System	Structural system for resisting lateral loads.	Shear-wall
BA3	Redundancy of Vertical Load Paths	When a building is only supported by a limited number of structural elements (e.g. 4 columns), floating debris damaging one or two columns may trigger disproportionate collapse of the structure.	3% wall-density on plan
BA4	Building Height	Number of stories. Will govern member sizes.	Low-rise
BA5	Openings (and break away walls)	Reduce the visible cross-sectional area to oncoming flow, so allows for the hydrostatic and hydrodynamic pressures not to accumulate on the front face of the building. (Ruangrassamee et al., 2006; EEFIT 2006; Suppasri et al., 2012)	10% openings
BA6	Shape and Orientation	Building orientation has a direct effect on induced drag forces (Dominey-Howes, D Papathoma, 2006; Lloyd, 2014) with bluff bodies experiencing a greater force than those with leading walls that are not orthogonal to the flow.	Bluff
BA7	Foundations	Deep foundations will reduce the vulnerability of the structure to scour around the base (Jackson et al.,2005; Ruangrassamee et al., 2006; Ghobarah, et al., 2006; Pomonis et al., 2011).	Shallow
BA8	Soil Conditions	Uplift forces will develop more quickly for buildings founded on porous soils (Harry; Yeh, Barbosa, Ko, & Cawley, 2014). Scour will be enhanced by erodible soils such as sand, and a lack of protection such as pavements (Rossetto et al., 2006; Pomonis et al., 2011).	Sand
BA9	Date of Construction	Affects the design standards followed during construction (e.g. pre/post seismic codes) and the likelihood that materials have degraded during the lifetime of the building.	Pre-code
BA10	Occupancy	Building use or line of business (for insurance modelling).	Commercial
BA11	Material of External Envelope	Lower DSs are defined by water ingress into the building footprint. Some building enveloped are more permeable (e.g. light cladding panels) than others (e.g. solid masonry).	Timber cladding

Issues with current damage data used in the literature are therefore summarized as follows:

- Inconsistency in damage scales,
- Uncertainties inherent in the data collection techniques,
- Specificity of the derived function to the area and environmental conditions being surveyed,
- Separation of seismic and tsunami damage,
- Inconsistency in building classes.

These issues will be considered in both the empirical and analytical assessments of this thesis.

2.3.3 The Fragility Function Explanatory Variable: Tsunami Intensity

The TIM (the x-axis of fragility functions, representing the explanatory variable in regression analysis) represents the structural demand that a given tsunami places on the building being investigated.

Table 2-6 lists existing tsunami intensity measures. The intensity measure most commonly seen in the published literature on tsunami fragility is inundation depth, as it is the most readily definable parameter from post-tsunami surveys and numerical inundation simulations. However, various studies have indicated that the sole use of inundation depth does not adequately describe observed damage at higher damage states (Charvet, et al 2014). Tsunami magnitude is not included as a TIM as it is a function of offshore wave characteristics only and is not building specific. Run-up is not included as it is not building-specific, though it can be used to estimate building-specific inundation depths. Additional building-specific parameters which would affect the TIM at building location include: distance/elevation from the shore, and sheltering by surrounding buildings and obstacles (shown to reduce flow velocities and the propensity of debris (Daniellsen, 2005; EEFIT, 2010, 2013)). However, these are not IMs but rather parameters which should be taken into account when estimating the TIM at building locations (discussed in section 2.4.1).

A single TIM may not capture all of the relevant tsunami information necessary to predict structural damage, and so it would be beneficial to consider additional intensity measures also. One possibility is to use complex TIMs which combine multiple simpler TIMs (e.g. momentum flux used by Koshimura et al. 2009). Alternatively, multiple regression allows for several intensity measures to be included in the model simultaneously (Figure 2-5). However, fragility surfaces are currently seldom used in practice for quantitative loss estimation and it is always the aim to develop a “parsimonious model” (the best model for the fewest predictors) as using additional intensity measures requires more data points and difficulties of obtaining these additional tsunami parameters must be overcome.

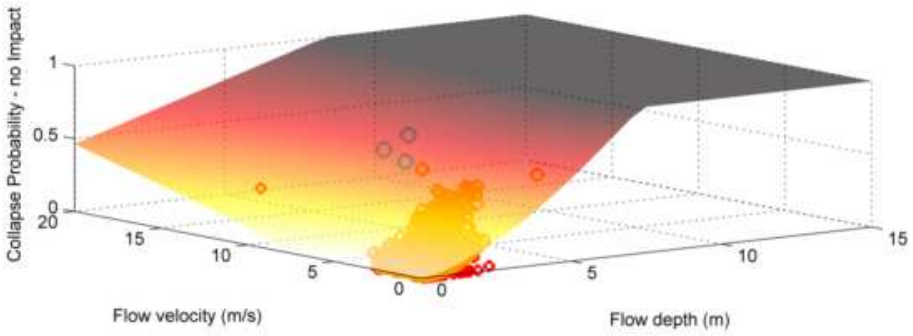

Figure 2-5: Seismic fragility surface considering two intensity measures (I Charvet et al., 2015)

Table 2-6: Tsunami Intensity Measures. Note all have been used in some existing studies, except duration of immersion. TIM1 – TIM3 will be considered in this thesis.

TIM		Comments
TIM1	Inundation Depth	Can be relatively well quantified in post tsunami surveys. It can also be calculated from inundation models more accurately than other flow parameters (see section 2.4.1).
TIM2	Flow Velocity	Hard to determine from observations and difficult to calculate accurately from inundation simulations (section 2.4.1).
TIM3	Fluid Forces	Cannot be directly measured in a post-disaster survey. Studies using this TIM rely on numerical inundation simulation and estimation of force using the standard functions of depth and velocity (section 2.4.1) (e.g. it can be represented by drag force or momentum flux). Tanaka & Kondo (2015) considers moment of momentum flux, as a measure of overturning potential.
TIM4	Duration of Immersion (and number of waves)	Additional waves provide multiple impulsive impacts on the structure. The structure also experiences load-reversal due both to inflow and draw-down. Longer duration loading allows for time-dependent deflections and dynamic effects to evolve, and increases degradation of non-engineered structural materials (e.g. wood). Difficult to obtain from post-tsunami surveys (eye-witness accounts may be inaccurate).
TIM5	Debris Impact	Debris impact has been shown to have a significant influence on tsunami-induced damage (Reese et al., 2011; Charvet et al., 2014a), however this is difficult to assess in post-disaster surveys as debris is rapidly removed after the event.
TIM6	Level of Preceding Damage	Buildings experiencing near-field tsunami may have been affected by preceding ground-shaking, which could have reduced structural capacity (Figure 2-1). Park et al. (2013) is currently the only existing study to consider this.

There are no existing studies that adopt a rigorous approach to quantifiably compare the TIMs used and many consider only one damage state (i.e. collapse) in their assessments. Furthermore, all force estimations considered in previous studies have been based on the standard form drag equation. However, this does not account for alternative estimations such as equivalent hydrostatic methods (MLIT, 2011a), bore

impact (Robertson and Riggs, 2011) or changes in flow regime (Qi et al. 2014). Park et al (2014) compares damage estimates for a case-study town in the USA using fragility functions for depth, velocity and momentum flux, concluding that velocity and momentum flux provide the most realistic damage estimates, though this is only based on a qualitative visual assessment of damage locations and the authors acknowledge that this conclusion must be verified with field data.

In fluvial flood modelling, Kreibich et al. (2009) compare Flood Intensity Measures (FIMs) of depth, velocity, momentum flux, and energy head according to the Bernoulli Equation. FIMs are compared using Spearman's Rho correlation coefficients on a dataset of 256 buildings across 5 damage states. They concluded that for fluvial flooding depth and energy head have the strongest correlation with observed damage, momentum flux has a weak correlation and flow velocity has no correlation, although it is acknowledged that a much larger sample size is required in order to draw conclusive results.

Tsunami-induced building damage can arise due to fluid forces (hydrostatic and hydrodynamic) and debris effects (impact and damming). Various TIMs have been used in recent fragility studies to describe flow conditions, such as depth, velocity and hydrodynamic force (Koshimura et al. 2009, Charvet et al. 2014, Tanaka and Kondo 2015).

TIMs in existing fragility studies rarely specifically describe debris-induced damage. Charvet et al. (2014) generate fragility functions considering that debris is mostly composed of the remains of collapsed buildings, and as such designates buildings as having been affected by debris if they are within a given distance (distances from 10m to 150m are tried) of a building that has been washed away. However, this method does not make any allowance for the size of collapsed buildings or the number of collapsed buildings (i.e. one small collapsed structure, has the same effect as several large collapsed structures).

A number of analytical seismic studies have compared seismic Intensity Measures (TIMs) using the criteria of "efficiency" (the level of uncertainty in structural response conditional on the IM value, (Luco and Cornell, 2001)), "sufficiency" (the ability of the IM to describe structural response independently of other IMs or hazard characteristics, (Ebrahimian, et al. 2015) and "computability" (the ease of calculating the IM value, e.g. Giovenale et al. 2004). Minas et al. (2014) compared the efficiency of multiple seismic IMs in an analytical study whereby numerical analysis was used to estimate structural response, in terms of continuous Engineering Demand Parameters (EDP), to a range of

IM levels. In the latter, efficiency was determined by using OLS parameter estimation to fit a power law relationship for each IM ($EDP = \beta_0 IM^{\beta_1}$, where β_0 and β_1 denote the model parameters), and comparing the standard error of the residuals. However, for empirical studies, using real observed damage data, structural response is denoted by discrete damage states, and so it is not appropriate to fit a direct relationship between IM and damage state, but instead to the probability of exceedance for each damage state (i.e. fragility curves). However, to date no existing study has compared efficiency of multiple TIMs based on empirical fragility curves fit to observed damage data.

Issues with current estimations of tsunami intensity, as highlighted by the literature, are therefore summarized as:

- Inconsistencies in tsunami parameter definitions,
- Alternative intensity measures to depth are not utilized,
- Limitations of empirical tsunami data (measuring inundation),
- Limitations of physical inundation modelling (experiment-derived tsunami data),
- Limitations of numerical inundation modelling (simulation-derived tsunami data).

These issues show that further investigation is required into the definition and derivation of an appropriate TIM for tsunami fragility functions.

2.3.4 Model Quality and Statistical Model Fitting

There is a very wide suite of statistical models and fitting techniques that have been used in the literature define fragility functions, each with their own limitations. This section outlines the various statistical procedures that will be used in this thesis to derive fragility functions from damage and intensity data. More detailed descriptions of model derivations and assumptions, and alternative models, are given in Appendix A.

2.3.4.1 Representing Fragility Functions

Where defining deterministic relationships is unrealistic (e.g. predicting with absolute certainty the exact damage caused by a tsunami to each of a population of buildings) then statistical approaches are more appropriate to estimate likely responses. Statistical models describe relationships between a response variable (e.g. building damage, described by a damage state) and an explanatory variable (e.g. a tsunami intensity measure, TIM, such as inundation depth), allowing predictions to be made. Model fitting refers to the definition of model parameters so that the defined model follows the provided data points as closely as possible.

Tsunami fragility functions are often represented as cumulative distribution functions, derived by applying statistical model fitting techniques to building damage data for different tsunami intensities, for the purpose of making damage predictions for future tsunami. Statistical model fitting applied to fragility functions assumes that the probability of damage exceedance is a function of the intensity (TIM) and calculates the nature of that function based on sample damage data (where damage exceedance is defined as the probability that the damage state experienced by a building, ds, will be greater than or equal to a defined damage state, DS):

$$P(ds \geq DS|TIM) = f(TIM) \quad \textbf{(2-1)}$$

The main types of statistical models used to define $f(TIM)$ in the literature are as follows:

- Parametric Models:
    - Standard linear regression models, with Ordinary Least Squares (OLS) parameter estimation (Anawat Suppasri, Mas, Koshimura, et al., 2012b; Anawat Suppasri et al., 2009; Tanaka & Kondo, 2015).
    - Generalized Linear Models (GLMs) (I Charvet et al., 2015; Leelawat, Suppasri, Charvet, & Imamura, 2014; A. Muhari, Charvet, Tsuyoshi, Suppasri, & Imamura, 2015; Reese et al., 2011).
- Non-parametric models (Masuda et al., 2012).

The vast majority of existing fragility curves are determined from aggregated empirical data using linear regression models and Ordinary Least Squares (OLS) parameter estimation. However, Charvet et al (2014) and Rossetto et al. (2014) show that OLS regression in these cases is not theoretically correct as several of the linear model assumptions are violated by the data. For example, OLS regression assumes that errors are normally distributed, when in fact damage data is binary (damaged/not damaged), or ordinal (falling into one of several categories). Charvet, et al. (2014) postulate that Generalized Linear Models (GLMs) should provide an improvement over OLS for deriving fragility curves, as they allow for a relaxation of some of the linear model assumptions. GLMs relate the mean of a response variable ($E(y)=\mu$) to the explanatory variables (x_i) via an arbitrary link function (g). The link function is selected dependent on the distribution of the response variable, typically transforming the response such that $g(\mu)$ is a continuous variable bounded by $[-\infty,+\infty]$. As such, GLMs can be used for variables with distributions other than the Gaussian distribution assumed in OLS linear regression models.

The various GLM methods for deriving tsunami fragility functions are summarized in Table 2-7. Note that Table 2-7 is included here as a reference. The various model components will be described in more detail in Chapter 4, as they are being utilized for empirical fragility function derivation. GLM models have three components:

- A link function (which transforms the mean of the response variable, Table 2-8)
- A systematic component (the linear predictor (η) describing the mean of the response variable, via the link function, Table 2-7)).
- A random component (the error distribution of the response variable, e.g. binomial for the case of binary data).

If rigorous diagnostics reveal that the chosen GLM do not provide a satisfactory fit to the data, alternative methods such as General Additive Models (GAM) or non-parametric regression can be used. However, an issue with non-parametric models is that they are susceptible to over-fitting, and their appropriateness in the context of fragility analysis has not yet been demonstrated.

When collecting damage data for deriving fragility functions then there are numerous rules of thumb regarding the minimum number of data points recommended in order to generate a regression model. Rossetto et al. (2014) recommends a minimum number of 10 data points per predictor variable. Green (2010) states that the minimum sample size for a linear regression analysis depends on three parameters:

- alpha, the probability of committing a Type I error (i.e. incorrectly rejecting the null hypothesis);
- power, one minus the probability of making a Type II error (i.e. not rejecting a false null hypothesis);
- and effect size, the degree to which the criterion variable is related to the predictor variables in the population.

These parameters should ideally be considered when defining sample size.

Table 2-7: Summary of the components of GLM regression used for tsunami fragility function derivation (adapted from Charvet, Rossetto, Macabuag (2016)).

<table>
<tr><td rowspan="6">Input Data</td><td>Number of Damage Levels</td><td colspan="3">0 to K damage states ⇔ $K+1$ damage levels ($k = \{1, \dots, K+1\}$).</td></tr>
<tr><td>Number of TIM Observations</td><td colspan="3">1 to J (j = {1, …, J }). Applies to either J TIM bins for aggregated data, or J individual building TIM observations (x_j) for disaggregated data.</td></tr>
<tr><td>Data Aggregation</td><td colspan="3">If data is aggregated as counts of $n_{j,k}$ buildings, then the total number of buildings in each TIM bin is N_j.</td></tr>
<tr><td>Number of Explanatory Variables</td><td colspan="3">1 to I (i = { 1, …, I }). Where explanatory variable $TIM_{i,j}$ is the jth observation of the ith explanatory variable.</td></tr>
<tr><td>Type of Damage Response</td><td>Binary
$Y_{jk} = \begin{cases} 1 & if\ ds \geq DS_k \\ 0 & if\ ds < DS_k \end{cases}$
$Y_{jk}|x_j = Binomial\left(P(ds \geq DS_k|TIM = x_j)\right)$</td><td colspan="2">Multi-level Classification
$Y_k = \begin{cases} 0 & if\ ds \leq DS_1 \\ 2 & if\ DS_1 < ds \leq DS_2 \\ \dots & \dots \\ K & if\ DS_k < ds \leq DS_{k+1} \end{cases}$
$Y_{jk}|x_j = Multinomial\left(P(ds \geq DS_k|TIM = x_j)\right)$</td></tr>
<tr><td colspan="4"></td></tr>
<tr><td rowspan="4">Model Components</td><td>Model Name</td><td>Generalized Linear Model</td><td colspan="2">Cumulative Link Model</td></tr>
<tr><td>Random component (statistical distribution)</td><td>Binomial Distribution
$P(n_{j.k}\ in\ N_j) = \binom{N_j}{n_{j.k}} p_{ds \geq DS_k}^{n_{j.k}} (1 - p_{ds \geq DS_k})^{N_j - n_{j.k}}$</td><td colspan="2">Multinomial Distribution
$P(Y_1 = 0, \dots, Y_k) = N_j! \prod_{k=0}^{K} \frac{p_{ds \geq DS_k}^{n_{j.k}}}{N_j!}$</td></tr>
<tr><td>Systematic component (Linear Predictor η)</td><td rowspan="2">$\eta_k = \beta_{0,k} + \sum_{i=1}^{I} \beta_{i,k} TIM_i$</td><td>Ordinal Model</td><td>Partially-ordered Model</td></tr>
<tr><td>$\eta_k = \beta_{0,k} + \sum_{i=1}^{I} \beta_i TIM_i$</td><td>$\eta_k = \beta_{0,k} + \sum_{i=1}^{I} \beta_{i,k} TIM_i$</td></tr>
<tr><td>Fragility Function (μ)</td><td colspan="3">$P(ds \geq DS | TIM_i = x_{i,j}) = \mu_k = g^{-1}(\eta_k)$
Where g is the link function (e.g. Probit, Logit, cloglog).</td></tr>
</table>

Table 2-8: Typical link functions suitable for use in fragility function derivation.

Probit	Logit	cloglog
$g(\mu) = \Phi^{-1}(\mu)$	$g(\mu) = log\left(\frac{\mu}{1-\mu}\right)$	$g(\mu) = log\left(-log(1-\mu)\right)$

2.3.4.2 Representation of Uncertainty and Assessing Model Fit

Sources of aleatoric uncertainty (statistical error due to random variations) and epistemic uncertainty (systematic error due to errors in knowledge or judgement) in the derivation of seismic fragility functions is summarized by Ioannou et al. (2012). Unfortunately, most existing tsunami fragility studies do not include a systematic treatment of uncertainty, though bootstrap methods for construction of confidence intervals are employed by I. Charvet, Ioannou, Rossetto, A. Suppasri & Imamura (2014).

A detailed methodology for model building and evaluation in the context of empirical vulnerability assessment can be found in Rossetto et al. (2014). Note that for seismic vulnerability functions there is a rating system, published by the Global Earthquake Model (GEM), which can be used for deciding on the most appropriate curves to use, however this method of rating has not been used for tsunami fragility functions. This thesis will utilize several "goodness of fit" tests in order to assess how well a statistical model fits the damage data, to quantitatively compare models, and to choose the model with the best fit. The coefficient of determination (R^2) can be calculated in various ways and has different interpretations for OLS regression models and GLMs, and so should be supplemented by additional tests, comparison with alternative regression techniques and inspection of the underlying model assumptions.

Guidelines set out by Rossetto et al. (2014) recommend the use of the Likelihood Ratio Test (LRT) to compare nested models, as conducted by some recent studies (I. Charvet, Ioannou, Rossetto, a. Suppasri & Imamura 2014; Muhari et al. 2015). The likelihood statistic of a model describes the likelihood of observing the observations on which the model was fit, given the error distribution defined by that model. A more complex statistical model (one with more explanatory variables) will always fit the data on which it was fit, as well or better than a simpler model fit to the same data. The LRT tests whether the improvement in fit of a more complex model is statistically significant. The test utilizes the likelihood ratio test statistic (*D*) of two nested models, which is a function of the ratio of the models' likelihood statistics (2-2).

$$D = -2\log\frac{L_{simple\ model}}{L_{complex\ model}} \qquad \textbf{(2-2)}$$

The distribution of the test statistic *D* is approximately a χ^2 distribution, with degrees of freedom equal to the difference between the degrees of freedom of the two models being tested ($df_{simple\ model} - df_{complex\ model}$). By assuming this χ^2 distribution, the probability (or p-value) of *D* can be computed, with a p-value < 0.05 indicating a greater than 5% chance that the difference in deviance statistics D was developed from random chance, and so the more complex model can be rejected. The likelihood ratio test will be used in this study to compare nested models.

Guidelines set out by Rossetto, Ioannou, Grant, & Maqsood (2014) also recommend the use of the Akaike Information Criteria to compare non-nested models (e.g. two models fit to the same data using the same TIMs, but different link functions). However these techniques cannot easily be used to directly compare cumulative models (multinomial

random component, models with separate models (i.e. those with binomial and multinomial distributions, Table 2-7), nor to compare models formed on aggregated and disaggregated data.

Cross-validation techniques can be used to compare all of the model types in Table 4-3, and so is used to compare all models considered. Cross-validation is an improvement over simply plotting the residuals, as it attempts to indicate the prediction error (i.e. the proportion of incorrectly classified outcomes) that would be experienced on data that has not been used to form the statistical model. *K*-fold cross-validation creates *K*-fold partitions in the total dataset, and for each of *K* validation experiments uses 1 fold as the testing set (a different 1 each time), and the remaining data as the training set. The average of the error rates for all iterations gives an estimate of the true prediction error rate (Equation (2-3)). Cross validation has been used to estimate tsunami fragility curve prediction error rates by Muhari et al., (2015) and Charvet, Suppasri et al. (2014).

$$Error\ rate = \frac{1}{K}\sum_{k=1}^{K}\frac{n_{incorrect}}{N_{test\ set}} \qquad \textbf{(2-3)}$$

2.4 Quantifying Tsunami Loads and Effects on Buildings

Tsunami building damage predictions require quantification of tsunami loads on buildings. However, there is not a consensus in the literature as to the exact nature of these tsunami loads due primarily to difficulties of obtaining detailed observational data from past tsunami, challenges of conducting physical experiments of sufficient scale to represent tsunami waves, and the computational expense to reproduce these flows and their interaction with the built environment. This leads to there being a great deal of uncertainty in the spatial and temporal distribution of pressures imposed by tsunami on buildings, as well as the magnitude of resultant loads.

This section summarizes the key analytical, experimental and numerical studies conducted to define fluid loading on on-shore structures due to a tsunami propagating inland, and subsequent structural analysis under those loads. The focus of this section is on quantifying fluid loading once flow parameters have been established, though brief discussion is first made on determination of flow parameters at building locations (section 2.4.1). Key tsunami loading studies are then presented (section 2.4.2) considering: the general time-history profile; engineering design guidance documents (representing the culmination of several key studies); recent studies into tsunami-like long-wave loading effects associated with super- and sub-critical flow around obstacles; and quantitative comparison of the various loading estimate methodologies presented. Finally, various methods of structural analysis under tsunami loading will be evaluated (section 2.4.3).

This review summarizes the current state-of-the-art and research gaps that will be addressed throughout this thesis.

2.4.1 Determination of Inundation Parameters

Estimation of tsunami forces on onshore structures requires the flow regime at the structure location to first be determined. This may be achieved via stochastic or deterministic methods. A deterministic approach requires modelling of the tsunami source, deep sea propagation, near-shore and onshore inundation, and finally force estimation resulting from flow impingement on the structure. Source and deep-sea propagation modelling is beyond the scope of this study, but inundation estimation based on offshore conditions will be briefly discussed here, as the accuracy of these methods directly impacts on the accuracy of the final load estimate. Stochastic methods extend deterministic methods to capture uncertainty in tsunami loading and are beyond the scope of this thesis.

Calculation of the exact tsunami load time-history on a building requires estimation of flow-depth and velocities at the building location, as well as information on the vertical and horizontal distribution of pressures across the exposed surfaces. Quantification of these parameters is complex as flow behaviour in the nearshore and onshore regions is highly non-linear, and heavily dependent on local bathymetry, topography and obstacles (conditions which may change throughout the inundation period). For empirical fragility function derivation based on data from past tsunami, inundation depth can be estimated from field surveys, but it is difficult to obtain other parameters with accuracy (Section 2.3.3). For estimating additional parameters, or for investigating sites with no historical data, flow conditions may have been estimated from either historical precedent (shown to be an inadequate method of predicting future events), empirical flow estimation methods, or numerical inundation modelling techniques.

2.4.1.1 Observation of Tsunami Events

For empirical studies of past tsunami, flow depth can be measured using for example local water marks, or debris hanging on trees. If flow depth cannot be measured directly from an affected building (for example, the building has been washed away), Various interpolation methods can be employed to estimate parameters between observation location (Mas et al., 2012), though there will be error introduced by the interpolation.

Fritz *et al.* (2006) and Fritz *et al.* (2012) uses Particle Image Velocimetry (PIV) image analysis (tracking the displacement of a particle / object in video footage or time-stamped imagery). There are however, very few locations where this has been applied.

Run-up may be obtained by examining tsunami deposits, which is particularly useful for historic tsunami. Estimation of the mean velocity can be estimated using deposit thickness and grain size distribution (Liu *et al.,* 2005), or boulder transport (Jackson *et al,.* 2005). However, velocity estimates by this method are error prone and do not pick up spatial variations in velocity.

2.4.1.2 Empirical Estimation of Inundation Parameters

Offshore wave parameters can be obtained from deep sea propagation modelling. Empirical formulae may then be used to estimate tsunami run-up based on these offshore flow parameters (e.g. wavelength, wave height, potential energy, see Charvet et al. (2013)). Alternatively, inundation maps created by a number of methodologies may be obtained from local authorities and other organisations, and values of run-up can be obtained from these.

FEMA (2008) then provides a procedure for determining flow conditions from the estimated runup. It proposed the use of empirical relationships such as that presented in equation (2-4), where $(hu^2)_{max}$ is maximum momentum flux experienced at the building location of base elevation *z* above the still water level due to tsunami flow of maximum runup *R*. It is noted that this is based on the simplifying assumption of a beach which is uniformly sloping at a gradient of 1:20.

$$(hu^2)_{max} = gR^2\left(0.125 - 0.235\left\{\frac{Z}{R}\right\} + 0.11\left\{\frac{Z}{R}\right\}^2\right) \quad \textbf{(2-4)}$$

For the case where the beach cannot be approximated as uniformly sloping then Chock (2014) recommends the use of Energy Grade Line Analysis (GLA). Energy GLA is a hydraulic method which defines inundation depth and velocity, where velocity is calculated according to a Froude Number (*Fr*, a non-dimensionalised measure of velocity as a function of depth) assumed to decay with distance inshore as given in (2-5). In (2-5) typically $Fr_0 = 1$ unless bore conditions exist, in which case it is higher (Fr_0=1.3), as derived from numerical simulations (Kriebel et al., 2017). Note that GLA does not account for the fact that peak depth and peak velocity are not coincident. Instead, peak depth and peak velocity are related by Fr, which is itself determined by distance onshore, x. Depth is then determined from energy lost over a transec.

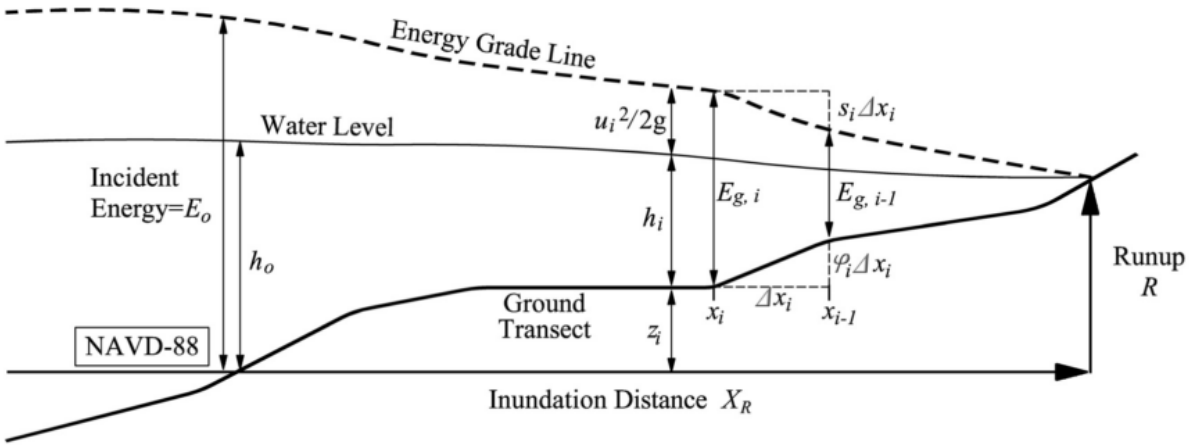

Figure 2-6: Grade Line Analysis (GLA) recommended in ASCE 7 (2016) (from G. Chock, 2014; Kriebel et al., 2017).

$$\boldsymbol{Fr = Fr_0\left(1 - \frac{x}{x_R}\right)^{0.5}} \quad \textbf{(2-5)}$$

Where it is not possible to accurately estimate flow velocities and pressures directly from an inundation model then it is useful to be able to estimate velocity (and pressure) from parameters that are more readily obtained from practical inundation simulations (i.e. inundation depth). There have been a number of studies to determine flow velocity as a function of depth during tsunami inundation, summarized in Lloyd (2014). Velocity

estimates are generally of the form shown in equation (2-6), consistent with the velocity estimate for the surge front from the classic dam-break problem (Keulegan, 1950). The definitions of both the constant term (*C*) and flow depth (*h*) vary between studies as shown in Figure 2-7. Foytong et al. (2013) related flow depths and velocities during the 2011 Japan Tsunami and found that the value of *C* in (2-6) varied between locations, indicating that a simple empirical estimate may not be sufficient for accurately calculating onshore flow velocities.

$$u = C\sqrt{gh} \qquad \textbf{(2-6)}$$

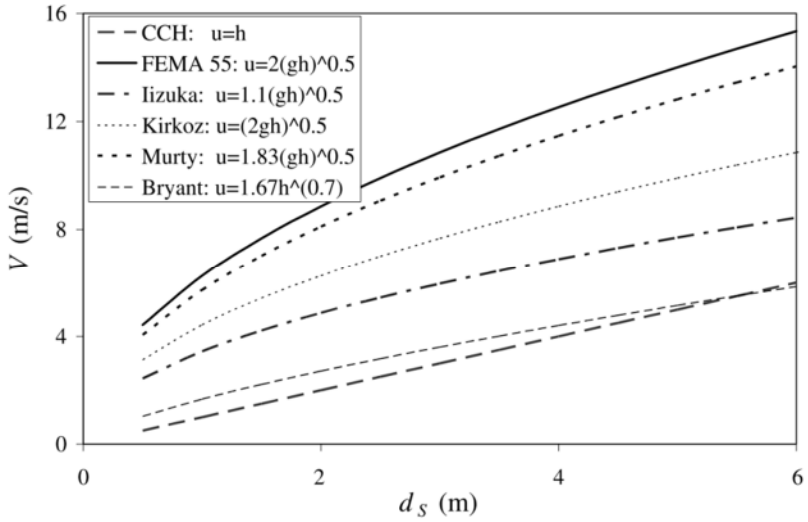

Figure 2-7: Tsunami flow velocities as defined by various studies and design standards (after Palermo et al. (2009)).

2.4.1.3 Numerical Modelling of Inundation

Numerical modelling of tsunami inundation is a complex problem in computational fluid dynamics where the surface of the fluid changes. Inundation models can vary in complexity from detailed 3D models considering flow around individual buildings, to simplified 2D models modelling built-up areas using a roughness factor and making assumptions regarding the depth distribution of velocities and pressures (Table 2-9). Full solution of the Navier-Stokes equations is too computationally expensive for resolving inundation flow parameters over large areas. Therefore, most tsunami inundation studies rely on simplified 2D approaches, whereby the wavelength to water depth ratio of a tsunami is large enough that it can be considered a shallow water wave, meaning that no vertical components of velocity or acceleration need to be included and pressure is regarded as hydrostatic. There are many proposals for shallow water wave simulation that have been used for tsunami modelling. Different techniques exist to solve the resulting equations, with the choice of technique (and so model) decided by considerations of complexity, accuracy and computational time.

Inaccuracies in inundation estimates stem from high sensitivity to the uncertainties/inaccuracies in the initial properties of the tsunami (shape and total energy) the near-shore bathymetry, the effect of wave breaking, the on-shore topography, the effect of buildings and other obstacles, which may move or alter throughout the inundation period. These inaccuracies are more pronounced for estimates of flow velocities and pressures (H. Park et al., 2014) unless a very fine mesh size is used which can accurately incorporate the effect of buildings and other obstacles. For inundation simulation in practice this is prohibitively time-consuming in both computation time and the required resources in accurately modelling a location and all buildings and obstacles to that accuracy. Furthermore, it is difficult to verify the accuracy of velocity and pressure estimates for the reasons highlighted above.

Table 2-9: A summary of numerical methods that have been used to define tsunami-induced forces on structures.

Inundation Modelling Methodology	Model Complexity	Formulation	Modelling of Buildings	Force resolution	Advantages	Disadvantages	Example software/ applications
2D model (no buildings)	Simplest ↓	Non-linear shallow water equations, or Boussinesq equation. Calculate depth-averaged flow properties.	Model topography only. Model urban areas as roughness factor, either one factor for whole zone.	2 methods: Difference in hydrostatic pressures on front face (calculated using Bernoulli's equation assuming stagnation at the face) and rear face of building (undisturbed flow depth). Form drag equation using undisturbed flow depth and velocity.	Simplest method (therefore most used in practice).	Accuracy of velocity calculation difficult to verify/validate in practice. Cannot capture any vertical components of flow. Cannot capture flow over/under structures.	Software: TUNAMI, MOST, COMCOT. Force resolution method 2 is that advocated in FEMA 646 and new ASCE 7-16.
2D model (with buildings)		As above	Buildings included in the model. Modify roughness factor per grid square based on the presence/absence of buildings.	Difference in hydrostatic pressures on front face and rear face of building (depths taken directly from the model).	Effects of urban environment on inundation more accurately captured.	Above cons of 2D modelling apply. Time-consuming to input individual buildings. Difficult to obtain accurate shape-size data for all buildings. Modelling grid resolution required to be adequately fine to allow individual buildings to be resolved.	Muhari et al. (2011) Software: as above.
Hybrid 2D-3D analysis		As above, for several vertical layers. Calculated quantities at the boundary of each layer, is used as the boundary condition for adjacent layer.	Both 2D methods above can be utilized.	As in 2D methods, for each vertical layer.	More vertical resolution of flow parameters. Flow over-under structures can be captured given sufficient vertical layer resolution.	More complex (set-up and computation) than 2D models.	Pringle et al. (2013)
3D model using Navier-Stokes equations	Most complex	Navier-Stokes equations.	Buildings/ structures in model.	Pressure distributions at structure surfaces taken directly from model.	Removal of 2D assumptions. Can capture turbulence complexities. Can capture flow over/under/through structure.	Computation prohibitively expensive for all but small-specific areas of interest (not practical for large-scale inundation calculation).	Software: DELFT 3D, STOC.

2.4.2 Tsunami Load Estimation Methods

Key fluid-structure interaction studies for tsunami-like inundations are presented here, as well as the engineering design guidance documents which represent the culmination of these studies. The relationships introduced in this section will be quantitatively compared and analysed so as to identify and justify the tsunami load estimation assumptions to be employed for empirical fragility function derivation (Chapter 4) and for use in structural analysis for analytical fragility function derivation (Chapter 5).

2.4.2.1 General Loading Profile

The leading edge of a tsunami wave inundates land in the form of a hydraulic bore or a surge. A bore is a broken wave with a steep, turbulent wave front, which propagates over quiescent water of a finite depth. A surge describes the motion of wave runup on a dry bed (Ian N Robertson & Riggs, 2011). Furthermore, tsunami waves tend to break offshore or near-shore, and so loads imposed by breaking waves are generally not applicable to onshore buildings away from the surf zone (Harry; Yeh et al., 2014).

Due to the very long wave period of tsunami, after impingement of the initial surge or bore, tsunami runup becomes quasi-steady (changes in flow parameters are slow, such that force components due to accelerations of the flow are negligible). The impingement of tsunami flow on structures is therefore thought to result in the general pressure time-history shown in Figure 2-8, where the impulsive bore impact pressure may or may not be greater than the sustained (quasi-steady) pressure.

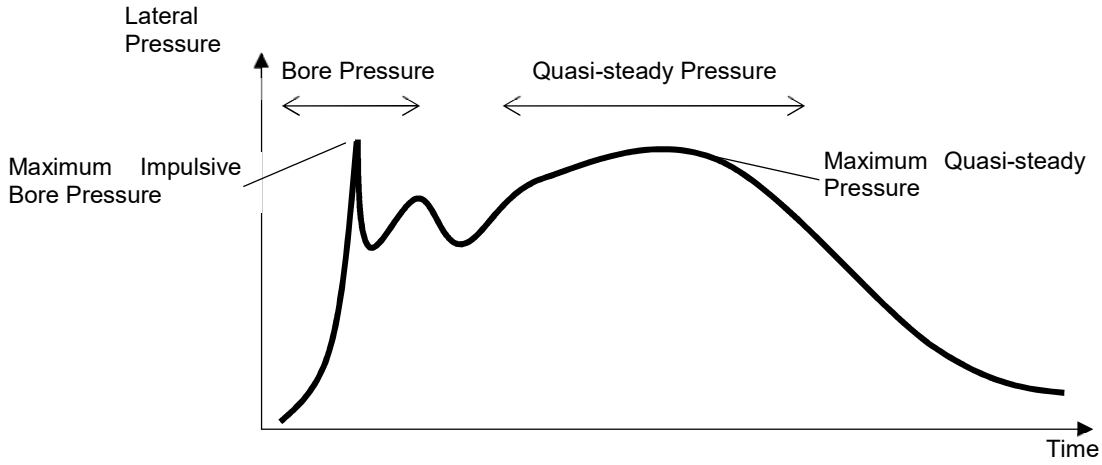

Figure 2-8: Typical load time-series for single bore impingement on an onshore structure, showing initial impulsive bore impact pressure followed by a sustained (quasi-steady) pressure (after Arikawa et al. (2012)). All tsunami-induced fluid loads in this thesis are categorized as either bore/surge or quasi-steady loads

In fluid mechanics two standard methods for estimating fluid-induced force on solid, non-compliant bodies are the hydrostatic force equation (2-7) and form-drag equation (2-8

). The standard hydrostatic force equation applies for a fluid, of density ρ and depth h, at rest exerting a pressure normal to a contacting surface, due to the isotropic nature of fluid pressure at rest and the weight of water above. The form-drag equation calculates the force experienced by an object (of width B perpendicular to the direction of flow) due to the movement of a fully enclosing fluid, derived from the idealized assumption that the fluid comes to a complete stop upon impingement on the normal surface of the object, building up stagnation pressure, and that turbulence is produced behind the object. The drag coefficient (C_D) in equation (2-8) is the ratio of drag for a real object to that of the ideal object and is an experimentally derived function of the object shape and orientation. Yeh et al. (2014) argues that (2-8) is appropriate for objects which penetrate the free surface (e.g. buildings in tsunami flow) where hB defines the wetted area perpendicular to the flow, noting that h and u are affected by the presence of the object.

$$F_{hydrostatic} = \frac{1}{2}\rho g h^2 B \qquad \text{(2-7)}$$

$$F_{drag} = \frac{1}{2}\rho C_d (hu^2) B \qquad \text{(2-8)}$$

2.4.2.2 Summary of Key Studies

There have been various investigations to define the magnitude, distribution and time-histories of tsunami-induced pressures loading on onshore structures. The main findings from recent studies are listed below for quasi-steady loading (Table 2-10) and bore impact (Table 2-11). A more detailed summary of these and historical studies is presented in Appendix C. The aim of this summary is to highlight conflicting views in the literature, some of which will be specifically tested in this thesis.

The studies summarized in Table 2-10 show conflicting findings related to peak load magnitude and the vertical pressure distribution of peak pressures for quasi-steady loads. Yeh et al. (2014), Nistor et al. (2004) and Lukkunaprasit et al. (2009) find the standard drag equation (2-8) to be a good approximation of peak quasi-steady load (the method adopted by US standards), though Nistor et al. (2010) highlights that this requires the estimation of velocity to be accurate. Alternatively, Tokyo University & BRI (2011) find that peak load can be approximated by a form of the hydrostatic equation linearly scaled by estimated Froude Number (adopted by Japanese guidance, discussed below) based on observational data from the 2011 GEJE. Arikawa et al. (2012) experimentally confirms that peak quasi-steady load is proportional to Froude Number. Yeh (2007) recommends applying a uniform vertical distribution (adopted by US standards), but Nistor et al. (2010), Nouri et al. (2010) and Nouri (2008) find from numerical and physical experiments that a triangular distribution is more appropriate. The effect of these differing findings will be investigated in a sensitivity analysis of structural response in Chapter 4.2.

Table 2-10: Quasi-steady load findings from literature.

	Findings		Research References	Adopting Standard
Peak Load Magnitude	Approximated by the standard form drag equation (2-7)	Found to be a good approximation based on physical experiments.	(Panitan Lukkunaprasit et al., 2009; Nistor et al., 2004; Harry; Yeh et al., 2014)	FEMA 646, ASCE 7-16
		Found to be a bad approximation when using empirical velocity estimation approaches.	(Nistor et al., 2010; Y. Nouri, 2008; Younes Nouri et al., 2010)	
	Approximated by a form of the hydrostatic equation (2-8)	Found to be a good approximation based on damage observations from 2011 GEJE.	(Tokyo University & BRI, 2011)	MLIT
		Found to be a good approximation based on numerical analysis.	(Takabatake & Kihara, 2014)	
		Found to be proportional to Froude Number based on physical experiments.	Arikawa et al. (2012)	
	Approximated considering flow regime (2-16)	Found force to be a function of flow regime (defined by Froude number) and blockage ratio (ratio of building width to clear width between adjacent buildings).	(Foster, Rossetto, & Allsop, 2017; Qi et al., 2014)	-
Pressure Distribution	Uniform vertical distribution.		(Harry Yeh, 2007)	FEMA 646 ASCE 7-16
	Triangular vertical distribution.		(Nistor et al., 2010; Y. Nouri, 2008; Younes Nouri et al., 2010)	MLIT
Other Loading Considerations	Buoyancy	Shown to soil-dependent, and to be a critical load component for structural failure calculations.	Yeh et al. (2014)	FEMA 646, ASCE 7-16, MLIT
	Openings	Argued to reduce global load (by reducing wetted area).	Lukkunaprasit et al. (2008)	FEMA 646, MLIT
		Thought not to reduce global load (due to blockage of openings caused by debris).	Chock (2013)	ASCE 7-16

Table 2-11: Impulsive bore impact findings from literature.

	Finding		Research References	Adopting Standard
Peak load magnitude	Approximated by a multiple of the drag equation (2-8)	An approximate estimate.	(Harry Yeh, 2007)	FEMA 646
	Approximated by a form of the hydrostatic equation (2-9)	Found to be a good approximation based on physical experiments.	(Asakura et al., 2000)	MLIT
		4x > quasi-steady pressure 7x > hydrostatic pressure	Arikawa et al. (2012)	-
	Approximated by a new equation		(Ian N Robertson & Riggs, 2011)	ASCE 7-16
	Approximated by a combination of drag and hydrostatic components		(Arimitsu, Ooe, & Kawasaki, 2013; Nistor et al., 2010; Y. Nouri, 2008; Younes Nouri et al., 2010)	-
	Relation to quasi-steady load	> quasi-steady for deep bores < quasi-steady for shallow bores	(Nistor et al., 2010; Y. Nouri, 2008; Younes Nouri et al., 2010)	-
		> quasi-steady for square columns < quasi-steady for circular and rhomboidal columns < quasi-steady for dry-bed surge	(Árnason, 2005; Arnason, Petroff, & Yeh, 2009)	-
		> estimate from added mass calculation	(Araki, Ishino, & Deguchi, 2010)	-
Pressure Distribution	Approximately triangular for dry-bed surge Approximately uniform for wet-bed bore		(Gomez-Gesteira & Dalrymple, 2004)	-
	Approximately hydrostatic for long waves		(Asakura et al., 2000)	MLIT
	Triangular (for a blockage ratio of 1)		(Ian N Robertson & Riggs, 2011)	ASCE 7-16
Other Conside-rations	Impulsive Uplift occurs on slabs where through-flow is prevented.		(I N; Robertson, Riggs, & Mohamed, 2008)	ASCE 7-16

2.4.2.3 Tsunami Design Guidance Documents

Tsunami load estimate formulae derived from some of the studies given in Table 2-10 and Table 2-11 are consolidated by various engineering design guidance documents primarily in the US and Japan. This section therefore summarizes the peak load expressions recommended by the documents in both countries, as these will be used for comparison with observational damage data for empirical fragility function derivation (Chapter 4) and for structural analysis for analytical fragility function derivation (Chapter 5).

It is noted that the guidance documents available are an excellent coverage of the subject, developed by experienced and accomplished researchers and engineers. However, the studies from which they are derived present sometimes conflicting conclusions (Table 2-10 and Table 2-11), and so these two sets of standards recommend different estimations of peak force and pressure distribution. Discrepancies are due to

different developmental paths, a lack of measurement data of actual tsunami actions on structures, and difficulties in recreating these effects experimentally or numerically.

Design Guidance in Japan

The evolution of tsunami-related design guidance in Japan prior to 2011 is summarized in Appendix D. A more complete treatment of the following analysis of Japanese design guidance is also included in Appendix D. Under the latest guidance (MLIT, 2011a, 2011b), peak load and the recommended pressure distribution are as shown in Figure 2-9.

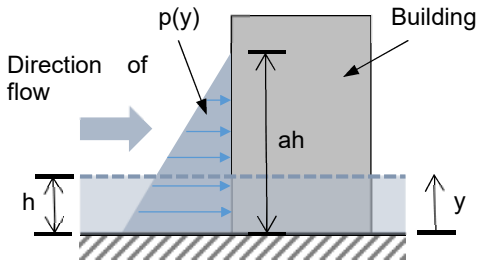

Figure 2-9 Equivalent static loading recommended as design loading in MLIT 2570. *p(y)* is defined in equation (2-9).

$$p(y) = \rho g(ah - y) \qquad \textbf{(2-9)}$$

Table 2-12: Tsunami loading coefficient (*a*) as a function of distance from water source and presence of sheltering structures (Fukuyama et al., 2012; MLIT, 2011c)**.**

	With shelter between the facility and the incoming wave		*No shelter between the facility and the incoming wave*
Distance from seashore or rivers:	> 500m	< 500m	Any distance
Water depth coefficient *a* (Figure 2-9):	1.5	2	3

Previous design guidance (Japan Cabinet Office, 2005) defined the hydrostatic pressure distribution approximation shown and set the depth coefficient (*a*)=3 based on a study by Okada et al. (2004) which carried out 84 2-dimensional hydraulic model experiments which measured the peak pressures exerted on structures positioned at various distances from the sea bed for various wave heights, periods and Froude Numbers.

The current guidance redefines *a* based on a study following the 2011 Great East Japan Earthquake and Tsunami which examined several case-study structures which experienced tsunami flow, including 35 buildings (RC structures between 1 and 4 stories) and 42 other structures (free-standing walls and pillars, monuments, bridges and sea defences, Asakura et al. (2000)). A relationship was observed between the equivalent hydrostatic force (Figure 2-9) and the observed collapse of structures, and so for

collapse-prevention design purposes (NB, not performance-based design purposes) it was considered that the use of an equivalent hydrostatic force, as per Japan Cabinet Office (2005), to estimate tsunami loading was adequate.

This hydrostatic approximation was also compared to a hydrodynamic approximation by assuming both the drag and hydrostatic approximations of the loading to be equivalent, so that *Fr* and a can be equated (equation (2-10)). The linear relationship proposed by equation (2-9) is evidenced by the experimental data of Asakura et al. (2000), up to the maximum value of *a* = 3 (Figure 2-10). The correlation between *Fr* and *α* can also be seen in Figure 2-11, which compares tsunami design loads calculated using the drag equation (Equation (2-8)) with *Fr* = 0.7, 1.0, 3.0) and equivalent hydrostatic equation (2-9) with *a* = 1, 1.5, 2, 3, corresponding to *Fr* = 0.71 , 1.06 , 1.41 , 2.12 respectively).

$$F_{hydrostatic} = F_{drag} \rightarrow \frac{\alpha^2}{2}(h^2\rho g) = Fr^2(h^2\rho g) \qquad \textbf{(2-10)}$$

$$\therefore \boldsymbol{\alpha = Fr\sqrt{2}}$$

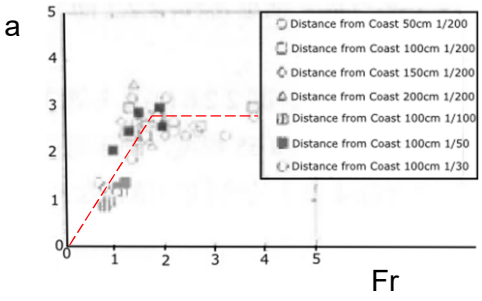

Figure 2-10: Relationship between a and Fr for lab experiments by Asakura et al. (2000).

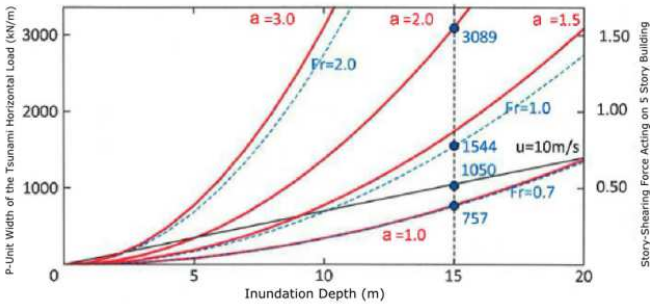

Figure 2-11: Comparison of design loads using drag equation (Equation (2-8)) with Fr = 0.7, 1.0, 3.0) and equivalent hydrostatic equation with α = 1, 1.5, 2, 3).

Therefore, the peak load estimation presented in equation (2-9) is not proposed as an accurate depiction of the flow regime (i.e. it is clearly not expected that tsunami flow will apply a purely hydrostatic load on one side of an onshore structure with no inundation pressure on the other side). Rather, it is proposed as an equivalent estimate of peak lateral load, depending only on the peak inundation (which is easier to calculate than other flow parameters such as velocity and momentum flux) and approximating the flow Froude number based on distance from the shore and the presence of seaward obstacles.

Design Guidance in USA

FEMA 646: Guidelines for Design of Structures for Vertical Evacuation from Tsunami (FEMA, 2008) provides guidance for calculating tsunami loads on structures, and

provides equations for hydrostatic, hydrodynamic and debris forces. Hydrodynamic drag is shown in Figure 2-12 and calculated as-per the standard drag equation).

The tsunami wave-train often consists of multiple waves and the largest wave is often not the leading one (e.g. where individual wave celerity exceeds group velocity during deep see propagation meaning that the largest proportion of the tsunami's energy is not carried in the leading waves). Hence, it is possible for there to be standing water on-shore during a tsunami bore inundation. This may lead to increased loads (Table 2-11), which are to be calculated as per equation (2-11).

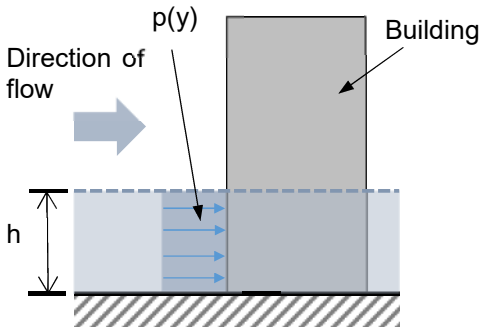

Figure 2-12: Uniformly distributed hydrodynamic loading recommended in FEMA 646.

$$F_{impulse} = 1.5 \times F_{drag} \qquad \textbf{(2-11)}$$

In ASCE 7-16 (G. Chock, 2014; G. Chock, Carden, Robertson, Olsen, & Yu, 2013; G. Y. K. Chock, 2013; G. Y. K. Chock, Robertson, & Riggs, 2013; Ian N Robertson, Chock, & Carden, 2014) drag and bore impact are to be calculated in a similar way to that recommended in FEMA 646 (Chock 2013), albeit with the momentum flux estimation procedure of FEMA 646 superseded by Energy Grade Line Analysis (GLA, Figure 2-6: Grade Line Analysis (GLA) recommended in ASCE 7 (2016) (from G. Chock, 2014; Kriebel et al., 2017).).

Gaps in Current Design Guidance Documents

The pseudo-static approach of Japanese guidance, shown to approximate to the standard hydrodynamic drag equation with varying Froude Numbers, avoids the need for inundation velocity estimates, which are difficult to obtain accurately. The approach is derived from the results of laboratory experiments adjusted to incorporate a statistical treatment of damage data from the 2011 Japan tsunami. Therefore, it inherently includes debris damage and other effects, such as proceeding earthquake damage. Conversely, US codes are a mathematical treatment from first principles, but require accurate inundation modelling to derive velocities. This requirement is overcome in the US by the provision of runup and offshore wave information suitable for numerical inundation

modelling or Grade Line Analysis (a 1D inundation calculation that may be performed manually), but other locations around the world will require a means of estimating flow velocities in the absence of this data.

Best practice for tsunami design of structures is subject to ongoing research. There is a great deal of uncertainty associated with determination of inundation parameters, such as accurate modelling of the tsunami generation mechanisms, and modelling of near-shore and onshore behaviour to the accuracy required for load estimation (Goda & Song, 2015). Regarding load estimation and structural performance, the areas not considered in current standards are summarized in Table 2-13.

Table 2-13: Considerations not yet sufficiently covered in current standards.

	Consideration	Description
Load Estimation	Load estimation considering flow regime and blockage ratio	Alternative load estimations consider how fluid loads are affected by flow depth changes between the front and rear of the building (Foster et al., 2017; Qi et al., 2014).
	Vertical distribution of lateral fluid pressure	Varying distributions exist in literature (e.g. triangular or uniform distributions) which affect global and member design (Macabuag, Rossetto, & LLoyd, 2014a).
	Time-dependent loads	Structural ductility, over-strength and dynamic properties play a central role in seismic design, and it is not clear if such considerations may have implications for tsunami design (Petrone et al., 2017).
Structural Response	Dynamic structural response	
	Ductility and overstrength	
	The combination of seismic and tsunami loads	The combination of seismic and tsunami damage for near-field tsunami may limit the capacity of the structure under tsunami loading, due to the cyclical degradation of structural materials loaded into the ductile range or damage to in-fill panels and stiffening elements, reducing capacity. Such effects are discussed in ASCE 7-16, but are yet to be quantified (e.g. Scott & Mason, 2017).

2.4.2.4 Load Estimates Considering Flow Regime

Two major gaps of the studies presented in section 2.4.2 are firstly that the effect of the presence of the building on the flow, and so resultant loads (e.g. increased/decreased flow depth upstream/downstream, respectively, of an object), is not expressly addressed in the force estimation methodologies in literature. Secondly, the vast majority of experimental studies into tsunami loading on structures have been based on short-wave experiments, which do not accurately recreate the wavelength of real tsunami. Recent studies addressing both of these gaps are presented below. Their findings will be included in the load comparison study of section 2.4.2.5.

Tsunami are very long waves, and as such after the initial bore impact inundating flow can be considered as quasi-steady. Qi et al. (2014) examines quasi-steady forces on

structures through flume experiments using a model building in a steady-state open-channel flow, and Foster, Rossetto, & Allsop, (2017) extends this study for long-tsunami like waves.

In these studies, the Blockage ratio (width of the building, *b*, divided by width of the channel, *w*) is varied from 10% to 40%. A distinction is made between sub-critical flow (where there is a small difference in upstream and downstream flow depths) and choked flow (where there is a large difference in upstream and downstream flow depths with a hydraulic jump downstream). Qi et al. (2014) identifies that the majority of previous studies on forces exerted on a fixed obstacle in open channel flow focus on the sub-critical regime, and so the paper derives force estimates for both the sub-critical and choked conditions over a range of blockage ratios.

Algebraic relationships are formed based on a one-dimensional analytical model (Figure 2-13) assuming preserved volume flux, and a semi-empirical form of the quasi-steady drag force, F_{QS}. This incorporates both form drag (a function of front-face wetted area and flow velocity) and hydrostatic drag (a function of the difference in flow depths on the front and rear faces of the structure) shown in Equation (2-12).

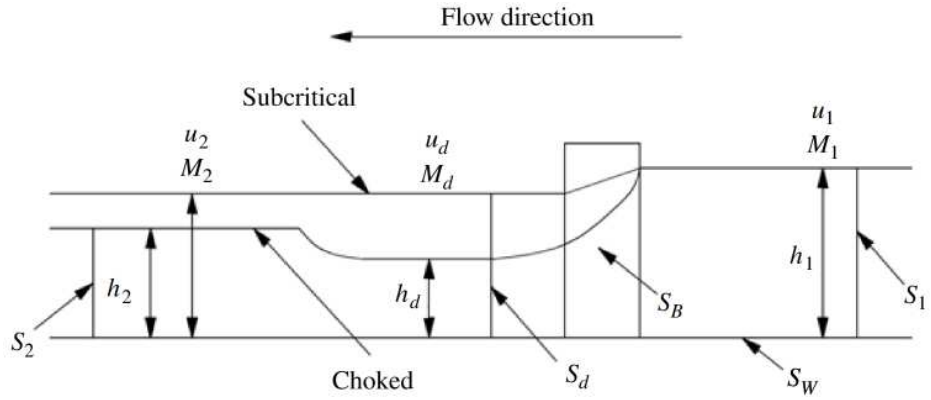

Figure 2-13: One dimensional model showing upstream and downstream conditions for subcritical and choked flow around a solid obstacle (Qi et al., 2014).

$$F_{QS} = \frac{1}{2}C_D\rho b u^2 h + \frac{1}{2}C_H\rho b g(h_1^2 - h_d^2) \quad \textbf{(2-12)}$$

C_D and C_H in Equation (2-12)) are empirically determined constants, and their determination for sub-critical and choked flow over a range of blockage ratios is the focus of Qi et al. (2014). The form-drag coefficient C_D is a function of blockage ratio. A wake is attached to the rear of an obstruction within a flow, where a wake is a region of recirculating flow. Volume flux is conserved upstream and downstream of an obstruction and so the flow velocity outside of the wake is increased. The obstacle experiences a force characterised by the average of the upstream and downstream flows, giving rise to Equation (2-14), where C_{D0} is the form-drag coefficient for an unbound flow (b/w=0).

$$C_D = C_{D0}\left(1 + \frac{C_{D0}b}{2w}\right)^2 \quad \text{(2-13)}$$

The unbound form-drag coefficient, C_{D0}, is also a function of ambient turbulence (taken as 5% for these experiments), for which C_{D0} = 1.9.

A relationship between upstream and downstream Froude Number (Fr_1 and Fr_d) is found by expressing Equation (2-12) in a non-dimensional form (Equation (2-14).

$$\left(1 - \frac{C_H b}{w}\right)\frac{1}{2Fr_1^{4/3}} + \left(1 - \frac{C_D b}{2w}\right)Fr_1^{2/3} = \left(1 - \frac{C_H b}{w}\right)\frac{1}{2Fr_d^{4/3}} + Fr_d^{2/3} \quad \text{(2-14)}$$

The critical condition at the onset of choked flow is found by differentiating Equation (2-14) to give Equation (2-15).

$$Fr_{dc} = \left(1 - \frac{C_H b}{w}\right)^{1/2} \quad \text{(2-15)}$$

An equation of force based on only up-stream parameters is defined. By defining depth and the sum of specific momentum flux and specific hydrostatic force as functions of volume flux and Froude Number, and considering that volume flux is invariant, Equation (2-16) is derived.

$$F_{QS} = \lambda \rho b g^{1/3} u_1^{4/3} h_1^{4/3} \quad \text{(2-16)}$$

$$\lambda = \tfrac{1}{2}C_D Fr_1^{2/3} + \tfrac{1}{2}C_H\left(\frac{1}{Fr_1^{4/3}} - \frac{1}{Fr_d^{4/3}}\right) \quad \text{(2-17)}$$

The aim of the experimental study outlined in Qi et al. (2014) was to verify the above analytically derived relationships and to empirically derive the form-drag coefficient (C_D) and hydrostatic drag coefficient (C_H), particularly in choked flow conditions. It was found that in the sub-critical case upstream and downstream depths are approximately equal, and so the sub-critical quasi-steady drag force (Equation (2-16)) tends towards the standard drag equation (Equation (2-8)), where C_D is calculated as a function of blockage ratio (Equation (2-13)). However, as upstream Froude Number approaches a critical value, downstream depth decreases, a hydraulic jump appears downstream, and downstream Froude Number increases rapidly to a critical value ($\lim_{Fr_1 \to Fr_c} Fr_2 = Fr_{2c}$), in which case the quasi-steady drag force is approximated by Equation (2-17)). The formulae presented above will be used to calculate F_{QS} for comparison with observed building damage data for empirical fragility function derivation (Chapter 4).

2.4.2.5 Quantitative Comparison of Tsunami Loading Estimation Methodologies

The forces presented in this section are quantitatively compared below for a case study topography and inundation. Vertical loads (buoyancy and residual water surcharge), debris impact forces and foundation effects are not considered here. The chosen load cases represent distinct and different loading scenarios covering bores, surges and steady flows. Therefore, the purpose of their comparison is not to assess their accuracy, but to demonstrate the variability in tsunami loading that can be experienced by an onshore structure and to present the range of input forces that could be calculated from application of the design guidelines. Square buildings oriented such that their flat surface is orthogonal to the oncoming flow are assumed

For this comparison, the case study chosen (Figure 2-14) is a uniform 1:20 beach (the topography for which FEMA 646 inundation formulae are derived), characterised by a Manning coefficient of n=0.05 (the value used most frequently in the presentation of Grade Line Analysis (GLA) by Kriebel et al., 2017), experiencing a tsunami with a runup arbitrarily selected as R=15m. For consistency, GLA will be used to determine the variation of depth and velocity up the beach for all load cases.

Comparison of Lateral Fluid Loads

Table 2-14 presents the load cases to be compared. The calculated lateral fluid force for the load cases are plotted against inundation depth, for the case study beach and tsunami runup. The comparison of the loads calculated for each load case is shown in Figure 2-15.

Table 2-14: Load cases used to generate tsunami push-over curves. Values for drag force coefficients (C_D, C_{D0}) are derived from their respective references.

Tsunami Load Case	Reference	Description of Loading	Determination of Flow Conditions as a Function of Inundation Depth (h)	Determination of Force (Equation)
LC1	MLIT 2570	Equivalent hydrostatic pressure. <500m from the water source with shelter from the incoming wave.	NA (no further parameters required)	(2-9) a = 1.5
LC2		Equivalent hydrostatic pressure. >500m from the water source with shelter from the incoming wave.		(2-9) a = 2
LC3		Equivalent hydrostatic pressure. No shelter from the incoming wave.		(2-9) a = 3
LC4	ASCE 7-16	Hydrodynamic drag.	Grade-Line Analysis R = 15m uniform 1:20 beach n=0.05	(2-8) C_D=2
LC5		Bore impact.		(2-11)
LC6	Foster et al. (2017)	Hydrodynamic drag accounting for flow regime (Fr). Sparse buildings.		(2-16), (2-17) C_{D0} = 1.9 b/w = 0.1
LC7		Hydrodynamic drag accounting for flow regime (Fr). Dense buildings.		(2-16), (2-17) C_{D0} = 1.9 b/w = 0.6

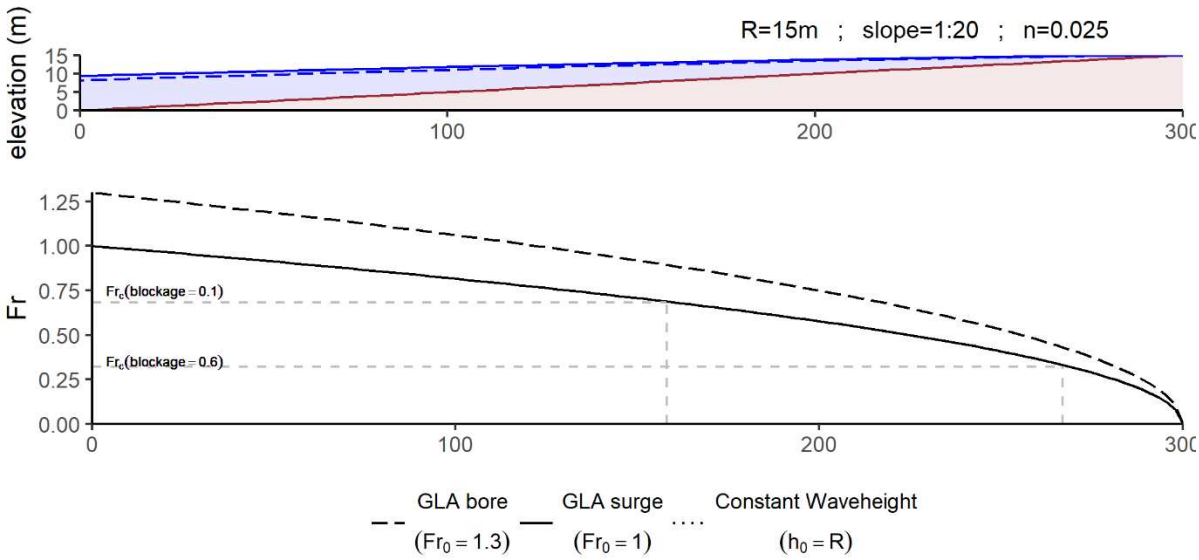

Figure 2-14: Case study topography and flow conditions derived from Grade Line Analysis for bore (Fr_0=1.3, LC5) and surge (Fr_0=1, load-cases: LC4, LC6, LC7) conditions. The critical Froude Numbers (Fr_c) defining choked and sub-critical flow in load cases LC6 and LC7 are shown, as well as the distance inland at which critical conditions cease. The shaded water-level indicates surge conditions defined by Grade Line Analysis (GLA).

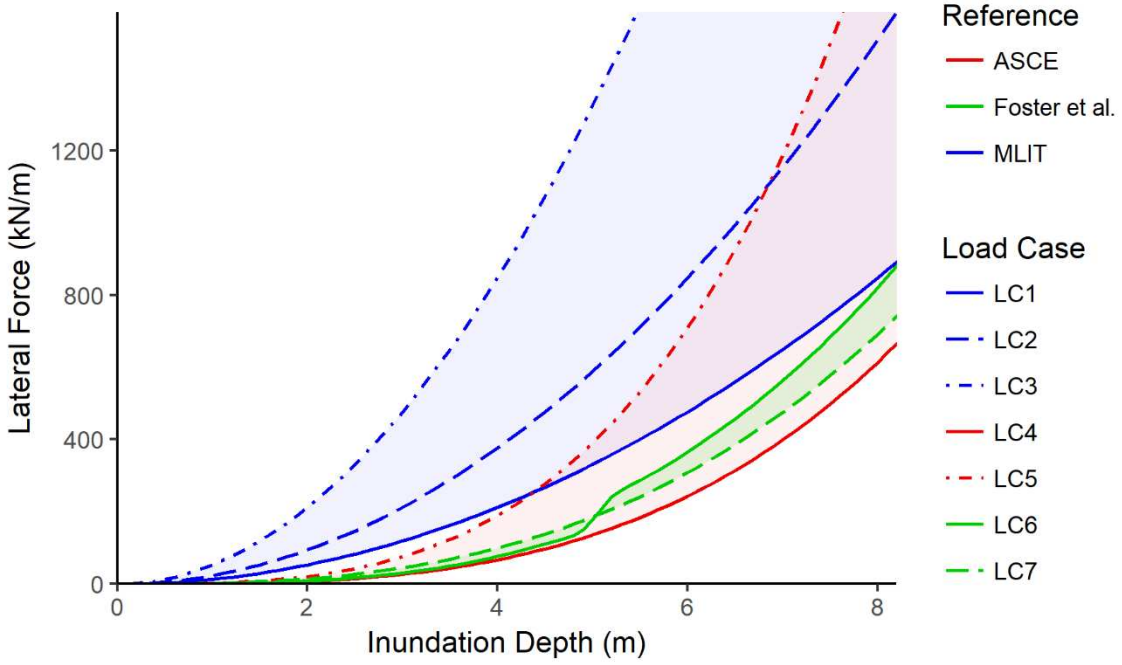

Figure 2-15: Comparison of loads for case study topography and inundation. Load case numbers correspond to those given in

Table 2-14 and shaded areas correspond to the upper and lower bounds for each load reference.

MLIT load cases (LC1-LC3) give conservative load estimates when compared with the drag load cases (LC4, LC6, LC7), which agrees with load comparison studies by Yeh, Robertson, and Preuss (2005).

Considering the Foster et al.,(2017) load estimates (LC6, LC7), the load applied to sparsely spaced buildings (i.e. low blockage ratio, LC6) shows a clear load increase at the change between sub-critical and choked flow (Figure 2-14, Figure 2-15). However, for more densely spaced buildings (i.e., high blockage ratio, LC7), flow is choked for almost all inundation depths (Figure 2-14), and so the load jump is not visible in Figure 2-15. Sub-critical loads defined by Foster et al.(2017) are very similar to the ASCE drag force (LC4). However, for choked conditions Foster et al.(2017) loads are higher than the ASCE drag force (LC4). This suggests that use of the standard drag force equation without considering flow regime may be unconservative, especially in dense urban environments.

Comparison of Loading Assumptions

A high degree of variability in the resulting load-estimates is shown above, demonstrating uncertainty in not only determining the tsunami inundation parameters, but also the effect on buildings. For the single case study topography and inundation chosen, it is shown above that load estimates in Japanese guidance are highly conservative, and that the standard drag equation (used by ASCE 7-16) may be unconservative for higher Froude Number and blockage ratio conditions where consideration of the flow regime would be preferred. The variability in load estimate is explored further below by graphically representing the underlying assumptions behind each considered load case (Figure 2-16), demonstrating that the flow scenarios differ for each case.

The load variability shown in Figure 2-15 is explained somewhat when considering the range of assumptions that have been made in deriving these load relationships. Table 2-15 summarizes the inundation parameters used for force estimation, and Figure 2-16 shows the range of blockage ratio and Fr assumptions for each load case. The MLIT load cases represent scenarios of fixed Fr (Figure 2-11). The specified depth coefficients (a) are correlated with building damage data from the 2011 tsunami, where in reality flow experienced a range of blockage ratios, and so a range is shown in Figure 2-16 (from a blockage ratio of 0.1 to 0.9). This leads to LC1-LC3 to be represented by straight lines, such that the Fr and blockage ratio combination represented by each load case can lie anywhere on its respective line. As the ASCE drag equation (LC4) may be unconservative for choked conditions, then LC4 is depicted in Figure 2-16 as the shaded

area defined by a Fr less than the critical Froude number for which conditions become choked ($Fr<Fr_c$, where Fr_c is a function of blockage ratio). The load factor applied to calculate ASCE bore impact loads (LC5, Figure 2-12) is derived from a series of flume experiments of various blockage ratios (Nistor et al., 2004), with Kriebel et al. (2017) defining Fr at the shore as 1.3. Figure 2-16 therefore shows LC5 as the area defined by Fr<1.3 for any blockage ratio. The Foster et al.,(2017) load estimate methodology can consider any Fr and blockage ratio, but in the case study scenario LC6 and LC7 take the specific values shown in Figure 2-16.

Table 2-15: Comparison of input variables required for force estimation formulae of the references considered.

Reference	Required Input Variables for Force Estimation	Notes
MLIT 2570	h, a	*a* is a function of distance inland and seaward barriers.
ASCE 7-16	h, v	
Foster et al. (2017)	h, v, b/w	*b/w* = building width / channel width, where channel width is the distance, orthogonal to flow, between adjacent obstacles either side of the building.

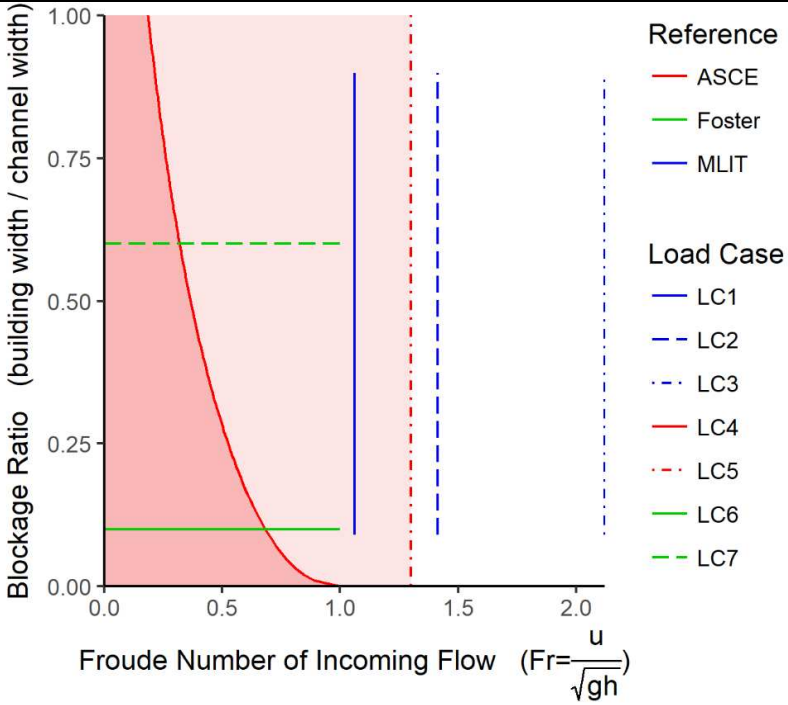

Figure 2-16: Comparison of blockage ratio and Froude Number assumptions for the conditions of the chosen case study. The blockage ratio and Froude Number assumptions are limited to points on the lines shown for each load case, with the exceptions of load cases LC4 and LC5 which may occupy any point within their respective shaded areas.

Figure 2-16 shows that the MLIT load cases, which apply the highest loads (Figure 2-15), consider the highest Fr scenarios. The LC4 area in Figure 2-16 is defined by the condition

$Fr<Fr_c$, which highlights that LC4 may be unconservative for many scenarios for which flow is expected to be choked. This is shown by the load cases of Foster et al. (2017), where LC6 (sparse buildings) is sub-critical for Fr values corresponding to lower inundation (so giving similar loads to LC4 at those inundations), but for LC7 (dense buildings) flow is mostly choked (leading LC4 to underestimate the load as shown in Figure 2-15).

2.4.3 Structural Analysis Under Tsunami Loading

The content of this section is specifically related to the various methods of structural analysis present in the analytical fragility function literature (summarized in section 2.3.1.3), which will inform the analysis of Chapter 5.

2.4.3.1 Methods of Structural Modelling and Analysis

Published studies adopt a number of techniques for structural analysis under tsunami loading that vary in complexity from time-history analysis of a 3D structural model (G. Chock et al., 2013), to simple mechanics-based models that consider particular failure mechanisms (W. Dias, Yapa, & Peiris, 2009). Furthermore, different assumptions are also made on how the pressure/forces imparted by the tsunami flow should be applied to the structure. Discussion on vertical distribution of lateral pressures is made in section 2.4.2.2.

A sensitivity analysis of structural response to multiple load distribution types is presented in Appendix E (based on Macabuag and Rossetto, 2014), showing that the structural response to tsunami loading is very sensitive to the vertical distribution of the applied lateral tsunami pressure. Furthermore, the various tsunami capacity curves are shown to be significantly different from seismic capacity curves, showing that seismic curves cannot be used for tsunami damage estimation (as conducted by Kircher & Bouabid, 2014).

Petrone et al (2017) compares the results of time-history analyses and non-linear static analyses of a 2D structural model and demonstrates that a novel varying height pushover approach provides an appropriate simplified analysis technique for the determination of structural response of engineered buildings under tsunami loading. Constant-Height PushOver (CHPO, e.g. Foytong et al. 2015) is compared with Variable Height PO (VHPO, e.g. Macabuag et al. 2014, Macabuag et al 2014a), both shown in Figure 2-17. It is shown that VHPO gives a better estimation of structural capacity (determined by Time-History Analysis, THA) than CHPO.

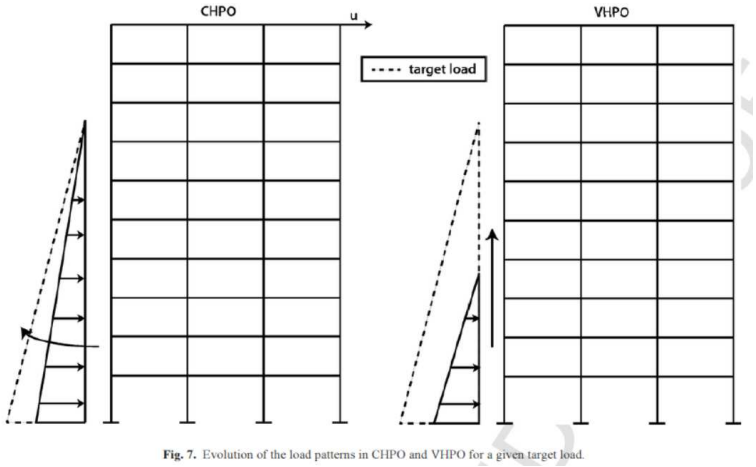

Fig. 7. Evolution of the load patterns in CHPO and VHPO for a given target load.

Figure 2-17: Definition of Constant Height PushOver (CHPO) and Variable Height PushOver (VHPO) from Petrone et al. (2017). For CHPO, height is fixed and velocity increased as shown. For VHPO, h in incremented and velocity is calculated according to a fixed Froude Number.

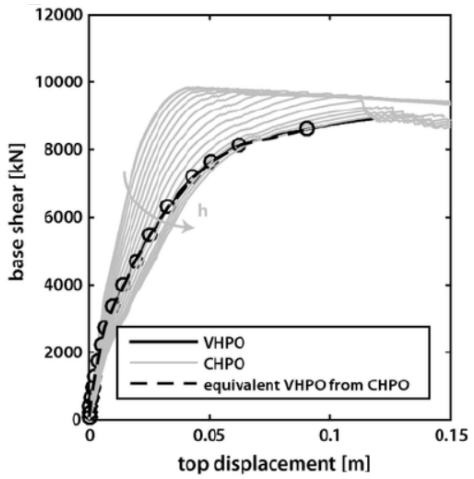

Figure 2-18: Pushover results for a case study building from Petrone et al. (2017).

2.4.3.2 Considerations for Damage Estimation

Attary et al. (2016) used Inter-storey Drift (ISD) as the Engineering Demand Parameter (EDP) and compared with seismic ISD-thresholds for each damage state, though it was acknowledged that new tsunami-specific EDP thresholds should be developed. A preliminary study of ISD thresholds suitable for tsunami analysis is presented in the Appendix E (based on Joshua Macabuag & Rossetto, (2014)), showing that seismic ISD thresholds are not suitable for tsunami damage estimation.

The fact that a pushover-type analysis can represent the structural response of a building under a tsunami time history implies the structure has a predominant response that can be represented by a single-degree of freedom system. Such an assumption is made by Park et al. (2012) in their structural idealization for the study of sequential earthquake and tsunami load effects on buildings (see section 2.3.1.3).

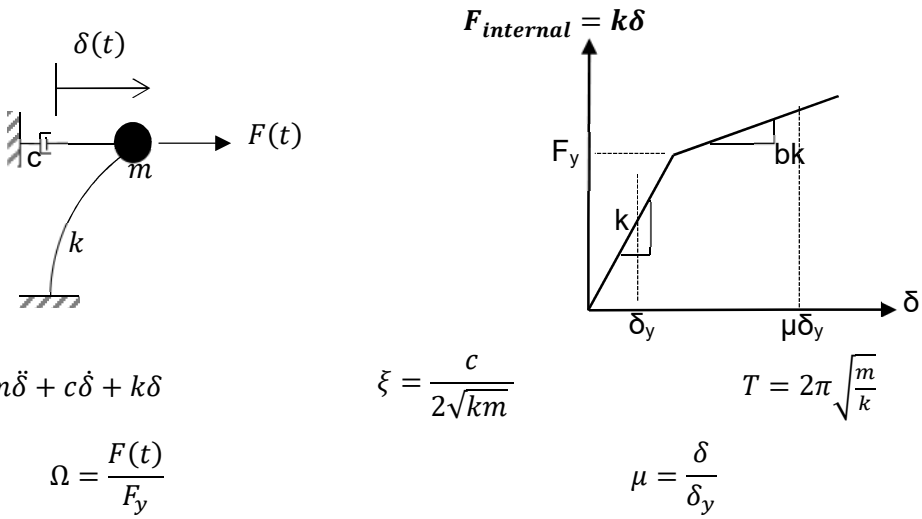

$$F(t) = m\ddot{\delta} + c\dot{\delta} + k\delta \qquad \xi = \frac{c}{2\sqrt{km}} \qquad T = 2\pi\sqrt{\frac{m}{k}}$$

$$\Omega = \frac{F(t)}{F_y} \qquad \mu = \frac{\delta}{\delta_y}$$

Figure 2-19: Equation of motion, performance curve, and terminology for a SDoF structure used in Chapter 5. *m* = structural mass. *c* = damping. c_c = critical damping. *k* = stiffness. *ξ* = damping ratio. *b* = strain-hardening ratio. *T* = natural period of vibration.

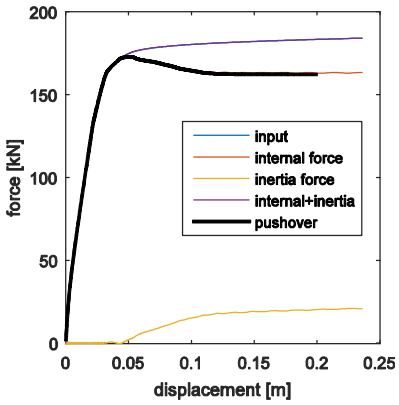

Figure 2-20: General performance curve of a structure loaded beyond yield. (Petrone et al.. 2017)

Current tsunami building codes require critical structures to be designed to resist elastically one or more tsunami loading combinations that are assumed to occur at specific points along a tsunami inundation time-history (e.g. at point of maximum inundation depth or maximum momentum flux). This elastic design criterion reflects the importance of these critical structures (which must remain functional after a tsunami) but also the fact that the study of tsunami forces and impacts on structures is a relatively new field, and that significant uncertainties still exist.

Whilst it is acceptable for design standards to be inherently conservative for critical infrastructure, in the context of damage prediction for analytical fragility function derivation, this conservatism can result in inaccurate fragility conclusions. In the case of seismic building codes unconservative design is addressed by introducing the concept of capacity design, which allows the structure to resist some of the earthquake loads through plastic deformation. The maximum amount of plastic deformation that the structure can sustain whilst still maintaining its vertical load carrying capacity is

represented by its structural ductility supply (μ = ratio of ultimate deformation to yield deformation). The word 'supply' is used here to distinguish the capacity of the structure from the 'demand' placed on it by the earthquake. In the codes, the structural ductility supply is related to an over-strength factor (i.e. the ratio of applied load to the structural yield strength, $\Omega = {F(t)}/{F_y}$) which is utilized to reduce the seismic design loads. This results in a more economic upfront design cost, and life-safety in cases where an earthquake occurs that deforms the building to within its ductility supply limit. In the latter case, the cost of repairing the building is assumed acceptable given the low frequency of such earthquake events.

The basis of these assumptions in seismic design derive from fundamental structural dynamics. As a structure deforms under a time-dependent load, it develops inertia forces, damping forces and internal (spring) forces (Figure 2-18). However, in contrast to the earthquake engineering literature, to date very limited attention has been given to the areas of structural damping, ductility, overstrength and other time-dependent effects by the tsunami research community.

Like earthquakes, tsunami flows impose a time-varying load on structures, with a strong horizontal component. The time-history, points of application and duration of this horizontal loading are however very different (section 2.4.2.1), and it is not yet clear as to whether the problem of structural analysis under tsunami loading should be treated as a dynamic problem or not.

2.5 Summary of Highlighted Research Needs

This chapter has outlined the key engineering principles of tsunami loading and damage of buildings, compared how these principles are addressed in US and Japanese standards, outlined considerations not yet covered (Table 2-13), and quantitatively compared code-prescribed lateral hydrostatic forces with an alternative force estimation method considering flow regime (indicated by Froude Number) and building density (Figure 2-15). In this context, the current suite of empirical and analytical fragility functions has been critically evaluated, and the main research needs highlighted throughout this chapter are outlined below.

2.5.1 RN1: Improved Statistical Methods in Fragility Function Derivation

Many existing studies derive fragility functions using linear regression models with Ordinary Least Squares parameters estimation. This has been shown to be inadequate, and various more recent studies go on to use Generalized Linear Models. There are still various improvements that can be made with the use of non-parametric models,

improved methods for selecting between alternative models and better methods for representing uncertainty.

2.5.2 RN2: A Method for Identifying the Preferred Tsunami Intensity Measures

Issues with current estimations of tsunami intensity, as highlighted by the literature, are summarized as:

- Inconsistencies in tsunami parameter definitions,
- Alternative intensity measures to depth are not utilized,
- Limitations of empirical tsunami data (measuring inundation),
- Limitations of physical inundation modelling (experiment-derived tsunami data),
- Limitations of numerical inundation modelling (simulation-derived tsunami data).

These issues show that further investigation is required into the definition and derivation of an appropriate TIM for tsunami fragility functions.

Force may be considered as a TIM for both empirical and analytical fragility functions, and must be accurately defined for use in structural analysis for analytical fragility function derivation. However, a range of loading definitions are available in the literature, and they have been shown to differ significantly (Figure 2-15). It is therefore necessary to define the loading definition which best explains building damage in empirical fragility function derivation, and to also demonstrate whether the differences in loading definition have implications for structural response (and damage assessment). It is also clear that observational damage data will be influenced by the presence of debris, and it unclear how the effects of this can be separated from that of other TIMs.

2.5.3 RN3: Improved Understanding of Tsunami Response of Structures

Compared to seismic studies, few fragility functions for buildings affected by tsunami exist, and the vast majority have all been based solely on empirical data (post-tsunami building damage surveys). However, the applicability of empirical tsunami fragility functions for buildings is limited by the availability and quality of data from past events. Similar construction types from different countries or regions can perform very differently under the same tsunami conditions, and so the correct application of empirical fragility functions is therefore very specific to the locations from where damage data was taken. Therefore, analytical techniques are required to generate or update tsunami fragility functions for the majority of at-risk locations around the world where tsunami damage data is not available.

Seismic design practice, draws heavily upon the reserve strength of a structure loaded beyond yield, with the structural ductility being fundamental for the analysis of structural performance. However, to date very limited attention has been given to the areas of structural damping, ductility, overstrength and other time-dependent effects by the tsunami research community, and it is not yet clear as to whether the problem of structural analysis under tsunami loading should be treated as a dynamic problem or not.

There is therefore a need to investigate the fundamental principle of whether ductility and dynamic effects are significant in determining structural performance under tsunami loading.

2.5.4 RN4: Feasibility of Using Simplified Approaches for Structural Modelling and Analysis

Structural analysis for fragility function derivation must be as simple as possible to allow multiple analyses of various structural configurations and tsunami loading scenarios. However, existing analytical fragility studies utilise a range of different structural analysis techniques (summarized in section 2.3.1.3), from simple Single-Degree-of-Freedom (SDoF) systems to full non-linear time-history analysis, with no consensus as to the preferred method.

There is therefore a need to identify simplified methods of analysis which can achieve suitable accuracy for analytical fragility function derivation.

3 Research Questions and Approach

Expanding on the aims outlined in section 1.2, this thesis looks to answer the following research question:

Research Question:

What are the most effective methods for quantifying fragility of buildings to tsunami damage, both using observational damage data, and in the absence of data?

In answering this question the research addresses, in part, several of the research needs highlighted in section 2.5. It does so by splitting the research question into a number of sub-questions (reference is made to the corresponding research needs, RN, summarized in section 2.5):

1 For empirical fragility assessments based on observed damage data:
   a. What are the most appropriate statistical methods for deriving tsunami fragility functions? (RN1)
   b. What is the most appropriate Tsunami Intensity Measure (TIM) for describing building damage via tsunami fragility functions? (RN2)
   c. Can the effect of debris on fragility function derivation be separated from that of other TIMs? (RN2)
2 For analytical fragility assessments in the absence of observed damage data:
   a. Are ductility and dynamic effects are significant in determining structural performance under tsunami loading? (RN3)
   b. What types of simplified structural models are most appropriate for analytical fragility function derivation? (RN4)

Figure 3-1 provides a flow chart connecting the various thesis sections with the above research questions.

Chapter 4 will address sub-question 1 above by identifying the key Tsunami Intensity Measures (among those used in literature, and the additional loading expressions defined in section 2.4.2) and improved statistical methods to be used for fragility function derivation. Empirical fragility functions will be derived and compared using advanced statistical methods applied to a unique, disaggregated building damage dataset, and numerical tsunami inundation model results. Finally, a preliminary methodology for quantifying debris-related effects on fragility functions will be presented.

Chapter 5 will address sub-question 2 above by conducting a preliminary investigation into the generation of analytical fragility functions appropriate for use with inundation model results. It will first be analytically investigated whether an Elastic-Perfectly-Plastic Single Degree of Freedom structure can maintain a load greater than its yield load for a

duration of time (i.e. if overstrength influences structural capacity considering the effect of damping, strain-hardening and load-duration. Finally, these findings will be expanded to investigate a simplified method of estimating structural capacity, suitable for use in the large number of analyses required to derive analytical fragility functions of populations of buildings.

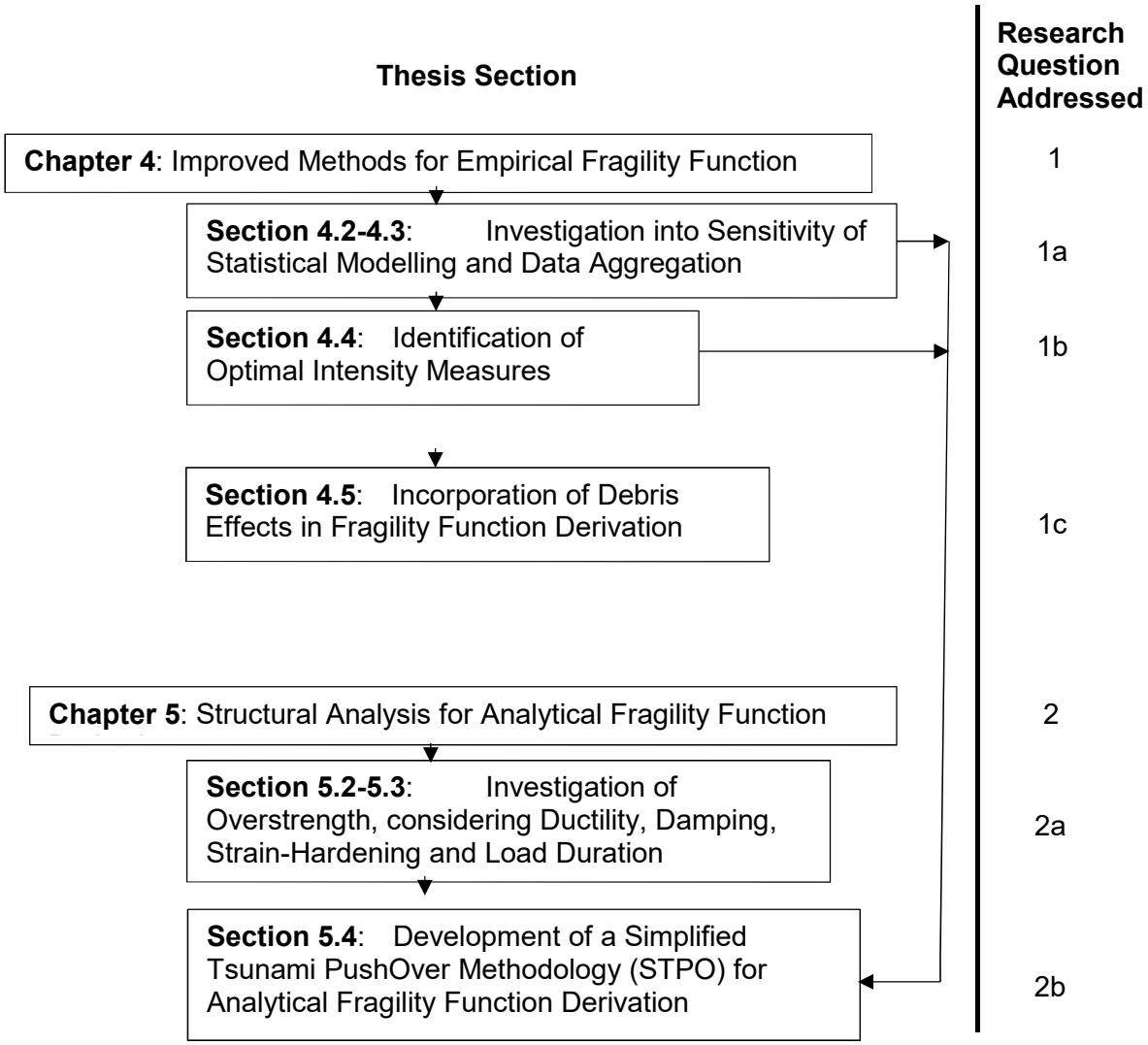

Figure 3-1: Flow chart of thesis sections addressing each research sub-question proposed above.

The research focus of this thesis is limited to the items outlined above. Of the many research gaps in the current literature highlighted in section 2.5, the following will not be addressed. As this thesis focuses on damage prediction once flow parameters have been defined, so source, propagation and inundation modelling approaches will not be discussed in detail. The focus of this thesis is on damage prediction for catastrophe modelling and loss estimation purposes, and so engineering applications (e.g. fragility functions used for performance-based design and prescriptive code-based design) will

not be considered. Similarly, financial and casualty loss estimation is beyond the scope of this thesis and will not be included here.

Research into analytical fragility functions is at an early stage, and so the research presented in Chapter 5 may be considered early steps towards the goal of deriving reliable and representative functions. Given the complexity of the full tsunami loading regime, this investigation will look to examine a simplified case whereby only lateral hydrodynamic fluid loads will be considered. I.e. debris, buoyancy net hydrostatic effects, foundation effects and preceding seismic damage will not be considered. Defining the optimal suite of tsunami loading scenarios which accurately characterizes uncertainty in loading, will be discussed briefly but not examined in detail. Definition of an adequate Engineering Demand Parameter (EDP) and related damage state threshold definitions for multiple damage states is presented in the Appendix E, but for the preliminary study in this thesis only the collapse damage state will be considered. Uncertainty in the structure will not be considered.

Several novel concepts are developed and presented in this investigation:

- Advanced statistical methods applied to disaggregated damage data, appropriate for use in both empirical and analytical fragility assessments.
- A complete methodology for defining the optimal TIM and statistical model for any given damage dataset.
- A proposed preliminary methodology for quantifying debris damage effects on fragility function derivation.
- Tsunami push-over analysis for analytical fragility function derivation.
- A simplified methodology for structural analysis, suitable for the many iterations required for analytical fragility function derivation for populations of buildings.

4 Improved Methods for Empirical Fragility Function Derivation

4.1 Introduction

Existing fragility assessments (section 2.3.1) use various Tsunami Intensity Measures (TIMs) with conflicting recommendations of which to use. This Chapter uses a unique, detailed disaggregated damage dataset from the 2011 Great East Japan Earthquake and tsunami (2011 GEJE). In order to do this several advanced statistical methods novel to the field of fragility assessment are used to identify the optimum TIM for describing observed damage. This is so as to address both sub-questions of research question 1 in Chapter 3, namely (a) what are the most appropriate statistical methods for deriving empirical tsunami fragility functions? And (b) what is the most appropriate Tsunami Intensity Measure (TIM) for describing building damage via tsunami fragility functions?

The chapter first sets out to explore the data and eliminate biases due to incomplete data entries using a multiple-imputations approach (section 4.2). Improvement to empirical fragility curve accuracy and reliability that are gained from using disaggregated datasets and appropriate statistical model fitting methods are then investigated (section 4.3). Finally, fragility curves derived for a series of different TIMs are compared using cross-validation techniques and semi-parametric regression methods in order to identify which TIM provides the best representation of the observed empirical damage data (section 4.4). Fragility surfaces are not considered as they are not currently widely used in practice, however multiple inundation parameters are represented in single, more complex TIMs allowing multiple inundation parameters to be represented in a single curve. Recommendations are then provided based on the findings for the future development of tsunami fragility functions.

Finally, a preliminary methodology for quantifying debris-related effects on fragility functions is presented. Buildings are identified which are most likely to have sustained significant debris damage, based on the proportion of nearby buildings which have been designated as “washed away” in their post-tsunami survey. Fragility curves are then constructed for observed inundation depth and simulated force, and fragility curves with/without debris impact are compared for each damage state. Complex models which include all buildings and additional parameters corresponding to debris impact are considered. The influence of debris model parameters on determining building damage is shown to be significant for all but the lowest damage state (“minor damage”). Furthermore, the more complex fragility functions which incorporate debris model parameters are shown to have a statistically significant better fit to the observed damage

data than models which omitted debris information. It is noted that the definition of debris impact is beyond the scope of this thesis, and the focus is to instead demonstrate whether it is feasible to identify debris impact, and to highlight what effect this might have on fragility functions.

By providing recommendations as to which are the most efficient TIMs and statistical model fitting approaches, and by introducing an advanced method for selecting optimal statistical models, these findings have the potential to change how both empirical tsunami fragility curves are constructed in the future. Furthermore, the TIMs inform the analytical fragility function research presented in Chapter 5 and highlight the need for these to include debris impact in the future.

4.2 Presentation of Data

4.2.1 Building Damage Dataset

The building damage data used in this chapter is taken from the GEJE (2011) building damage database compiled by Japan's Ministry of Land Infrastructure Tourism and Transport (MLIT). The database is comprised of relevant information (including the number of floors, construction material, and building usage) for each individual building (circa 250,000) located within the inundation area of the 2011 Japan, though information is generally not included for every field for each building. The database represents a combination of government census data obtained before and after the 2011 Japan tsunami, and damage survey data obtained by the Japanese Ministry of Land Infrastructure, Tourism and Transport (MLIT) immediately after the tsunami. All buildings are allocated a damage state from DS0 to DS6 based on the damage scale presented in Table 4-1, and assigned an observed inundation depth. As discussed by Charvet et al. (2014) DS5 and DS6 do not represent progressively worse damage states, and so should be combined for fragility function derivation. For the remainder of this study, damage states 5 and 6 are combined and collectively termed as DS5*. It is also noted that although each building is allocated an observed inundation depth, there is error within the observation data as they are derived from the MLIT 100m-mesh inundation database, whereby the highest observation for each 100mx100m grid-square was assigned to all buildings within that grid-square. Inundation observations were primarily obtained from water marks or survivor interviews, and where no observations were present in a grid-square interpolation was conducted based on the nearest observations.

Table 4-1: Damage state definitions used by the Japanese Ministry of Land Infrastructure Tourism and Transport following the 2011 Great East Japan Earthquake and Tsunami. Descriptions from Japan Cabinet Office (2013), usage descriptions are after Suppasri et al. (2014).

Damage State			Description	Use
DS0		No Damage	Water does not enter into the building footprint	Immediate occupancy
DS1		Minor Damage	Water enters below the ground floor	Possible to use immediately after minor floor and wall cleanup
DS2		Moderate Damage	Water inundates to less than 1m above the ground floor	Possible to use after moderate repairs
DS3		Major Damage	Water inundates to more than 1m above the floor (but below the ceiling)	Possible to use after major repairs
DS4		Complete Damage	The building is inundated above the ground floor level	Major work is required for re-use of the building
DS5	DS5*	Collapsed	Structural elements are significantly damaged	Not repairable
DS6		Washed Away	The building is completely washed away except for the foundation	Not repairable

In the present study, the largest detailed dataset used to date for deriving empirical tsunami fragility curves for Japan is adopted. Three case-study locations are considered, namely the towns of Ishinokami, Onagawa, and Kesennuma (shown in Figure 4-1), which represent 80%, 15%, and 5%, respectively, of the combined dataset (67,125 buildings). Kesennuma and Onagawa experienced much deeper inundations than Ishinomaki (see Figure 4-1), and also display a higher proportion of collapsed buildings (DS5*). The distinctly different damage state distributions give rise to different fragility curves if data from each town is considered separately, as shown in Figure 4-1. Despite Kesennuma and Onagawa providing large individual datasets, most of the buildings in these towns sustained damage level DS5*, resulting in fragility curves for lower damage states associated with low confidence. A closer look at the data shows that the distributions of buildings with different construction materials is similar for the three towns and that together they provide a better coverage of a range of inundation depths. Hence, it is reasonable to combine the data from the three towns in order to derive more reliable fragility curves.

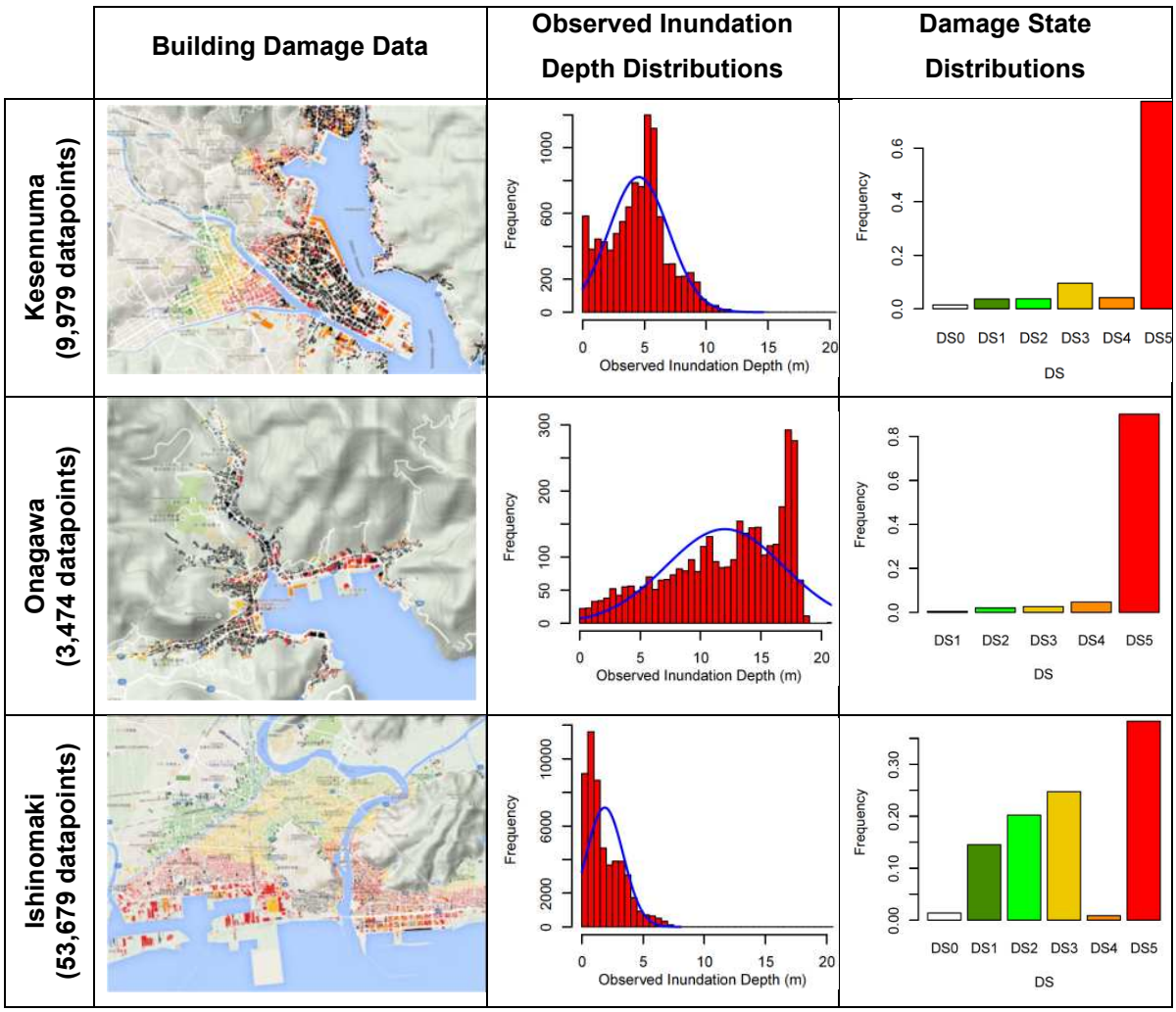

Figure 4-1: Case-study locations with GIS images, Damage State and depth distributions, and example fragility curves. GIS images have buildings coloured according to their observed damage state (right), where: white buildings indicate no damage (DS0), black indicates that buildings have been washed away (DS6) and all other damage states are coloured based on a scale from green (DS1) to red (DS5). Fragility curve are ordered probit models for engineered (RC and Steel) construction materials using complete-case analysis of disaggregated data.

The construction material of a building has been shown to significantly affect the building damage probability (Suppasri et al. 2012a). However, producing fragility curves for each construction material requires splitting the data into small datasets for some materials (e.g. Kesennuma has only 112 steel buildings, spread over the 5 damage states), which can result in larger errors associated with the model parameter estimates. Figure 4-3 shows that damage state distributions for wood and masonry, typically associated with non-engineered constructions, are very similar to each other. The same can be observed of the damage distributions associated with reinforced concrete (RC) and steel construction materials, usually associated with engineered buildings. Comparison between the damage distributions of engineered and non-engineered buildings instead shows significant differences. Hence, in this chapter fragility curves are developed for engineered and non-engineered structures, in order to account for the significant

differences in the fragilities of such buildings, whilst maintaining large enough datasets to avoid greatly increasing uncertainty in the model parameter estimates.

Figure 4-2 shows the distribution of construction materials aggregated across all case study locations. Buildings of unknown construction material (denoted “unknown”) make up 18.1% of the total dataset within the inundated area, representing a significant proportion of the data. Previous studies (e.g. Suppasri et al. 2013) generally conduct complete-case analysis, i.e. they remove any partial data, such as buildings of unknown material, from their fragility analysis. However, not dealing with missing data leads to a loss of statistical power and bias if the missing data is informative.

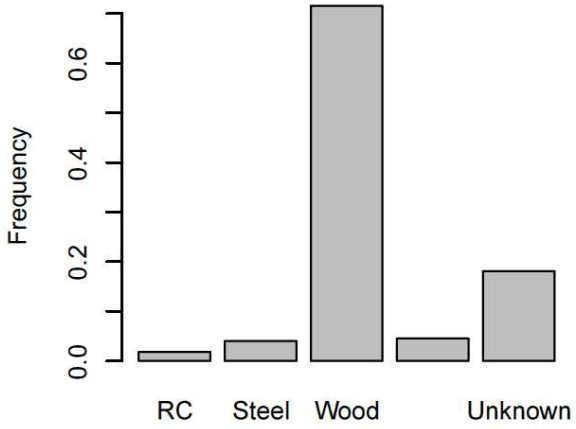

Figure 4-2: Construction materials aggregated across all case study locations (67,125 datapoints) for (from left to right) RC.

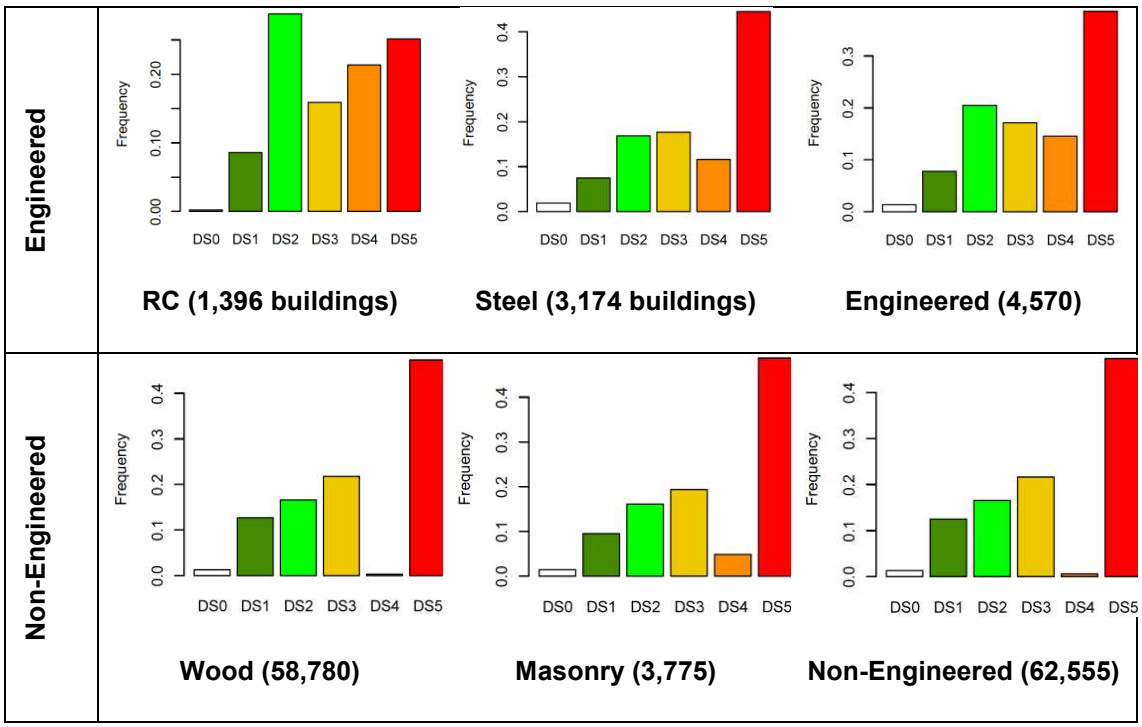

Figure 4-3: DS bar plots showing that engineered and non-engineered buildings (aggregated across all case study locations) exhibit different DS distribution.

According to the guidelines set out by Ware et al. (2012), the approach to be used for dealing with missing data depends on whether the data is Missing Completely At Random (MCAR), Missing At Random (MAR), or Missing Not At Random (MNAR). MCAR refers to the case where the data is missing purely by chance. In the present case this means that there should be no relationship between the buildings that have missing material data and other attributes such as the building height, size and use. However, analysis of building footprint sizes (Figure 4-4) suggests that engineered buildings (RC and steel) are generally larger than non-engineered buildings (wood and masonry), with buildings of unknown material representing the smallest footprints. This suggests that many buildings of unknown material may represent non-engineered buildings. A Kolmogorov-Smirnoff test is conducted and confirms that footprint areas for the buildings of unknown material are not of the same distribution as for the total dataset (i.e. they have different probability density functions). Therefore, the missing building material data is not MCAR. MNAR refers to the case where the missing information is related to the reason that the information is missing, for example wooden buildings are more likely to have missing material data because they are wooden. However, not all the missing material data can be associated just with the non-engineered construction types. Hence, the missing building material data is not MNAR. MAR refers to the case where the information is not missing completely at random but can be accounted for by using other attributes (e.g. where small buildings are more likely to have missing material data, but this has nothing to do with material after accounting for size). This is more likely to be

the case here, and according to Ware et al. (2012) if complete-case analysis (i.e. removing data with unknown construction material) were to be carried out with MAR data, bias would be introduced into the fragility analysis. Hence, here we adopt a Multiple Imputation (MI) approach to assign building data for which construction material information is missing to either the engineered or non-engineered building categories.

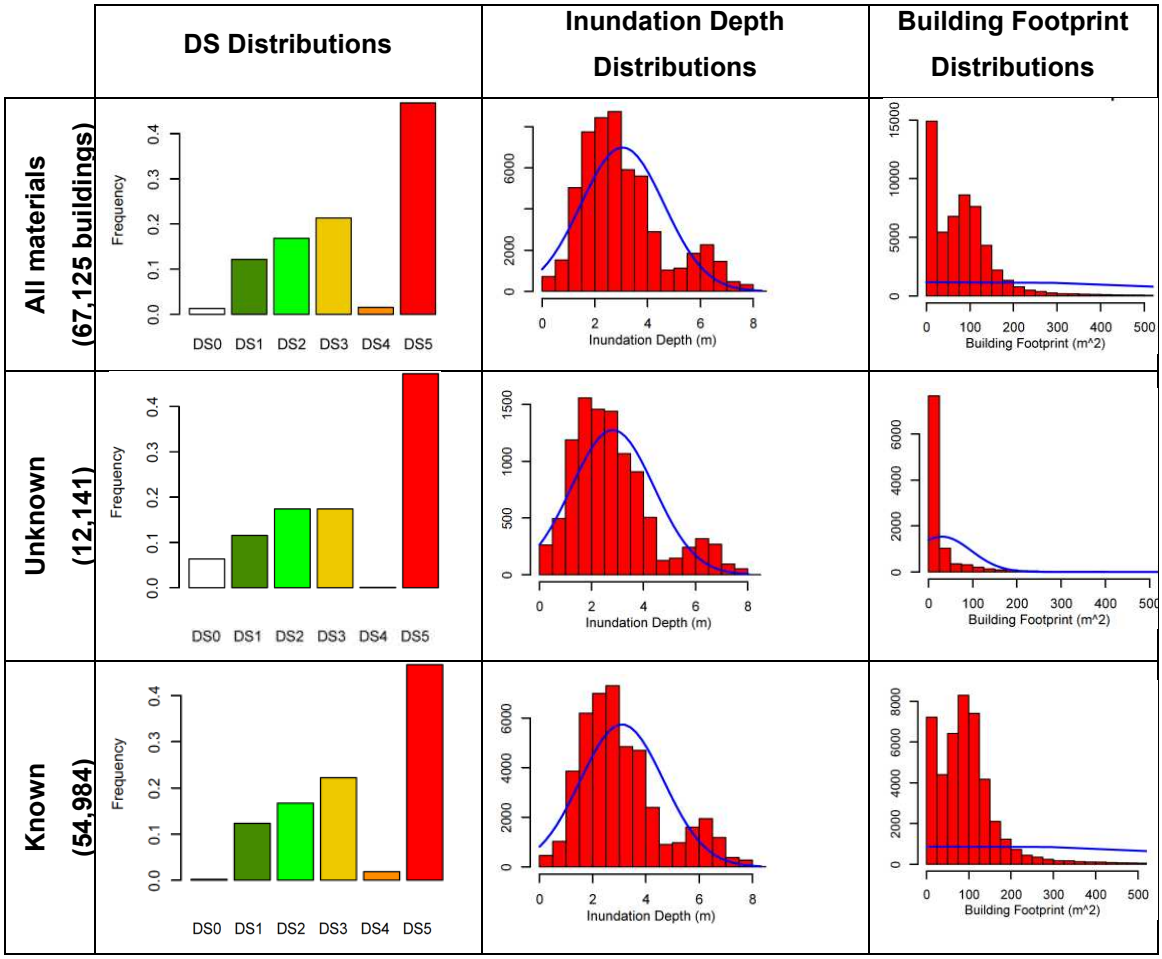

Figure 4-4: Damage State distributions, showing that buildings of unknown material type have a greater proportion of undamaged (DS0) buildings than buildings of known material type. Histograms and normal curves for building inundation depths and footprint areas for all buildings (left), buildings of unknown material only (centre), and buildings of known material (right).

MI involves replacing missing observed data with substituted values estimated multiple times via stochastic regression models built on the other attributes (used as explanatory variables), with all of the imputations being combined in order to derive the final estimate (Rubin, 1987). But, which attributes should be used for the imputation? It has already been shown that building footprint is an indicator of construction material. Figure 4-4 also shows that buildings of unknown material show a large proportion of undamaged (DS0) buildings. Given that the dataset is a combination of census data and damage survey data, it might be speculated that building material was only recorded during the damage survey, which did not investigate undamaged buildings in detail. Visualization of building

location by construction material shows no obvious spatial correlation of the unknown buildings. However, a Kolmogorov-Smirnov test performed on the observed inundation depths for unknown and known materials indicates that there is a very low probability (<5%) that the two datasets are drawn from the same underlying distribution. Figure 4-4 shows that the distributions of inundation depths for buildings of unknown material do have a slight increase in the number of buildings at low simulated inundation depths. As undamaged buildings are more likely to fall within the unknown material category, and buildings are more likely to remain undamaged at the outskirts of the inundation area, then it is to be expected that there are slightly more unknown buildings experiencing low inundation depths. In addition, building use shows some correlation with construction material. Therefore, Multiple Imputation analysis, with 4 imputations, is conducted in order to estimate building material based on footprint area, damage state, building use, and observed inundation depth. The effect of imputation on results is presented in section 4.3.1.

4.2.2 Tsunami Inundation Simulation Data

To supplement the observed inundation depth data, numerical inundation simulation is conducted for the case-study locations and the quality of fit is assessed for fragility curves derived for the alternative TIMs shown in Table 4-2. TIM1-TIM6 have already been discussed in the context of existing studies. The drag force is proportional to the local momentum flux and so is proportional to TIM4. Tanaka and Kondo (2015) recommend changing fragility curves dependent on the Froude Number, and so two additional TIMs will be considered here. Froude number will also be considered directly as a TIM (TIM6).

TIM7 (F_{QS}) is the equivalent quasi-steady force proposed by Qi et al., (2014) and discussed in section 2.4.2.4. It is evaluated via two different flow regimes determined by Froude Number. As outlined in section 2.4.2.4, the drag coefficient (C_D) is calculated from equation (2-13) (drag coefficient as a function of blockage ratio). The upstream critical Froude Number, which determines the separation between sub-critical and choked flow, is calculated by back-substituting equation (2-15) (the definition of downstream critical Froude Number, FR_{dc})) into equation (2-14) (the relationship between upstream and downstream Froude Number). The hydrostatic drag coefficient (C_H) and form drag coefficient for unbound flow (C_{D0}) are defined in Qi et al. (2014), and blockage ratio (b/w) is calculated from the flume and model widths for the long-wave flume experiments (section 2.4.2.4):

- C_H = 0.58
- C_{D0} = 1.9
- b/w = 0.25

The calculated values are as follows:

- C_D = 2.91
- Fr_{dc} = 0.92
- Fr_{1c} = 0.52

All of the simulated TIM values are calculated at the geometrical centres of each building footprint for each time-step of the simulation, and the peak values extracted, with the exception of the equivalent peak momentum flux (MF_{equiv}, TIM5) and quasi-steady force estimation (F_{QS}, TIM7) both of which are calculated using the separate peak depth and peak velocity values (which do not occur at the same time). This is because inundation simulations used in practice often do not provide all of the above TIMs as standard outputs, due to added computational expense, and so the effect of using the non-coincident peak depth and peak velocity to calculate more complex TIMs is investigated here, via the comparison of TIM4 and TIM5.

Table 4-2: Alternative TIMs considered in this investigation. "Equivalent" denotes that values are not extracted as peak values directly from the inundation simulation, but calculated separately from the non-coincident peak depth and peak velocity.

TIM		Symbol	Description
TIM1	Observed inundation depth	h_{obs}	Peak *observed* inundation depth
TIM2	Simulated inundation depth	h_{sim}	Peak *simulated* inundation depth
TIM3	Flow speed	v	Peak simulated velocity (v_{peak})
TIM4	Momentum flux	MF	$(hv^2)_{peak}$
TIM5	Equivalent peak momentum flux	MF_{equiv}	$(h)_{peak}.(v^2)_{peak}$
TIM6	Froude number	Fr	$\left(\frac{v}{\sqrt{gh}}\right)_{peak}$
TIM7	Equivalent quasi-steady force	F_{QS}	Alternative steady-state force estimation considering choked and sub-critical flow. See text above for calculation procedure.

The numerical tsunami inundation model is presented in detail and validated by Adriano and Koshimura (2016). The tsunami source model used in this study is the time-dependent slip propagation model presented in Satake et al. (2013). The wave propagation and inundation calculation solves discretized non-linear shallow-water equations (Imamura et al. 1995; Suppasri et al. 2012) over six computational domains in the nested grid system shown in Figure 4-5. The non-linear shallow-water equation includes the effects of flow resistance, which is parameterised using the Manning's roughness coefficient (n). A uniform value of n = 0.025 is chosen to account for the flow

resistance from obstacles (such as buildings and trees) in the urban case study areas. Figure 4-5 and Figure 4-6 show inundation simulation results for Ishinomaki. The results shown are the peak values for each grid square over the simulation period.

The source model was calibrated to observations from offshore buoy data by scaling the source model (the amount of fault slip or the initial tsunami height) to optimise the *K*-value, a spatial correlation index proposed by Aida (1978) which compares simulated and observed flow parameters, where 1 indicates a good agreement. For Ishinomaki, the original tsunami source model gave a K-value of 0.75, and the calibrated source model achieved a final *K*-value of 1.06. However, it is noted that the improved *K*-value does not necessarily mean good agreement between observed and simulated inundation depth at each building location.

Figure 4-7 compares observed and simulated inundation depths for all 67,125 buildings. On average the simulation over-estimates the observed depth by 0.1m (Figure 4-7b), but tends to overestimate values at lower depths, and underestimate higher depths (Figure 4-7c). These discrepancies are expected because local increases in flow depth at obstacle locations is not considered in the model, but the observed field measurements will include traces that will exhibit this increased depth. Furthermore, spatial and temporal variation of the flow resistance due to the destruction of obstacles is not modelled. It is also important to note that there may be error in the observed depth values, for the reasons outlined in section 4.2.1, so the discrepancies shown in Figure 4-7 should not be considered as due to simulation error only, but due to errors in both observations and simulations.

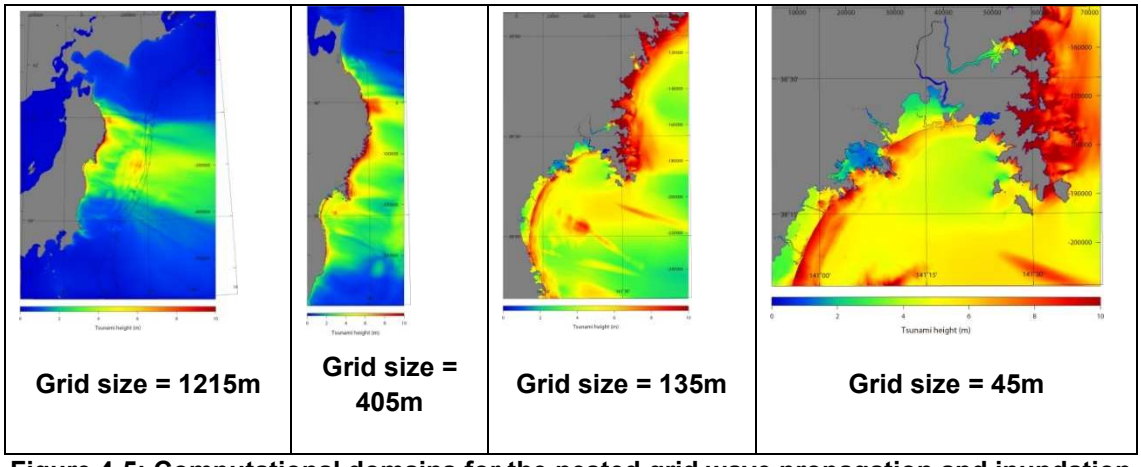

Figure 4-5: Computational domains for the nested grid wave propagation and inundation model used for Ishinomaki (dx indicates the grid size). Results for grid size = 15m inundation simulation are shown below in Figure 4-6.

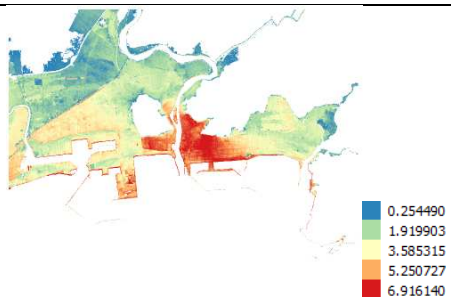

TIM2: Simulated Inundation Depth (m)

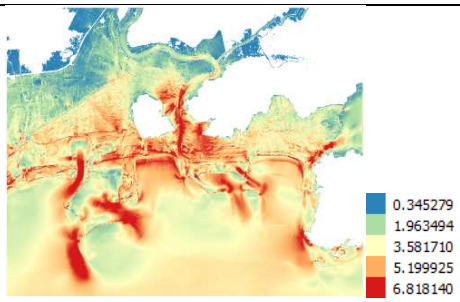

TIM3: Flow Speed (m/s)

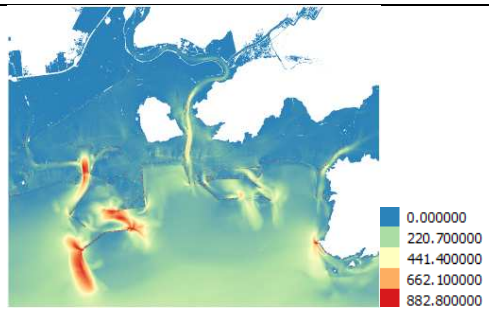

TIM4: Momentum Flux (m.(m/s)^2)

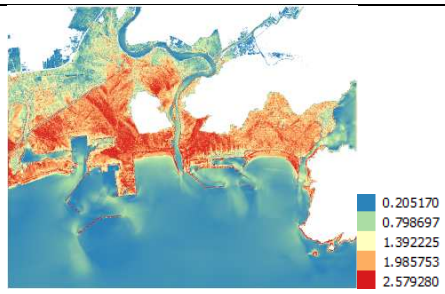

TIM6: Froude Number

Figure 4-6: Inundation simulation results for Ishinomaki.

Whilst it is possible to validate simulated inundation depth results, there is insufficient velocity observation data to make a meaningful comparison beyond that presented in Adriano and Koshimura (2015). Park et al. (2013) compares simulated depth, velocity and momentum flux values to experimental results, and Park et al. (2014) conducts a sensitivity analysis of the same TIMs to friction coefficient and modelling software. Both studies find that where changes in simulation parameters may lead to small changes in depth, changes in velocity and momentum flux can be much greater (a 15% change in depth was reported to correspond to a change in velocity and momentum flux of 95% and 208% respectively). This is likely due to the fact that the mass of water on land will be reasonably well predicted (because the flux is essentially calibrated from the flow data). However, the flow speed depends on the fidelity of the flow dynamics in the model. Therefore, the discrepancies in Figure 4-7 suggest the possibility of much greater potential error in TIMs related to velocity and momentum flux, though this cannot be verified with the available data. The Implications of these potential discrepancies are discussed in section 4.4.

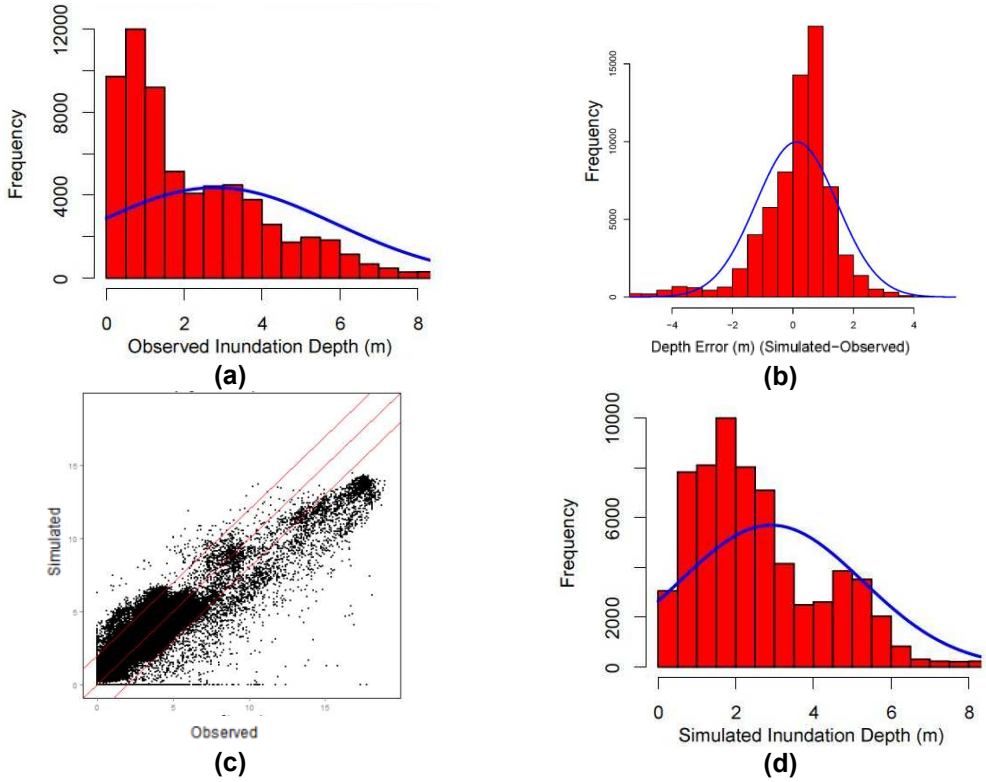

Figure 4-7: Comparison between observed and simulated inundation depths. (a) and (d) show the distribution of observed and simulated depth respectively, with corresponding Gaussian curves. (c) shows their correlation (correlation coefficient 0.91), with the outer red diagonals indicating the 2m error band. (b) shows the distribution of the error (simulated – observed), with corresponding Gaussian curves.

4.3 Investigation into Sensitivity of Statistical Modelling and Data Aggregation

It is necessary to select at least two statistical models with which to conduct the comparison of Tsunami Intensity Measures (TIMs) in section 4.4, so as to draw conclusions which are non-model-specific. In this section, a sensitivity analysis of several statistical methods for fragility curve derivation is presented. General conclusions are drawn regarding the suitability of various models and the methods used to select between them, and the models used for the TIM comparison of section 4.4 are selected. It is noted that the TIM used in this section is the observed inundation depth reported in the MLIT database, and therefore this investigation is independent of the inundation simulation, which is discussed further in section 4.4.

4.3.1 Further Exploratory Analysis Using Statistical Models

Further exploratory analysis is first conducted in order to investigate the influence of construction material and the data imputation presented in section 4.2.2. The fragility of the Japanese building inventory is empirically assessed following the procedure proposed by GEM (Rossetto et al. 2014), extended to use cross-validation techniques to assess model fit. According to the GEM methodology, a statistical model suitable for the

available data should be constructed. Statistical models are used to construct a relationship between building damage and the TIM, which accounts for the uncertainty in damage prediction. The statistical models can be parametric (e.g. Generalised Linear Models (GLMs), Cumulative Link Models (CLMs), or linear models with Ordinary Least Squares (OLS) parameter estimation), semi-parametric (e.g. Generalised Additive Models, GAMs) or non-parametric (e.g. kernel smoothers).

As part of the exploratory analysis of the available database, ordinal cumulative link models are fit to all 67,125 data, where fragility curves corresponding to the five damage states (DS1-DS5*) are determined by assigning a damage response indicator, *ds*, to each building, which is considered to follow a multinomial distribution. Each building is also assigned a TIM value, x_j. The main advantage of this model over separate GLMs fitted to binary data, is its ability to use all available information regarding the data in the database, it recognises that the damage is an ordinal categorical variable and accounts for the main conclusions of the exploratory analysis (Charvet et al 2014a). A probit link function is used (the inverse standard cumulative normal distribution). The model equation is given in (4-1) where β_0 and β_1 are the unknown regression parameters (the intercept and slope, respectively) estimated by a maximum likelihood optimisation algorithm. Uncertainty is quantified using bootstrap methods employed by Charvet et al. (2014) based on 1,000 iterations.

$$ds = \{0,1,2,3,4,5^*\}, \qquad ds|x_j \sim Multinomial\left(P\left(ds = DS_i|TIM = x_j\right)\right)$$

Random Component

$$\text{Where,} \quad P\left(ds = DS_i|TIM = x_j\right) = \begin{cases} 1 - P\left(ds \geq DS_i|x_j\right) & i = 0 \\ P\left(ds \geq DS_i|x_j\right) - P\left(ds \geq DS_{i+1}|x_j\right) & 0 < i < N_{DS} \\ P\left(ds \geq DS_i|x_j\right) & i = N_{DS} \end{cases} \qquad \textbf{(4-1)}$$

Systematic Component

$$\text{and } probit\left(P\left(ds \geq DS_i|TIM = x_j\right)\right) = \beta_{0,i} + \beta_{1,i}x_{j,k}$$

Parameter Estimation

and $\beta_{0,i}$, $\beta_{1,i}$ estimated via Maximum Likelihood

Curves are constructed for engineered and on-engineered building categories and the influence of these construction material groups is examined by fitting the cumulative link model expressed by (4-1) to the data corresponding to the two material groups. Figure 4-8 shows that fragility curves for engineered and non-engineered buildings differ in both slopes and intercepts, and so it is appropriate to consider these material groups separately. Consequently, the TIM comparison of section 4.4 is conducted for each material group separately, and results are compared.

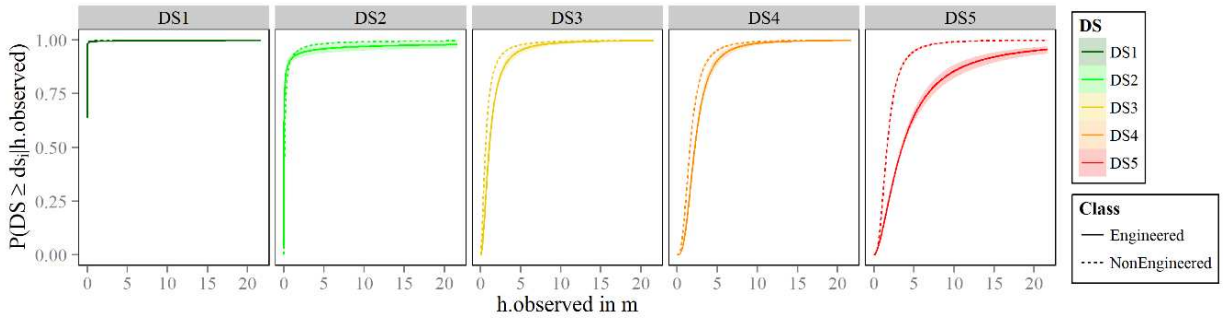

Figure 4-8: Comparison of fragility curves for engineered and non-engineered material groups, for each damage state, formed on disaggregated data.

The next question that should be addressed is whether the Multiple Imputation process outlined in section 4.2.1 yields significantly different fragility curves, compared to those derived from the database where the missing data are ignored. Figure 4-9 shows a sensitivity analysis whereby fragility curves are compared for engineered buildings formed on the imputed data and the original data (with missing data removed). The difference in the mean curves with and without using MI confirms that the removal of data with missing information on construction material leads to a bias for the case of this dataset. Furthermore, the limited variation in the mean curve for each of the imputations shows that although 18.2% of the data is missing, materials estimated using MI provide relatively stable results. All analysis conducted throughout the remainder of this study is conducted on the completed (imputed) data (Figure 4-9a).

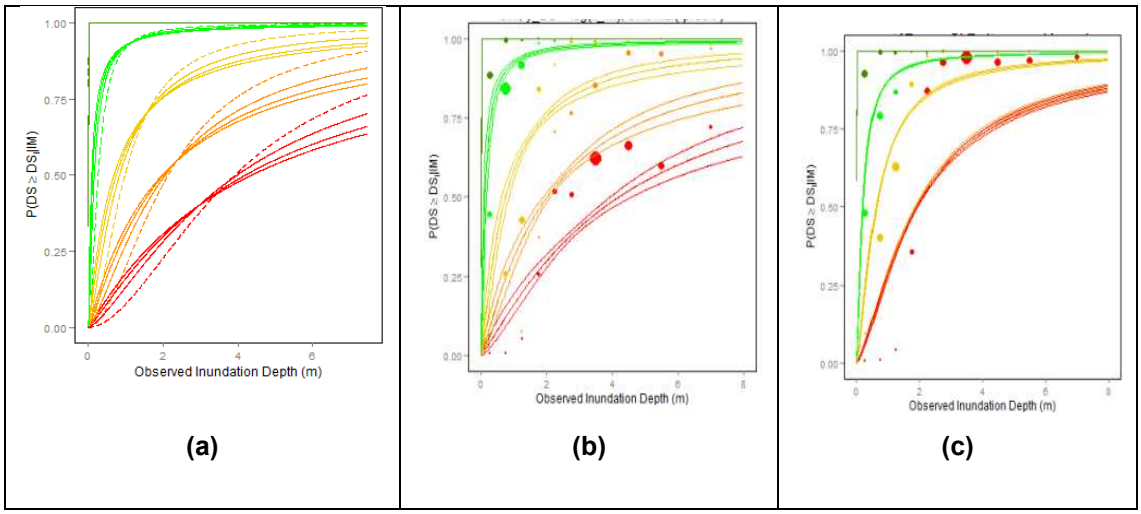

Figure 4-9: Imputed data. (a) shows a sensitivity analysis of derived fragility curves for engineered structures to the multiple imputation method applied to estimate unknown building materials. Dashed-lines show curves formed using complete-case analysis (ignoring missing data). Solid lines show the mean curve for the imputed dataset which is used throughout the remainder of this study, and the indicated range for each curve shows the maximum/minimum values for the mean curves derived separately on each of the four imputations. (b) and (c) show the ordered probit models for engineered and non-engineered material groups respectively, formed on the imputed dataset.

4.3.2 Sensitivity Analysis of Statistical Methods and Data Aggregation

4.3.2.1 Sensitivity Analysis Methodology

Three stages of analysis are conducted in order to identify suitable statistical models for representing the imputed dataset: first a comparison of ordered and partially-ordered cumulative link models, then a sensitivity analysis of data aggregation and parameter estimation techniques, finally a sensitivity analysis of semi-parametric model parameters. The models considered are summarized in Table 4-3.

This study utilizes several "goodness of fit" tests in order to assess how well a statistical model fits the damage data, to quantitatively compare models, and to choose the model with the best fit. The coefficient of determination (R^2) can be calculated in various ways and has different interpretations for OLS regression models and GLMs, and so alternative tests are considered here. Guidelines set out by Rossetto et al. (2014) recommend the use of the Likelihood Ratio Test to compare nested models (e.g. when testing the addition of explanatory variables, or when comparing multinomial and ordinal models), and the Akaike Information Criteria to compare non-nested models (e.g. two models fit to the same data using the same TIMs, but different link functions). However, these techniques cannot be used to directly compare cumulative models (multinomial random component, models M1.1, M1.2, M2.1, M2.3) with separate models (binomial random component, models M2.2, M2.4, M3.1, M3.2), nor to compare models formed on aggregated and disaggregated data.

Cross-validation techniques (introduced in section 2.3.4.2) can be used to compare all of the statistical models in Table 4-3, and so is used here. Cross validation has been used to estimate tsunami fragility curve prediction error rates by Muhari et al. (2015) and Charvet, Suppasri et al. (2014), who also propose a penalized error estimation method for multinomial models that is used in this study. In (4-2), N_{DS} refers to the number of damage states (6 in this case, including DS0), and the predicted damage state ($ds_{j,predicted}$) for the j^{th} observation is taken as the damage state that has the greatest probability of occurrence. For each model, the penalized error rate is repeatedly estimated until the difference between the running average and that of the previous iteration reduces to below 10^{-5}. Results are provided in Table 4-3, and discussed in the subsequent sub-sections.

$$Error\ rate(multinomial) = \frac{1}{K}\sum_{k=1}^{K}\left[\sum_{j}^{N_{test\ set}} \frac{\left|ds_{j,predicted} - ds_{j,observed}\right|}{N_{DS}-1}\right] \qquad \textbf{(4-2)}$$

where $ds_{j,predicted} = \underset{DS_i \in \{DS_0:DS_6\}}{\operatorname{argmax}} P\left(ds = DS_i \middle| TIM = x_j\right)$

Table 4-3: Summary of models used in sensitivity analysis of statistical methods. The number of damage levels is 6 (DS0-DS5*, defined in Table 4-1). The number of explanatory variables is always 1 (observed inundation depth). CLM = Cumulative Link Model, OLS = Ordinary Least Squares, GAM = Generalized Additive Models. The prediction error-rate is calculated via 10-fold cross-validation using (4-2)).

Model	Input Data - Aggregation	Model Type	Model Components		Prediction Error-Rate
			Random Component	Systematic Component	
M1.1	N	CLM	Multinomial	Partially-ordered probit model	11.3%
M1.2				Ordered probit model	19.7%
M2.1	Y (constant bin width)	CLM	Multinomial	Partially-ordered probit model	11.6%
M2.2		OLS	Binomial	Assumed lognormal CDF	20.0%
M2.3	Y (constant #datapoints / bin)	CLM	Multinomial	Partially-ordered probit model	11.1%
M2.4		OLS	Binomial	Assumed lognormal CDF	18.3%
M3.1	N	GAM	Binomial	Probit model with 4 knots	10.3%
M3.2				Probit model with 7 knots	10.5%

4.3.2.2 Testing of Ordinal Models

Multinomial data can be assessed using either partially-ordered or ordered probit models (models M1.1 and M1.2 respectively). For ordered models the slope parameters (β_1 in Equation (4-1))) are assumed to be equal for all damage states so as to avoid undesirable effects such as the crossing of curves. Partially-ordered models relax this assumption. Guidelines set out by Rossetto et al (2014) recommend the use of the Likelihood Ratio Test to compare nested models (e.g. when testing the addition of additional parameters, or when comparing multinomial and ordinal models). The more complex model (partially-ordered model, M1.1) will always fit the data as well as or better than the simpler model (M1.2), as shown by the error rates given in Table 4-3. The likelihood ratio test results given in Table 4-4 confirm that there is less than a 1% chance that the improvement of fit for the more complex model could be observed by random chance, and therefore the partially ordered model is to be used for the TIM comparison in section 4.4.

Table 4-4: Likelihood Ratio Test results for ordered and partially ordered models, showing that the partially ordered model provides a significantly better fit than the ordered.

Model		logLikelihood	Likelihood Ratio Statistic	P (χ^2)
M1.1	Partially Ordered Model	-4964.4	1734	<2.2e-16 ***
M1.2	Ordered Model	-5831.4		

4.3.2.3 Sensitivity Analysis of Data Aggregation and Parameter Estimation Technique

Many existing studies use Ordinary Least Squares (OLS) parameter estimation to fit Normal or Lognormal Cumulative Distribution Functions (CDFs) to aggregated model data, as set out in Koshimura, Oie, et al. (2009). Unlike CLMs which consider all damage states simultaneously, OLS models fit separate models for each of *i* damage states, by assigning an indicator, $I_{ij,}$ to each of *j* buildings (Equation (4-3)). The linear model assumption violations of OLS models are highlighted by Charvet, Ioannou, et al. (2014a), though the effect of these violations are not quantified. OLS models are considered here to identify whether these model violations make them unsuitable for the TIM comparison of section 4.4.

$$\mu_i = P\left(ds > DS_i \middle| TIM = x_j\right)$$

$$\Phi^{-1}\, P(ds > DS_i|TIM) \sim normal(\mu_i, \sigma^2),$$

$$where \mu_i = \begin{cases} \theta_{1i} ln\left|x_j\right| + \theta_{0i} & cumulative\ lognormal \\ \theta_{1i} x_j + \theta_{0i} & cumulative\ normal \end{cases} \quad \textbf{(4-3)}$$

where θ_{1i} and θ_{0i} are estimated via Ordinary Least Squares

Data aggregation must be carried out in order to form OLS models, as the inverse normal distribution function (Φ^{-1}) is undefined at 0 and 1. Different studies aggregate data using different methods (e.g. splitting the IM range into bins of constant width, or selecting bin widths so as to ensure a constant number of observations per bin). Data aggregation by any method results in some information being lost (e.g. data distributions within IM bins are no longer accounted for), and so it is expected that model predictive power decreases and uncertainty increases. However, these effects have not been quantified in previous studies, and so it is not known if they are significant.

The effect of data aggregation is first examined by fitting a partially-ordered CLM (Equation (4-1)) to the data aggregated into 10 IM bins of equal width (model M2.1). Table 4-3 shows that the predictive error rate is higher than that of the corresponding

model fit to disaggregated data (model M1.1), confirming that data aggregation can reduce model accuracy. The effect of parameter estimation is then examined by fitting an OLS model (Equation(4-3)) to the same aggregated data (model M2.2). Table 4-3 shows that the predictive error rate is higher than that of the corresponding aggregated CLM model (M2.1), showing that the OLS linear model violations do reduce the accuracy of the model. Sensitivity to aggregation method is then examined by fitting CLM and OLS models (M2.3 and M2.4, respectively) to data aggregated into 10 IM bins, where bin width is determined so that each bin contains the same number of buildings. Table 4-3 shows that the predictive error rates are different from the corresponding models fit to data aggregated by alternative methods (M2.1 and M2.2 respectively) showing that results are sensitive to the aggregation approach. It is also noted that aggregated data prevents the use of imputation methods and much of the exploratory analysis presented in this study, meaning that it is more difficult to identify and remove bias and complete missing data.

Given that data aggregation reduces model predictive accuracy by an amount which is dependent on aggregation approach suggests that disaggregated data must always be preferred, and so existing studies which use aggregated data from the 2011GEJE should be considered superseded by those which use disaggregated data. This issue is compounded for OLS models where the linear model assumption violations have been shown to result in a further reduction in model accuracy, and increased sensitivity to aggregation method.

4.3.2.4 Sensitivity Analysis to Select an Optimized Semi-Parametric Model

An alternative model is still required to conduct the TIM comparison of section 4.4, so as to draw conclusions which are non-model-specific. Generalized Additive Models (GAMs, developed by Hastie and Tibshirani (1990) are semi-parametric models that fit GLMs in a piecewise regression system with a number of separation points (or knots). Whilst there are dangers in using non-parametric and semi-parametric methods for prediction purposes (Chandler, 2014), they are suitable for comparing the influence of different explanatory variables (TIMs) to describe response variable observations. However, an issue with non-parametric and semi-parametric models is that they are susceptible to over-fitting, and their appropriateness in the context of fragility analysis has not yet been demonstrated. Therefore, GAMs are introduced here and a sub-sensitivity method for overcoming over-fitting is adopted.

Goodness of fit measures based on examination of residuals (e.g. R^2) are biased by overfitting, indicating a better fit to the underlying population than is really the case.

Cross-validation techniques are less biased by overfitting than techniques that simply consider residuals, and so comparison of the cross-validation error rates can be used to select the optimal non-parametric or semi-parametric model (e.g. to select the number of knots when using GAMs). For this dataset, Figure 4-10 shows that for a series of GAMs fit to disaggregated data, the model using 4 knots provides the lowest error rate and so provides the optimal fit over GAMs with more knots, which exhibit signs of overfitting.

Table 4-5: 10-fold cross-validation error rates for GAMs over a range of knots. The best and worst models are shown in Figure 4-10.

Knots	1	2	3	4	5	6	7	8
Error Rate	10.48%	10.47%	10.48%	10.35%	10.39%	10.40%	10.62%	10.52%

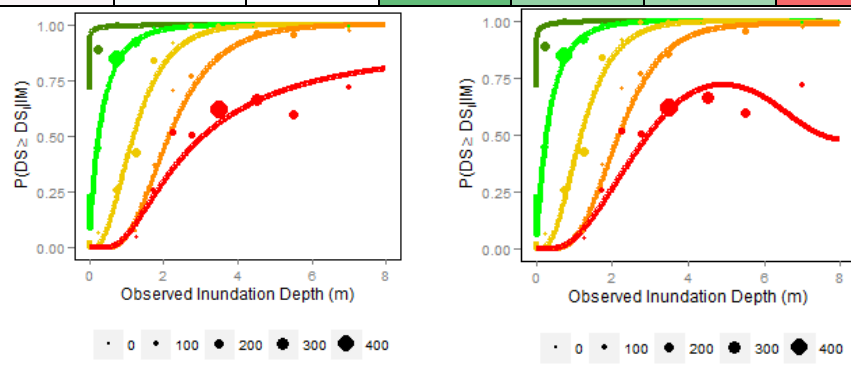

M3.1: 4 knots **M3.2: 7 knots**

Figure 4-10: Comparison of fragility curves for Generalized Additive Models (probit link function) with 4 (M1.3) and 7 (M1.4) knots, showing optimal and over-fit curves respectively. Note that aggregated datapoints are shown for graphical reference, but have not been directly used in the regression analysis, which has been conducted on the imputed disaggregated dataset.

As GAMs are a piecewise system of GLMs, and as overfitting can be avoided using the cross-validation sub-sensitivity method outlined above, GAMs are used (alongside CLM model M1.1) to conduct the TIM comparison of section 4.4. Note that the sub-sensitivity presented above is repeated so as to identify the optimal GAM model for each TIM in turn.

4.4 Identification of Optimal Intensity Measures

This section compares several Tsunami Intensity Measures (TIMs) in their ability to describe the observed damage data. Further exploratory analysis is first conducted to examine fragility curve sensitivity to potential inaccuracies in the inundation model used to derive the TIMs. Partially-ordered probit model (model M1.1) are then fit to the disaggregated data of the MLIT building damage database for each of the TIMs identified in Table 4-2, and their relative fits are compared using prediction error rates estimated

via 10-fold cross-validation. The same procedure is then conducted using Generalized Additive Models (GAMs), with the number of knots for each model selected using the sub-sensitivity analysis outlined in section 4.3.2.4. Finally, the TIMs are ranked by their predictive error rates for both the CLM and GAM model groups.

4.4.1 Sensitivity to Inundation Simulation Accuracy

Given the discrepancy between observed and simulated inundation depth highlighted in section 4.2.2, it is necessary to examine what effect this may have on the produced fragility functions. Figure 4-11 confirms that fragility curves for observed and simulated depths are different, and it is also noted that the model fit to simulated inundation depth gives a higher error rate than that fit to observed depth. Figure 4-12a and Figure 4-12b presents fragility curves where outliers have been removed, where outliers are assessed as corresponding to discrepancies between observed and simulated inundation depths of 1m and 2m respectively. These figures show that the mean curves are not sensitive to removal of outliers corresponding to at least 2m discrepancy (8.9% of buildings), but narrowing the allowable discrepancy to 1m (32.3%) has a large effect on the mean curves. The selection of a threshold beyond which to remove outliers is subjective, and discrepancies between observed and simulated results do not prevent the assessment of the relative accuracy of various simulated TIMs in describing observed damage, as the same outliers are present for all TIMs. Therefore, the remainder of this study uses the complete dataset (with no outliers removed), but it should be noted that following the arguments set out in section 4.2.2 the expected error for simulated TIMs relating to velocity and force are expected to be greater than those associated with depth only.

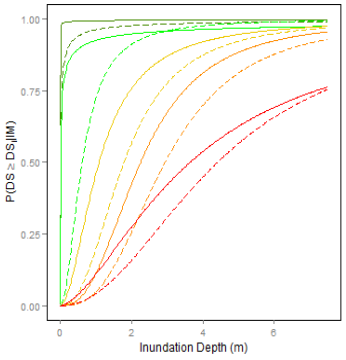

Figure 4-11: Comparison of fragility curves for simulated (dashed line, error rate=15.9%) and observed (solid line, error rate=11.3%) inundation depth, for engineered buildings (partially-ordered probit model).

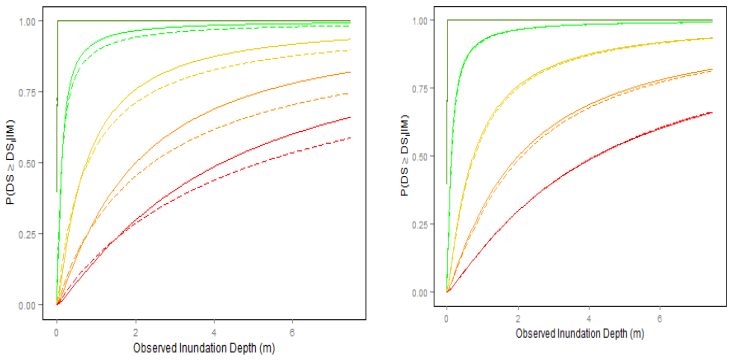

(a) **(b)**

Figure 4-12: Sensitivity to outliers. Probit models for observed inundation depth and engineered (RC and Steel) construction materials using the imputed disaggregated dataset, with datapoints of more than a (a) 1m discrepancy and (b) 2m discrepancy removed (corresponding to a loss of 32.3% and 8.9% of datapoints respectively).

4.4.2 Results of Intensity Measure Comparison

Table 4-6 and Table 4-7 compare the prediction error rates for CLMs and GAMs fit to each additional TIM, for engineered and non-engineered buildings, respectively. For engineered buildings the quasi-steady force estimation (F_{QS}) and simulated inundation depth (h_{sim}) appear to give the best fit. The fact that the results for CLMs and GAMs are similar suggest that the results are not model-specific. For non-engineered buildings, the GAMs fit to each TIM follow a similar pattern to that for the engineered buildings, i.e. that F_{QS} and h_{sim} appear to give the best fit. However, the CLMs fit to non-engineered data do not fit this pattern (Table 4-7), showing both momentum flux estimations (MF and MF_{equiv}) as the optimal TIMs, though with error rates very close to F_{QS}. This discrepancy suggests that the results are model-specific for the non-engineered category, and so further statistical models should be considered in order to build confidence in these results.

Table 4-6: Engineered Buildings: Comparison of prediction error rates for partially ordered cumulative link models. The colour scale indicates the goodness of fit, with the lowest error rates (indicating the best fit) shown in green.

	Alternative Intensity Measures						Optimal IM	
	TIM2	TIM3	TIM4	TIM5	TIM6	TIM7	1st	2nd
	h_{sim}	v	MF	MF_{equiv}	Fr	F_{QS}		
CLMs	16.0%	22.9%	17.3%	16.2%	27.5%	15.3%	F_{QS}	h_{sim}
GAMs	13.4%	19.9%	16.6%	15.7%	24.3%	14.1%	h_{sim}	F_{QS}

Table 4-7: Non-engineered Buildings. Comparison of prediction error rates for partially ordered cumulative link models. The colour scale indicates the goodness of fit, with the lowest error rates (indicating the best fit) shown in green.

	Alternative Intensity Measures						Optimal IM	
	TIM2	TIM3	TIM4	TIM5	TIM6	TIM7	1st	2nd
	h_{sim}	v	MF	MF_{equiv}	Fr	F_{QS}		
CLMs	28.7%	26.3%	19.7%	19.5%	28.4%	20.1%	MF_{equiv}	MF
GAMs	10.9%	17.4%	13.2%	12.1%	21.5%	10.9%	F_{QS}	h_{sim}

Velocity and Froude number alone are consistently the worst TIMs. However, F_{qs} (a function of *h, v* and *Fr*) generally performs better than the traditional force measure of momentum flux (a function of *h* and *v* only). The implications of these findings for the construction of future empirical and analytical fragility functions are that force should be used as a TIM, where either force accounts for the flow regime (for 2D curves) or an indicator of the flow regime (e.g. Froude Number) should be investigated as an additional TIM (for fragility surfaces).

The equivalent peak momentum flux is seen to provide a better fit to the data than the instantaneous peak momentum flux (*MF*). This suggests that the non-coincident depth and velocity can be combined without significant loss of damage predictive power. That is not to say that momentum flux calculated from non-coincident peak depth and velocity is an accurate estimate of instantaneous peak momentum flux (this has been shown to not be the case by Park et al., 2013), but that equivalent momentum flux is as good a descriptor of building damage as peak momentum flux. However, velocity outputs of the inundation model should be further validated in order to verify this result. It is noted that F_{QS} (consistently amongst the best performing TIMs) is an equivalent value calculated from the non-coincident peak depth, velocity and Froude number.

It is highlighted that this outcome has been reached despite the likely greater observation errors in simulated velocity and momentum flux than depth discussed in section 4.2.2. This indicates that depth is a preferred TIM where inundation simulation accuracy is thought to be low, and measures of force are the preferred TIMs where simulation accuracy is thought to be high, or where velocity can be validated (e.g. through experiments such as carried out by Park et al., 2013). However, to verify this conclusion it would be necessary to use models that take into account measurement error, and optimally to use sets of data with low and high measurement error.

4.5 Incorporation of Debris Effects in Fragility Function Derivation

This section presents a preliminary investigation to address the following research questions:

1. How does the presence of debris in tsunami inland flow affect fragility functions?
2. Is it possible to quantify this effect by separating fluid and debris-induced damage in fragility function derivation?

Buildings which are thought to have been damaged by debris effects are removed from the dataset and fragility functions are formed based only on buildings for which debris was less likely to be the main factor in defining building damage.

4.5.1 Method of Debris Designation

A major source of large debris within tsunami inland flow is from collapsed buildings (I Charvet et al., 2015), therefore buildings close to other collapsed buildings will be removed from the dataset. A regular grid of 500m is applied to each case study location, the total footprint area of all “washed away” (DS6) buildings is calculated for each grid, and if this area exceeds a threshold proportion of the total building footprint area for that grid all buildings of that grid are deemed to have been affected by debris and so removed from the dataset. Threshold proportions (washed away area/total area) of 20%, 35% and 50% are tried.

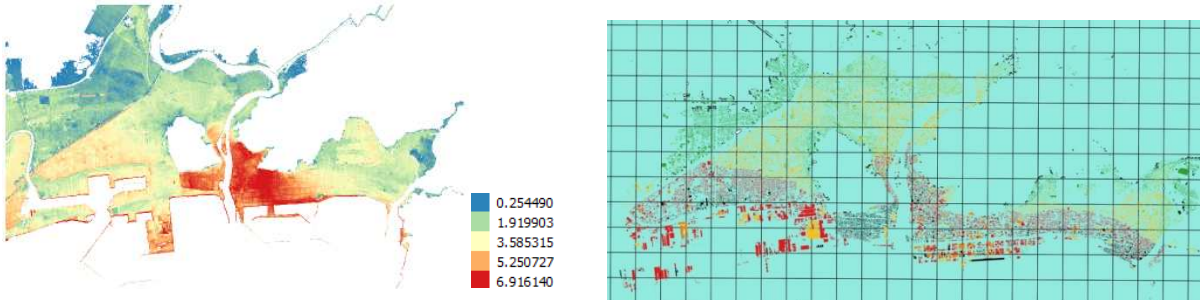

Figure 4-13: Plan views of Ishinomaki, Japan showing simulation results for inundation depth (left) and the 500m grid used for debris analysis (right) with buildings shown coloured according to their damage state (from DS1, green, to DS5, red, with washed away buildings denoted in black).

4.5.2 Exploratory Analysis of Debris Dataset

Table 4-8 shows the proportions of the dataset remaining after debris-affected buildings have been removed, according to each of the collapse area thresholds. It can be seen that the lowest collapse area threshold (of 20%) leads to the greatest number of buildings being removed from the dataset. Figure 4-14 shows histograms for all engineered buildings and for buildings not affected by debris (according to the 20% threshold), showing that buildings affected by debris fall into higher DS categories and at higher TIM values.

Table 4-8: proportions of data designated as debris-affected under various collapse area thresholds.

Threshold $\left(=\frac{Footprint\ area\ of\ 'washed\ away'\ buildings\ within\ gridsquare}{Total\ area\ of\ all\ buildings\ in\ gridsquare}\right)$	Number of buildings deemed to not be affected by debris	% of total dataset unaffected by debris
No buildings removed from dataset	4570	100%
50% of total grid building area	3982	87.1%
35% of total grid building area	3792	83.0%
20% of total grid building area	3130	68.5%

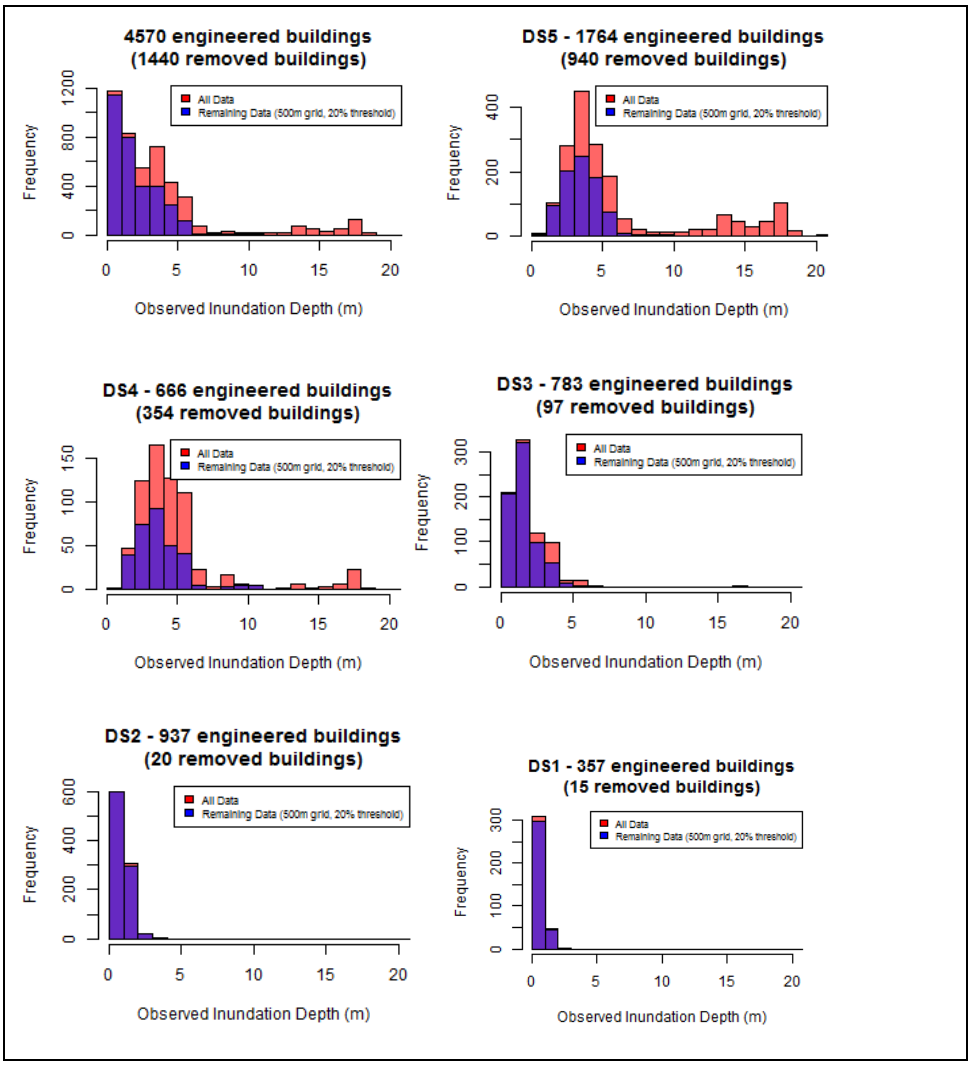

Figure 4-14: Histograms of observed inundation depth for engineered buildings for each DS. Distributions are shown for all engineered buildings (red) and for buildings deemed not to be affected by debris (blue, based on a 500m grid and 20% collapse area threshold).

4.5.3 Debris Removal Results

Figure 4-15 compares fragility functions formed for all engineered buildings and for those designated as unaffected by debris, for collapse area thresholds of 50%, 35% and 20%. Deviation from the fragility functions formed for all engineered buildings increases with lower threshold values (i.e. the greatest difference is seen for functions formed on data for the 20% collapse area threshold). The fragility functions for all engineered buildings and for the 20% area threshold are therefore also shown in link function (probit) space in Figure 4-16, and the model parameters for the inundation depth fragility functions are given in Table 4-9.

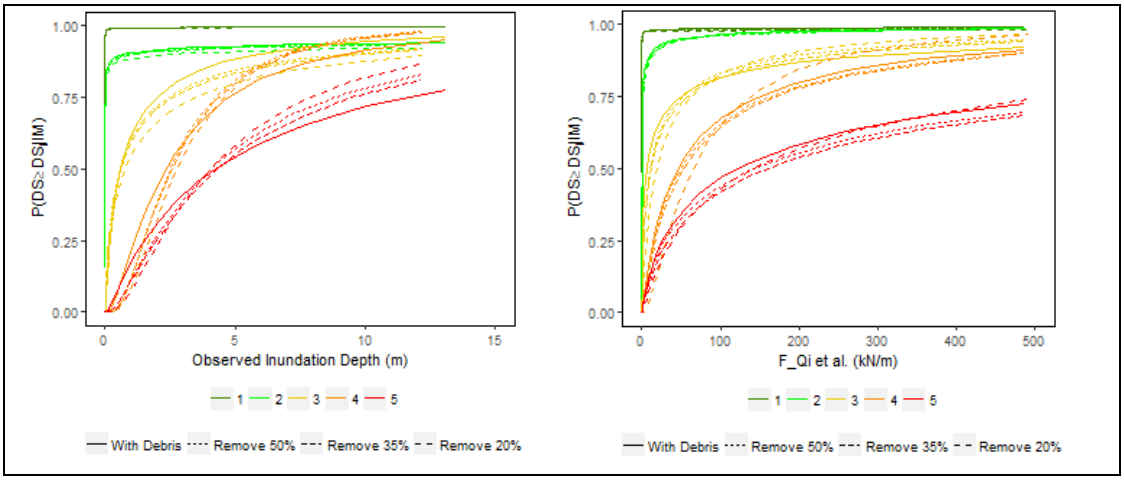

Figure 4-15: Fragility functions for engineered buildings with/without data removed (based on collapse area thresholds of 20%, 35% and 50%).

Table 4-9: Changes in model parameters for observed inundation depth (model M1.1). Green colour scale indicates decreasing values, red colour scale indicates increasing values.

		No Debris removal	50% threshold	35% threshold	20% threshold
β_0	0|1.(Intercept)	2.47	2.49	2.49	2.44
	1|2.(Intercept)	1.32	1.29	1.28	1.20
	2|3.(Intercept)	0.29	0.26	0.24	0.11
	3|4.(Intercept)	-0.80	-1.20	-1.21	-1.41
	4|5.(Intercept)	-0.95	-1.23	-1.25	-1.45
β_1	0|1 . $\ln\|h_{obs}\|$	0.09	0.09	0.08	0.08
	1|2 . $\ln\|h_{obs}\|$	0.10	0.10	0.10	0.09
	2|3 . $\ln\|h_{obs}\|$	0.57	0.47	0.45	0.46
	3|4 . $\ln\|h_{obs}\|$	0.95	1.30	1.28	1.38
	4|5 . $\ln\|h_{obs}\|$	0.66	0.87	0.85	1.03

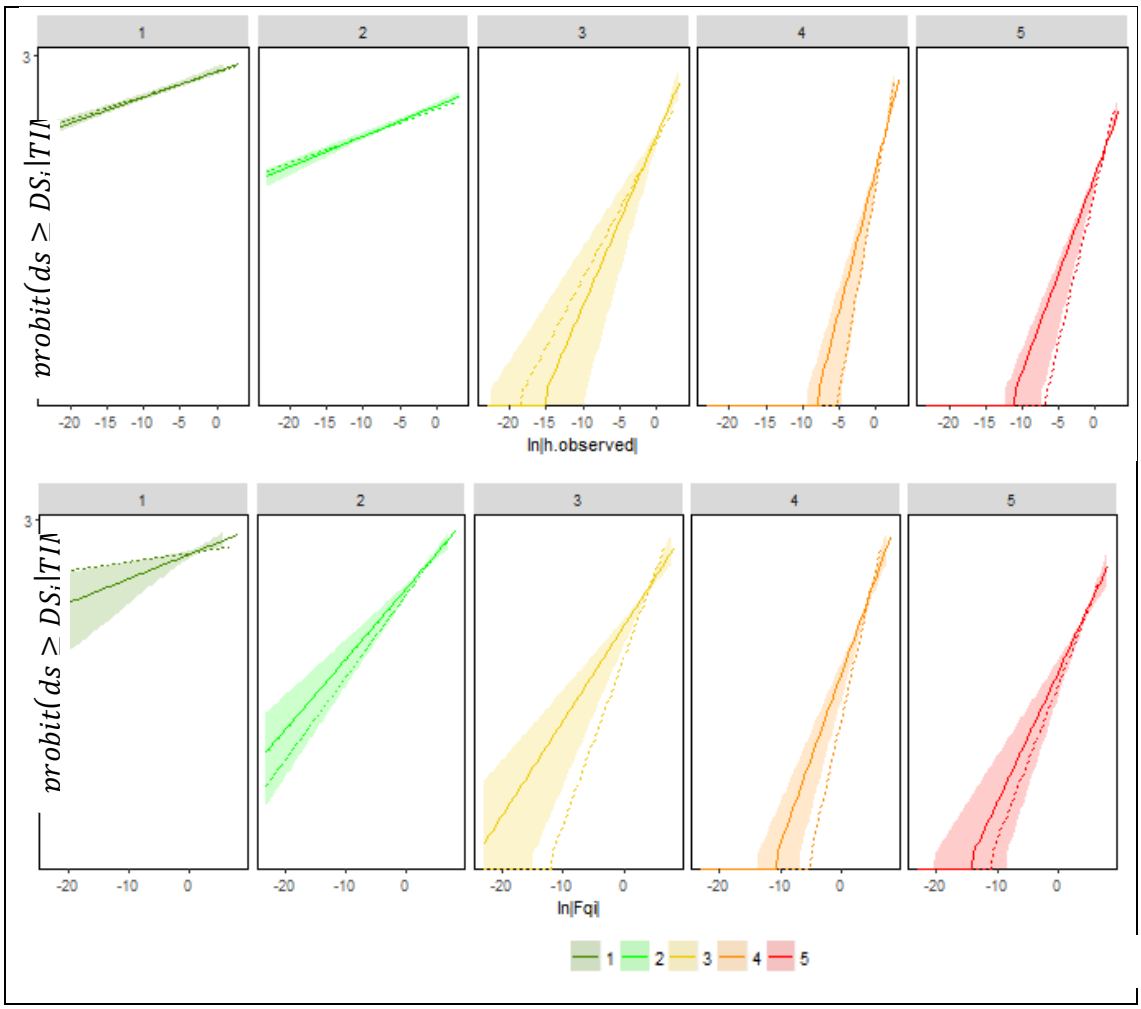

Figure 4-16: Link functions for observed inundation depth (top) and simulated force (bottom) for fragility functions derived for all engineered buildings (solid line, with 95% bootstrap confidence intervals) and buildings not affected by debris (for the 20% collapse area threshold).

The above figures show the trend that where buildings affected by debris are removed from the dataset, for higher damage states (DS4 and DS5*) the probability of damage exceedance is reduced for lower TIM values, but increased for higher TIM values. As more buildings are removed from the dataset (i.e. as the collapse area threshold decreases) the curve becomes steeper, accentuating the effect of reduced damage exceedance probabilities at lower TIM values but higher probabilities at higher TIM values (Figure 4-15). The opposite is true for lower damage states.

Intuitively, lower damage exceedance probabilities are expected in the absence of debris-related damage (i.e. a given flow depth may be deemed as more likely to cause damage if debris is also present in the flow). However, higher damage exceedance probabilities at higher TIM values are counterintuitive, and so the reason for this must be examined further.

4.5.4 Significance of Debris Parameter

A possible explanation for the removal of debris-damaged buildings from the dataset leading to increased damage exceedance probabilities at higher TIM values may be that this is simply due to the steepening of the curve (reduction in uncertainty or spread of the data, represented by the slope term, β_1) as a result of their being less data available (Table 4-8).

The significance of including debris data in the model can be investigated by forming a more complex model which includes a binary debris indicator variable, $debris_j$, indicating whether or not the building has been affected by debris (4-4) (i.e. $debris_j$ = 1 for all buildings within grid squares which have a ratio of washed away footprint area to total area above the threshold percentage). The parameter $\beta_{2,i}$ in equation (4-4) adjusts the intercept of the model and equation (4-5) includes a fourth parameter $\beta_{2,i}$ which adjusts the slope of the model (an interaction term). In this way a single model can be formed which includes all engineered buildings and the significance of each parameter can be determined by their p-values (Table 4-11). A likelihood ratio test is then carried out to determine whether there is a significant increase in model accuracy with the addition of the debris terms (Table 4-10).

$$probit\left(P\left(ds \geq DS_i \middle| TIM = x_j\right)\right) = \beta_{0,i} + \beta_{1,i}x_{j,k} + \beta_{2,\mathrm{i}}debris_j \quad \textbf{(4-4)}$$

$$probit\left(P\left(ds \geq DS_i \middle| TIM = x_j\right)\right) = \beta_{0,i} + \beta_{1,i}x_{j,k} + \beta_{2,\mathrm{i}}debris_j + \beta_{3,\mathrm{i}}x_{j,k}debris_j \quad \textbf{(4-5)}$$

The p-values in Table 4-11 show that all debris parameters are significant and that null hypothesis (that debris has no influence on damage state) can be rejected with the exception of the debris and debris interaction terms for DS1 ($\beta_{2,DS1}$ and $\beta_{3,DS1}$). The LRT results in Table 4-10 give p-values << 0.001 showing that the reduction in the residual sum of squares for the more complex model is statistically significant, so inclusion of debris improves the performance of fragility functions.

Table 4-10: Likelihood ratio test results comparing models of increasing complexity based on observed inundation depth.

Model Number	no.par	AIC	logLik	LR.stat	df	Pr(>Chisq)
(4-1)	10	11177.14	-5578			
(4-4)	15	10546.54	-5258	640.5995	5	<2.2e-16 ***
(4-5)	20	10399.99	-5180	156.5459	5	<2.2e-16 ***

Table 4-11: Parameters of model 4-5). Significance codes are: *** = p<0.001, ** = p<0.01, * = p<0.05.

		Estimate	Std. Error	p	Significance
β_0	0|1.(Intercept)	2.44	0.08	1.14E-189	***
	1|2.(Intercept)	1.20	0.03	5.01E-294	***
	2|3.(Intercept)	0.11	0.03	2.89E-05	***
	3|4.(Intercept)	-1.41	0.05	1.31E-190	***
	4|5.(Intercept)	-1.45	0.05	2.93E-163	***
β_1	0|1 . ln|$h_{obs\,j}$|	0.08	0.01	2.69E-31	***
	1|2 . ln|$h_{obs\,j}$|	0.09	0.01	3.38E-52	***
	2|3 . ln|$h_{obs\,j}$|	0.46	0.02	1.62E-124	***
	3|4 . ln|$h_{obs\,j}$|	1.38	0.04	3.71E-296	***
	4|5 . ln|$h_{obs\,j}$|	1.03	0.04	1.72E-119	***
β_2	0|1 . $debris_j$	0.13	0.21	5.36E-01	
	1|2 . $debris_j$	1.06	0.15	2.83E-12	***
	2|3 . $debris_j$	1.67	0.10	1.57E-64	***
	3|4 . $debris_j$	1.58	0.12	2.90E-38	***
	4|5 . $debris_j$	0.89	0.11	2.37E-15	***
β_3	0|1 . ln|$h_{obs\,j}$|. $debris_j$	0.04	0.02	1.62E-02	*
	1|2 . ln|$h_{obs\,j}$|. $debris_j$	0.91	0.23	6.58E-05	***
	2|3 . ln|$h_{obs\,j}$|. $debris_j$	-0.24	0.04	1.74E-08	***
	3|4 . ln|$h_{obs\,j}$|. $debris_j$	-0.61	0.08	1.44E-15	***
	4|5 . ln|$h_{obs\,j}$|. $debris_j$	-0.46	0.07	6.89E-11	***

4.6 Empirical Fragility Function Summary and Discussion

This chapter has collated, compared and expanded on the current state-of-the-art methodologies for tsunami fragility assessment, in order to determine the optimal Tsunami Intensity Measure (TIM) for describing building damage data observed during the 2011 Great East Japan Earthquake and Tsunami (2011 GEJE).

Exploratory analysis is conducted on a detailed, disaggregated building damage dataset, unique in the fields of both tsunami and seismic fragility assessment. Buildings of unknown construction material present a significant proportion of the total dataset (18.2%) and so in order to avoid the introduction of bias when producing fragility curves by material, missing material data is estimated using multiple imputation techniques.

The first stage of fragility assessment consists of a sensitivity analysis of several statistical methods for fragility curve derivation, so as to select at least two statistical models with which to conduct the TIM comparison. General conclusions are drawn

regarding the suitability of various models and the methods used to select between them, with Cumulative Link Models and Generalised Additive Models selected for the TIM comparison.

Numerical inundation simulation results are used to consider several alternative TIMs. Comparison of observed and simulated inundation depths shows some disagreement, suggesting that there may be further (and perhaps more significant) error in simulated velocity and other parameters. Partially-ordered probit models are derived for several TIMs and their 10-fold cross-validation results are compared. The same procedure is repeated using GAMs to show that the results are not model-specific. It is shown that the quasi-steady force estimation (F_{QS}) and inundation depth consistently provides the best fit to the observed damage.

This chapter has also presented a preliminary methodology for quantifying debris-related effects on fragility functions, by developing tsunami fragility curves for engineered buildings in Japan for observed inundation depth and simulated force, considering the presence of debris in the flow. A 500m grid is applied to three case-study locations and buildings of each grid are deemed to have been affected by debris if the ratio of “washed away” building area to total building area within that grid exceeds a threshold proportion. Exploratory analysis is conducted of the total dataset of all buildings of engineered construction material (RC or steel) and of the debris-affected datasets. Fragility functions formed for all engineered buildings, and those deemed not to be affected by debris are compared, so that the effect of removing debris-damaged buildings from the regression dataset can be assessed. More complex regression models are then formed incorporating a debris indicator variable (denoted 1 for all buildings considered to be affected by debris, and 0 for all other buildings) and an interaction term, so that the statistical significance of the debris parameters for each damage state can be examined. Finally, the models with and without debris parameters are compared using likelihood ratio tests so as to determine whether the inclusion of debris indicators in the model produce a significant improvement in the model fit.

The main conclusions of this chapter can be summarized as follows:

Exploratory Analysis

1. Missing data can only be removed if it can be shown to be Missing Completely At Random. This is shown to be not the case for the 2011 MLIT Japan data, meaning that all previous studies which have generated curves according to any sub-category (e.g. material, age, height etc) using complete-case analysis (removal of buildings with missing data) may have introduced a bias in the results.
2. Multiple Imputation (MI) has been shown to be an acceptable method for estimating missing data, and is recommended for use on future fragility studies where data cannot be shown to be Missing Completely At Random.

Statistical Modelling

3. *K*-fold cross-validation (KFCV) is shown to be a suitable method for comparing model fits for various model types, and the methodology for conducting this for multinomial models is demonstrated. It is recommended that KFCV be used for evaluation of model fits in future fragility studies.
4. Data aggregation has been quantifiably shown to reduces model predictive accuracy by an amount which is dependent on the aggregation approach. Hence, existing studies that use aggregated data from the 2011 GEJE should be considered superseded by those that use disaggregated data directly.
5. Ordinary Least Squares parameter estimation is quantitatively shown to be unsuitable for fragility function estimation as it suffers from the issues of data aggregation, and violates several linear model assumptions leading to reduced predictive accuracy and increased uncertainty.
6. Semi-parametric methods are seen to be suitable for comparative fragility assessments, and the issue of over-fitting can be avoided through the use of cross-validation techniques, as demonstrated.

Optimal Tsunami Intensity Measure

7. Measures of force provide the most efficient TIMs, if the inundation simulation from which they are derived is sufficiently accurate, or simulated velocity can be validated. Depth is an acceptable TIM for low-accuracy simulations of inundation. The required accuracy is the subject of further research.

8. Inundation simulations outputs recommended for fragility assessment are depth, velocity and Froude number, as instantaneous force values (calculated at each time-step) do not appear to give better fits to observed damage than equivalent values calculated from separate (non-coincident) peaks of depth, velocity and Froude Number. Further research is needed to investigate the sensitivity of this result to inundation simulation accuracy.
9. Flow regime (indicated by Froude Number) is a significant consideration when conducting fragility assessments, or quantifying tsunami-induced forces on structures.

Debris

10. Buildings thought to be affected by debris mostly experienced higher TIM values and higher damage states (debris designation occurs in the vicinity of other 'washed away' buildings, which as more likely to occur in locations of high TIM values).
11. The removal of buildings thought to be affected by debris resulted in changes to both the slope and intercept of the fragility functions. This indicates that the inclusion of debris-damaged buildings in the dataset (as is the case for most existing empirical fragility functions) does have an effect on fragility functions that may not be captured by purely flow regime-related TIMs.
12. The difference between the intercept and slope (in link space) for fluid-only and debris-influenced fragility functions can be quantified by inclusion of debris-indicator terms in the fragility functions.
13. The influence of debris model parameters on determining building damage was shown to be significant for all but the lowest damage state ("minor damage").
14. More complex fragility functions which incorporate debris model parameters were shown to have a statistically significant better fit to the observed damage data than models which omitted debris information. This suggests that inclusion of debris information in fragility functions improves the accuracy of the model.

It is noted that the method of identifying debris-damaged buildings within a dataset has not been the focus of this section. The use of a grid, the grid size (500m) and the collapse area thresholds (50%, 35% and 20%) are all subjective, and selected in order to allow the demonstration of the proposed methodology for quantifying debris effects on fragility function derivation. The optimal method of identifying and quantifying debris impact is the subject of further study, and along with the preliminary findings of this thesis, will contribute to defining how fragility curves can be adjusted to account for increased damage probabilities in locations of increased likelihood of debris.

Based on the conclusions above, this thesis recommends that existing fragility assessments should be re-examined for potential bias if they have been based on complete-case analysis of data subsets (e.g. construction material), aggregated data (where disaggregated data is available), and OLS parameter estimation. With the introduction of several concepts novel to the field of fragility assessment (MI, GAMs, KFCV for model optimization/comparison) and the finding that force measures considering flow regime provide the most efficient TIM for high accuracy inundation simulations, this study has significant implications for the future generation of empirical and analytical fragility functions.

5 Structural Analysis for Analytical Fragility Function Derivation

5.1 Introduction

The previous chapter has focussed on analysing damage data from a past tsunami. Analytical fragility functions, on the other hand, are derived from synthetic damage data generated by structural analysis. Analytical functions are required to quantify risk in the many locations around the world for which damage data from past tsunami is not available. This Chapter therefore examines the issue of how to efficiently derive synthetic damage data, on which the statistical techniques developed in the previous chapter may be applied.

Existing analytical fragility studies utilise a range of different structural analysis techniques (summarized in section 2.3.1.3), from pushover of simple Single-Degree-of-Freedom (SDoF) models to full non-linear time-history analysis of Multi-Degree-of-Freedom (MDoF) systems, with no consensus as to the preferred method. Furthermore, tsunami design procedures for buildings (evaluated in section 2.4.3) do not currently account for the ductility of structures, nor their dynamic behaviour (section 2.4.3.2). Seismic design practice, on the other hand draws heavily upon the reserve strength of a structure loaded beyond yield, with the structural ductility being fundamental for the analysis of structural performance. This Chapter therefore investigates the fundamental principle of whether ductility and dynamic effects are significant in determining structural performance under tsunami loading, and demonstrates the implications of these findings on methods of structural analysis for analytical fragility function derivation.

It is first shown analytically that an Elastic-Perfectly-Plastic (EPP) Single Degree of Freedom (SDoF) structure can maintain a load (F) greater than its yield load (F_y) for a duration of time (section 5.2). The overstrength factor ($\Omega = F/F_y$) is shown to scale with the displacement ductility demand (μ_{peak}) according to dimensionless parameters that relate (a) the structural yield force, (b) natural period to the peak applied load and (c) the duration for which the load exceeds yield. The relationship for peak ductility demand is defined analytically for tsunami loading idealised as linear, triangular and parabolic time-histories, and these relationships are verified numerically. These analytical relationships are then used to define envelopes of peak applied load and the duration for which the load exceeds yield, for a series of ductility demands. This is to identify whether structural dynamics and time-dependent effects should be considered in structural analysis for analytical fragility function derivation.

A sensitivity analysis is then conducted (section 5.3) to determine the effect of damping, strain-hardening and load-duration on overstrength. Using realistic tsunami load time-histories it is shown that although there is a difference between applied and internal forces because of the time-dependent effects of damping and inertia, these effects are typically insufficient to prevent collapse under tsunami-like loading for all but the most transient cases (e.g. global failure due to bore impact). This finding suggests that 'elastic' strength-based approaches to building tsunami response analysis can be used for analytical fragility function derivation.

Building on this result, the Chapter concludes by proposing a simplified method of estimating structural capacity under tsunami loading (section 5.4), suitable for use in the large number of analyses required to derive analytical fragility functions of building populations. The effect of this approximation on analytical fragility function derivation is demonstrated by comparison with the results of full non-linear time-history analysis.

Given the complexity of the full tsunami loading regime, this investigation looks to examine a simplified case whereby only lateral hydrodynamic fluid loads will be considered. I.e. other loads and effects outlined in section 2.2 will not be considered. A preliminary discussion on the definition of an adequate Engineering Demand Parameter (EDP) and related damage state threshold definitions for multiple damage states is presented in Appendix E, but for the analysis in this chapter only the collapse damage state is considered.

5.2 Investigation of Overstrength, considering Ductility and Time-varying Loads

In order to investigate the fundamental principle of whether ductility and dynamic effects are significant in determining structural performance under tsunami loading, this section investigates whether structural overstrength (Ω) and displacement ductility demand (μ) under time-varying load ($F(t)$) can be determined analytically. This is so that the peak displacement ductility demand (μ_{peak}) for a structure under a given load time-history can be predicted.

5.2.1 Analytical Derivation of an Overstrength vs Ductility Relationship for an Elastic Perfectly-Plastic Structure

Initially, an undamped, elastic-perfectly-plastic (EPP), single degree-of-freedom (SDoF) structure of mass, m, is considered, as shown in Figure 2-19. Once the applied force exceeds the yield force of the structure, F_y, then the structure will behave plasticly, and

so a subscript *p* shall be used to denote variables measured from the yield-point onwards (e.g. F_p=F-F_y, t_p=t-t_y, etc). The dynamic behaviour is governed by the standard equation of motion with damping and stiffness coefficients both zero (Figure 2-19, c=0, k=0). In the post-yield (plastic) region for the EPP structure the internal force remains at F_y, and so the acceleration of the structure is determined by the net force (F-F_y=F_p) as shown in (5-1). The plastic velocity and plastic deflection ($\delta_p(t) = \delta(t) - \delta_y$) are then found by integration (5-2).

$$\ddot{\delta}_p(t_p) = \frac{F_p(t_p)}{m} \qquad (5\text{-}1)$$

$$\delta_p(t_p) = \frac{1}{m}\iint F_p(t_p)\, dt_p^2 \qquad (5\text{-}2)$$

Overstrength and ductility, with respect to time, both then follow from the definitions of these parameters (5-3) (5-4). Note that the plastic displacement ductility demand, μ_p, is a function of the applied load, the yield force, and the natural period of the structure, T. The derivation of ductility demand and definition of period below show that the period influences ductility demand as it contains information about both the structural mass (which governs acceleration) and structural stiffness (which governs the deflection at yield).

$$\Omega_p(t_p) = \frac{F_p(t_p)}{F_y} \qquad (5\text{-}3)$$

$$\mu_p(t_p) = \frac{\delta_p(t_p)}{\delta_y} = \frac{\frac{1}{m}\iint F_p(t_p)\, dt_p^2}{F_y/_k} = \left(\frac{2\pi}{T}\right)^2 \frac{1}{F_y}\iint F_p(t_p)\, dt_p^2 \qquad (5\text{-}4)$$

where T is the structural natural period defined by: $T = 2\pi\sqrt{\frac{m}{k}}$

The overstrength-ductility relationship is evaluated for three load time-histories: a linearly increasing load (Figure 5-1a); a triangular forcing function where the gradients of the upward and downward ramps are equal (Figure 5-1b); and a parabolic forcing function (Figure 5-1c).

a

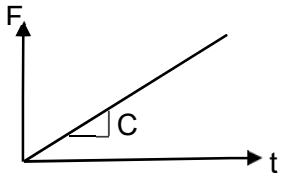

$$F(t) = Ct$$

b

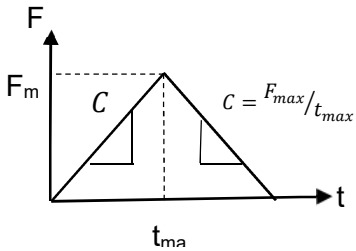

$$F(t) = \begin{cases} Ct, & t < t_{peak} \\ C(2t_{peak} - t), & t \geq t_{peak} \end{cases}$$

c

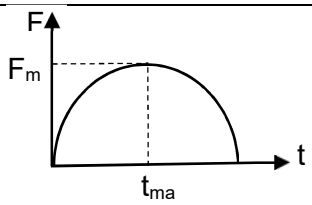

$$F(t) = \left(\frac{2F_{max}}{t_{peak}}\right)t - \left(\frac{F_{max}}{t_{peak}^2}\right)t^2$$

Figure 5-1: General definitions of the three load-cases applied: a linearly increasing load (a), a triangular forcing function (b), and a parabolic forcing function (c).

For an EPP structure under a linearly increasing forcing function (Figure 5-1a), the overstrength and ductility with respect to time can be calculated from (5-3) and (5-4), to give the relationships shown in (5-5) and (5-6). A direct relationship between overstrength and ductility ($\Omega_p(\mu_p)$) can then be found by eliminating *t*, (5-7). Therefore, structures with the same ratio of T/F_y should be expected to have identical Ω_p-μ_p curves when subjected to the same linearly increasing load.

$$\Omega_p(t_p) = \frac{Ct_p}{F_y} \qquad \textbf{(5-5)}$$

$$\mu_p(t_p) = \left(\frac{2\pi}{T}\right)^2 \frac{C}{6F_y} t_p^3 \qquad \textbf{(5-6)}$$

$$\Omega_p = A{\mu_p}^{1/3} \quad ; \qquad A = \left(\frac{C\sqrt{3}}{\pi\sqrt{2}}\right)^{2/3} \cdot \left(\frac{T}{F_y}\right)^{2/3} \qquad \textbf{(5-7)}$$

For an EPP structure under a triangular forcing function (Figure 5-1b) which exceeds the yield force for a duration of time ($t_{dur} = 2t_{p_{peak}}$), plastic overstrength follows directly from the definition of the forcing function (5-8), and using the same method as for linear ramps above plastic ductility demand is found to be represented by (5-9). Note that the structural deflection will continue to increase even after the applied force has reduced back below the yield force, due to the developed inertia. The peak deflection is therefore

defined where $\dot{\delta}_p = 0$ (5-10) (5-11), giving rise to the analytical definition of peak deflection ductility demand shown in (5-12).

$$\Omega_p(t_p) = \begin{cases} \frac{C}{F_y} t_p, & t_p < t_{p\,peak} \\ \frac{C}{F_y}(t_{dur} - t_p), & t_{p\,peak} \le t_p \le t_p|_{\dot{\delta}=0} \end{cases} \quad \textbf{(5-8)}$$

$$\mu_p(t_p) = \begin{cases} \frac{1}{6}\left(\frac{2\pi}{T}\right)^2 \frac{C}{F_y} {t_p}^3, & t_p < t_{p\,peak} \\ \frac{1}{2}\left(\frac{2\pi}{T}\right)^2 \frac{C}{F_y}\left[-\frac{1}{3}{t_p}^3 + t_{dur}{t_p}^2 - \frac{1}{2}{t_{dur}}^2 t_p + \frac{1}{12}{t_{dur}}^3\right], & t_{p\,peak} \le t_p \le t_p|_{\dot{\delta}=0} \end{cases} \quad \textbf{(5-9)}$$

where t_{dur} = duration for which applied load exceeds F_y, and $\Omega_{p_{peak}} = \frac{F_{max} - F_y}{F_y}$.

$$\dot{\delta}_p(t_p) = \frac{1}{m}\int F_p(t_p)\, dt_p = \frac{C}{m}\left[-\tfrac{1}{2}t_p^2 + t_{dur}t_p - \tfrac{1}{4}t_{dur}^2\right] \quad \textbf{(5-10)}$$

at $\dot{\delta} = 0$: $\quad t_p = t_{dur}\left(1 + \frac{1}{\sqrt{2}}\right)$ **(5-11)**

$$\therefore\ \mu_{p\,max} = \mu_p\left(t_{p_{\dot{\delta}=0}}\right) = \left(\frac{1}{2} + \frac{\sqrt{2}}{3}\right)\pi^2 \Omega_{p_{peak}}\left(\frac{t_{dur}}{T}\right)^2 \quad \textbf{(5-12)}$$

For an EPP structure under a parabolic forcing function (Figure 5-1c) using the same method overstrength and ductility demand can be shown to be defined by (5-13) and (5-14), with peak ductility demand given by (5-15).

$$\Omega_p(t_p) = 4\frac{\Delta F_{max}}{F_y}\left[\left(\frac{1}{t_{dur}}\right)t_p - \left(\frac{1}{t_{dur}^2}\right)t_p^2\right] \quad \textbf{(5-13)}$$

$$\mu_p(t_p) = \frac{1}{3}\left(\frac{2\pi}{T}\right)^2 \frac{\Delta F_{max}}{F_y}\left[\left(\frac{2}{t_{dur}}\right)t_p^3 - \left(\frac{1}{t_{dur}^2}\right)t_p^4\right] \quad \textbf{(5-14)}$$

$$\mu_{p\,max} = \mu_p\left(t_{p_{\dot{\delta}=0}}\right) = \frac{9}{4}\pi^2 \Omega_{p_{peak}}\left(\frac{t_{dur}}{T}\right)^2 \quad \textbf{(5-15)}$$

(5-12) and (5-15) both show that under both triangular and parabolic loading, the maximum ductility demand (μ_{max}) is determined by only two dimensionless parameters:

$$\left(\frac{t_{dur}}{T}\right), \left(\frac{\Delta F_{max}}{F_y}\right)$$

5.2.2 Numerical Verification of Analytical Formulae

This section compares the analytically derived overstrength and ductility relationships with numerical results. Structural calculations are carried out using a SDoF structure with a bilinear performance curve (Figure 2-19) in OpenSees, and all subsequent analysis is conducted in the statistical programming language R (R Development Core Team, 2008).

(5-7) suggests that EPP structures with the same ratio (T/F_y) should have identical Ω-μ curves when subjected to the same linear ramp forcing function. To test this conclusion the 7 structures in Table 5-1 are defined such that they can be grouped into three

different (F_y/T) ratios, and are subjected to a linear ramp forcing function (Figure 5-1a, with C=1kN/s). (5-4) suggests that structural period, T, is sufficient for capturing information about the structural mass and stiffness. To test this conclusion structures S3 and S4 are defined to have identical periods, but with different mass and stiffness values.

Figure 5-2 shows the response of structure S3 subjected to the linear ramp forcing function. Figure 5-2a shows that post-yield the applied force is resisted by the internal (i.e. spring) force of the structure (which remains at F_y for an EPP structure) plus the inertia force of the yielded structure, as hypothesised in section 2.4.3.2. This results in the structural motion shown in Figure 5-2b, with the analytical and numerical results showing good agreement. Figure 5-2c shows good agreement between the numerical and analytically derived overstrength vs ductility relationship. Minor discrepancies are because the assumptions of zero velocity and acceleration at the yield point are not true. The further discrepancy is also introduced as it is not always true that Ω=1 when μ=1 (due to the dynamic oscillations of the structure in the elastic region).

Table 5-1: Structures to be considered in this study. Structure S3 is highlighted as it will be the base-case structure used throughout this chapter. All structures are initially considered with no damping.

Structure Number	F_y (kN)	T (s)	Mass (tons)	k (kN/m)	F_y/T
S1	5	1	14	553.6	5
S2	7.5	1.5	31.6	553.6	5
S3	10	1	14	553.6	10
S4	10	1	8.2	325.2	10
S5	5	0.5	3.5	553.6	10
S6	10	0.5	3.5	553.6	20
S7	20	1	14	553.6	20

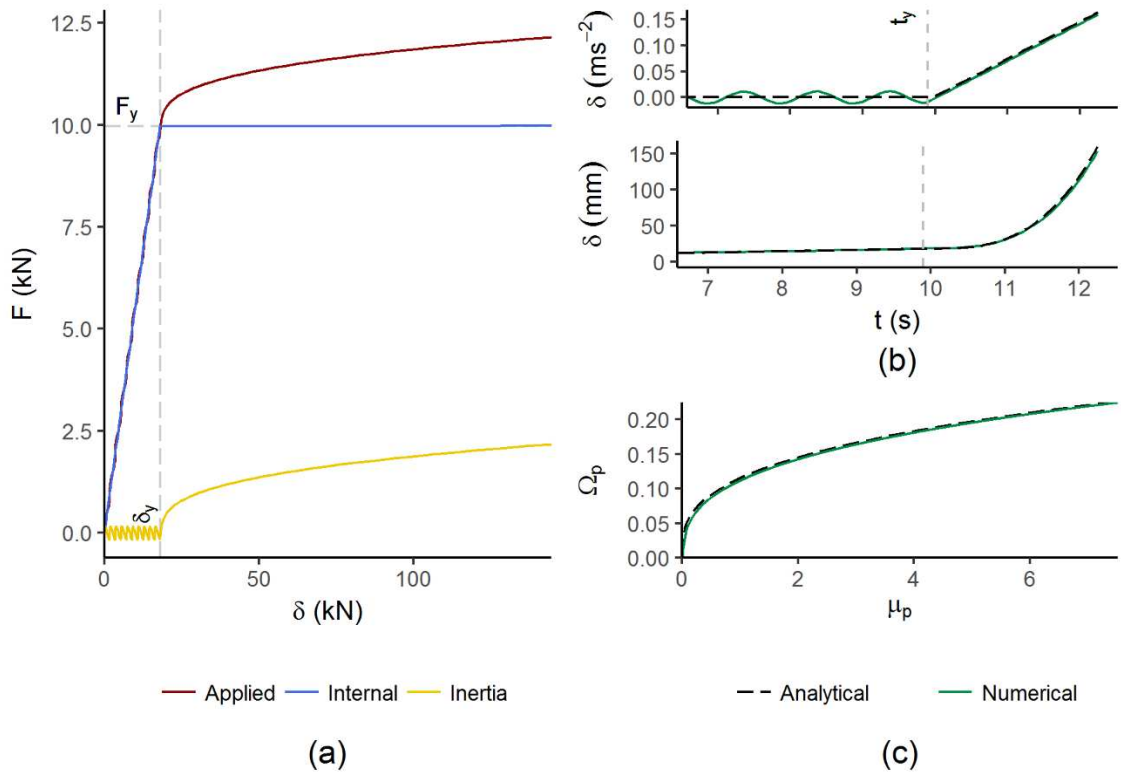

Figure 5-2: Responses of structure S3 (Table 5-1) subjected to a linear ramp forcing function (Figure 5-1a) with *C*=1kN/s. (a) performance curve (dashed vertical lines indicate *μ*=1:8). (b) analytical and numerical comparison of structural motion vs time. (c) analytical and numerical comparison of overstrength vs ductility relationship.

Figure 5-3 shows the overstrength vs ductility relationships for all seven structures in Table 5-1. As expected, structural responses collapse onto three curves defined by the three F_y/T ratios. In addition, the response curves for structures S3 and S4 are identical despite having different masses and stiffnesses, showing that structural period, T, is indeed sufficient for capturing the structural behaviour.

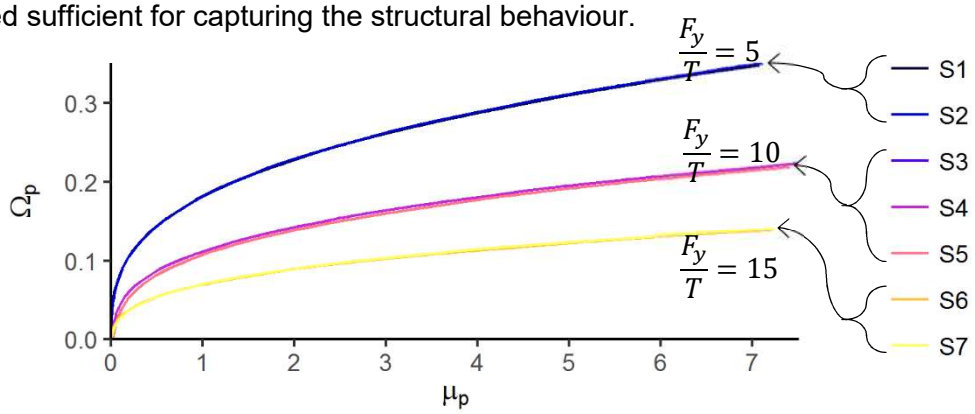

Figure 5-3: 7 test structures subjected to a linear ramp forcing function (Figure 5-1a, with C=1kN/s). The $\Omega_{plastic}$ vs $\mu_{plastic}$ responses collapse onto 3 curves, defined by F_y/T ratio.

To consider loading under a triangular forcing function, Figure 5-4 compares the analytically and numerically derived response of structure S3 (F_y=10kN, T=1s) subjected to a triangular time-history defined by Figure 5-1b, with C=1kN/s and F_{max}=11kN. Figure

5-4a and b both confirm the analytical assumption that the structure will continue to deflect even after the applied load has again reduced to below the yield force, due to the structure's inertia. Figure 5-4c and d show a good match between analytical and numerically derived structural motion and the overstrength vs ductility relationship. The analytical results slightly underestimate the peak ductility demand. This is due to a number of reasons. The analytical model assumes negligible acceleration and velocity prior to yield $\left(\ddot{\delta}_p(t) = \dot{\delta}(t) = 0, \quad t < t_y\right)$, though Figure 5-4 suggests that the numerical model may have non-zero acceleration and velocity at the yield point, giving rise to the slight discrepancy between deflections shown. In addition, the point of yield (t_y) is not coincident for the numerical and analytical models. For the numerical model yield occurs where the structure's internal (spring) force exceeds *Fy*, where the internal force differs from the applied force due to inertial and damping loads (though ζ=0 in this case). However, the analytical model assumes no inertia or damping forces (as $\ddot{\delta}_p(t) = \dot{\delta}(t) = 0, \quad t < t_y$), and so implicitly assumes yield at the point where the applied load exceeds F_y.

Similar results are obtained for a parabolic forcing function, as shown in Figure 5-5.

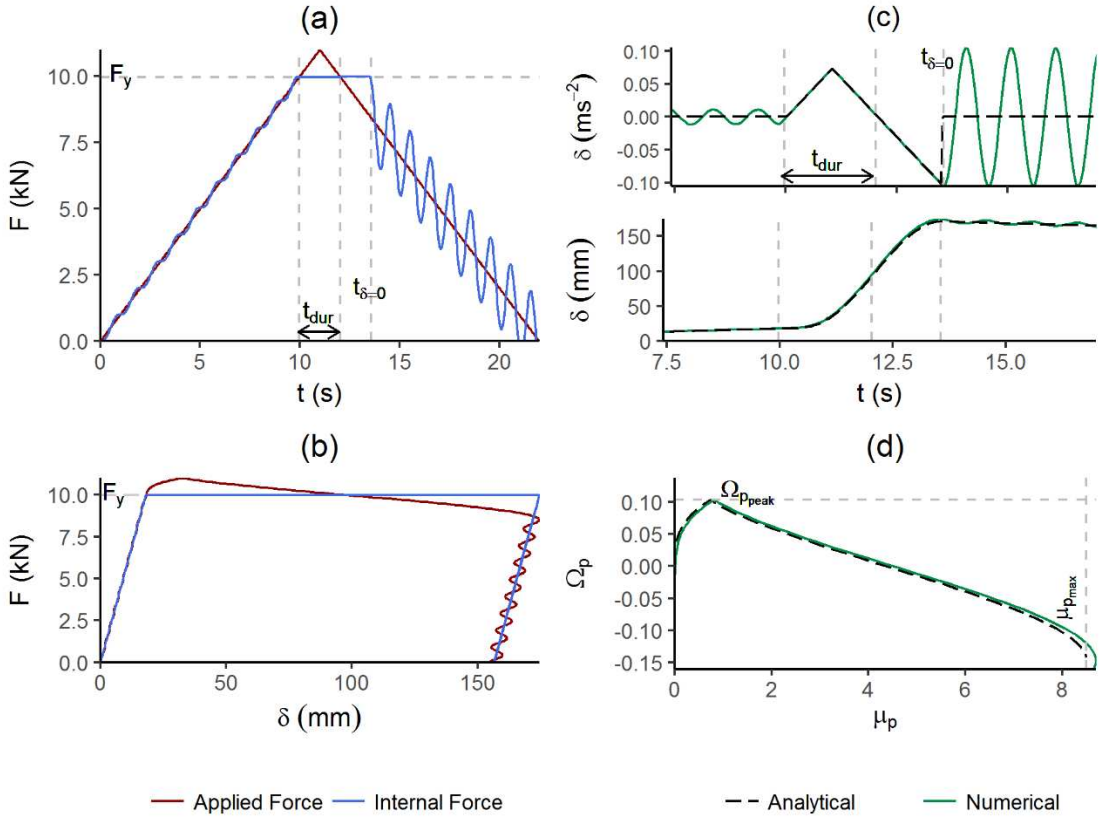

Figure 5-4: Responses of structure S3 (Table 5-1) subjected to a triangular forcing function (Figure 5-1b) with *C*=1kN/s and F_{max}=11kN. (a) applied and internal force w.r.t. time. (b) performance curve. (c) analytical and numerical comparison of structural motion w.r.t. time. (d) analytical and numerical comparison of overstrength vs ductility relationship.

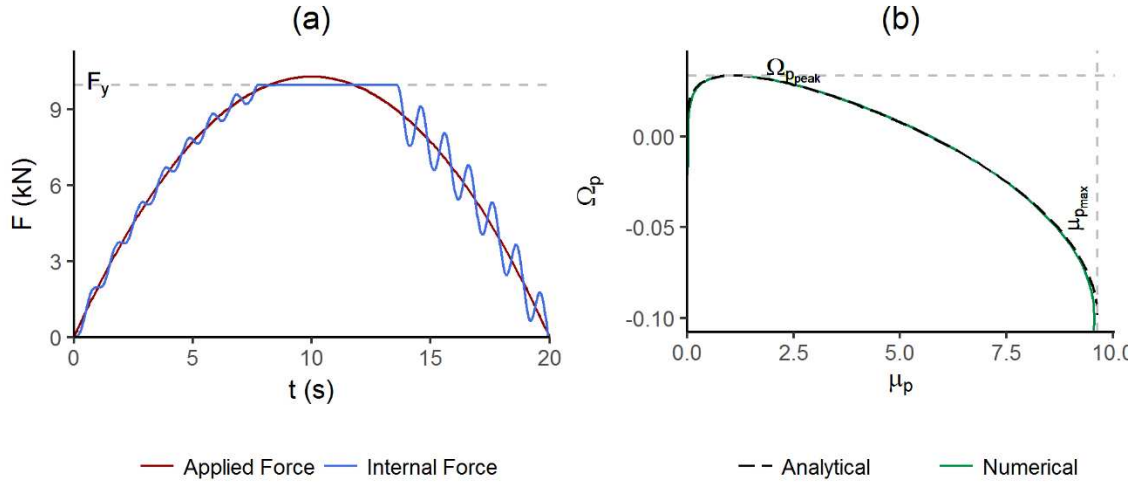

Figure 5-5: Responses of structure S3 (Table 5-1) subjected to a parabolic forcing function (Figure 5-1c) with F_{max}=10.3kN. (a) applied and internal force w.r.t. time. (b) analytical and numerical comparison of overstrength vs ductility relationship.

5.2.3 Overstrength Envelope

The previous section has shown the analytical estimations of structural performance to be in agreement with numerical results. Therefore, if triangular or parabolic load time-histories can be considered representative of tsunami loading then for a given undamped EPP structure (defined by F_y, T) under a given tsunami loading (defined by ΔF_{max}, t_{dur}) the peak ductility demand can be calculated from (5-12) or (5-15), and the structure is deemed to have failed if $\mu_{demand} > \mu_{supply}$. Therefore, (5-12) or (5-15) can also be used to define the relationship between peak plastic overstrength demand ($\Omega_{p_{peak}}$) and the duration for which the applied load exceeds the yield load non-dimensionalised by the structural period ($\frac{t_{dur}}{T}$), for a series of target peak plastic ductility demands ($\mu_{p\,max}$). These analytical relationships for $\mu_{p\,max} = 1{:}8$ are shown in Figure 5-6.

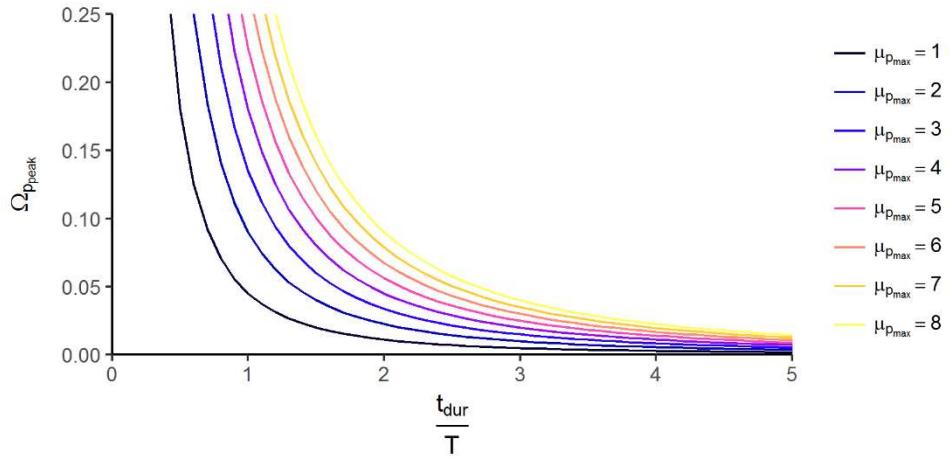

Figure 5-6: $\Omega_{p\ peak}$ vs (t_{dur}/T) curves for μ_{peak} = [1:8] (defined by (5-12)) for an undamped EPP structure.

Figure 5-6 shows that structures can only achieve an overstrength of greater than 5% when subjected to loads which exceed the structural yield load for a duration of between 1 and 3 natural periods. If typical natural periods are in the range 0.1s-1s then this allows for yield exceedance for between 0.3s and 3s. This overstrength cannot therefore be utilised by structures during the quasi-steady period of the tsunami load time-history (Figure 2-8), as the duration of this loading phase will exceed the allowable durations defined in Figure 5-6 for the overwhelming majority of cases.

However, the relationships identified here may be of design significance for structures experiencing bore impact, which may well be within the allowable durations defined in Figure 5-6. For these rapidly applied load-cases, however, it will be necessary to make some compensation for the structural oscillations experienced in the elastic pre-yield period.

5.3 Sensitivity of Overstrength to Damping, Strain-Hardening and Load Duration

The previous section showed that undamped EPP structures are unable to utilise ductility and overstrength for anything other than highly transient load-cases. The sensitivity of this result is tested by the introduction of damping and strain-hardening (section 5.3.1). Finally, the results are demonstrated for realistic tsunami load time-histories obtained from numerical inundation simulation (section 5.3.2).

5.3.1 The Effect of Damping and Strain-Hardening on the Overstrength Relationship

To investigate the effect of damping on the overstrength relationship, structure S3 (Table 5-1, T=1s, F_y=10kN) with increasing damping ratios (ξ) are subjected to a linear ramp forcing function (Figure 5-1a with C=1kN/s) and the responses are shown in Figure 5-7. After yield has occurred, the difference between the applied force and the structure's internal (spring) force is resisted by both the structure's inertia and damping. The damped structures accelerate more slowly than an undamped structure, and so increased damping corresponds to an increased overstrength achieved for a given ductility demand. Therefore, when these same structures are subjected to a load which exceeds yield for a finite amount of time structural damping slows the structure's movement reducing the peak displacement and so peak ductility demand, as shown in Figure 5-8.

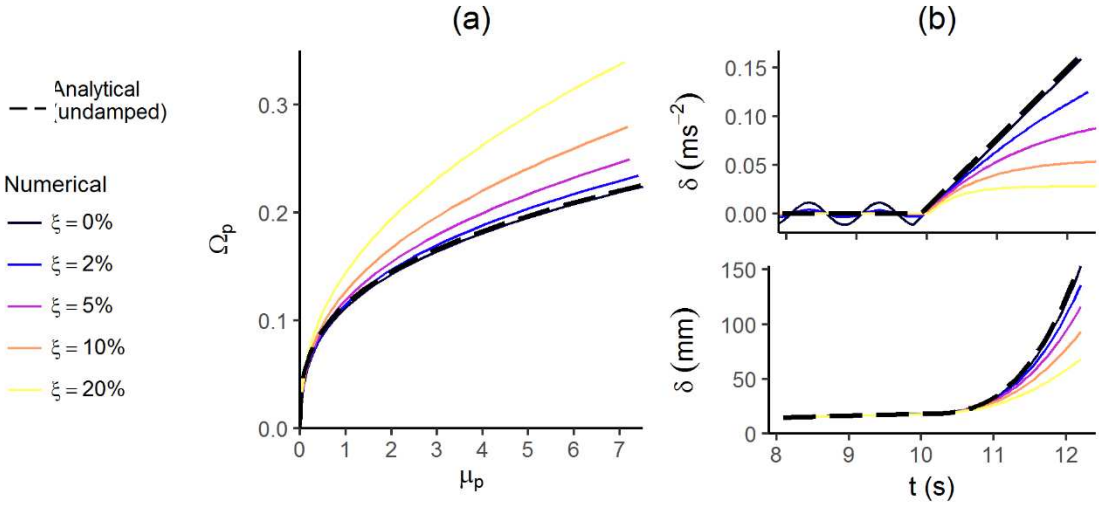

Figure 5-7: Response of structure S3, with a range of damping ratios (*ξ*), subjected to a linear ramp forcing function (Figure 5-1a with *C*=1kN/s). (a) Plastic overstrength vs plastic ductility demand. (b) Structural motion vs time.

To investigate the effect of strain-hardening on the overstrength relationship, structure S3 (Table 5-1, T=1s, F_y=10kN) with increasing strain-hardening ratios (b) are subjected to a linear ramp forcing function (Figure 5-1a with C=1kN/s) and the responses are shown in Figure 5-9. After yield the structure oscillates about the plastic hardening line of its performance curve, with the period of the oscillation dependent on the gradient of this line (Figure 5-9a and b). A parabolic forcing function (Figure 5-1c with F_{max}=10.3kN) is then applied to the same set of structures, showing that strain hardening reduces the peak ductility demand, as shown in Figure 5-9.

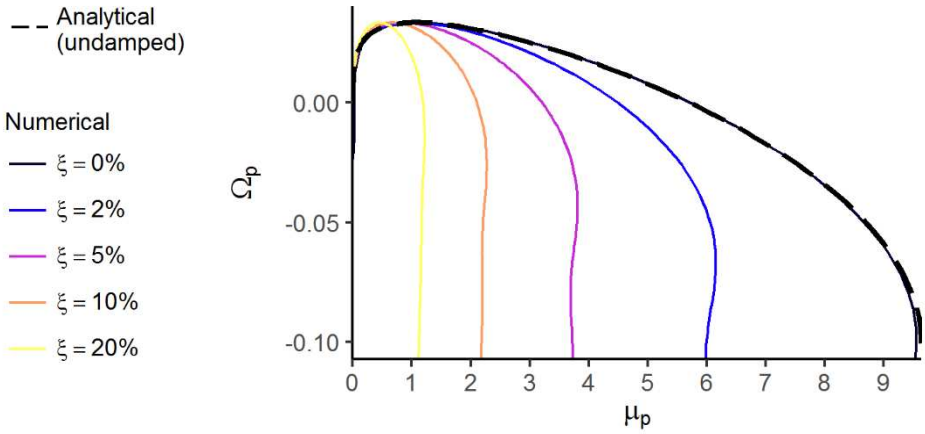

Figure 5-8: Response of structure S3, with a range of damping ratios (ξ), subjected to a parabolic forcing function (Figure 5-1c with F_{max}=10.3kN). The analytically derived peak ductility demand for undamped EPP structure is also shown (dashed).

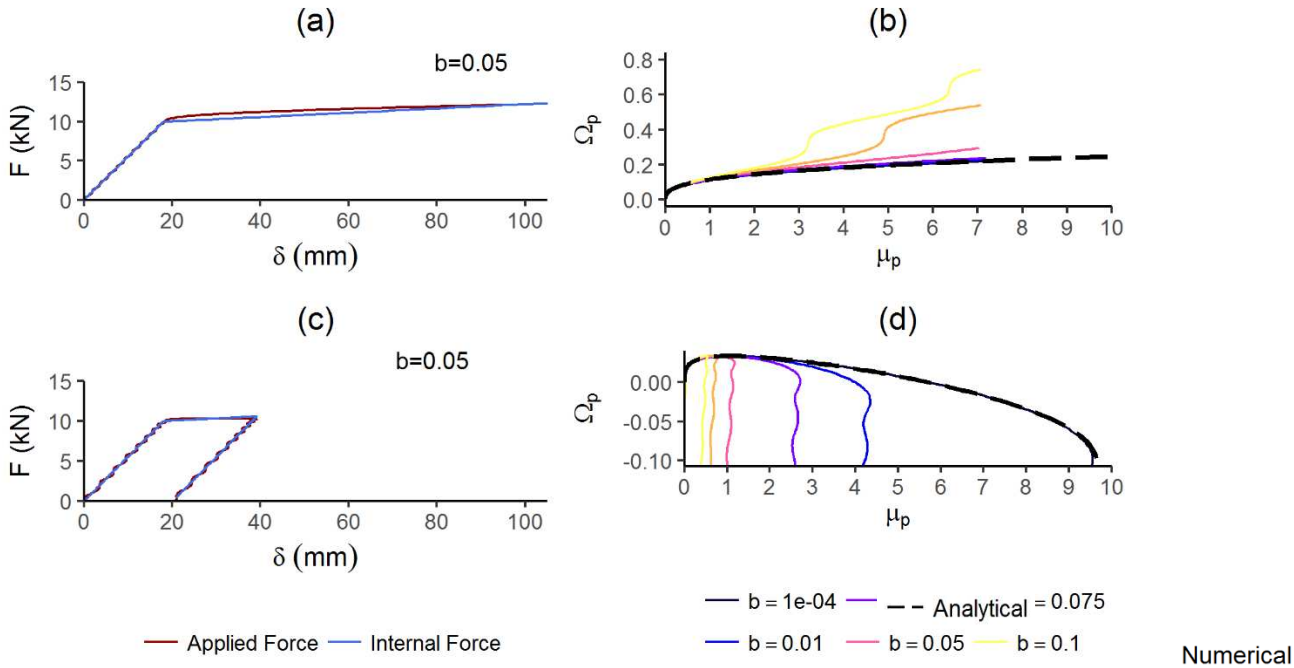

Figure 5-9: The force-displacement and overstrength-ductility relationships for structure S3 (undamped), with a range of hardening ratios (*b*), subjected to: (a) (b) a linear ramp forcing function (Figure 5-1a with *C*=1kN/s). (c) (d) a parabolic forcing function (Figure 5-1c with Fmax=10.3kN).

Therefore, damping and strain-hardening both reduce the peak ductility demand imposed on a structure by a time-varying load.

5.3.2 Comparison with Realistic Tsunami Records

In order to investigate whether the demonstrated overstrength relationship is significant for structures subjected to realistic tsunami time-histories, numerically-derived load time-histories are obtained applied to structure S3 with varying levels of strain-hardening and damping (Table 5-2). The time-histories are obtained from the numerical inundation simulations of (Petrone et al., 2017), providing a total of 803 records each with depth, velocity and two force time-histories. The two force time-histories are calculated as per (Foster et al., 2017; Qi et al., 2014) with blockage ratios of 0.1 and 0.6, respectively.

The force time-histories represent net force in kN/m, and so a method must be chosen for applying this to the simple SDoF structure used throughout this analysis. A vertical pressure distribution (over the inundation depth) must be assumed, the SDoF structure must be assigned a height, and as in any finite element method the distributed loads must then be converted to equivalent nodal loads which will give the same reactions and nodal deflections as the original distributed load. For this investigation, a structure height of 4m (single-storey) is chosen, and the 42 records which achieve a maximum depth

between 3m-4m are applied to the structure. Equivalent nodal loads are found by calculating equivalent nodal deflection and moment reaction, as shown in Figure 5-10 (note that shear reaction equivalency would be achieved by an additional load applied at the base of the model, though as shear failure is not considered here this additional load is omitted for clarity). The assumed parameters in this calculation are given in Table 5-2 and the results for one record are shown in Figure 5-11.

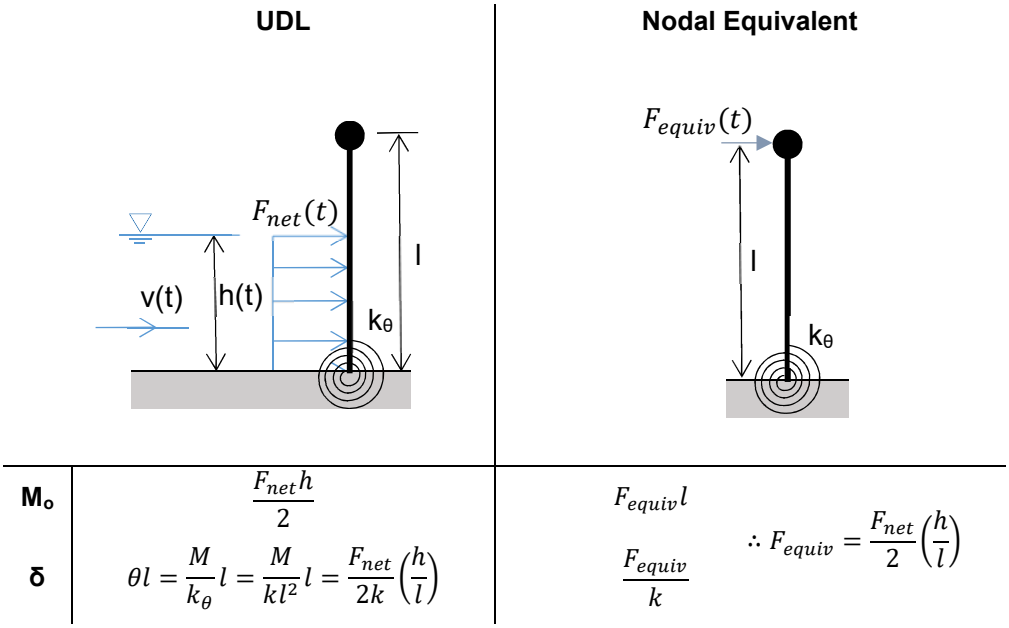

Figure 5-10: Equivalent nodal load for a SDoF system, modelled as a rigid beam element with a rotational spring (k_θ) at its base, subjected to a uniform pressure distribution.

Table 5-2: Loading and structural parameters for equivalent nodal load calculation and numerical analysis.

Loading Parameter	Assumed Value
Flow Blockage Ratio	0.6
Loading Width	2m
Pressure Distribution	Uniform

Structure (Table 5-1)	μ_{max}	l	b	ζ
S3.1	8	4m	0	0%
S3.2			0	5%
S3.3			0.05	0%
S3.4			0.05	5%

Figure 5-11 shows a representative tsunami time-history and the corresponding responses of the structures in Table 5-2. For the structure without strain hardening (S3.1, S3.2 in Table 5-2), the structure fails shortly after the yield load is exceeded, and long before the applied load can drop back below yield. The presence of ductility in the structure (S3.2) is insufficient for preventing or significantly slowing structural failure. However, structures with strain-hardening (S3.3, S3.4 in Table 5-2) continue to maintain the increasing load beyond yield, over the duration for which it is applied. For the structures which strain-harden, velocities and accelerations (and so damping and inertia forces) remain close to zero.

The record shown in Figure 5-11 demonstrates the general result, that realistic tsunami time-histories are very unlikely to exceed the yield force of an EPP structure, or ultimate load capacity of a strain-hardening structure, for a short enough duration for ductility to prevent collapse. The presence of damping does not significantly change this result for realistic tsunami time-histories. This agrees with the very short allowable durations indicated by Figure 5-6.

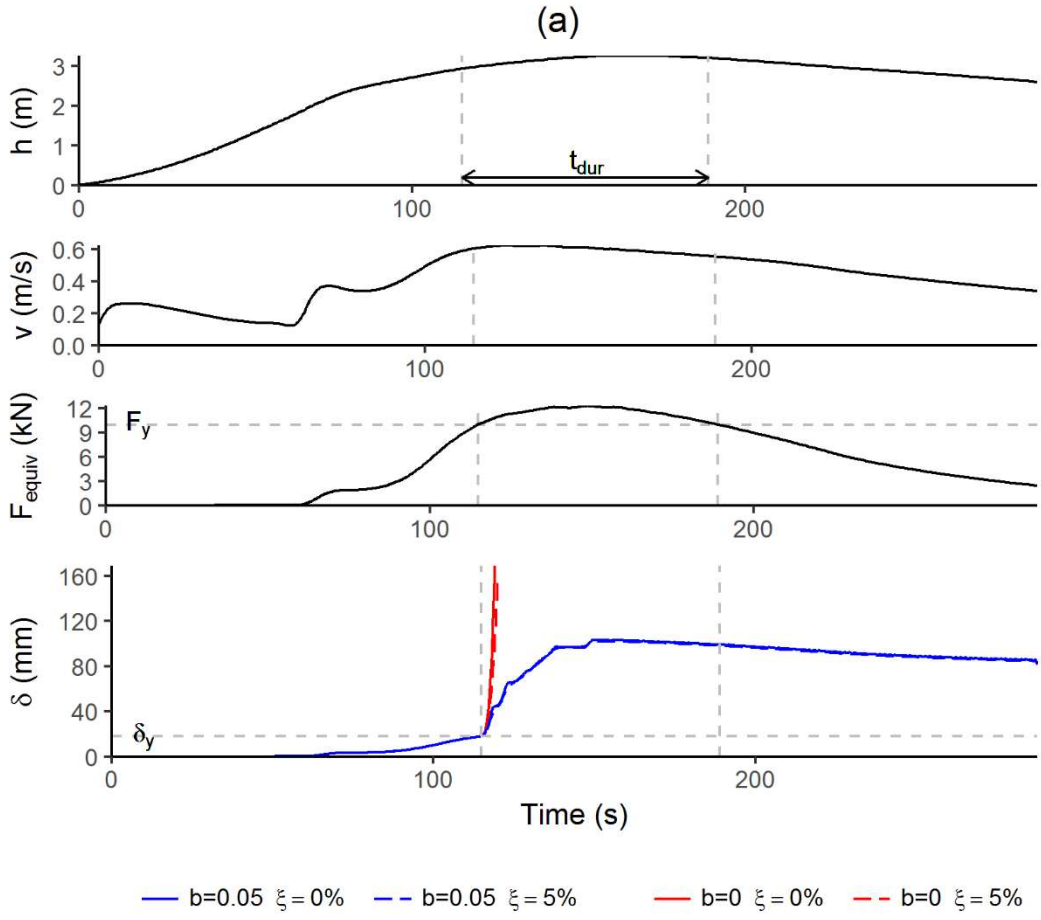

Figure 5-11: Structural response under a numerically-derived inundation time-history. (a) Inundation depth (*h*), velocity (*v*), equivalent nodal force (F_{equiv}, calculated as per Figure 5-10), and structural displacement (*δ*). (b) Force vs structural displacement for structure S3.1 (top) and S3.2 (bottom) (as per Table 5-2)

If dynamic effects can be ignored then from the definitions of plastic overstrength, plastic ductility and the strain-hardening ratio it is trivial to show that the static overstrength-ductility relationship is given by (5-16). Figure 5-12 shows the comparison between the predicted peak ductility demand predicted from this static relationship, with that obtained from numerical analysis for structures with a range of strain-hardening ratios. Generally, (5-16) is shown to predict the peak ductility demand well, with the greatest accuracy for structures with higher strain-hardening ration. This appears to confirm that dynamic affects do not greatly influence the post-yield behaviour for strain-hardening structures.

$$\Omega_p = b\mu_p \qquad (5\text{-}16)$$

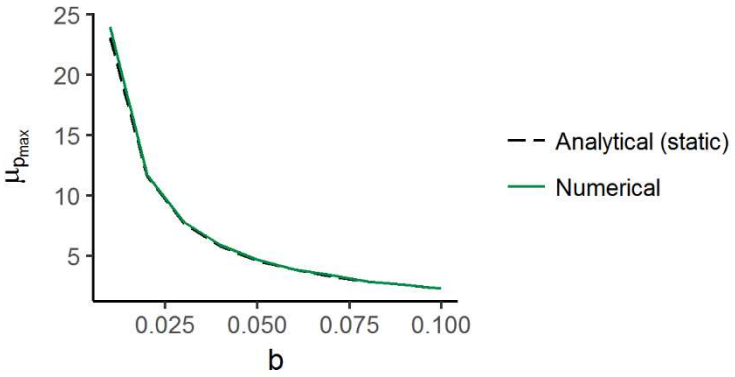

Figure 5-12: Comparison of static analytical prediction of peak plastic ductility demand (5-16) with dynamic numerical results. The analysed structures are based on S3 (Table 5-1) with a range of strain-hardening ratios (*b*), subjected to the tsunami time-history shown in Figure 5-11.

Furthermore, some of the ductility demands shown in Figure 5-12 are unrealistically high for most structures. Therefore, a structure can be considered to have collapsed once it has reached its ultimate ductility capacity (a function of the structural detailing), and the maximum corresponding load that can be achieved is determined by (5-16).

5.4 Implications for Analytical Fragility Function Derivation

The previous sections show that if ductility and damping are insufficient for time-dependent effects to permit an overstrength to develop (i.e. for long tsunami-like load durations), then damage states for a structure can be defined by directly comparing an applied load to static force threshold values ($F_{capacity}$) for the structure. $F_{capacity}$ values for the respective damage states can therefore be obtained from a static pushover of the structure. However, the preliminary investigation presented in Appendix E (based on Joshua Macabuag et al. (2014b)) shows that capacity curves derived from seismic pushover and various tsunami pushover methods differ significantly. The method for deriving $F_{capacity}$ is therefore key, and so will be examined in this section.

Uncertainty in analytical fragility functions (in terms of both the slope of the curve, and the confidence intervals) arises from uncertainty in $F_{capacity}$ (a function of the structure) and $F_{applied}$ (a function of the intensity measure, IM). Uncertainty in $F_{capacity}$ can arise due to variation in geometry, material properties, workmanship etc. These variations may occur over a single building, or a population of buildings (depending on the purpose of the derived fragility function). $F_{capacity}$ must be calculated for each structural variation, leading to a potentially large number of analyses. This section therefore investigates a proposed Simplified Tsunami PushOver (termed STPO) technique to speed up the calculation and allow for more iterations when generating synthetic damage data (and so a better characterisation of aleatoric uncertainty).

The scenario modelled in this section is of a simplified flow (quantified by TIM7 in Table 4-2, the optimal force TIM resulting from the analysis in Chapter 4), applied to an idealised 2D structural model, modelled into the non-linear post-yield range. In order to demonstrate the methodology, only a single building will be considered here. It is noted that, the demonstrated methodology is not proposed for addressing the engineering problem of fragility for a single facility (for which a detailed structural model may be warranted), but for fragility of a population of buildings for the purpose of loss modelling (for which large numbers of analyses of simplified structural models are required). This section is therefore to be considered a simplified proof-of-concept of more detailed analysis to be carried out in future studies, accounting for structural variability.

5.4.1 Development of a Simplified Tsunami PushOver Methodology (STPO)

It has been shown in sections 5.2 and 5.3 that collapse ($DS_{collapse}$) occurs if the applied load exceeds structural capacity ($F_{applied} > F_{capacity}$), where $F_{capacity}$ can be defined as the

peak force on the capacity curve obtained from a static pushover of the structure (i.e. there is no need for Time-History Analysis or other time-dependent considerations unless t_{dur} < ~3T, as per Figure 5-6). This section therefore compares peak load capacity of a case study building for a Variable Height PushOver (VHPO) analysis (section 2.4.3), to that for a proposed Simplified Tsunami PushOver methodology (STPO).

So as to compare STPO results with established VHPO and THA results, the case-study building will be chosen from an existing study: Petrone et al. (2017) (discussed in sections 2.3.1.3 and 2.4.3). In order to assess the structural capacity, all of the damage mechanisms outlined in Figure 2-3 should be considered. However, the VHPO results of Petrone et al. (2017) consider only global failure (Figure 5-14), and therefore so as to directly compare STPO and VHPO results, the same global failure mechanism will be considered in this study.

5.4.1.1 Numerical Model of Case Study Building

The case study building to be used in the remainder of this section is that presented by Petrone et al. (2017): a 10-storey, multi-bay RC structure (Figure 5-13). In Petrone et al. (2017) the structure is loaded laterally under both Constant-Height PushOver (CHPO), VHPO and Time-History Analysis (THA). VHPO is shown to give comparable estimates of structural capacity to THA, and so the VHPO results will be used in this section to benchmark the proposed simplified methodology. See section 2.4.3 for detailed discussion of Petrone et al. (2017).

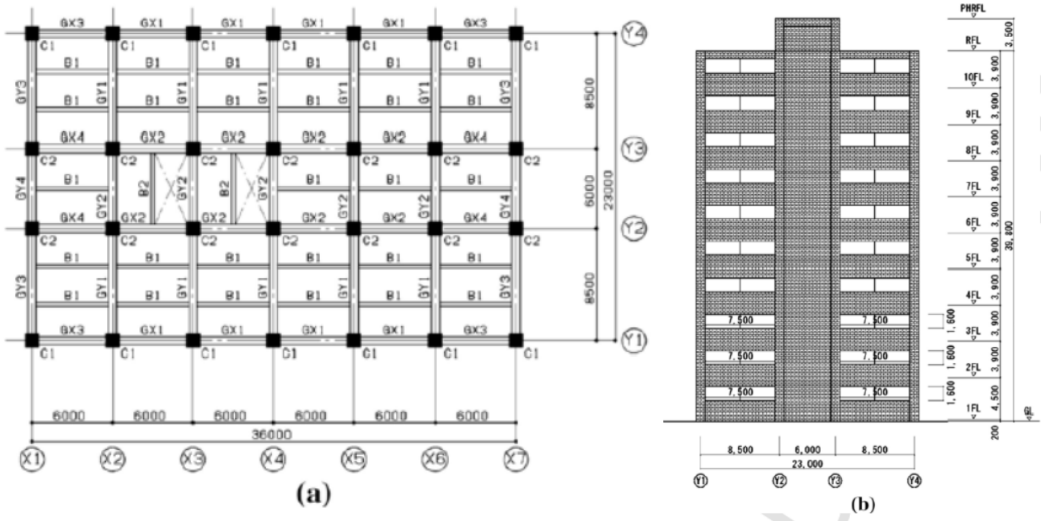

Figure 5-13: Case study structure from Petrone et al. (2017).

Structural calculations are carried out using OpenSees, with structural parameters outlined in Appendix F. In agreement with the analysis of section 4.4, Petrone et al. (2017) also finds that the quasi-steady load estimate methodology of Foster et al. (2017)

and Qi et al. (2014) (TIM7 in Table 4-2) to be the optimal force-related TIM. This load estimation method will therefore be used for the remainder of this section.

Petrone et al. (2017) notes that 1-storey local mechanisms (i.e. softstorey-type collapse, Figure 5-14) leads to the failure of the structure for the wave traces considered. They also show that the structural strength associated with this mechanism is contained within a narrow range of base shear values. This softstorey-type failure mechanism is caused by plastic hinges forming at the tops and bottoms of the ground-1st floor columns, as shown in Figure 5-14, where F is representative of the cumulative lateral load that can be considered applied at the 1st-floor floor-level.

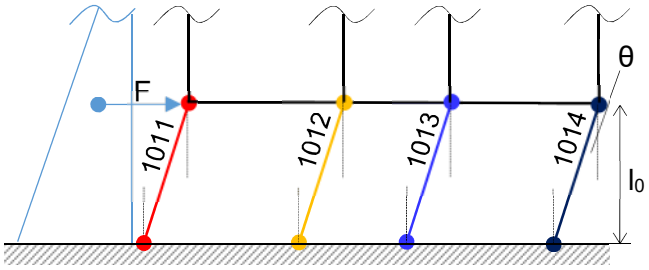

Figure 5-14: Soft-storey-like collapse mechanism observed for all simulations of Petrone et al., 2017), defined by plastic hinges forming in ground-to-1st floor columns as shown. F is representative of the cumulative lateral load that can be considered applied at the 1st-floor floor-level. l_{01} indicates the ground-to-1st floor height. Column colours and column numbers correspond to those used in Figure 5-16 and Figure 5-18.

Modelling only the observed failure mechanism (Figure 5-14) is more rapid than modelling a full load distribution over an entire structure. Therefore, considering only this mechanism, it is investigated to what extent the load profile and structural model can be simplified so as to derive a comparable structural capacity to that obtained from VHPO analysis.

5.4.1.2 Initial Proposal for a Simplified Tsunami PushOver Methodology ($STPO_1$)

The initial proposal for a Simplified Tsunami PushOver methodology (termed $STPO_1$) is to maintain the full structural model (Figure 5-13) but to recreate the soft-storey-type failure mechanism (Figure 5-14) by replacing the applied VHPO load distribution (Figure 2-17) with an equivalent lateral point load applied at 1st-floor slab level.

Figure 5-15 compares results for Simplified Tsunami PushOver (STPO) with the equivalent Variable Height PushOver (VHPO) curve obtained from the Constant Height PushOver (CHPO) results presented by Petrone et al. (2017). Each CHPO curve represents a fixed inundation depth and increasing flow velocity, with force calculated according to Foster et al. (2017). Performance points are then obtained on each CHPO corresponding to Froude number Fr=0.6. The connection of these performance points

forms the equivalent VHPO curve shown in Figure 5-15, which Petrone et al. (2017) showed to be the same as the true VHPO performance curve (calculated by applying a VHPO load case to the structure).

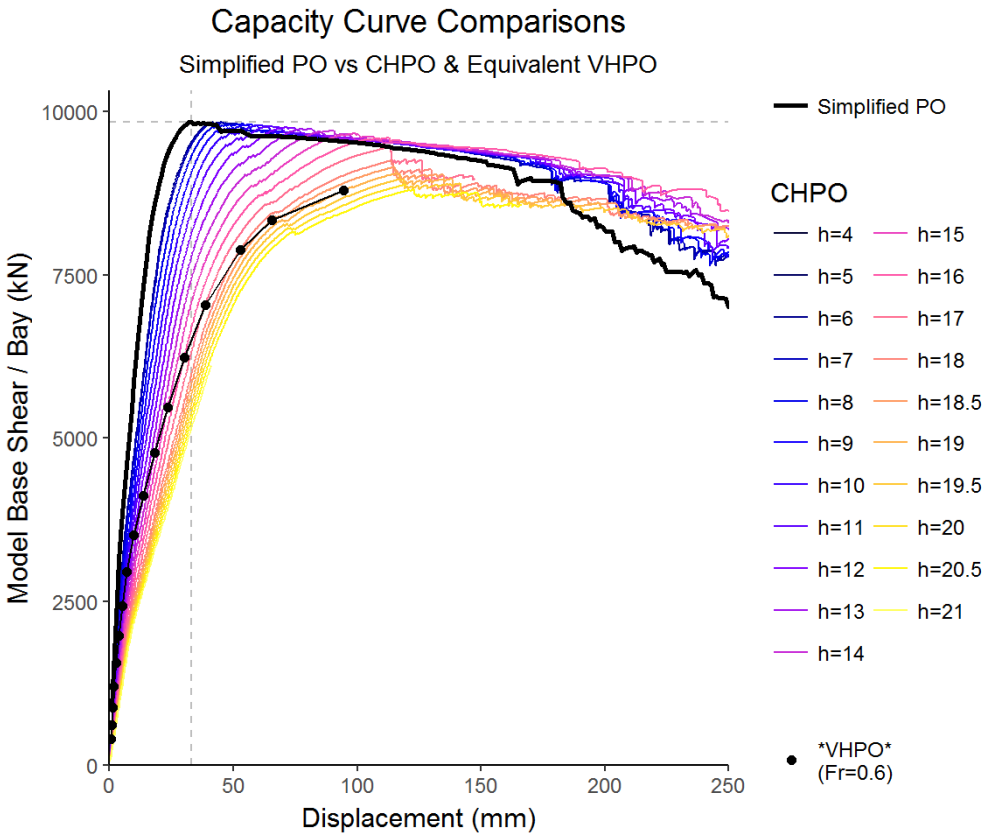

Figure 5-15: Comparison of STPO$_1$ OpenSees results with those from the full structure VHPO analysis of Petrone et al. (2017).

Figure 5-15 shows that structural capacity (the maximum load resisted by the structure) is 12% higher under the STPO (9,836kN) scenario as compared with VHPO (8,800kN). This may be expected, as the vertical distribution of lateral loads for VHPO and STPO (Figure 2-17 and Figure 5-14 respectively) is different, and so their respective global overturning moments differ. This results in different member forces, both at failure (Table 5-3) and when compared at the same base shears. The most notable differences are seen in the column axial loads (Figure 5-16). This is due to the different lever arms of the applied lateral loads, between the VHPO and STPO loadcases. That the discrepancy between axial loads is due to differing lever arms (rather than differences in net weight) is also evidenced by the fact that the sum of the column axial load differences (shown in Figure 5-16, right) remains zero for all calculation steps.

Therefore, an investigation is carried out in section 5.4.1.4 on whether the structural capacity estimate can be improved by applying an additional load to account for this difference in lever arm.

Table 5-3: VHPO & STPO column forces at failure in local axis directions (Fr=0.6, h=19m). The sum of the column shears equates to the total applied lateral load. The sum of the column axial forces equates to the weight of the structure (and so is unchanged at each calculation step)

	Column forces (kN)			
	Shear (local x)		Axial (local y)	
	VHPO	STPO	VHPO	STPO
col1011	1,508	2,104	1,085	2,382
col1012	2,338	2,668	4,154	4,505
col1013	2,687	2,775	6,470	5,652
col1014	2,267	2,289	4,850	4,021
sum:	**8,800**	**9,836**	**16,560**	**16,560**

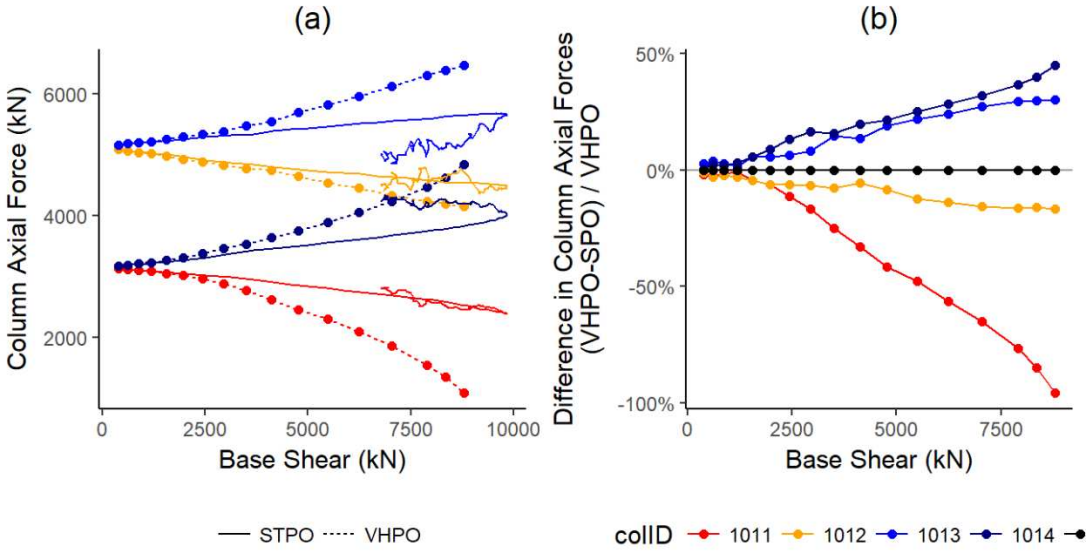

Figure 5-16: Comparison between $STPO_1$ and VHPO cases: (a) ground-to-1st floor column axial forces vs base shear, and (b) difference between VHPO and $STPO_1$ cases. Note that VHPO results are obtained at CHPO performance points for Fr=0.6, and, shear and axial loads are the same at both ends of the columns due to the OpenSees model lumping mass at the column tops.

5.4.1.3 Comparison with Manual Plastic Hinge Analysis

The plastic hinge mechanism shown in Figure 5-14 can also be used to calculate the load capacity analytically by the use of virtual work (5-17).

$$P(\theta l) = 2M_{p1}\theta + 2M_{p2}\theta + 2M_{p3}\theta + 2M_{p4}\theta$$

$$\therefore F_{capacity} = \frac{2M_{p1} + 2M_{p2} + 2M_{p3} + 2M_{p4}}{l} \qquad \textbf{(5-17)}$$

It is highlighted that each column's plastic moment (M_p) is affected by the axial load in the column, which itself is a function of the horizontal load applied. Therefore, individually

calculating column capacities and then combining these, as in the equation above, is an iterative calculation (as the $F_{capacity}$ found will alter the values of M_p, which will in-turn change $F_{capacity}$, and so on). In the first instance, in order to identify whether the virtual work method provides a good estimate of structural capacity, the column capacities are first extracted from the numerical model of section 5.4.1.2. Table 5-4 shows the peak moment capacities observed during analysis for each ground-to-1st floor column at each end (top and bottom).

Table 5-4: Peak Moment Capacities for ground-1st floor columns of OpenSees model (full structure, simplified load). Note: end 1 = ground floor, end 2 = 1st floor.

Column:	1011		1012		1013		1014		
	end1 z1	end2 z2	end1 z1	end2 z2	end1 z1	end2 z2	end1 z1	end2 z2	
Peak Moment Capacity (kNm)	4,910	4,930	6,096	6,079	6,463	6,463	5,410	5,426	
Axial Load at M=M_c	2,489	2,575	4,511	4,459	5,678	5,680	4,036	4,077	
M_c/h_1 (kN)	1,091	1,096	1,355	1,351	1,436	1,436	1,202	1,206	Sum: 10,173kN

The result of applying equation (5-17) (10,173kN, the sum shown in Table 5-4 where the plastic moment capacities (M_p) have been obtained from the numerical model of section 5.4.1.2) is higher than the structural capacity obtained from $STPO_1$ (9,836kN, Figure 5-15), as the peak moment capacities are not achieved at the same timestep for all columns, however the results are within 4% of each other. $STPO_1$ provides a structural capacity estimate closer to that obtained by VHPO than the virtual work capacity. Therefore, although the virtual work calculation provides a useful check of results, $STPO_1$ is a preferred method for estimating structural capacity and so is expanded on below.

5.4.1.4 Updated Simplified Tsunami PushOver ($STPO_2$)

In order to address the differing global overturning moments between $STPO_1$ and VHPO cases, the load vectors shown in Figure 5-16 are added to column tops, as shown in Figure 5-17. This will not alter the vertical and horizontal equilibrium, but should correct the disparity in overturning moment discussed above.

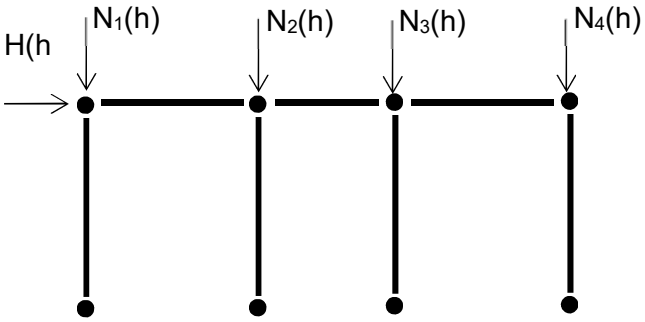

Figure 5-17: Updated Simplified Tsunami PushOver (STPO⁺). H(h) is chosen so as to match the lateral component of the applied VHPO loading. *N*(h) is chosen so as to match the vertical force applied at each column under the applied VHPO loading. *N*(h) must account for both the constant component due to structural weight, and the varying components due to the overturning moment of the VHPO load applied.

$\boldsymbol{N} = \begin{bmatrix} N_1 \\ N_2 \\ \dots \end{bmatrix}$=vector of additional loads to apply to the structure to compensate for the difference in overturning moment between STPO and VHPO case. ***N*** is to be calculated as a function of inundation depth (***N***(*h*)), but in the first instance in order to identify whether the proposed $STPO_2$ method provides an accurate estimate of structural capacity, ***N*** is simply taken as the difference between the VHPO and $STPO_1$ axial column loads (Figure 5-16).

The $STPO_2$ structural capacity (9,748kN) is closer to the VHPO-derived capacity (8,965kN) than the $STPO_1$ case (9,947kN), however there is still discrepancy. Column shear (shown in Appendix F) and axial forces (Figure 5-18, left) show good match between the $STPO_2$ and VHPO cases. However, column end-moments between the two cases do show some discrepancy (Figure 5-18, right).

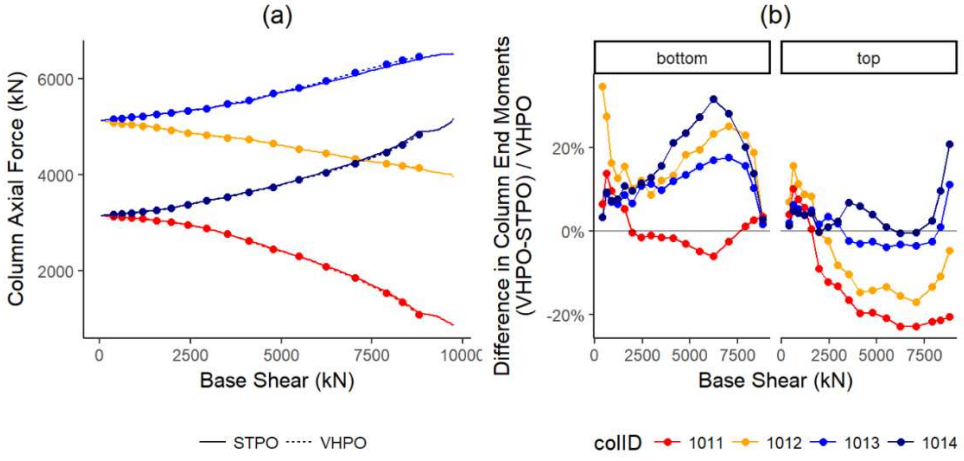

Figure 5-18: Comparison between $STPO_2$ and VHPO cases: ground-to-1st floor column axial forces vs base shear (left), and difference between VHPO and $STPO_2$ cases (right). Note that VHPO results are obtained at CHPO performance points for Fr=0.6, and, shear and axial loads are the same at both ends of the columns due to the OpenSees model lumping mass at the column tops.

An important factor that may contribute to the discrepancy between STPO and VHPO results are the P-Δ effects present in both models. For the STPO cases, the only lateral load is at ground floor, so all deformation is concentrated at the ground-1st level, and the upper floors are not significantly deforming laterally. However, for the VHPO case lateral load is applied at multiple floors causing inter-storey drift at each floor where load is applied. This means that the columns at each floor are subjected to an additional P-Δ moment due to the eccentrically-applied axial load from the floors above. This additional P-Δ moment would accumulate down the structure resulting in an additional moment at the ground-1st floor columns.

Given that comparison is being made to an existing study (Petrone et al., 2017) for which P-Δ effects are included, it is not feasible to remove the P-Δ effect in this analysis. However, as the $STPO_2$-derived structural capacity is within 10% of the VHPO-derived capacity $\left({}^{STPO_2 - VHPO}/_{VHPO} = 8.7\%\right)$ then the proposed $STPO_2$ methodology can be taken as a suitable preliminary estimate of structural capacity under the soft-storey-type failure mechanism investigated, and it is now investigated what effect the discrepancy observed has on fragility function derivation.

5.4.2 Investigating the Effect on Derived Fragility Functions

$F_{capacity}$ defined by $STPO_2$ is faster to calculate than for VHPO, but is slightly higher. However, it is unclear what effect this has on analytical fragility function derivation, and so fragility functions are derived and compared here. The following analysis is conducted in the statistical programming language R (R Development Core Team, 2008).

5.4.2.1 Estimating the Tsunami Hazard

The analysis of sections 5.2 and 5.3 imply that collapse ($DS_{collapse}$) occurs if the applied load exceeds structural capacity ($F_{applied} > F_{capacity}$) unless $F_{capacity}$ is exceeded for a duration less than roughly 3 times the structural period (Figure 5-6). Therefore, synthetic damage data can be generated by comparing $F_{capacity}$ to a catalogue of applied tsunami loadcases. Section 2.4.3 outlines methods for estimating tsunami loads on buildings from knowledge of the local building inundation, however, it is not clear what distribution of inundation parameters may be experienced by a building population, which must also be captured in the analytical models used for fragility function derivation. Methods of quantifying uncertainty in the loading (aleatoric uncertainty derives from information which is not captured by the TIM), and the structural parameters are not widely addressed in the current literature. For this study, flow parameter distributions are extracted from the inundation simulation conducted by Petrone et al. (2017). As

discussed in section 2.3.1.3, Petrone et al. (2017) derived 803 tsunami inundation records from which peak applied loads can be obtained.

Section 4.4 shows the optimum TIMs for the Japanese case-study locations considered (which are also the case-study locations of Petrone et al. (2017)) to be inundation depth (h) and a quasi-steady force estimate accounting for flow-regime (F_{QS}) as defined by (Foster et al., 2017; Qi et al., 2014)). Therefore, the same TIMs will be considered here. Figure 5-19 shows the distribution of tsunami peak applied loads for the 803 records of Petrone et al. (2017), plotted against depth and force TIM bins.

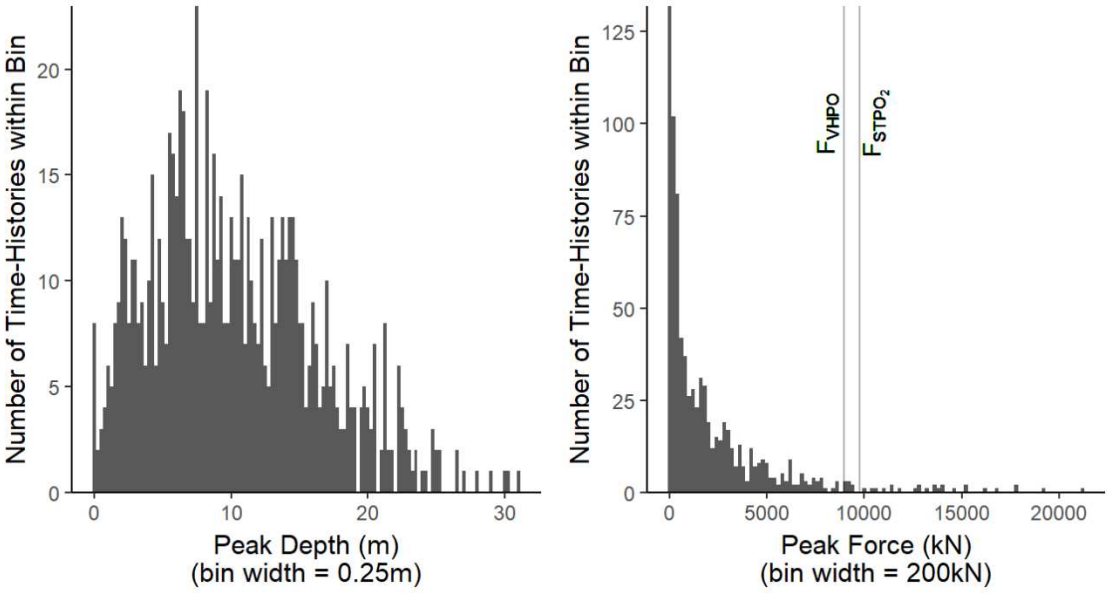

Figure 5-19: Distributions of the 803 records of Petrone et al. (2017) used in this study. (a) Peak depth distribution, and (b) peak force distribution. Vertical lines in (b) indicate the structural capacities calculated using VHPO and $STPO_2$, showing that few records fall within the discrepancy between these records.

Figure 5-19 shows that very few of the 803 records chosen fall between $F_{capacity}^{STPO_2}$ and $F_{capacity}^{VHPO}$ (Figure 5-19b). Fragility functions for $STPO_2$ and VHPO are therefore formed on very similar input records, meaning that it is expected that the functions are unlikely to differ greatly.

5.4.2.2 Fragility Function Comparison

Eigenvalue analysis of the model gives a structural period of T_1=0.73s. And therefore, considering Figure 5-6 it is only necessary to consider overstrength for loads which exceed $F_{capacity}$ for t<3T ≈ 2.2s (for an overstrength of approximately 5%). Review of the available data reveals that none of the records fall into this category, and so all tsunami records for which peak applied load exceeds $F_{capacity}$ can be deemed to have caused collapsed. Figure 5-20 therefore shows a comparison of fragility functions considering

$F_{capacity}$ derived from $STPO_2$ and VHPO, for the optimal TIMs identified in Chapter 4: inundation depth and force.

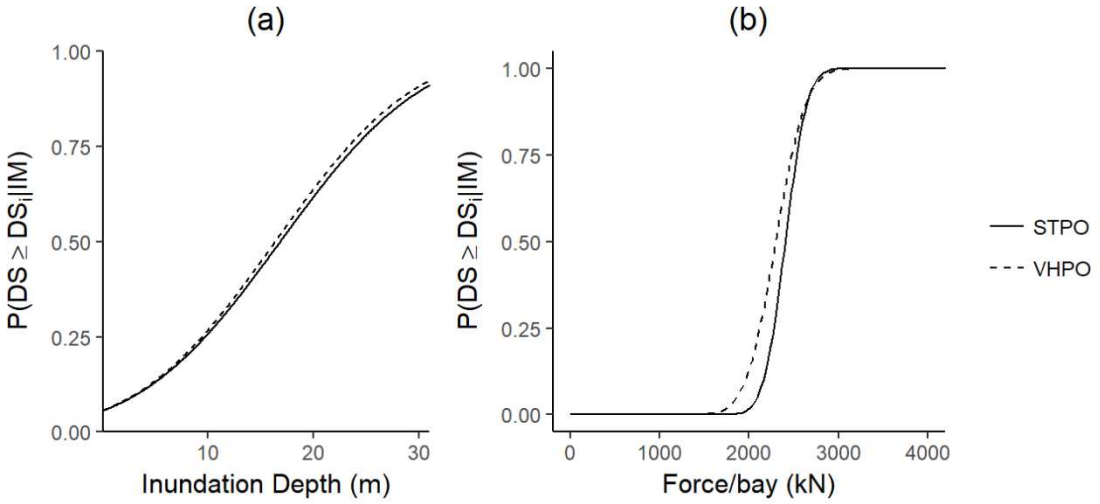

Figure 5-20: Comparison of collapse damage-state fragility functions considering $F_{capacity}$ derived from $STPO_2$ and VHPO, for TIMs of (a) depth and (b) force. Note that the force capacity in (b) appears different from those shown in Figure 5-19 because the force shown is that when discounting the load applied below the bottom half of the ground floor, for consistency with Petrone et al. (2017).

Figure 5-20 shows that, as expected, $F_{capacity}^{SPO_2}$ is sufficiently close to $F_{capacity}^{VHPO}$ so as to generate very similar fragility functions. This suggests that for the purposes of generating analytical fragility functions, using the tsunami inundation catalogue provided, $STPO_2$ provides a sufficiently accurate estimate of $F_{capacity}$.

It would be preferable to compare these analytical curves to empirical curves. However, in order to demonstrate the STPO methodology only a single building has been considered here (i.e. structural variability has not been considered). There are no empirical curves for a suitably similar structural type, and so a comparison between analytical and empirical curves would not be meaningful, and will instead be the focus of future studies accounting for structural variability.

5.5 Analytical Fragility Function Summary and Discussion

This chapter has presented research related to structural analysis for analytical fragility function derivation. The fundamental principle of whether ductility and dynamic effects are significant in determining structural performance under tsunami loading has been investigated, and the implications of these findings on methods of structural analysis for analytical fragility function derivation has been demonstrated.

It has been shown analytically that an Elastic Perfectly-Plastic (EPP) Single Degree of Freedom (SDoF) structure can maintain a load greater than its yield load (F_y) for a

duration of time, and that peak displacement ductility demand (μ_{peak}) for a SDoF EPP structure is defined by two dimensionless parameters, where the relationship $\mu_{peak}\left(\Omega_{p_{peak}}, \left\{\frac{t_{dur}}{T}\right\}\right)$ has been defined analytically for tsunami loading idealised as triangular and parabolic time-histories. However, it has also been shown that for realistic values of t_{dur} and T, the peak overstrength permitted is negligibly small and so dynamic effects may be ignored for the purposes of design and damage assessment.

This result is upheld for a SDoF structure with strain-hardening (idealised by a bilinear performance curve) indicating that the ultimate ductility demand placed on a bilinear SDoF structure can be defined by the strain hardening ratio (b) and the required overstrength. However, real structures will not harden indefinitely and should be considered to also have a maximum load capacity (F_{max}). Dynamic performance of the structure will become a consideration if, before the ductility capacity is reached, the applied load exceeds the maximum load capacity of the structure.

Therefore, although there is a difference between applied and internal forces due to the time-dependent effects of (viscous) damping and inertia (the accelerating mass of the structure), it has been shown that these affects are insufficient to prevent collapse under tsunami-like loading for all but the most transient cases. This is because tsunami loading is a predominantly unidirectional load applied externally for a long duration relative to typical structural periods (i.e. it is effectively a force-controlled condition, rather than the displacement-controlled seismic problem). Therefore, unlike seismic design practice, structural dynamics do not play a significant role in performance under tsunami loading, and ductility cannot be utilized in all but very transient cases.

By using the above analysis to justify ignoring dynamic effects and ductility in analytical fragility function derivation, a mechanistic approach is proposed for the derivation of structural capacities for analytical tsunami fragility functions. A Simplified Tsunami PushOver (STPO) technique is proposed and its feasibility for use is investigated. The STPO considers building failure due to a softstorey-type collapse mechanism only, so as to speed up the fragility function derivation calculation and allow for more iterations (and so a better characterisation of aleatoric uncertainty). $F_{capacity}$ defined by STPO was significantly faster to calculate than for VHPO, but is 12% higher for the case study building, with the discrepancy considered to be due to P-Δ effects. However, for a chosen catalogue of tsunami inundations, the resulting fragility functions are shown to be very close to each other, and therefore the STPO analysis proposed provides a sufficiently accurate estimate of $F_{capacity}$ so as to generate analytical fragility functions.

The analysis presented in this chapter makes significant assumptions in both the structural modelling and the tsunami loading, but is based on fundamental structural dynamics and the current state-of-the-art in tsunami load characterization. Further work is required to verify the results of this chapter for more realistic structures, to extend the analysis to intermediate damage states, and to accurately characterize uncertainty in fragility function derivation of both the structure and the suite of tsunami loading scenarios.

Regarding the intermediate damage states, it is necessary in future research to better define the damage state thresholds used in structural analysis. In several studies (section 2.3.1.3) Inter-Storey Drift (ISD) has been assumed, due to its popularity in seismic analytical fragility function derivation. However, this assumption will need to be examined as alternative EDP's may be more appropriate for tsunami damage prediction, and it may prove more accurate to define damage states based directly on element performance.

By considering structural dynamics and ductility effects, this chapter has presented research which furthers the field of knowledge related to structural analysis for analytical fragility function derivation.

6 Summary and Conclusions

6.1 Overview of Thesis

This thesis has presented improved methods of empirical fragility function derivation, and research towards the development of a method for constructing analytical fragility functions based on structural analyses. The over-arching aim of this research has been to identify the most effective methods for quantifying fragility of buildings to tsunami damage, both using observational damage data, and in the absence of data. For empirical fragility assessments based on observed damage data, the aim has been to identify the most appropriate statistical methods and the most appropriate Tsunami Intensity Measure (TIM) for tsunami fragility functions, as well as to quantify the effect of debris on fragility function derivation. For analytical fragility assessments in the absence of observed damage data, the aims have been to investigate whether ductility and dynamic effects are significant in determining structural performance under tsunami loading, and to identify what types of simplified structural models are most appropriate for analytical fragility function derivation.

Chapter 2 presented a critical review of the literature related to the prediction of building damage due to tsunami. Types of building damage observed due to tsunami were categorized and the current state of the art on probabilistic damage prediction was reviewed, highlighting that methods are required to generate fragility functions by structural analysis. Therefore, definitions of tsunami loading were also critically reviewed and quantitatively compared, and methods of structural analysis under tsunami loading were examined. Finally, the following research needs were highlighted:

- Improved statistical methods in fragility function derivation
- A method for identifying the preferred tsunami intensity measures
- Improved understanding of tsunami response of structures
- Feasibility of using simplified approaches for structural modelling and analysis

Based on these research needs Chapter 3 framed the research question and sub-questions that will enable the step-wise investigation of improved methods for developing empirical fragility functions, and methods for deriving analytical fragility functions in the absence of past damage data.

Chapter 4 identified the key Tsunami Intensity Measures (TIMs) and improved statistical methods to be used for fragility function derivation, and derived empirical fragility

functions using a detailed, disaggregated building damage dataset. Firstly, exploratory analysis of the dataset was conducted, and then regression analysis was conducted to demonstrate improved statistical methods proposed to define the optimal fragility functions. The analysis was then repeated using numerical tsunami inundation model results to identify the TIM which most successfully describes the observed damage. Finally, a preliminary methodology for quantifying debris-related effects on fragility functions was presented.

Chapter 5 investigated the fundamental principle of whether ductility and dynamic effects are significant in determining structural performance under tsunami loading, and demonstrated the implications of these findings on methods of structural analysis for analytical fragility function derivation. It was first shown analytically that an Elastic-Perfectly-Plastic Single Degree of Freedom structure can maintain a load greater than its yield load for a duration of time, i.e. if overstrength influences structural capacity. A sensitivity analysis was then conducted to determine the effect of damping, strain-hardening and load-duration on overstrength. The chapter concluded by investigating a simplified method of estimating structural capacity under tsunami loading on the basis of the above analyses, suitable for use in the large number of analyses required to derive analytical fragility functions of populations of buildings.

6.2 Main Conclusions

Discussion of results is made at the end of each chapter. The main conclusions of this study can be summarized as follows:

Exploratory Analysis of Empirical Damage Data

1. Missing data can only be removed if it can be shown to be Missing Completely At Random. This is shown to be not the case for the 2011 MLIT Japan data, meaning that all previous studies which have generated curves according to any sub-category (e.g. material, age, height etc) using complete-case analysis (removal of buildings with missing data) may have introduced a bias in the results.
2. Multiple Imputation (MI) has been shown to be an acceptable method for estimating missing data, and is recommended for use on future fragility studies where data cannot be shown to be Missing Completely At Random.

Statistical Modelling for Both Empirical and Analytical Fragility Functions

3. *K*-fold cross-validation (KFCV) is shown to be a suitable method for comparing model fits for various model types, and the methodology for conducting this for multinomial models is demonstrated. It is recommended that KFCV be used for evaluation of model fits in future fragility studies.
4. Data aggregation has been quantifiably shown to reduces model predictive accuracy by an amount which is dependent on the aggregation approach. Hence, existing studies that use aggregated data from the 2011 GEJE should be considered superseded by those that use disaggregated data directly.
5. Ordinary Least Squares parameter estimation is quantitatively shown to be unsuitable for fragility function estimation as it suffers from the issues of data aggregation, and violates several linear model assumptions leading to reduced predictive accuracy and increased uncertainty.
6. Semi-parametric methods are seen to be suitable for comparative fragility assessments, and the issue of over-fitting can be avoided through the use of cross-validation techniques, as demonstrated.

Optimal Tsunami Intensity Measure for Both Empirical and Analytical Fragility Functions

7. Measures of force provide the most efficient TIMs, if the inundation simulation from which they are derived is sufficiently accurate, or simulated velocity can be validated. Depth is an acceptable TIM for low-accuracy simulations of inundation. The required accuracy is the subject of further research.
8. Inundation simulations outputs recommended for fragility assessment are depth, velocity and Froude number, as instantaneous force values (calculated at each time-step) do not appear to give better fits to observed damage than equivalent values calculated from separate (non-coincident) peaks of depth, velocity and Froude Number. Further research is needed to investigate the sensitivity of this result to inundation simulation accuracy.
9. Flow regime (indicated by Froude Number) is a significant consideration when conducting fragility assessments, or quantifying tsunami-induced forces on structures.

Debris-Effects on Empirical Fragility Function Derivation

10. Buildings thought to be affected by debris mostly experienced higher TIM values and higher damage states (debris designation occurs in the vicinity of other 'washed away' buildings, which as more likely to occur in locations of high TIM values).
11. The removal of buildings thought to be affected by debris resulted in changes to both the slope and intercept of the fragility functions. This indicates that the inclusion of debris-damaged buildings in the dataset (as is the case for most existing empirical fragility functions) does have an effect on fragility functions that may not be captured by purely flow regime-related TIMs.
12. The difference between the intercept and slope (in link space) for fluid-only and debris-influenced fragility functions can be quantified by inclusion of debris-indicator terms in the fragility functions.
13. The influence of debris model parameters on determining building damage was shown to be significant for all but the lowest damage state ("minor damage").
14. More complex fragility functions which incorporate debris model parameters were shown to have a statistically significant better fit to the observed damage data than models which omitted debris information. This suggests that inclusion of debris information in fragility functions improves the accuracy of the model.

Structural Analysis for Analytical Fragility Function Derivation

15. Overstrength is a function of two parameters: 1) the ratio between the maximum applied load and the statically determined capacity of the structure, and 2) the ratio between the structural period and the duration of the loading exceeding the statically determined capacity of the structure. Where, overstrength is the ability of the structure to absorb through plastic deflection loads greater than peak strength
16. Overstrength is insufficient to prevent collapse under tsunami-like loading for all but the most transient cases. This is despite the demonstrated difference between applied and internal forces due to the time-dependent effects of (viscous) damping and inertia (the accelerating mass of the structure).
17. Structures must therefore be designed such that their maximum capacity is greater than that applied by the design tsunami.
18. By ignoring dynamic effects and ductility, mechanistic approaches to structural capacity derivation are proposed to be adequate for analytical fragility function derivation.
19. A proposed Simplified Tsunami PushOver (STPO) technique is demonstrated to give a sufficiently accurate estimate of structural capacity so as to generate analytical fragility functions

By providing recommendations as to which are the most efficient TIMs and statistical model fitting approaches, and by introducing an advanced method for selecting optimal statistical models and quantifying debris damage, these findings have the potential to change how both empirical tsunami fragility curves are constructed in the future. Furthermore, by considering structural dynamics and ductility effects, this chapter has presented research which furthers the field of knowledge related to structural analysis for analytical fragility function derivation.

6.3 Limitations and Future Work

This thesis focuses on the prediction of building damage subjected to tsunami onshore flow, and so source, propagation and inundation modelling approaches have not been discussed in detail. This thesis has specifically focused on damage prediction applications in catastrophe modelling, and so engineering applications (e.g. fragility functions used for performance-based design) and prescriptive code-based design have not been considered. Codes have however been discussed in the context of their presentation of tsunami loading definitions. An important application of the future development of the work on debris-influence on fragility function derivation, will be to define how fragility curves could be adjusted to account for locations of increased likelihood of debris (e.g. downstream of ports or areas of lightly constructed buildings likely to collapse in tsunami flow) for both the engineering and insurance industries.

Research into analytical fragility functions is at an early stage, and so the research presented in Chapter 5 may be considered early steps towards the goal of deriving reliable and representative functions. The structural analysis presented makes significant assumptions in both the structural modelling and the tsunami loading, but is based on fundamental structural dynamics and the current state-of-the-art in tsunami load characterization. Further work is required to verify the results for more realistic structures than the Single Degree of Freedom used throughout. Given the complexity of the full tsunami loading regime, this investigation has looked to examine a simplified case whereby only lateral hydrodynamic fluid loads have been considered. I.e. debris, buoyancy, net hydrostatic effects, foundation effects and preceding seismic damage have not been considered. Definition of an adequate Engineering Demand Parameter (EDP) and related damage state threshold definitions for multiple damage states is presented in the Appendix E, but for the preliminary study in this thesis only the collapse damage state was considered. Furthermore, it will also be necessary to investigate the

accurate characterization of uncertainty in both the structural model (by considering several buildings modelled as a series of geometric and material parameters defined as random variables of defined distributions) and the suite of tsunami loading scenarios, considering how to incorporate the possibility of bore and debris impact. The focus of this thesis was on damage prediction for catastrophe modelling and loss estimation purposes, and so engineering applications (e.g. fragility functions used for performance-based design and prescriptive code-based design) has not been considered. Similarly, financial and casualty loss estimation is beyond the scope of this thesis and has not been included here.

7 References

Adriano, B., Koshimura, S., Hayashi, S., Gokon, H., & Mas, E. (2016). Understanding the extreme tsunami inundation in onagawa town by the 2011 tohoku earthquake, its effects in urban structures and coastal facilities. *Coastal Engineering Journal*, *58*(4). https://doi.org/10.1142/S0578563416400131

Aida, I. (1978). Reliability of a tsunami source model from fault parameters. *J. Phys. Earth*, *26*, 57–73. Retrieved from https://www.jstage.jst.go.jp/article/jpe1952/26/1/26_1_57/_pdf

Alam, M. S., Barbosa, A. R., Scott, M. H., Cox, D. T., & van de Lindt, J. W. (2017). Development of Physics-based Tsunami Fragility Functions considering Structural Member Failures. *Journal of Structural Engineering, ASCE*.

Amakuni, K., & Terazono, N. (2011). Basic Analysis on Building Damages by Tsunami due to The 2011 Great East Japan Earthquake Disaster Using. In *15 World Conference on Earthquake Engineering*. Retrieved from http://www.iitk.ac.in/nicee/wcee/article/WCEE2012_3628.pdf

Araki, S., Ishino, K., & Deguchi, I. (2010). Stability of Girder Bridge Against Tsunami Fluid Force. *Coastal Engineering*.

Arikawa, T., Shimosako, K., & Ishikawa, N. (2012). Structural failure by impulsive tsunami force. In *5th International Conference on Protection of Structures against Hazards* (pp. 1–14).

Arimitsu, T., Ooe, K., & Kawasaki, K. (2013). Evaluation Method of Tsunami Wave Pressure Acting on Land Structure. *Coastal Dynamics*, *3*(651), 3–11. Retrieved from http://www.coastaldynamics2013.fr/pdf_files/010_Arimitsu_Tsuyoshi.pdf

Armijo, R., Lacassin, R., & Delorme, A. (2010). *Preliminary Evaluation of the Chile, February 27, 2010 earthquake tsunami runup at Constitucion*.

Árnason, H. (2005). *Interactions between an Incident Bore and a Free-Standing Coastal Structure*. University of Washington. Retrieved from https://www.google.co.uk/url?sa=t&rct=j&q=&esrc=s&source=web&cd=1&cad=rja&uact=8&ved=0CCIQFjAA&url=http%3A%2F%2Ffaculty.washington.edu%2Fcpetroff%2FHalldor%2520dissertation.pdf&ei=fkz8VJjfCIav7Ab7jYDgDw&usg=AFQjCNFFE-t9eKGbChn-ezNZWmcS6_rjqg&sig2=2UG3t-6MR9SEflAgrdU7DQ&bvm=bv.87611401,d.ZGU

Arnason, H., Petroff, C., & Yeh, H. (2009). Tsunami Bore Impingement onto a Vertical Column. *Journal of Disaster Research*, *4*(6), 391–403.

Asakura, R., Iwase, K., Ikeya, T., Takao, M., Kaneto, T., Fujii, N., & Omori, M. (2000). Experimental research on wave power of tsunami surged over the land beyond the upright seawalls (in Japanese). *Coastal Engineering Journal, , Japan Society of Civil Engineering*, *No.47*, 911–915.

Attary, N., van de Lindt, J. W., Unnikrishnan, V. U., Barbosa, A. R., & Cox, D. T. (2016). Methodology for Development of Physics-Based Tsunami Fragilities. *Journal of Structural Engineering, ASCE*, 1–12. https://doi.org/10.1061/(ASCE)ST.1943-541X.0001715.

Baker, J. W. (2013). Efficient analytical fragility function fitting using dynamic structural analysis.

Camfield, F. E. (1980). *Tsunami Engineering. US Army. Special Report*.

Chandler, R. (2014). Classical Approaches for Statistical Inference in Model Calibration with Uncertainty. In K. Beven & J. Hall (Eds.), *Applied Uncertainty Analysis For Flood Risk Management* (p. pp.60-67). Imperial College Press, London.

Charvet, I. (2012). *Experimental Modelling of Long Elevated and Depressed Waves Using a New Pneumatic Wave Generator*.

Charvet, I., Eames, I., & Rossetto, T. (2013). New tsunami runup relationships based on long wave experiments. *Ocean Modelling*, *69*, 79–92. https://doi.org/10.1016/j.ocemod.2013.05.009

Charvet, I., Ioannou, I., Rossetto, T., Suppasri, A., & Imamura, F. (2014a). Empirical fragility assessment of buildings affected by the 2011 Great East Japan tsunami using improved statistical models. *Natural Hazards*. https://doi.org/10.1007/s11069-014-1118-3

Charvet, I., Ioannou, I., Rossetto, T., Suppasri, a., & Imamura, F. (2014b). Empirical fragility assessment of buildings affected by the 2011 Great East Japan tsunami using improved statistical models. *Natural Hazards*, *73*(2), 951–973. https://doi.org/10.1007/s11069-014-1118-3

Charvet, I., Suppasri, A., Kimura, H., Sugawara, D., & Imamura, F. (2015). Fragility estimations for Kesennuma City following the 2011 Great East Japan Tsunami based on maximum flow depths,velocities and debris impact, with evaluation of the ordinal model's predictive accuracy. *Natural Hazards*, *79*(3), 2073–2099. https://doi.org/10.1007/s11069-015-1947-8

Charvet, I., Suppasri, a., & Imamura, F. (2014). Empirical fragility analysis of building damage caused by the 2011 Great East Japan tsunami in Ishinomaki city using ordinal regression, and influence of key geographical features. *Stochastic Environmental Research and Risk Assessment*, *28*(7), 1853–1867. https://doi.org/10.1007/s00477-014-0850-2

Chock, G. (2014). The ASCE-7 Tsunami Loads and Effects Design Standard for the U.S. In M. Esteban, H. Takagi, & T. Shibayama (Eds.), *Coastal Disasters: Lessons Learnt for Engineers and Planners*. Elsevier, S&T Books.

Chock, G., Carden, L., Robertson, I., Olsen, M., & Yu, G. (2013). Tohoku Tsunami-Induced Building Failure Analysis with Implications for U.S. Tsunami and Seismic Design Codes. *Earthquake Spectra*, *29*(S1), S99–S126. https://doi.org/10.1193/1.4000113

Chock, G., & Robertson, I. (2013). Webinar: Development of Tsunami Design Provisions. NEES. Retrieved from https://nees.org/resources/6277/supportingdocs

Chock, G. Y. K. (2013). Development of Tsunami Structural Design Provisions for the USA. In *10th International Conference on Urban Earthquake Engineering*.

Chock, G. Y. K., Robertson, I. N., Kriebel, D., Francis, M., & Nistor, I. (2013). *Tohoku, Japan, Earthquake and Japan of 2011: Performance of Structures under Tsunami Loads*. ASCE. https://doi.org/DOI: http://dx.doi.org/10.1061/9780784412497

Chock, G. Y. K., Robertson, I., & Riggs, H. R. (2013). Tsunami Structural Design Provisions for a New Update of Building Codes and Performance-Based Engineering. In *ASCE 2011 Solutions to Coastal Disasters 2011 SOLUTIONS TO COASTAL DISASTERS 2011* (pp. 423–435). https://doi.org/10.1061/41185(417)38

Daniellsen, F. (2005). The Asian Tsunami: a protective role for Coastal Vegetation. *Science*, *310*.

De Risi, R., Goda, K., Mori, N., & Yasuda, T. (2016). Bayesian tsunami fragility modeling considering input data uncertainty. *Stochastic Environmental Research and Risk Assessment*. https://doi.org/10.1007/s00477-016-1230-x

De Risi, R., Goda, K., Yasuda, T., & Mori, N. (2017). Is flow velocity important in tsunami empirical fragility modeling? *Earth-Science Reviews*, *166*, 64–82. https://doi.org/10.1016/j.earscirev.2016.12.015

Dias, W. P. S., Yapa, H. D., & Peiris, L. M. N. (2009). Tsunami vulnerability functions from field surveys and Monte Carlo simulation. *Civil Engineering and Environmental Systems*, *26*(2), 181–194. https://doi.org/10.1080/10286600802435918

Dias, W., Yapa, H., & Peiris, N. (2009). Tsunami vulnerability functions from field surveys and Monte Carlo simulation. *Civil Engineering and Environmental Systems*, (26), p181-194.

Dominey-Howes, D Papathoma, M. (2006). Validating a tsunami vulnerability assessment model (the PTVA model) using field data from the 2004 Indian Ocean Tsunami. *Natural Hazards*, *40*(1), 113–136. https://doi.org/10.1007/s11069-006-0007-9

Ebrahimian, H., Jalayer, F., Lucchini, A., Mollaioli, F., & Manfredi, G. (2015). Preliminary ranking of alternative scalar and vector intensity measures of ground shaking. *Bulletin of Earthquake Engineering*. https://doi.org/10.1007/s10518-015-9755-9

EEFIT. (2010). *The Mw 8.8 Maule Chile Earthquake of 27th February 2010 a Preliminary Field*. Retrieved from http://www.istructe.org/webtest/files/75/75e4cc0c-34d9-4f40-b797-c80f40370e1a.pdf

EEFIT. (2011a). Field Report: Earthquake and Tsunami of 11th March 2011, (March).

EEFIT. (2011b). The Mw9.0 Tōhoku Earthquake and Tsunami of 11th March 2011: A Field Report by EEFIT.

EEFIT. (2013). *Field Report (Return Mission): Earthquake and Tsunami of 11th March 2011*.

FEMA. (n.d.). *Hazus –Hurricane Model - Technical Manual*. Retrieved from http://www.fema.gov/media-library-data/20130726-1820-25045-9850/hzmh2_1_hr_tm.pdf

FEMA. (2008). *Fema 646: Guidelines for Design of Structures for Vertical Evacuation from Tsunamis*. Retrieved from http://www.fema.gov/library/viewRecord.do?id=3463

FEMA. (2012). FEMA 646: Guidelines for Design of Structures for Vertical Evacuation from Tsunamis.

Foster, A. S. J., Rossetto, T., & Allsop, W. (2017). An experimentally validated approach for evaluating tsunami inundation forces on rectangular buildings. *Coastal Engineering*.

Foytong, P., Ruangrassamee, A., Lukkunaprasit, P., & Thanasisathit, N. (2015). Behaviours of reinforced-concrete building under tsunami loading. *IES J Part A: Civil Struct Eng*, *8*, 101–110. https://doi.org/http://dx.doi.org/10.1080/19373260.2015.1013998

Foytong, P., Ruangrassamee, A., Shoji, G., Hiraki, Y., & Ezura, Y. (2013). Analysis of Tsunami Flow Velocities during the March 2011 Tohoku, Japan, Tsunami. *Earthquake Spectra*, *29*(S1), S161–S181. https://doi.org/10.1193/1.4000128

Fraser, S., Raby, A., Pomonis, A., Goda, K., Chian, S. C., Macabuag, J., … Sammonds, P. (2012). Tsunami damage to coastal defences and buildings in the March 11th 2011 M w 9.0 Great East Japan earthquake and tsunami. *Bulletin of Earthquake Engineering*. https://doi.org/10.1007/s10518-012-9348-9

Fukuyama, H., Kato, H., & Ishihara, T. (2013). Categorization of Damage to Buildings Caused by the 3.11 Tsunami. In *14th U.S.-Japan Workshop on the Improvement of Structural Design and Construction Practices* (pp. 1–8). Retrieved from https://www.atcouncil.org/files/ATC-15-13/Papers/03_FUKUYAMApaper.pdf

Fukuyama, H., Kato, H., Ishihara, T., Tajiri, S., Tani, M., Okuda, Y., … Nakano, Y. (2012). Structural Design Requirement on the Tsunami Evacuation Buildings. In *14th U.S.-Japan Workshop on the Improvement of Structural Design and Construction Practices*. Retrieved from http://www.nehrp.gov/pdf/UJNR_2013_Tsunami_Manuscript.pdf

Giovenale, P., Cornell, C. A., & Esteva, L. (2004). Comparing the adequacy of alternative ground motion intensity measures for the estimation of structural responses. *Earthquake Engineering & Structural Dynamics*, *33*(8), 951–979. https://doi.org/10.1002/eqe.386

Goda, K., & Song, J. (2015). Uncertainty modeling and visualization for tsunami hazard and risk mapping: a case study for the 2011 Tohoku earthquake. *Stochastic Environmental Research and Risk Assessment*. https://doi.org/10.1007/s00477-015-1146-x

Gokon, H., Koshimura, S., & Matsuoka, M. (2009). Developing tsunami fragility curves for structural destruction in American Samoa. *Journal of Japan Society of Civil Engineers*. Retrieved from http://www.enveng.titech.ac.jp/midorikawa/rsdm2010_pdf/04_gokon_paper.pdf

Gomez-Gesteira, M. ., & Dalrymple, R. A. . (2004). Using a Three-Dimensional Smoothed Particle Hydrodynamics Method for Wave Impact on a Tall Structure. *Journal of Waterway, Port, Coastal and Ocean Engineering*, (April), 63–69. https://doi.org/10.1061/?ASCE?0733-950X?2004?130:2?63? CE

Government Office for Science. (2012). *Foresight Reducing Risks of Future Disasters: Priorities for Decision Makers*. Retrieved from http://reliefweb.int/sites/reliefweb.int/files/resources/12-1289-reducing-risks-of-future-disasters-report.pdf

Green, S. B. (2010). How Many Subjects Does It Take To Do A Regression Analysis. *Multivariate Behavioral Research*, (January 2015), 37–41. https://doi.org/10.1207/s15327906mbr2603

Guha-Sapir, D., Below, R., & Hoyois, P. (2015). EM-DAT: international disaster database. Retrieved from http://www.emdat.be/database

Hastie, T., & Tibshirani, R. (1990). *Generalized Additive Models*. Chapman & Hall/CRC

Monographs on Statistics & Applied Probability. Retrieved from http://www.amazon.co.uk/Generalized-Additive-Monographs-Statistics-Probability/dp/0412343908

Hayashi, S., Narita, Y., & Koshimura, S. (2013). Developing Tsunami Fragility Curves from the Surveyed Data and Numerical Modeling of the 2011 Tohoku Earthquake Tsunami (in Japanese). *Journal of Japan Society of Civil Engineers (Coastal Engineering)*, *69*, 1–5. https://doi.org/http://doi.org/10.2208/kaigan.69.I_386

Imamura, F., Gica, E., Takahashi, T., & Shuto, N. (1995). Numerical Simulation of the 1992 Flores Tsunami: Interpretation of Tsunami Phenomena in Northeastern Flores Island and Damage at Babi Island. *Pure and Applied Geophysics*, *144*, p555-568.

Ioannou, I., Rossetto, T., & Grant, D. N. (2012). Use of regression analysis for the construction of empirical fragility curves. In *15 World Conference on Earthquake Engineering*. Retrieved from http://www.iitk.ac.in/nicee/wcee/article/WCEE2012_2143.pdf

Japan Cabinet Office. (2005). *Tsunami Evacuation Building Guidelines (津波避難ビル等に係るガイドライン)*. Retrieved from http://www.bousai.go.jp/kohou/oshirase/h17/pdf/guideline.pdf

Japan Cabinet Office. (2013). *Residential Disaster Damage Accreditation Criteria Operational Guideline.pdf*. Retrieved from http://www.bousai.go.jp/taisaku/unyou.html

Karafaglial, S., Fotopoulou, S., & Pitilakis, K. (2017). Tsunami fragility curves for seaport buildings and warehouses.

Kelman, I., & Spence, R. (2004). An overview of flood actions on buildings. *Engineering Geology*, *73*(3–4), 297–309. https://doi.org/10.1016/j.enggeo.2004.01.010

Kircher, C. A., & Bouabid, J. (2014). New Building Damage and Loss Functions for Tsunami. In *10th International Conference on Urban Earthquake Engineering*.

Koshimura, S., & Gokon, H. (2012). Structural vulnerability and tsunami fragility curves from the 2011 Tohoku earthquake tsunami disaster. *Journal of Japan Society of Civil Engineers, Ser. B2 (Coastal Engineering)*, *68*(2), I_336-I_340. https://doi.org/10.2208/kaigan.68.I_336

Koshimura, S., & Kayaba, S. (2010). Tsunami fragility inferred from the 1993 Hokkaido Nansei-oki earthquake tsunami disaster. *Journal of Japan Association for Earthquake Engineering*, *10*(3), 87–101. Retrieved from https://www.jstage.jst.go.jp/article/jaee/10/3/10_3_3_87/_article/-char/ja/

Koshimura, S., Oie, T., Yanagisawa, H., & Imamura, F. (2009). Developing fragility functions for tsunami damage estimation using numerical model and post-tsunami data from banda aceh, indonesia. *Coastal Engineering Journal, , Japan Society of Civil Engineering*, *51*(3), 243–273.

Kreibich, H., Piroth, K., Seifert, I., Maiwald, H., Kunert, U., Schwarz, J., … Thieken, a. H. (2009). Is flow velocity a significant parameter in flood damage modelling? *Natural Hazards and Earth System Science*, *9*(5), 1679–1692. https://doi.org/10.5194/nhess-9-1679-2009

Kriebel, D. L., Lynett, P. J., Cox, D. T., Petroff, C., Robertson, I. N., & Chock, G. Y. K. (2017). Energy Method for Approximating Overland Tsunami Flows. *Journal of Waterway, Port, Coastal and Ocean Engineering*, *143*(5). https://doi.org/https://doi.org/10.1061/(ASCE)WW.1943-5460.0000393#sthash.WXoVTfrP.dpuf

Leelawat, N., Suppasri, A., Charvet, I., & Imamura, F. (2014). Building damage from the 2011 Great East Japan tsunami: quantitative assessment of influential factors. *Natural Hazards*, *73*(2), 449–471. https://doi.org/10.1007/s11069-014-1081-z

Lloyd, T. O. (2014). *An experimental investigation of tsunami forces on coastal structures*. University College London.

Luco, N., & Cornell, C. A. (2007). Structure-Specific Scalar Intensity Measures for Near-Source and Ordinary Earthquake Ground Motions. *Earthquake Spectra*, *23*(2), 357–392. Retrieved from http://www.earthquakespectra.org/doi/abs/10.1193/1.2723158

Lukkunaprasit, P., Ruangrassamee, A., & Thanasisathit, N. (2008). Tsunami loading on buildings

with openings. In *14th World Conference on Earthquake Engineering*.

Lukkunaprasit, P., Thanasisathit, N., & Yeh, H. (2009). Experimental Verification of FEMA P646 Tsunami Loading. *Journal of Disaster Research*, *4*(6), 45–53. Retrieved from http://www.fujipress.jp/finder/xslt.php?mode=present&inputfile=DSSTR000400060005.xml

Lynett, P., Borrero, J., Liu, P., & Synolakis, C. (2003). Field survey and numerical simulations: a review of the 1998 Papua New Guinea tsunami. *Pure and Applied Geophysics*, *160*, p21119-2146.

Macabuag, J., & Rossetto, T. (2014). Towards the Development of a Method for Generating Analytical Tsunami ragility Functions. In *2nd European Conference on Earthquake Engineering and Seismology*.

Macabuag, J., Rossetto, T., & Ioannou, I. (2016). Investigation of the Effect of Debris-Induced Damage for Constructing Tsunami Fragility Curves for Buildings. In *1st International Conference on Natural Hazards & Infrastructure*. Chania, Greece.

Macabuag, J., Rossetto, T., Ioannou, I., Suppasri, A., Sugawara, D., Adriano, B., … Koshimura, S. (2016). A proposed methodology for deriving tsunami fragility functions for buildings using optimum intensity measures. *Natural Hazards*, *84*(2). https://doi.org/10.1007/s11069-016-2485-8

Macabuag, J., Rossetto, T., & Lloyd, T. (2014). Structural Analysis for the Generation of Tsunami fragility functions. In *Proceedings of the 10th National Conference in Earthquake Engineering*. https://doi.org/10.4231/D3JH3D34N

Macabuag, J., Rossetto, T., & LLoyd, T. (2014a). Sensitivity Analysis of a Framed Structure Under Several Tsunami Design-Guidance Loading Regimes. In *2nd European Conference on Earthquake Engineering and Seismology*. Istanbul.

Macabuag, J., Rossetto, T., & LLoyd, T. (2014b). Structural Aanalysis for the Generation of Analytical Tsunami Fragility Functions. In *10th International Conference on Urban Earthquake Engineering*.

Maruyama, Y., Kitamura, K., & Yamazaki, F. (2013). Tsunami damage assessment of buildings in Chiba Prefecture , Japan using fragility function developed after the 2011 Tohoku-Oki Earthquake. In E. & F. Deodatis (Ed.), *Safety, Reliability, Risk and Life-Cycle Performance of Structures & Infrastructures*. Taylor & Francis. Retrieved from http://ares.tu.chiba-u.jp/~papers/paper/2013/2013ICOSSAR_Maruyama.pdf

Mas, E., Koshimura, S., Suppasri, A., Matsuoka, M., Matsuyama, M., Yoshii, T., … Imamura, F. (2012). Developing Tsunami fragility curves using remote sensing and survey data of the 2010 Chilean Tsunami in Dichato. *Natural Hazards and Earth System Science*, *12*(8), 2689–2697. https://doi.org/10.5194/nhess-12-2689-2012

Masuda, M., Williams, C., Shahkarami, A., Rafique, F., & Bryngelson, J. (2012). Tsunami Vulnerability Function Development Based on the 2011 Tohoku Earthquake in Japan. In *15 World Conference on Earthquake Engineering*.

Meslem, A., & Ayala, D. D. (2012). Toward Worldwide Guidelines for the Development of Analytical Vulnerability Functions and Fragility. In *15 World Conference on Earthquake Engineering* (Vol. 2001).

MLIT. (2011a). *Concerning Setting the Safe Structure Method for Tsunamis which are Presumed when Tsunami Inundation Occurs - Note 1318*.

MLIT. (2011b). *Further Information Concerning the Design Method of Safe Buildings that are Structurally Resistant to Tsunamis - Technical Advice No. 2570.pdf*.

MLIT. (2011c). *Further Information Concerning the Design Method of Safe Buildings that are Structurally Resistant to Tsunamis - Technical Advice No. 2570.pdf*.

Muhari, A., Charvet, I., Tsuyoshi, F., Suppasri, A., & Imamura, F. (2015). Assessment of tsunami hazards in ports and their impact on marine vessels derived from tsunami models and the observed damage data. *Natural Hazards*. https://doi.org/10.1007/s11069-015-1772-0

Muhari, a., Imamura, F., Koshimura, S., & Post, J. (2011). Examination of three practical run-up models for assessing tsunami impact on highly populated areas. *Natural Hazards and Earth*

System Science, *11*(12), 3107–3123. https://doi.org/10.5194/nhess-11-3107-2011

Murao, O., & Nakazato, H. (2010). Vulnerability Functions for Buildings Based on Damage Survey Data in Sri Lanka After the 2004 Indian Ocean Tsunami. In *International Conference on Sustainable Built Environment (ICSBE-2010) Kandy,* (pp. 371–378). Retrieved from http://www.civil.mrt.ac.lk/ICSBE_2010/vol_02/55.pdf

Nanayakkara, K. I. U., & Dias, W. P. S. (2016). Fragility curves for structures under tsunami loading. *Natural Hazards*, *80*(1), 471–486. https://doi.org/10.1007/s11069-015-1978-1

Narita, Y., & Koshimura, S. (2015). Classification of Tsunami Fragility Curves Based on Regional Characteristics of Tsunami Damage. *Journal of Japan Society of Civil Engineers (Coastal Engineering)*, *71*(2), 331–336. https://doi.org/http://doi.org/10.2208/kaigan.71.I_331

National Geophysical Data Center NOAA (National Oceanic and Atmospheric Administration). (n.d.). National Geophysical Data Center / World Data Service (NGDC/WDS): Global Historical Tsunami Database. https://doi.org/doi:10.7289/V5PN93H7

Nihei, Y., Maekawa, T., Ohshima, R., & Yanagisawa, M. (2012). Evaluation of Fragility Functions for Tsunami Damage in Coastal District in Natori City , Miyagi Prefecture and Mitigation Effects of Coastal Dune. *Journal of Japan Society of Civil Engineers*, *68*(2), I_276-I_280. Retrieved from https://www.jstage.jst.go.jp/article/kaigan/68/2/68_I_276/_pdf

Nistor, I., Palermo, D., Cornett, A., & Al-Faesly, T. (2010). Experimental and Numerical Modeling of Tsunami Loading on Structures. *Coastal Engineering Proceedings*, *32*, 1–14. https://doi.org/http://dx.doi.org/10.9753/icce.v32.currents.2

Nistor, I., Palermo, D., Nouri, Y., & Murty, T. (2004). Tsunami-Induced Forces on Structures. In Y. C. Kim (Ed.), *Handbook of Coastal and Ocean Engineering* (pp. 261–286). World Scientific Publishing Co. Pte. Ltd. Retrieved from http://www.scribd.com/doc/77272681/3/Tsunami-Induced-Forces-on-Structures

Nouri, Y. (2008). *The Impact of Hydraulic Bores and Debris on Free Standing Structures*. University of Ottawa.

Nouri, Y., Nistor, I., Palermo, D., & Cornett, A. (2010). Experimental Investigation of Tsunami Impact on Free Standing Structures. *Coastal Engineering Journal*, *52*(1), 43–70. https://doi.org/10.1142/S0578563410002117

Okada, T., Sugano, T., Ishikawa, T., Ohgi, T., Takai, S., & Hamabe, C. (2004). *Structural Design Method of Buildings for Tsunami Resistance*. Retrieved from http://www.bcj.or.jp/src/c06_course/bltr/2004/bltr465.pdf

Palermo, D., Nistor, I., Nouri, Y., & Cornett, A. (2009). Tsunami loading of near-shoreline structures: a primer. *Canadian Journal of Civil Engineering*, *36*(11), 1804–1815. https://doi.org/10.1139/L09-104

Papathoma, M., Dominey-Howes, D., Zong, Y., & Smith, D. (2003). Assessing tsunami vulnerability, an example from Herakleio. *Natural Hazards and Earth System Science*, *3*, p377-389.

Park, H., Cox, D. T., Lynett, P. J., Wiebe, D. M., & Shin, S. (2013). Tsunami inundation modeling in constructed environments: A physical and numerical comparison of free-surface elevation, velocity, and momentum flux. *Coastal Engineering*, *79*, 9–21. https://doi.org/10.1016/j.coastaleng.2013.04.002

Park, H., Wiebe, D., Cox, D., & Cox, K. (2014). Tsunami Inundation Modeling: Sensitivity of Velocity and Momentum Flux to Bottom Friction With Application to Building Damage at Seaside, Oregon. *Coastal Engineering*, 1–12. Retrieved from https://icce-ojs-tamu.tdl.org/icce/index.php/icce/article/view/7557/pdf_985

Park, S., Lindt, J. W. Van De, Cox, D., & Gupta, R. (2013). Concept of Community Fragilities for Tsunami Coastal Inundation Studies. *Natural Hazards Review*, 220–228. https://doi.org/10.1061/(ASCE)NH.1527-6996.0000092.

Park, S., van de Lindt, J. W., Cox, D., Gupta, R., & Aguiniga, F. (2012). Successive Earthquake-Tsunami Analysis to Develop Collapse Fragilities. *Journal of Earthquake Engineering*, *16*(6), 851–863. https://doi.org/10.1080/13632469.2012.685209

Peiris, N. (2006). Vulnerability functions for tsunami loss estimation. In *First European Conference on Earthquake Engineering and Seismology*.

Petrone, C., Rossetto, T., & Goda, K. (2017). Fragility assessment of a RC structure under tsunami actions via nonlinear static and dynamic analyses. *Engineering Structures*.

Pomonis, A., & Peiris, N. (2005). December 26 , 2004 Indian Ocean Tsunami: Vulnerability Functions for Loss Estimation in Sri Lanka. In *International Conference on Geotechnical Engineering for Disaster Mitigation & Rehabilitation* (pp. 411–416).

Pringle, W., & Yoneyama, N. (2013). The Application of a Hybrid 2D / 3D Numerical Tsunami Inundation-Propagation Flow Model to the 2011 off the Pacific Coast of Tohoku Earthquake Tsunami. *Journal of Japan Society of Civil Engineers (Coastal Engineering)*, *63*(2), 3–7. Retrieved from file:///C:/Users/cege-lpt/Documents/Engineering/2.0 Research/2.1 EngD/2.1.5 Resources/Wave & Inundation Modelling/Pringle. W,2013, Hybrid 2D 3D fluid modelling.pdf

Qi, Z. X., Eames, I., & Johnson, E. R. (2014). Force acting on a square cylinder fixed in a free-surface channel flow. *Journal of Fluid Mechanics*, *756*, 716–727. https://doi.org/10.1017/jfm.2014.455

Rabinovich, A., & Thomson, R. (2007). The 26 December 2004 Sumatra Tsunami: Analysis of Tide Gauge Data from the World Ocean Part 1. Indian Ocean and South Africa. *Pure and Applied Geophysics*, *164*, p261-308.

R Development Core Team. (2008). *R: A language and environment for statistical computing*. Vienna, Austria. Retrieved from http://www.r-project.org.

Reese, S., Bradley, B. a., Bind, J., Smart, G., Power, W., & Sturman, J. (2011). Empirical building fragilities from observed damage in the 2009 South Pacific tsunami. *Earth-Science Reviews*, *107*(1–2), 156–173. https://doi.org/10.1016/j.earscirev.2011.01.009

Robertson, I. N., Chock, G., & Carden, L. (2014). *Tsunami Design Examples*.

Robertson, I. N., & Riggs, H. R. (2011). OMAE2011-49487 Tsunami Bore Forces on Walls. In *Proceedings of the ASTM 2011 30th Internal Conference on Ocean, Offshore and Arctic Engineering*.

Robertson, I. N., Riggs, H. R., & Mohamed, A. (2008). OMAE2008-57525 Experimental Results of Tsunami Bore Forces on Structures. In *Proceedings of the ASTM 2011 30th Internal Conference on Ocean, Offshore and Arctic Engineering* (pp. 1–9).

Rossetto, T. (2013). Presentation: Engineering Resilience in Earthquake Scenarios. University College London.

Rossetto, T., Allsop, W., Charvet, I., & Robinson, D. I. (2011). Physical modelling of tsunami using a new pneumatic wave generator. *Coastal Engineering*, *58*(6), 517–527. https://doi.org/10.1016/j.coastaleng.2011.01.012

Rossetto, T., & Elnashai, A. (2005). A new analytical procedure for the derivation of displacement-based vulnerability curves for populations of RC structures. *Engineering Structures*, *27*(3), 397–409. https://doi.org/10.1016/j.engstruct.2004.11.002

Rossetto, T., Ioannou, I., & Grant, D. (2012). *Guidelines for empirical vulnerability assessment - Phase I: Single surveys*.

Rossetto, T., Ioannou, I., Grant, D. N., & Maqsood, T. (2014). *Guidelines for Empirical Vulnerability Assessment Report produced in the context of the Vulnerability Global Component project*. Retrieved from http://www.nexus.globalquakemodel.org/gem-vulnerability/posts/guidelines-for-empirical-vulnerability-assessment

Ruangrassamee, A., Yanagusawa, H., Foytong, P., & Al., E. (2006). Investigation of tsunami-induced damage and fragility of buildings in Thailand after the December 2004 Indian Ocean tsunami. *Earthquake Spectra*, *22*(S3), p377-401. https://doi.org/10.1193/1.2208088

Satake, K. (1995). Linear and Non Linear Computations of the 1992 Nicaragua Earthquake Tsunami. *Pure and Applied Geophysics*, *144*.

Satake, K., Fujii, Y., Harada, T., & Namegaya, Y. (2013). Time and Space Distribution of

Coseismic Slip of the 2011 Tohoku Earthquake as Inferred from Tsunami Waveform Data. *Bulletin of the Seismological Society of America*, *103*(2B), 1473–1492. https://doi.org/10.1785/0120120122

Scott, M. H., & Mason, H. B. (2017). Constant-ductility response spectra for sequential earthquake and tsunami loading. *Earthquake Engineering & Structural Dynamics*, *46*(9), 1549–1554. https://doi.org/10.1002/eqe.2871

Siripong, A. (2006). Andaman Seacoast of Thailand Field Survey after the December 2004 Indian Ocean Tsunami. *Earthquake Spectra*, *22*, p187-202.

Suppasri, A., Charvet, I., Imai, K., & Imamura, F. (2014). Fragility curves based on data from the 2011 Great East Japan tsunami in Ishinomaki city with discussion of parameters influencing building damage. *Earthquake Spectra*, *31*(2), 841–868. Retrieved from http://earthquakespectra.org/doi/pdf/10.1193/053013EQS138M

Suppasri, A., Koshimura, S., & Imamura, F. (2009). Tsunami fragility curves and structural performance of building along the Thailand coast. In *8th International Workshop on Remote Sensing for Disaster Management* (pp. 3–8).

Suppasri, A., Koshimura, S., & Imamura, F. (2011). Developing tsunami fragility curves based on the satellite remote sensing and the numerical modeling of the 2004 Indian Ocean tsunami in Thailand. *Natural Hazards and Earth System Science*, *11*(1), 173–189. https://doi.org/10.5194/nhess-11-173-2011

Suppasri, A., Mas, E., Charvet, I., Gunasekera, R., Imai, K., Fukutani, Y., … Imamura, F. (2012). Building damage characteristics based on surveyed data and fragility curves of the 2011 Great East Japan tsunami. *Natural Hazards*, *66*(2), 319–341. https://doi.org/10.1007/s11069-012-0487-8

Suppasri, A., Mas, E., Charvet, I., Gunasekera, R., Imai, K., Fukutani, Y., … Imamura, F. (2013). Building damage characteristics based on surveyed data and fragility curves of the 2011 Great East Japan tsunami. *Natural Hazards*, *66*(2), 319–341. https://doi.org/10.1007/s11069-012-0487-8

Suppasri, A., Mas, E., Koshimura, S., Imai, K., Harada, K., & Imamura, F. (2012a). Developing Tsunami Fragility Curves From the Surveyed Data of the 2011 Great East Japan Tsunami in Sendai and Ishinomaki Plains. *Coastal Engineering Journal*, *54*(1), 1250008–1. https://doi.org/10.1142/S0578563412500088

Suppasri, A., Mas, E., Koshimura, S., Imai, K., Harada, K., & Imamura, F. (2012b). Developing Tsunami Fragility Curves From the Surveyed Data of the 2011 Great East Japan Tsunami in Sendai and Ishinomaki Plains. *Coastal Engineering Journal*, *54*(1). https://doi.org/10.1142/S0578563412500088

Takabatake, D., & Kihara, N. (2014). Revisit the Tsunami Hydrodynamic Force on the Front Face of Onshore Structures. *Coastal Engineering Proceedings*, *34*, 1–6. Retrieved from https://icce-ojs-tamu.tdl.org/icce/index.php/icce/article/view/7659/pdf_852

Tanaka, N., & Kondo, K. (2015). Fragility curve of region of wooden building washout due to tsunami based on hydrodynamic characteristics of the Great East Japan Tsunami. *Ocean Engineering*.

Tanaka, N., Onai, A., & Kondo, K. (2015). Fragility Curve of Different Damage of Wooden Building Due To Tsunami Based on Tsunami Fluid Force and its Moment (in Japanese). *Journal of Japan Society of Civil Engineers (Coastal Engineering)*, *71*(1), 1–11. https://doi.org/http://doi.org/10.2208/kaigan.71.1

Tarbotton, C., Dall'Osso, F., Dominey-Howes, D., & Goff, J. (2015). The use of empirical vulnerability functions to assess the response of buildings to tsunami impact: Comparative review and summary of best practice. *Earth-Science Reviews*, *142*, 120–134. https://doi.org/10.1016/j.earscirev.2015.01.002

Tinti, S., Tonini, R., Bressan, L., Armigliato, A., Gardi, A., Guillande, R., … Scheer, S. (2011). *Handbook of Tsunami Hazard and Damage Scenarios (EUR 24691 EN)*. https://doi.org/10.2788/21259

Tokyo University, & BRI. (2011). *Interim report of the Building Standards Improvement promotion*

project No.40, A study of Improvement of Building Standards etc in the tsunami critical areas. Retrieved from http://www.mlit.go.jp/common

Valencia, N., Gardi, A., Gauraz, A., Leone, F., & Guillande, R. (2011). New tsunami damage functions developed in the framework of SCHEMA project: application to European-Mediterranean coasts. *Natural Hazards and Earth System Science*, *11*, p2835-2846.

Ware, J. H., Harrington, D., Hunter, D. J., & D'Agostino, R. B. (2012). Missing Data. *New England Journal of Medicine*, *367*(14), 1353–1354. https://doi.org/10.1056/NEJMsm1210043

Wilson, L. I., Dengler, L. A., Legg, M. R., Long, K., & Miller, K. M. (2010). The 2010 Chilean tsunami on the California Coastline.

Yanagisawa, H., & Yanagisawa, H. (2012). Fragility Function of House Damage by the 2011 off the Pacific Coast of Tohoku Earthquake Tsunami. *Journal of Japan Society of Civil Engineers, Ser. B2 (Coastal Engineering)*, *68*(2), I_1401-I_1405. https://doi.org/10.2208/kaigan.68.I_1401

Yeh, H. (2007). Design Tsunami Forces for Onshore Structures, *2*(6), 531–536.

Yeh, H., Barbosa, A. R. ., Ko, H., & Cawley, J. G. (2014). TSUNAMI LOADINGS ON STRUCTURES: REVIEW AND ANALYSIS. *Coastal Engineering Proceedings*, *34*. https://doi.org/http://dx.doi.org/10.9753/icce.v34.currents.4

Yeh, H., Robertson, I., & Preuss, J. (2005). *Development of design guidelines for structures that serve as tsunami vertical evacuation sites*. Retrieved from http://nctr.pmel.noaa.gov/tsu400/documents/Course_3_Day_3/Session_8/ofr05-4.pdf

Appendices

Contents

A. Statistical Modelling

A.1 Representing Damage and Intensity Data

Data may be collected describing the damage state and corresponding intensity (e.g. inundation depth) for a number of buildings. Considering a single damage state (e.g. collapse) this building-by-building data represents a binary dataset (did the building collapse, yes or no?), which can be represented graphically as shown by the datapoints of the left-hand image of Figure A.1. The general fragility function shown attempts to describe the trend in the data.

In some studies (I. Charvet, Ioannou, Rossetto, et al., 2014a) only aggregated data is available, describing the numbers of buildings within a series of TIM ranges (or bins) for each damage state (e.g. for 1m<inundation depth<1.5m, 55 buildings were damaged to DS4 etc. For an example dataset see the appendix). Note that this is generally the form of available data for seismic fragility functions, and so much of the tsunami analysis derived from seismic analysis assumes aggregated datasets. The right-hand graph of Figure A.1 shows example aggregated data and the corresponding general fragility function. The process of aggregation reduces the accuracy of the data (e.g. the exact TIM value of each datapoint will instead be rounded to the median of whichever TIM bin it falls within).

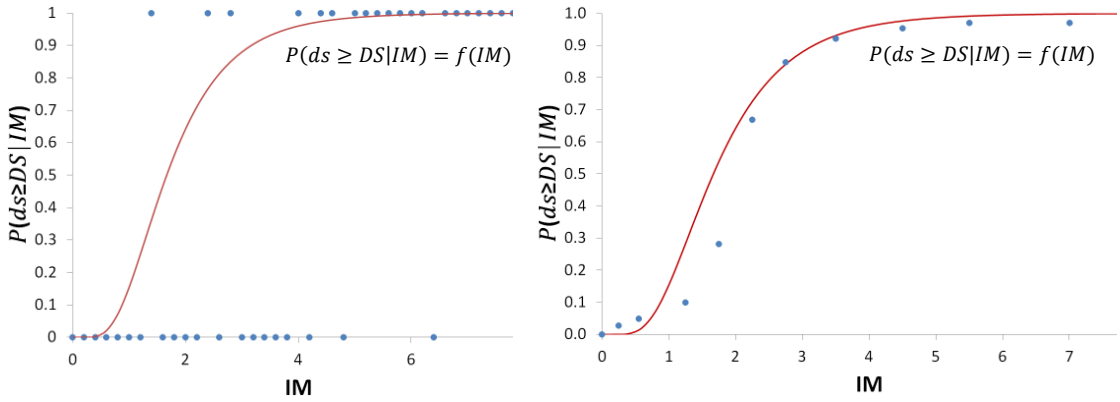

Figure A.1: An example fragility function for a single damage state (e.g. collapse). The left-hand image shows disaggregated (building-by-building) data (P=1 represents collapse, P=0 represents non-collapse). The right-hand image shows aggregated data (P represents the proportion of buildings within each TIM range which have collapsed. E.g. in the range 1<TIM<1.5 15% of buildings, say, have collapsed).

A.2 Representing Fragility Functions

The main types of statistical models used in the literature are as follows:

- Parametric Models:
  - Standard linear regression models, with Ordinary Least Squares (OLS) parameter estimation (Anawat Suppasri et al., 2009; Anawat Suppasri, Mas, Koshimura, et al., 2012b; Tanaka & Kondo, 2015).
  - Generalized Linear Models (GLMs) (I Charvet, Suppasri, Kimura, et al., 2014; Leelawat, Suppasri, Charvet, & Imamura, 2014a; Muhari, Charvet, Tsuyoshi, Suppasri, & Imamura, 2015; Stefan Reese et al., 2011).
- Non-parametric models (Masuda et al., 2012).

For parametric models (i.e. algebraic functions defined by several model parameters, or coefficients), fragility functions are often represented as standard cumulative distribution functions (CDFs) of known distributions. The majority of the existing empirical fragility functions presented in the appendix are presented as either normal (also known as Gaussian) or lognormal cumulative distribution functions (Table A.1).

Normal CDF	**Lognormal CDF**
$P(ds \geq DS\|IM) = \Phi\left[\frac{IM - \mu}{\sigma}\right]$	$P(ds \geq DS\|IM) = \Phi\left[\frac{\log(IM) - \mu}{\sigma}\right]$

Table A.1: Fragility functions expressed as normal and lognormal Cumulative Distribution Functions. Φ is the Normal (Gaussian) CDF function. The fragility function is entirely defined by the two model parameters (*μ* and *σ*).

The use of Normal or Log-Normal CDFs has strong precedent in seismic risk analysis (Porter, Kennedy, & Bachman, 2007) and Rossetto et al. (2012) notes that the lognormal CDF may be appropriate due to the following three properties of the distribution:

- The lognormal CDF is constrained in the *y*-axis between [0, 1]
  - I.e. it is always true that: $0 < P(ds \geq DS|IM) < 1$.
- The lognormal CDF is constrained in the *y*-axis between [0, +∞]
  - I.e. it is always true that the TIM (e.g. inundation depth) is non-negative.
- This distribution appears to be skewed to the left, and thus it can provide a better estimate for the smaller TIM values (where typically the majority of the data lies).

Non-parametric models are not represented as algebraic functions. They will be discussed below.

A.2.1 Standard Linear Regression Models

A.2.1.1 General Form

A linear regression model assumes that the relationship between the mean of a response variable (also known as dependent variable, *y*) and *I* explanatory variables (also known as predictors or independent variables, x_i or an *n*-length vector *X*) is linear. As shown in equation (A.1), this is represented by a linear combination of the products of the explanatory variables and regression coefficients (also known as model parameters, β_i or vector β) plus an error term (an unobserved random variable, ϵ).

$$\mathrm{Y} = \beta_0 + \sum_i^I \beta_i x_i + \varepsilon \qquad \textbf{(A.1)}$$

A.2.1.2 Parameter Estimation: Ordinary Least Squares

A standard method for estimating the regression coefficients is Ordinary Least Squares (OLS, also known as linear least squares), which consists of minimizing the sum of the squared errors (i.e. the difference, measured on the y-axis, between the data points and the theoretical curve to be fitted, Equation (A.2)) to define a function (or curve if only using a single predictor) such that the data is normally distributed about the mean (or curve). The majority of existing fragility functions utilize this method.

$$\hat{\beta} = \min_{\beta} \sum \left[Y_{observed} - \left(\beta_0 + \sum_i^I \beta_i x_i \right) \right]^2 \qquad \textbf{(A.2)}$$

A.2.1.3 Assumptions

Linear regression models with regression coefficients estimated by OLS rely on the following assumptions:

1. Linearity

2. The **errors** are:
    a. Normally distributed
    b. Average to zero
    c. Have a constant variance (homoscedasticity)
    d. Independent of each other
    e. Spatially independent.
3. The predictors (values of X) are measured without errors, and are non-random.
4. The observations are equally reliable.

Violating these assumptions would lead to a non-optimal model (i.e. information is not captured), bias in the parameters (i.e. bad precision), and an impossibility of drawing inferences (i.e. confidence intervals).

A.2.1.4 Application to Fragility Functions

For fragility functions, it is necessary to estimate the model parameters (μ and σ) shown in Table A.1. Several studies (e.g. Suppasri et al. 2009; Gokon et al. 2010; Koshimura et al. 2009; Park et al. 2013), use a method of linearization previously used in seismic fragility function analysis set out by Porter et al. (2007):

1. Aggregate the data (Figure A.2, left-hand graph).
2. Linearize the model equation (Table A.1) to obtain a function in the form of Equation (A.1).
3. Use OLS to estimate the model parameters (i.e. fit a straight line to the transformed aggregated data) (Figure A.3, central graph).
4. Draw the fragility function CDF in probability-space (Figure A.4, right-hand graph).

Normal CDF	**Lognormal CDF**
$IM = \mu + \sigma.\Phi^{-1}[P(ds \geq DS\|IM)]$	$\ln IM = \mu + \sigma.\Phi^{-1}[P(ds \geq DS\|IM)]$

Table A.2: Linearized fragility function expressions.

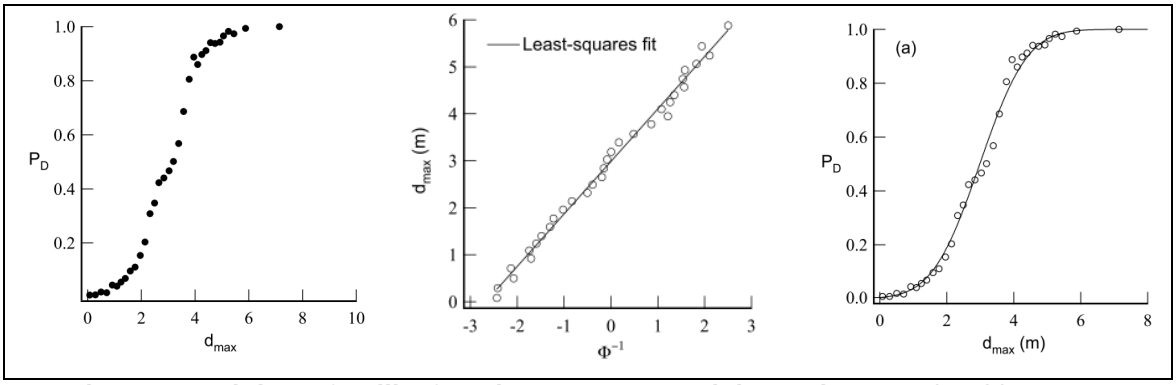

Figure A.5: Fitting a fragility function to aggregated data using OLS (Koshimura, Namegaya, et al., 2009)**.**

For data consisting of multiple damage states, this process can be repeated for each damage state, where the binary data for each building indicates damage state exceedance.

A.2.1.5 Disadvantages of OLS for Fragility Function Derivation

The method shown in Figure A.5 cannot be used for disaggregated data as the inverse normal distribution function is undefined at 0 and 1. Therefore data must be aggregated, as shown. This results in information being lost (e.g. data distributions within TIM bins

are no longer accounted for), increasing the uncertainty in the model. Furthermore, data aggregation does not prevent probabilities of 0 and 1 from appearing in the dataset, corresponding to bins for which all buildings either fall above or below the specific damage state. Some studies vary the bin widths in order to obtain a constant number of buildings in each bin, others simply dismiss the corresponding data points, therefore losing some data. The results are sensitive to the bin sizes chosen. Furthermore, each datapoint of the aggregated dataset represents data from varying numbers of buildings. However, this is not accounted for in the OLS regression methodology, meaning that all datapoints are given the same weighting, whether they correspond to a small or large number of buildings (e.g. P=0.5 if 1 of 2 buildings exceed the given damage state, or if 400 of 800 buildings exceed the given damage state). Therefore, outliers corresponding to small numbers of buildings can have a significant effect on the results, dependent on the selection of bin widths. This highlights also that the results are sensitive to the selection of bin-widths, a somewhat arbitrary user-decision which varies between studies.

Damage state data is either binary (true or false, when considering damage state exceedance for a given damage state) or categorical (each building is categorizes as either damage state 1, 2, 3 etc). Linear regression assumes normally distributed responses, but binary or categorical variables cannot be normally distributed (they are instead categorized by Bernoulli, Binomial or Multinomial distributions). In addition, the OLS methodology generates separate fragility functions for each damage state, so does not account for the ordinal, categorical nature of damage data, which can result in fragility functions crossing, so giving results that cannot be interpreted.

When using parametric regression, assumptions should be systematically validated as part of the regression analysis. If these assumptions are not met then the error and variance between the regressed curve and the true population trends will be larger for this model than for other models. The OLS model assumptions are rarely investigated in the various studies in the appendix.

A.2.2 Generalized Linear Model (GLM)

A.2.2.1 General Form

GLMs have been employed in some recent studies (I. Charvet, Suppasri, & Imamura, 2014; Leelawat, Suppasri, Charvet, & Imamura, 2014b; Muhari et al., 2015; Stefan Reese et al., 2011) as they overcome many of the shortcomings of OLS linear regression models outlined above. In particular they are suitable for binomial, multinomial and ordered response variables, which is the case for building damage data.

GLMs relate the mean of a response variable ($E(y)=\mu$) to the explanatory variables (x_i) via an arbitrary link function (g). The link function is selected dependent on the distribution of the response variable, typically transforming the response such that $g(\mu)$ is a continuous variable bounded by $[-\infty,+\infty]$. As such, GLMs can be used for variables with distributions other than the Gaussian distribution assumed in OLS linear regression models.

GLM models have three components:

- A link function (which transforms the mean of the response variable, Table A.3)

- A systematic component (the linear predictor (η) describing the mean of the response variable, via the link function, Equation (A.3)).
- A random component (the error distribution of the response variable, e.g. binomial for the case of binary data).

$$g(\mu) = \beta_0 + \sum_i^I \beta_i x_i + \varepsilon \quad \textbf{(A.3)}$$

Probit	Logit	cloglog
$g(\mu) = \Phi^{-1}(\mu)$	$g(\mu) = log\left(\frac{\mu}{1-\mu}\right)$	$g(\mu) = log(-log(1-\mu))$

Table A.3: Typical link functions suitable for use in fragility function derivation.

A.2.2.2 Parameter Estimation: Maximum Likelihood

Maximum-likelihood Estimation (MLE) is a method of estimating the parameters of a statistical model so as to maximize the "agreement" of the selected model with the observed data (Mc Cullagh & Nelder, 1989; Myung, 2003).

Consider the example of aggregated building damage data for the single damage state of collapse, where *n* collapses are observed from *N* buildings within TIM bin *j*. This is a binomial trial (n_j observations denoted by "success" or "failure", of N_j trials), and so the probability (*P*) of seeing the obtained observation for this TIM bin is denoted by the binomial distribution (Equation (A.4)).

For each TIM bin *j*:

$$P(observing\ n_j\ collapses\ out\ of\ N_j\ buildings) = \binom{N_j}{n_j} p_{collapse,j}^{n_j} (1 - p_{collapse,j})^{N_j - n_j} \quad \textbf{(A.4)}$$

Where: $\binom{N}{n}$ are the binomial coefficients, expressed as $\frac{N!}{n!(N-n)!}$,

$p_{collapse}$ is the probability that a particular building will collapse at the given TIM, I.e. $p_{collapse,j} = P(ds \geq DS_{collapse} | IM_j)$.

For *J* TIM bins, the likelihood of seeing all of the observations obtained for each TIM bin (i.e. the intersection of the independent observations at each of *J* TIM bins, denoted $P\left(\binom{N_1}{n_1} \cap \binom{N_2}{n_2} \cap \ldots \cap \binom{N_j}{n_j}\right)$) is defined as the product of the likelihoods for each bin, giving the likelihood function (Equation (A.5)).

$$Likelihood = \prod_{j=1}^{J} \binom{N_j}{n_j} p_{collapse,j}^{n_j} (1 - p_{collapse,j})^{N_j - n_j} \quad \textbf{(A.5)}$$

The aim of a fragility function for the collapse damage state is to define the probability of a building collapsing for a given TIM (i.e. to define $p_{collapse}$ in Equation (A.5)). Maximum likelihood states that the most likely value of $p_{collapse}$ is one which gives the maximum probability of seeing all of the obtained observations. This requires an expression for $p_{collapse}$ ($p_{collapse}$ = f(*TIM*)) and then the application of optimization techniques to maximize the likelihood function and so estimate the parameters of $p_{collapse}$.

For the example of a probit link function, the collapse probability is denoted as shown in Table A.1. Substituting this expression for collapse probability into Equation (A.5), shows that the expected model parameters ($\hat{\mu}$, $\hat{\sigma}$) are obtained by solving Equation (A.6).

$$\{\hat{\mu}, \hat{\sigma}\} = \max_{\mu,\sigma} \prod_{j=1}^{J} \binom{N_j}{n_j} \Phi\left[\frac{\log IM - \mu}{\sigma}\right]^{n_j} \left(1 - \Phi\left[\frac{\log IM - \mu}{\sigma}\right]\right)^{N_j - n_j} \quad \textbf{(A.6)}$$

Numerically, it is easier to find the solution of a sum rather than a product and so the maximum of the log-likelihood function (the logarithm of the Equation (A.6)) is usually computed in order to define the model parameters (Baker, 2011). The equivalent of Equation (A.6) can be formed for any of the link functions in Table A.3 by substituting them into Equation (A.5) and maximizing the log-likelihood function.

A.2.2.3 Application to Fragility Functions

For fragility function derivation, Equation (A.5) can be solved for each damage state (for any link function), based on the observations at that damage state. Extensions of this methodology that have been used for fragility function derivation include the consideration of various random components of the regression model, including multinomial (or "partially ordered") regression (utilizing a multinomial distributions accounting for the categorical nature of damage state data), and ordinal regression (accounting for the ordered nature of damage state data) (I. Charvet, Ioannou, Rossetto, Suppasri, & Imamura, 2014b; T Rossetto, Ioannou, Grant, & Maqsood, 2014).

Note that Equation (A.5) can be evaluated even if n=0 (i.e. some bins of an aggregated dataset are empty), or if N=1 (i.e. disaggregated datasets can be evaluated).

A.2.2.4 Advantages of GLMs for Fragility Function Derivation

Contrary to the nonlinear and linear models, generalized linear models provide a better representation of the post-tsunami data given the following considerations (Charvet, Rossetto, Macabuag 2016):

1. They can be used with discrete probability distributions to model discrete outcomes / responses, such as a damage level.
2. They successfully relax the assumption of linearity by use of a link function and linear predictor.
3. They successfully relax the assumption of constant variance of residuals by accommodating for smaller uncertainty in the tails of the fragility curve, and higher in the middle.
4. They do not require the aggregation of observations, and so disaggregated, building-by-building data can be evaluated.
5. If only aggregated data is available, they take into account the fact that some data points have a larger overall number of buildings associated with them than others, without the need of a weighting system (n and N in Equation (A.5)).
6. Ordinal regression prevents the crossing of fragility functions, ensuring that derived functions are always physically meaningful.

Myung (2003) notes that MLE satisfies the following:

- sufficiency
    - complete information about the parameter of interest is contained in its MLE estimator;
- consistency
    - the true parameter value that generated the data is recovered asymptotically, for sufficiently large samples;
- efficiency
    - lowest-possible variance of parameter estimates achieved asymptotically;

- and parameterization invariance
    - same MLE solution obtained independent of the parametrization used.

It can be shown that using the GLM for a Gaussian family (i.e. Normal error structure) results in an identical parameter estimation to that of a linear regression model, as ordinary least squares is the maximum likelihood estimator where the linear regression model assumptions are met. But for fragility function derivation, where error structures are not of Gaussian distribution, the Generalized Linear Model (GLM) should be used instead.

A.2.3 Non-Parametric Regression

When all assumptions cannot be met, an alternative approach is to use non-parametric (e.g. Kernal Smoothers) regression or semi-non-parametric (e.g. Generalized Additive Models, GAMs, developed by Hastie and Tibshirani (1990)) methods.

The local polynomial kernel method is presented in (Rossetto, Ioannou, & Grant 2012b), consisting of using a well-known function (kernel) successively centred on each datapoint and using a number of surrounding data points (defined by the bandwidth) to estimate the resulting function. Signal processing is a typical application of Kernels smoothers, (Schuenemeyer & Drew 2011). An issue is that the final curve is very sensitive to the choice of bandwidth.

If rigorous diagnostics reveal that the chosen GLM do not provide a satisfactory fit to the data, alternative methods such as General Additive Models (GAM) or non-parametric regression can be used. However, an issue with non-parametric models is that they are susceptible to over-fitting, and their appropriateness in the context of fragility analysis has not yet been demonstrated.

A.3 Assessing Model Fit

Several regression methods have been presented and so a rigorous method is required to be able to choose between them. There are several “goodness of fit” tests which can be employed to assess how well a statistical model fits the damage data, and these can be used to quantitatively compare models and choose that with the best fit. The references given provide details of each of these tests, but it is important that when deriving fragility functions several statistical modelling techniques are employed, the assumptions inherent with each method are examined, and several tests are then used to quantitatively select the best model.

The “goodness of fit” of a statistical model describes how well it fits observational data. Measures of “goodness of fit” summarize the error between observed values and the values predicted by the model. These measures can be either relative (only meaningful when comparing measurements between alternative models), or absolute.

Assessments of model fit can have two aims:

1. Model selection
    - Identifying the “optimal” statistical model from a number of alternative models.
2. Performance estimation
    - Identifying how accurately the model predicts outcomes in the true population.

A detailed methodology for model building and evaluation in the context of empirical vulnerability assessment can be found in Rossetto et al. (2014). This section summarizes the main concepts used in tsunami fragility literature. Alternative statistical tests which have not been used in tsunami fragility studies (e.g. Cox & Snell R^2 test, Hosmer & Lemeshow Test) will not be included here.

Note that for seismic vulnerability functions there is a rating system, published by the Global Earthquake Model (GEM), which can be used for deciding on the most appropriate curves to use (Porter (2011)), however this method of rating has not been used for tsunami fragility functions.

A.3.1 Coefficient of Determination (R^2)

The coefficient of determination (R^2) denotes the proportion of the variance in the dependent variable that is predictable from the independent variable. It can be calculated in various ways and has different interpretations for OLS regression models and GLMs, and so must be interpreted with caution.

Most studies will consider a regression analysis as satisfactory if they result in a high value for the coefficient of determination (R^2) (Gokon, Koshimura, & Matsuoka (2010); Suppasri et al., (2011)). However, R^2 does not indicate whether:

- the independent variables are a cause of the changes in the dependent variable;
- omitted-variable bias exists;
- the correct regression methodology was used;
- the most appropriate set of explanatory variables has been chosen;
- there is collinearity present in the data on the explanatory variables;
- the model might be improved by using transformed versions of the existing set of independent variables;
- there are enough data points to make a justified conclusion.

Therefore, the use of R^2 should be supplemented by additional tests, comparison with alternative regression techniques and inspection of the underlying model assumptions.

A.3.2 Deviance

The likelihood statistic of a model describes the likelihood of observing the observations on which the model was fit, given the error distribution defined by that model (defined in Equation (2.6) for a general model with a binomial error distribution). Log-likelihood, is the logarithm of the likelihood function.

The deviance of a model is a measure of the model's fit to the observed data, and is a function of the model's log-likelihood statistic (Equation (2.8)). It is reported in some tsunami fragility studies (Muhari et al. 2015), when comparing nested models (one model is nested in another if they are fit to the same data, and all of the parameters of the simpler model are contained in the more complex model), as a model's deviance is used in the likelihood ratio test.

$$Model\ Deviance = -2 \log L\left(\hat{\beta} \middle| y\right) \quad \textbf{(2.8)}$$

Where: y are the observations on which the model is fit.

$\hat{\beta}$ is the vector of model parameters estimated through maximum likelihood estimation.

and $L(\hat{\beta}|y)$ is the model's likelihood statistic (L_{model}).

A.3.3 Likelihood Ratio Test

This method is used by some studies to compare nested models (I. Charvet, Ioannou, Rossetto, a. Suppasri & Imamura 2014; Muhari et al. 2015), and is recommended by the guidelines set out by T Rossetto et al. (2014). Its use is for when testing the addition of additional parameters, or when comparing multinomial and ordinal models (the nested model).

A more complex statistical model (one with more explanatory variables) will always fit the data on which it was fit, as well or better than a simpler model fit to the same data. The likelihood ratio test tests whether the improvement in fit of a more complex model is statistically significant.

The test utilizes the likelihood ratio test statistic (D) of two nested models, which is a function of the ratio of the models' likelihood statistics (Equation (2.9)), and equates to the difference between the models' deviances (Equation (2.8)).

$$D = -2\log\frac{L_{simple\ model}}{L_{complex\ model}} = -\left(2\log L_{simple\ model} - 2\log L_{complex\ model}\right) \quad \textbf{(2.9)}$$

The distribution of the test statistic D is approximately a χ^2 distribution, with degrees of freedom equal to the difference between the degrees of freedom of the two models being tested ($df_{simple\ model} - df_{complex\ model}$). By assuming this χ^2 distribution, the probability (or p-value) of D can be computed, with a p-value < 0.05 indicating a greater than 5% chance that the difference in deviance statistics D was developed from random chance, and so the more complex model can be rejected.

A.3.4 AIC

The comparison of the fit of both nested and non-nested models (e.g. two models fit to the same data using the same IMs, but different link functions) can be assessed by the use of the Akaike information criterion (AIC, Equation (2.10)) following the recommendations of Rossetto et al. (2014).

$$AIC = 2I - 2\log L \quad \textbf{(2.10)}$$

Where: I is the number of parameters in the statistical model.

The model with the smallest AIC value is considered to provide a relatively better fit to the available data.

A.3.5 Graphical Tools

Graphically examination of the model errors (or Pearson residuals , Mc Cullagh & Nelder, 1989) for each curve (Figure 2.17), can be used to investigate the following effects:

- Influential points or outliers,

- Over-dispersion (if the values of the residuals or errors are more than two standard deviations away from the mean).
- Patterns or trends in the residuals, indicating that the error is not random (aleatoric) but systematic (epistemic).
- Changes in variance with the linear predictor (i.e. the assumption of constant variance can be examined).

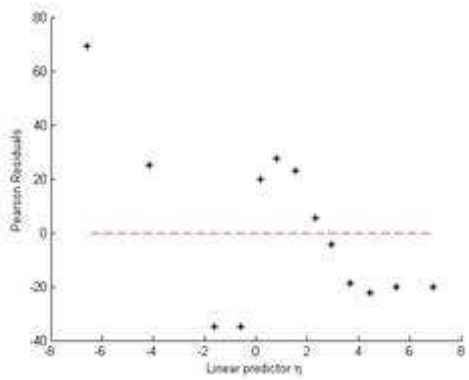

Figure 2.18: Pearson's residual plot - patterns in the residual suggest a poor fit .

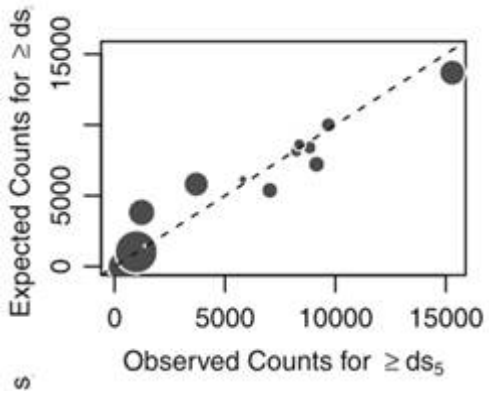

Figure 2.19: Observed vs predicted counts of buildings with damage exceeding a given damage state (DS5 in this example). Each point represents the observed and predicted counts for one TIM bin for the specified DS (I. Charvet, Ioannou, Rossetto, a. Suppasri & Imamura 2014).

An alternative graphical assessment tool is to plot observed versus predicted building counts (Figure 2.19), where points adhering to a 45° line shows good model fit, and trends may indicate epistemic uncertainty.

A.3.6 Cross-Validation

The prediction error rate (i.e. the proportion of incorrectly classified outcomes) indicates how accurately a model will make predictions. Goodness of fit measures are biased by overfitting, indicating a better fit to the underlying population than is really the case. I.e. residuals will be biased downwards (indicate less prediction error) for overfit models as they are assessing prediction error based on the data (observations) that was used to fit the regression model.

Cross-validation is an improvement over simply looking at the residuals, as it attempts to indicate the prediction error that will be experienced on data that has not been used to form the statistical model, and is useful for overcoming the problem of over-fitting (a term which refers to when the model requires more information than the data can provide).

This can be achieved by forming the model based on a subset of the total available data (a training set), and then calculating the prediction error based on the remaining data (the testing set, of size $N_{test\ set}$), known as the Holdout Method. The resulting error rate, however is sensitive to the selection of the training and testing sets, and so the following resampling methods may be employed:

- Random subsampling
    - Repeat the validation experiment *K* times, randomly selecting a different testing set each time.

- K-fold cross-validation
    - Create *K*-fold partitions in the total dataset, and for each of *K* validation experiments use 1 fold as the testing set (a different 1 each time), and the remaining data as the training set.
- Leave-one-out cross-validation
    - As k-fold cv where *K* equals the number of observations in the total dataset. i.e. in each validation experiment, one observation is the testing set, and all other observations make up the training set.

In each of these resampling methods, the model is fit to the resampled training set for each of *K* iterations, and the average of the error rates for all iterations gives the true prediction error rate (Equation (2.11)).

$$Error\ rate = \frac{1}{K}\sum_{k-1}^{K}\frac{n_{incorrect}}{N_{test\ set}} \quad \textbf{(2.11)}$$

Where: *K* is the number of iterations (experiments).

Cross validation has been used to estimate tsunami fragility function prediction error rates by Muhari et al. (2015) and I Charvet, Suppasri, Kimura, et al. (2014). I Charvet, Suppasri, Kimura, et al. (2014) also proposes a penalized error estimation method for multinomial models.

Method	Figure	Comments
Holdout	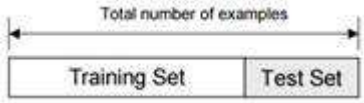	Prediction error rate sensitive to selection of training and testing sets.
Random subsampling	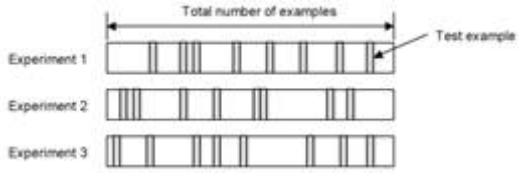	Iteration reduces the sensitivity to the selection of training sets. But some data may be used for model training more than others, introducing a bias.
K-fold cross-validation	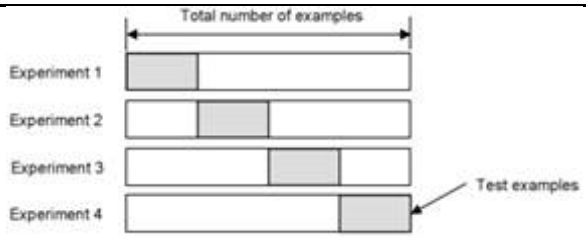	All observations in the dataset will be used for both training (K-1 times) and testing (once). One K^{th} of the data is wasted (not used for model fitting) in each experiment.
Leave-one-out	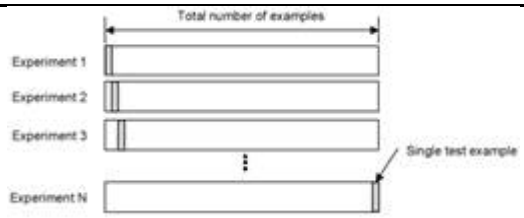	More accurate estimation of prediction error rate, but computationally expensive for large datasets.

Table A.4: Validation Methods

A.4 Representation of Uncertainty

Sources of aleatoric uncertainty (statistical error due to random variations) and epistemic uncertainty (systematic error due to errors in knowledge or judgement) in the derivation of seismic fragility functions is summarized in Figure A.6.

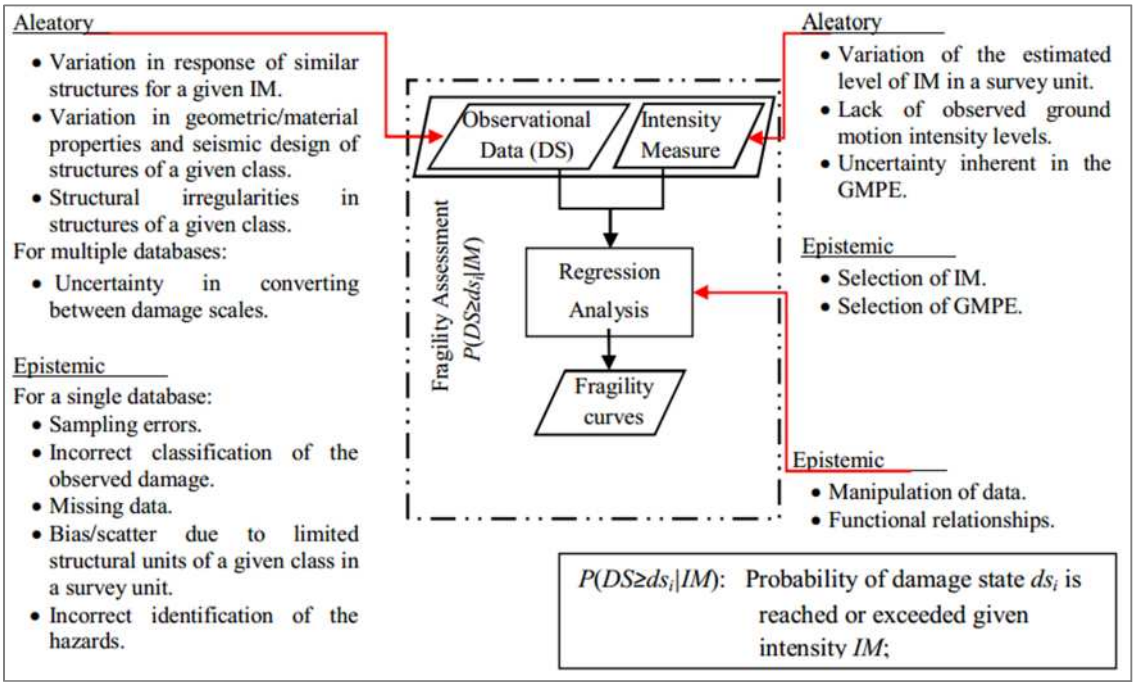

Figure A.6: Sources of uncertainty in seismic empirical fragility function derivation (Ioannou, Rossetto, & Grant, 2012).

Uncertainty can be quantified by the use of confidence intervals, which give an indication of the variability of the mean curves and can be calculated using numerous methods. They can be calculated directly from the standard errors calculated for each regression coefficient, but these calculations are dependent on the chosen random component of the regression model (i.e. the error structure), and so if the error structure is incorrectly identified for the data used, then the inferences from confidence intervals will be wrong.

Unfortunately, most existing tsunami fragility studies do not include a systematic treatment of uncertainty. Bootstrap methods are employed by I. Charvet, Ioannou, Rossetto, A. Suppasri & Imamura (2014).

B. Tsunami Damage Scales

Prior to the 2004 Indian Ocean disaster, no thorough tsunami damage survey was performed as most studies focussed mostly on collection of inundation data (e.g. Imamura *et al.* (1995); Shuto & Matsutomi (1995)), whilst some surveys made rough estimations of damage with no real definition of damage states (Tsuji *et al.,* 1995). Recent post-tsunami surveys directly use earthquake damage assessment scales (EMS98 – Grunthal (1998)) to assess tsunami damage (Rossetto *et al.* 2010).

Since the 2004 Indian Ocean Tsunami, tsunami damage has been assessed more rigorously and similarly to earthquake damage, but also accounting for damage induced by fast flowing waters (Pomonis et al. 2006). Such a scale ranks the data into damage classes according to the degree of non-structural and structural damage to a building as shown in Figure B.1 to Figure B.3. A damage scale that differs significantly from Figure B.1 is one of the scales used in Japan (Figure B.4) for which the hazard intensity measure (depth in this case) is embedded in the damage state definition (i.e. the assigned damage level is defined by depth of water rather than the assessed structural damage), assuming a very high correlation between hazard and loss.

Damage level	Description
No damage (D0)	No visible damage to the structure observed during the survey. Suitable for immediate occupancy
Light damage (D1)	Flood damage to contents. Some non-structural (fittings, windows) damage. Damage is minor and repairable. Suitable for immediate occupancy
Moderate damage (D2)	Out-of-plane failure or collapse of parts of or whole sections of masonry infill walls and windows at ground storey. Repairable damage from debris impact to structural members (columns, beams, walls). No structural member failure. Scouring at corners of the structures leaving foundations partly exposed but repairable by backfilling. Unsuitable for immediate occupancy but suitable after light repair
Heavy damage (D3)	The structure stands but is severely damaged. Infill panels above the 1st storey have been damaged or have failed. Structural and non-structural members have been damaged. Failure of a few structural members which are not critical to structure stability (e.g. failure of infill concrete walls). Roofs are damaged and have to be totally replaced or repaired. Significant scouring at corners of the structures leaving foundations exposed, with minor repairable tilting. Structure requires extensive repair and is unsuitable for immediate occupancy
Collapse (D4)	Partial or total collapse of the building. Collapse of large sections of foundations or structure due to heavy scouring or debris impact. Excessive foundation settlement and tilting beyond repair. Damage to the structure cannot be repaired and must be demolished

Figure B.1: EEFIT tsunami damage scale for RC frame or RC shearwall buildings of EMS-98 structural vulnerability class D and E, i.e. Moderate and high earthquake resistant design respectively, of up to 6 storeys height (Fraser et al., 2013)

Damage level	Description
No damage (D0)	No visible damage to the structure observed during the survey. Suitable for immediate occupancy
Light damage (D1)	Flood damage to contents. Some damage to the exterior of the building's cladding above foundation level and windows/fittings at ground-floor level. Damage is minor and repairable. Suitable for immediate occupancy
Moderate damage (D2)	Ground-floor cladding has been destroyed partially but structure is standing and may be reoccupied after substantial repairs. Contents and fittings in the ground-floor level will need to be replaced. Not suitable for immediate occupancy, but in most cases damage is repairable
Heavy damage (D3)	Ground-floor cladding has been destroyed, and there may be some damage to cladding at the 2nd storey. The load-bearing timber frame has been damaged by water flow or debris impact, but the building is still standing. In many cases these buildings will have to be demolished, as damage to the timber structure is too extensive. Not suitable for occupancy
Collapse (D4)	The building has extensive structural damage due to flow or debris impact, has collapsed partially or totally, or has been washed away. The building will require demolition if still standing. Tsunami flow in these buildings is usually above 3 m (measured from ground-floor level)

Figure B.2: EEFIT tsunami damage scale for timber frame buildings of EMS-98 structural vulnerability class D (Fraser et al., 2013)

Damage level	Description
No damage (D0)	No visible damage to the structure observed during the survey. Suitable for immediate occupancy
Light damage (D1)	Flood damage to contents. Some non-structural (fittings, windows) damage. Damage is minor and repairable. Suitable for immediate occupancy
Moderate damage (D2)	Out-of-plane failure or collapse of parts of or whole sections of infill walls, cladding and windows at ground storey. Repairable damage from debris impact to structural members (steel columns and beams). No structural member failure. Scouring at corners of the structures may leave foundations partly exposed but repairable by backfilling. Unsuitable for immediate occupancy but suitable after repair
Heavy damage (D3)	The steel frame is still standing, structural columns and beams are in their pre-tsunami position despite some damage due to pressure or debris impact, damming. Non-structural steel members may be buckled or fractured. The interior of the building and the cladding have been destroyed, washed-away, at 2nd storey or above. Scouring at corners of the structures may leave foundations partly exposed but repairable by backfilling. The building may be re-occupied after reconstruction of all the non-structural elements and fittings
Collapse (D4)	The building has partially or totally collapsed due to debris impact or debris damming effects. Multiple structural columns are buckled or fractured and cannot be replaced without loss of stability, even though the building is still standing. Building will have to be demolished

Figure B.3: EEFIT tsunami damage scale for steel frame buildings of EMS-98 structural vulnerability class E (Fraser et al., 2013)

Additional caution needs to be applied when comparing studies which use different damage state definitions as the order of the defined states can differ, as shown in Figure B.4 where damage state 1 represents “Washed Away” and subsequent damaged states represent lower states of damage.

Code	Damage State	Description (MLIT)
D1	Total Collapse (Wiped)	Buildings completely washed away
D2	Total Collapse	Only building structures left. It is not financially reasonable to rebuild.
D3	Total Collapse (Inundated 1st floor ceiling level)	Water reached above 1st floor ceiling level. It required major effort to reconstruct buildings in this category.
D4	Major Half Collapse	Water level exceeded 1m above 1st floor level but lower than 1st floor ceiling level.
D5	Half Collapse (Inundated above 1st floor level)	Water level was between 1m above 1st floor level and 1F level. (Minor repair costs expected)
D6	Partial Damage (Inundated below 1st floor)	Water level did not reach 1st floor level. (Only debris removal is required to be operational)
D7	No Damage	No damage
D0	Unknown	Unknown

Figure B.4: Damage states as defined in (Masuda et al., 2012)

Some numerical codes also assume a high correlation between hazard and loss (as in Figure B.4) and use tsunami intensity measure directly to estimate structural collapse (e.g. HAZUS, Life Safety Model) based on a simple collapse threshold (e.g. (Lumbroso *et al.* 2011)). Various thresholds have been given in the literature: for example, Suppasri et al. (2012) suggest that wooden structures in Japan would collapse for h > 4.5m; Reese et al. (2007) give a threshold of 2m for wood/bamboo structures in Indonesia to be destroyed; and guidance in Japan assumes that all buildings collapse at inundation depths greater than 2m (Koshimura, Namegaya, & Yanagisawa, 2009).

Such a scale ranks the data into damage classes according to the degree of non-structural and structural damage to a building (EEFIT, 2006, or the example given in Table3). Issues may arise if the hazard intensity measure (i.e. flow depth) is embedded in damage scale used, thus not allowing clear distinction between the response and explanatory variable. This was the case, for example, for the scale used in the study by Masuda et al. (2012), where most of the damage damage where defined by the actual inundation level or water height.

Some numerical codes also assume loss can be perfectly predicted by one tsunami IM (flow depth) and use this measure directly to estimate structural collapse (e.g. HAZUS, Life Safety Model) based on a simple collapse threshold (Lumbroso et al., 2011). Various thresholds have been given in the literature: for example, Suppasri et al. (2012) suggest that wooden structures in Japan would collapse for h > 4.5m; Reese et al. (2007) give a threshold of 2m for wood/bamboo structures in Indonesia to be destroyed.

Table B.1 shows description of building damage states due to tsunami flow, proposed to be used in HAZUS (a GIS-based loss assessment tool by FEMA). Table B.2 shows a mapping between HAZUS and MLIT damage states for the 2011 Japan Tsunami.

<table>
<tr><td rowspan="2">Model Building Type (Height/Weight)</td><td colspan="3">Damage States</td></tr>
<tr><td>Moderate</td><td>Extensive</td><td>Complete</td></tr>
<tr><td colspan="4">Structure Damage due to Tsunami Flow</td></tr>
<tr><td>Low-Rise – Light MBTs (W1, W2, S3, MH)</td><td rowspan="4">Limited, localized damage to elements at lower floors. Diagonal cracks in shear walls, limited yielding of steel braces, cracking and hinging of flexural elements – no or only minor permanent offsets (i.e., less than ½ inch per floor).</td><td rowspan="3">Localized failure of elements at lower floors. Large diagonal cracks in shear walls, failure of steel braces, large flexural cracks/buckling of rebar, buckled flanges and connection failures – large permanent offsets of lower stories. Localized erosion or scour, limited foundation settlement</td><td rowspan="3">A significant portion of structural elements have exceeded their ultimate capacities; critical elements/connections have failed resulting in dangerous permanent offset, partial collapse, full collapse or building moved off foundation (e.g., "washed away"). Extensive erosion or scour, substantial foundation settlement</td></tr>
<tr><td>Low-Rise - Other</td></tr>
<tr><td>Mid-Rise - All</td></tr>
<tr><td>High-Rise - All</td><td></td><td></td></tr>
<tr><td colspan="4">Nonstructural Components Ruined by Tsunami Flood (floors fully inundated, unless noted otherwise)</td></tr>
<tr><td>Low-Rise - 1-Story</td><td></td><td>Floor 1 (1/2 height)</td><td>Floor 1</td></tr>
<tr><td>Low-Rise - 2-Story</td><td></td><td>Floor 1</td><td>Floors 1 - 2</td></tr>
<tr><td>Mid-Rise - 5-Story</td><td>1st Floor</td><td>Floors 1 - 3</td><td>Floors 1 - 5</td></tr>
<tr><td>High-Rise - 12-Story</td><td>1st Floor</td><td>Floors 1 - 6</td><td>Floors 1 - 12</td></tr>
<tr><td colspan="4">Contents Ruined by Tsunami Flood (floors fully inundated, unless noted otherwise)</td></tr>
<tr><td>Low-Rise - 1-Story</td><td></td><td></td><td>Floor 1 (3 feet)</td></tr>
<tr><td>Low-Rise - 2-Story</td><td></td><td>Floor 1 (3 feet)</td><td>Floors 1 – Floor 2 (3 ft.)</td></tr>
<tr><td>Mid-Rise - 5-Story</td><td>Floor 1 (3 feet)</td><td>Floors 1 – 2, 3 (3 ft.)</td><td>Floors 1 – 4, 5 (3 ft.)</td></tr>
<tr><td>High-Rise - 12-Story</td><td>Floor 1 (3 feet)</td><td>Floors 1 – 5, 6 (3 ft.)</td><td>Floors 1 – 11, 12 (3 ft.)</td></tr>
</table>

Table B.1: Qualitative description of building damage states due to tsunami flow, proposed to be used in HAZUS (Kircher & Bouabid, 2014)**.**

<table>
<tr><th colspan="2">Japanese Damage Level/State</th><th>HAZUS Damage State</th></tr>
<tr><td>1</td><td>Washed Away</td><td rowspan="2">Complete</td></tr>
<tr><td>2</td><td>Collapsed</td></tr>
<tr><td>3</td><td>1st Floor Inundation</td><td rowspan="2">Extensive</td></tr>
<tr><td>4</td><td>Major</td></tr>
<tr><td>5</td><td>Moderate</td><td>Moderate</td></tr>
<tr><td>6</td><td>Slight</td><td rowspan="2">Slight/None</td></tr>
<tr><td>7</td><td>None</td></tr>
</table>

Table B.2: Mapping of Japanese Damage Descriptions to HAZUS Damage States (Eguchi et al., 2014)

区分	全壊 （流失）	全壊	全壊 （１階天井以上浸水）
主な建物状況	基礎だけ残して、建物が完全に流されている	主要構造が損壊しており補修により元通りに再使用することが困難	１階天井以上浸水しており、大規模修繕等による再使用も可能
サンプル写真			
棟数※	約 78,000	約 34,000	約 8,000

区分	大規模半壊	半壊 （床上浸水）
主な建物状況	床からおおむね１m以上（天井未満）浸水している	床から概ね１m未満の床上浸水（一部補修により再利用可能）
サンプル写真		
棟数※	約 36,000	約 40,000

区分	一部損壊 （床下浸水）	棟数合計	
主な建物状況	床下の泥を取り除けば再利用可能		
サンプル写真		被災建物総計	うち全壊
棟数※	約 23,000	約 219,000	約 120,000

建物被災状況
（イメージ）

Figure B.5: Original MLIT damage scale used in 2011 GEJE.

Similarly, a damage scale (DS) was developed for floods (Table B.3) by Kelman (2002). Each damage level represents a threshold in which the hazard event affects the building in a fundamentally different, and more damaging, manner. This scale defines a boundary between non-failure (often with damage) and failure (obviously with damage):

- DS0 represents non-damage (and thus non-failure).
- DS1 and DS2 represent damage but not failure.
- DS3 represents the transition from non-failure to failure in that a residence component fails.
- DS4 and DS5 represent structural failure.

Damage Scale (DS) Level	Water Interaction with Structure
DS0	No water contact with structure.
DS1	Water contacts outside of structure but does not enter.
DS2	Water infiltrates (i.e. seeps or leaks in through small apertures). OR External features are damaged or removed by water or debris.
DS3	Water or debris penetrates through a closed or covered opening (probably by breaking the opening); for example, a window or a door.
DS4	Water or debris penetrates through a route not including an opening (structural integrity is attacked); for example, a wall or roof.
DS5	Structure is damaged beyond repair; for example, walls collapse, the structure moves, or the foundation is undermined.

Table B.3 Damage Scale for Floods (Kelman 2002)

Type	Survey Method	Typical Sample Sizes	Typical Building Classes	Typical No. of Damage States	Reliability of observations	Typical issues
Damage	Rapid Surveys	Large	All buildings	2-3	Low	Safety not damage evaluations.
	Detailed "Engineering" Surveys	Large to Small	Detailed Classes	5-6	High	Possibility of unrepresentative samples.
	Surveys by Reconnaissance Teams	Very Small	Detailed classes	5-6	High	Possibility of unrepresentative samples.
	Remotely sensed	Very Large	All buildings	3-5	Low	Only collapse or very heavy damage states may be reliable. Misclassification errors.
Economic Loss	Tax assessor data	Very large	All buildings/ Detailed classes	-	High	Often focus on damaged buildings only.
	Claims data	Very large	All buildings	-	High	Often focus on damaged and/or insured buildings only.
Casualties	Government Surveys	Very large	All buildings	1-2	Low	Unlikely association with building damage and causes of injuries.
	Surveys by NGOs/ hospitals	Varies	All buildings	1-5	Low	
	Detailed Casualty Surveys	Very Small	Detailed classes	3-5	High	Possibility of unrepresentative samples.

Table B-4: summarizes typical features of data collected post-disaster.

C. Key Figures from Tsunami Loading Studies

Table C.1: Relevant studies on fluid-structure interaction for tsunami-like waves

Reference	Type	Time-histories?	Pressure distributions?	Description	Key Findings
Keulegan (1950)	Analytical	N	N	Analytical Study of Dam-break propagation parameters.	$u \approx 2\sqrt{gh_i}$ h_i = impingement depth
Cumberbatch (1960)	Analytical	N	N	Considered the case of symmetric normal impact of a water wedge on a wall.	
Cross 1967	Analytical	N	N	Developed a simple theory assuming the leading tip of the advancing tsunami as a rigid body (i.e. neglecting convective acceleration) to determine the profile and relevant characteristics of the surge.	$F = \frac{1}{2}\rho g h_b^2 + \rho h_b v_j^2$
Camfield (1980)	Review of existing analytical studies	N	N	A report by the US Army Corps of Engineers which offers Design guidelines specifically addressing tsunami forces	If the tsunami acts as a rapidly rising tide, most damage will be caused by buoyant and hydrostatic forces. When the tsunami forms a bore the expected flood velocities are substantially higher. $u = 2\sqrt{gh}$ h = "the surge height at any point,"
(Dames & Moore, 1980)				A report submitted to FEMA on Design and Construction Standards for Residential Construction in Tsunami-prone Areas in Hawaii	$u = 2\sqrt{gh}$ h = "the height of the bore or surge" For "surge force" (F_s): $F_s = 4.5bBh^2\rho$ where hs is the height of the surge front, B is the breadth of the structure in the plane normal to the flow direction, and ρ is the fluid density. Note that "surge force" is caused by the leading edge of running-up water on a dry bed impinging on a structure. Surge force is derived from the summation of the hydrostatic force with the linear momentum flux at the surge front; the momentum flux is computed with the velocity given by Eq. (1).

Reference	Type	Time-histories?	Pressure dist.?	Description	Key Findings
Zhang et al. (1996)				Extended the work of Cumberbatch (1960) to an oblique impact	
Matsutomi 1991					
(Jerald Day Ramsden, 1993; Jerald D Ramsden, 1996; Jerald Day Ramsden & Raichlen, 1990)	Physical experiments	Y	N	Experimental investigation of the interaction of bores and drybed surges with a vertical wall. In these experiments, three flow conditions were analyzed: (1) turbulent bores (initial still water downstream of the gate); (2) dry-bed surges (no initial water depth downstream of the gate); and (3) solitary waves.	Forces and overturning moments due to bores and dry-bed surges were recorded and calculated, to derive empirical formulae for the maximum force and moment exerted on a vertical wall due to the bore impact respectively. $\frac{F}{F_l} = 1.325 + 0.347\left(\frac{H}{h}\right) + \frac{1}{58.5}\left(\frac{H}{h}\right)^2 + \frac{1}{7160}\left(\frac{H}{h}\right)^3,$ $\frac{M}{M_l} = 1.923 + 0.454\left(\frac{H}{h}\right) + \frac{1}{8.21}\left(\frac{H}{h}\right)^2 + \frac{1}{808}\left(\frac{H}{h}\right)^3,$ where F is the force on the wall; Fl is the force on the wall due to a runup equal to twice the wave height, assuming hydrostatic pressure; H is the wave height at the wall; h is still water depth; M is the moment on the wall; and Ml is the moment corresponding to Fl. • Pressure distribution during impact is essentially non-hydrostatic. • Transition from undular to turbulent bores led to a discontinuous increase in water-surface slope, followed by an increase in measured runup, pressure head, and exerted forces and moments. • Recorded forces gradually increased to an approximately constant value for both the case of a surge and a bore. • No impulsive (shock) force exceeding the hydrodynamic force was observed. • An initial impulsive pressure equal to three times the pressure head, corresponding to the measured runup, was recorded. • No overshoot was observed for conditions of dry flume beds.
Asakura, Ikeno, Omori		N	N	Okada et al.conducted a survey of previous studies on tsunami wave forces and pressures.	Five empirical formulae were identified for tsunami-induced forces or pressures (it was found that calculation of tsunami load on structures using these formulae would result in approximately the same magnitude of load) • Tsunami wave pressure without soliton breakup • Tsunami wave pressure with soliton breakup • Tsunami wave pressure without soliton breakup • Tsunami-induced wave forces on houses • Tsunami force exerted on houses

Reference	Type	Time-histories?	Pressure dist.?	Description	Key Findings
Asakura et al (2000)	Physical experiments	N	N	Laboratory experiments, considering two different tsunami waveforms: a single longwave, and several short waves riding on the long wave. He measured the fluid force due to overflowing tsunami acting on structures constructed behind seawalls. Previous design guidance (Japan Cabinet Office, 2005) defined the hydrostatic pressure distribution approximation shown and set the depth coefficient (*a*)=3 based on a study by Okada et al. (2004) which carried out 84 2-dimensional hydraulic model experiments which measured the peak pressures exerted on structures positioned at various distances from the sea bed for various wave heights, periods and Froude Numbers.	• The pressure distribution on the structure is close to hydrostatic when the wave period is long • The pressure head could become three times that of the maximum ambient flow depth when the incident (single) wave is short. • Smaller waves riding on a single long wave exert additional pressure on the lower portion of the structure • Note that the maximum ambient flow depth is the water depth of the runup motion at the site of the structure, which may not be the same as the maximum inundation depth.
Hamzah et al. [10]	Experimental and numerical			Experimental and numerical investigations on the hydrodynamic pressure of a bore on a vertical barrier with some stillwater depth.	The maximum impulsive pressure was found to occur at some height from the stillwater surface.
Mizutani and Imamura (2000)	Experimental			Measured the wave pressure due to bore acting on sloping structures.	
Ikeno et al. (2005)				Measured the wave pressure due to tsunami with soliton fission acting on vertical breakwaters.	
Mizutani et al. (2006)				measured the tsunami fluid force acting on containers on aprons in a harbor.	

Reference	Type	Time-histories?	Pressure dist.?	Description	Key Findings
Araki et al. (2010)	Experimental			The horizontal and vertical components of the fluid force and pressure acting on a girder bridge due to a tsunami-like solitary wave are measured in a hydraulic experiment. The peak of the impact fluid force is estimated on the basis of the change in the added mass of the structure. The wave pressure acting on the seaward side of the girder of the bridge is also estimated. The critical force for the stability of the girder bridge is estimated as the strength of bolts used in the shoes against shear stress.	- In the time history of the vertical component of the tsunami fluid force Fz, two peaks were measured in the case of a just breaking wave while just one peak was measured in the case of a post breaking wave. - The horizontal and vertical components of the maximum fluid forces in the case of a post breaking wave were smaller than those in the case of a just breaking wave. - The impact force was considerably greater than that estimated from the change in the added mass of the model bridge in the transition from emerged to submerged conditions. - The equation proposed by Tanimoto et al. (1983) over-estimated the quasi-static pressure and underestimated the peak of the impact pressure.
Gomez-Gesteira & Dalrymple (2004)	Numerical			Study demonstrating the validity of the Smoothed-Particle Hydrnamics method for numerical modelling of 3D wave problems such as collision between waves and structures.	Used SPH to recreate small-scale experimental results of Yeh and Petroff at University of Washington. Good agreement. Also showed vertical distribution of pressure as shown in Figure C.11
Árnason 2005; Arnason et al. (2009)				Measured forces exerted on rectangular, rhomboidal, and circular structures due to a hydraulic bore on a dry bed. Presented analysis of the structure's effect on the bore behaviour.	It was observed that the surge force overshot the hydrodynamic force in the case of a square column for small bore heights (Fig. 11.5). However, no overshoot was recorded for the case of circular and rhomboidal columns.(Figure C.8) Arnason (2005) observed the initial impact (surge force) overshoot the drag force owing to the passing bore in the case of a square column for small bore heights. The maximum surge force was equivalent to 1.5 times the subsequent hydrodynamic force. On the other hand, this overshoot was not observed for larger bore heights. Also, no overshoot was recorded for the case of circular or rhomboidal columns. The lack of overshoot in a dry-bed surge is attributed to the relatively mild slope of the wave- front profile, while the impact momentum increases when the bore front becomes steep
P. Lukkunaprasit, 2008.			Y	A series of experiments to investigate the pressure distribution as well as the tsunami forces acting on 3D building models.	At large flow depths, the tsunami force was found to be significantly smaller than that computed based on Coastal Construction Manual FEMA-55 with the maximum measured velocity used in the computation.

Reference	Type	Time-histories?	Pressure dist.?	Description	Key Findings
Lukkunaprasit et al. (2009)	Physical Experiments	Y	N	verifying the method stipulated in FEMA P646 through laboratory experiments, assuming the beach condition similar to Kamala beach in Phuket, Thailand	The estimation of flow behaviors and characteristics based on the classic dam-break problem may mislead the predictions of tsunami runup actions near the shore- line. This is because substantial momentum can be carried from the “bore collapse (or momentum exchange)” phenomenon at the shoreline. On the other hand, the quasi- steady tsunami force (hydrodynamic force) can be modelled favorably by the drag-force Eq. (4) with the drag coefficient Cd =2. The method recommended in FEMA P646 – Eqs. (4) and (5) – yields a reasonable upper bound for maximum design force. The h in the velocity calculation proposed by (Camfield, 1980; Dames & Moore, 1980) ($u=2\sqrt{gh}$) cannot be the bore height, and nor can it be the maximum inundation depth.
Nouri et al. (2010); Nistor et al. (2010); Nouri (2008)				Experimental dam-break study measuring force time-histories on square and circular columns.	It was observed that surge, run-up, and drag forces are generated when turbulent bores impact the structural shapes tested. The drag force was the largest force component for the smaller impoundment depths (shallower bores), and the surge and run-up were more critical for the larger im- poundment depths (deeper bores). The run-up force was greater than the surge force for all bore depths. The surge force was best estimated using a combination of hydrostatic and drag force components. The force–time and bore height – time histories indicate that different bore heights are associated with the surge and drag force components, and therefore, using a single bore height in the estimation of the force components may not be suitable. The drag force was not well predicted using currently available design formulations. This was a direct result of the inaccurate flow velocity assumed by design codes.
Nistor et al. (2010)	Numerical			Numerical study to compliment experimental (validate SPH method)	Moderate agreement between numerical and experimental.
Robertson et al. (2008)	Experimental			A series of experiments carried out at the Tsunami Wave Basin (TWB) at Oregon State University (OSU). Equipped with a piston-type wavemaker capable of generating clean solitary waves. The facility was used to model tsunami bores breaking over coastal reefs and their impact on structural components, including columns, walls, and horizontal members, such as building floors and bridge decks. This paper focuses on the fluid forces of a bore impacting a wall/floor system	• Impulsive uplift loads induced on floor slabs when a tsunami bore is prevented from flowing through the building can be significantly larger than the uplift capacity of typical concrete floor construction. • The maximum impulsive uplift loads occur when the bore depth is equal to the story height. Bore depths that exceed the story height produce uplift loads equal to this maximum condition. Bore depths smaller than the story height produce lower uplift loads. • There is significant variability in the impulsive uplift pressures induced on the slab soffit. This is attributed to the turbulent nature of the incoming bore, and is more significant for the condition where the bore travels over standing water in its approach to the model.

Reference	Type	Time-histories?	Pressure dist.?	Description	Key Findings
(Ian N Robertson & Riggs, 2011)				An experimental laboratory study to quantify the lateral load applied to a vertical wall when subjected to different size tsunami bores.	A method is proposed to predict the peak lateral force on the vertical wall given only the incoming jump height, hj, and the standing water depth, ds. $F = \frac{1}{2}\rho g h_b^2 + \rho h_j v_j^2 + \rho g^{1/3}\left(h_j v_j\right)^{4/3}$ $v_j = \sqrt{g d_s\left[\frac{1}{2}\left(\frac{h_b}{d_s}\right)^2 + \frac{1}{2}\left(\frac{h_b}{d_s}\right)\right]}$ The proposed method provides a good estimate of the experimental force for various bore heights and standing water depths. The average error for a particular standing water level is generally less than 10%. This is an improvement over prior expressions found in the literature.
(Philippe; St-Germain, Nistor, & Townsend, 2012a)				the simulation of the impact with structures of tsunami-like bores rapidly advancing on dry and wet beds is performed using a three-dimensional numerical model based on the Smoothed Particle Hydrodynamics (SPH) method	the resulting time-histories of the pressures and net force acting on a square column and a vertical wall due to the impact of these bores are compared qualitatively
(Philippe; St-Germain, Nistor, & Townsend, 2012b)				the simulation of the violent impact of tsunami-like bores with a square column is performed using a single-phase, weakly compressible three-dimensional Smoothed Particle Hydrodynamics (SPH) model	Good agreement with experiments except impulsive load. As observed in previous breaking wave impact studies, results show that the magnitude and duration of the impulsive force at initial bore impact depend on the degree of entrapped air in the bore-front
(Philippe St-Germain, Nistor, Asce, Townsend, & Shibayama, 2014)				Summary of above studies ((Philippe; St-Germain et al., 2012a, 2012b)) and further advancements	Numerical time histories of the water surface elevation and net base horizontal force acting on the column are compared with the results of large-scale physical experiments, conducted by the authors.
(Ioan Nistor, Palermo, Nouri, & Murty, 2004)				Short-wave experiment - Measured and non-dimensional force time-histories for a small column	Drag equation good prediction, with additional peak for bore impact (Figure C.8).
(T O Lloyd & Rossetto, 2012)				Long-wave tsunami-generator tests	Differences between short and long waves. Sub-critical to choked flow back to sub-critical within one wave .
(Asakura et al., 2000)					

Reference	Type	Time-histories?	Pressure dist.?	Description	Key Findings
(Arikawa, Shimosako, & Ishikawa, 2012)				Presents an experimental approach on the structural failure by impulsive tsunami force using physical model experiments. First, the classification and definition of tsunami force hitting land structures are described. Second, the tsunami laboratory test was conducted to examine the tsunami pressure, which was found to be related to both inundation height and the Froude number. Third, the structural failure test was performed for various concrete plates under impulsive tsunami force.	(1) The maximum sustainable tsunami front pressure was proportional to the Froude number. (2) The impulsive bore pressure occurred in the Froude numbers of 1.3-1.5 and did not appear less than 1.15 within the range of the tests. (3) The maximum bore pressure became about 4 times larger than the maximum sustainable pressure and 7 times larger than the hydrostatic pressure.
(Aguíñiga et al., 2013) (cox and Van de Lindt)	Experimental			experiments on a horizontal flume to simulate tsunami waves with the dam-break method making impact on a vertical plexiglass wall.	It was found that the forces predicted by two methods (ASCE and Miles) are lower than those measured in the experiments, while three other methods (Honolulu building code, Coastal Engineering Technical Note, and Cross) estimated larger forces than measured in this study. Ramsden and Raichlen's method seemed to predict forces that match our experimental results closely
(Harry; Yeh, Barbosa, Ko, & Cawley, 2014)				The existing design guidelines are reviewed. We point out that some of the force-estimation methods recommended in the guidelines are rational, while others are not. Using the tsunami inundation data of the 2011 Tsunami in the town of Onagawa, we demonstrated that the buoyancy-force calculations are essential to evaluate global building failures.	• adapting the concept of drag force in fluid mechanics, the hydrodynamic force for a partially submerged building in quasi-steady flows is well founded and supported by laboratory experiments. • The hydrostatic force is for the "static" condition acting on a surface. Applications of buoyancy force to the buildings must consider the effects of soil and foundation, because the buoyancy force acts on the bottom of the building. • We point out that existing methods to estimate the impulsive forces and the debris impact forces are ambiguous and more or less rely on engineering "judgment." • To estimate the overturning moment, a necessary flow parameter is the square of the product of inundation depth and flow speed $(hU)^2$, whereas it is well known that the parameter – the specific force hU^2 – is needed to evaluate the horizontal hydrodynamic forces. The maxima of those parameters should be added to the list of parameters to extract from the numerical hydrodynamic simulations for structural analysis.
(Thomas, Asce, & Cox, 2012)	Experimental			Physical experiments to test the reduction of forces for onshore structures due to seawalls	$\frac{F_{max}}{(F_b)_{max}} = -0.331\left(\frac{H_w}{H_b}\right) + 0.027\left(\frac{H_w}{H_b}\right)^2 + 0.341\left(\frac{x}{L}\right) - 0.076\left(\frac{x}{L}\right)^2 + 1.109$ (1) $\frac{F_{ave}}{(F_b)_{ave}} = -0.204\left(\frac{H_w}{H_b}\right) - 0.003\left(\frac{H_w}{H_b}\right)^2 + 0.118\left(\frac{x}{L}\right) - 0.500\left(\frac{x}{L}\right)^2 + 0.847$ (2)

Reference	Type	Time-histories?	Pressure dist.?	Description	Key Findings
(Takabatake & Kihara, 2014)	Numerical			3D numerical simulation of tsunami waves striking obstacles of various blockage ratios.	there are three characteristic phases on the hydrodynamic force. First one is the impulsive force generated just after tsunami hit a structure. Although the impulsive force is violent, the effect of the impulsive force is limited because of very short duration time and very local acting area. Second one is the local maximum force generated when the water mass, which is flied upward induced by the flip-through, is fallen and touched onto the water surface. Last one is the quasi-steady force whose pressure distribution is approximated by hydrostatic force with the water level on the front face of a structure. Because the time scales of two forces generated just after tsunami hit as structure, which are the impulsive force and the local maximum force, is much shorter than the time scale of tsunami in general and the local maximum force is predicted to be smaller than that when subsequent flow reaches a structure, the quasi-steady force defined in our numerical simulations is defined as the maximum hydrodynamic force acting on the front face of a structure. Focusing on the quasi-steady force, the **estimation method of this force based on the specific energy is proposed.** $$F = \frac{1}{2}\rho g H_{up}^2 W \quad (4)$$ Hup is the specific energy defined at upstream region which is about 5 hin far from the front of a structure
(P Lukkunaprasit, Ruangrassamee, & Thanasisathit, 2008)	exerimental			One-to-one hundred scale building models with square shape in plan were tested in a 40 m long hydraulic flume with 1 m x 1 m cross section. Two opening configurations of the front and back walls were investigated, viz., 25% and 50% openings. Pressure sensors were placed on the faces of the model to measure the pressure distribution. A high frequency load cell was mounted at the base of the model to record the tsunami forces. A	The influence of openings on the peak pressures on the front face of the model is found to be practically insignificant. For 25% and 50% opening models, the tsunami forces reduce by about 15% and 30% from the model without openings, respectively. The

Table C.2: Relevant studies on fluid-structure interaction for tsunami-like waves

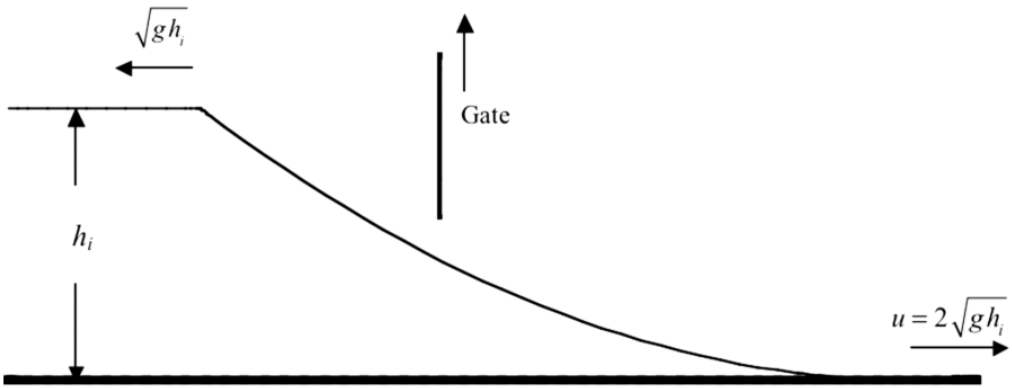

Figure C.1: The classic dam-break problem. An initially quiescent volume of impoundment depth h_i, generates a surge front of velocity u (Panitan Lukkunaprasit et al., 2009)**.**

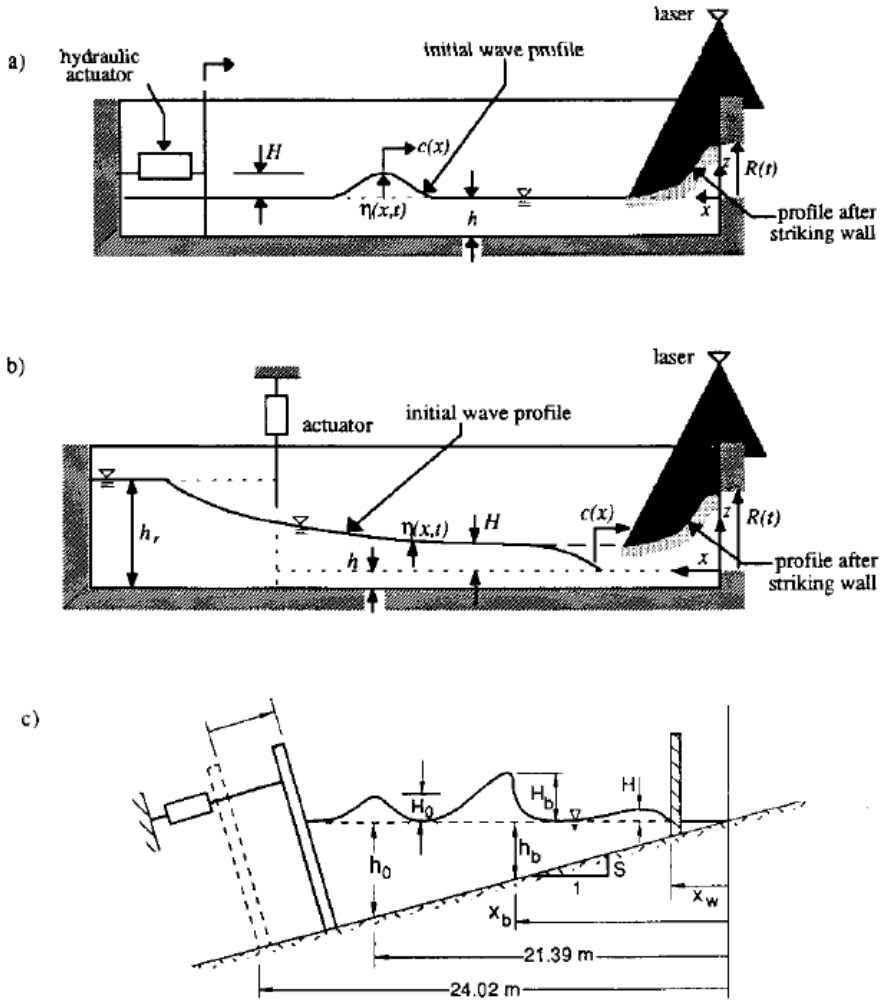

Figure C.2: Definition Sketch of Experimental Arrangement for (a) Solitary Waves in Horizontal Tank; (b) Bores and Dry Bed Surges in Horizontal Tank; and (c) Broken Solitary Waves in Tilted Tank with 1/50 Slope (Jerald D Ramsden, 1996)

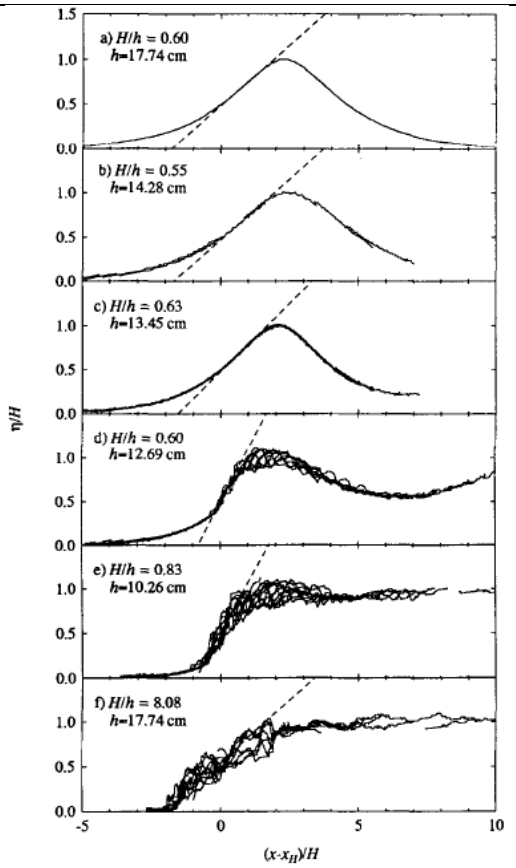

Figure C.3: Several Composite Wave Profiles Showing Variation of Maximum Wave Slope as Function of Relative Wave Height (Jerald D Ramsden, 1996)**.**

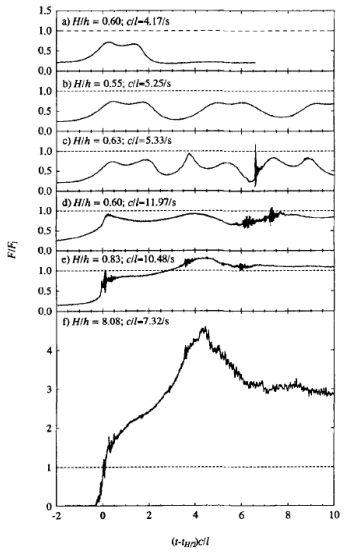

Figure C.4: Experimental Force Time Histories Measured During Impact of Solitary Wave and Bores. The force F on the wall has been normalized by a linear force scale F_I

, $F_I = \frac{1}{2}\gamma b(2H + h_w)^2$ **, which is the force on the wall due to a runup of twice the wave height, assuming a hydrostatic pressure distribution. The reflection of long waves, with a very small relative wave height, would produce maximum forces equivalent to FI', -y = weight of water per unit volume; b = width of the wall; and hw=water depth at the wall** (Jerald D Ramsden, 1996)**.**

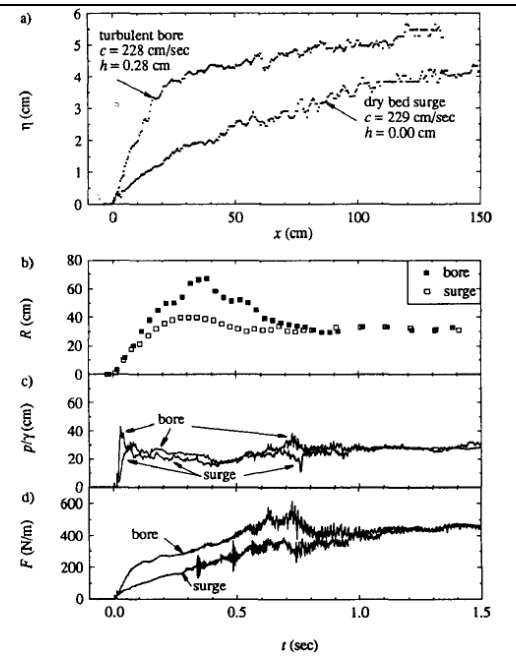

Figure C.5: Comparison of Experimental (a) Wave Profile; (b) Runup; (c) Pressure Head; and (d) Force due to Strong Turbulent Bore and Dry-Bed Surge with Same Celerity. (Jerald D Ramsden, 1996)

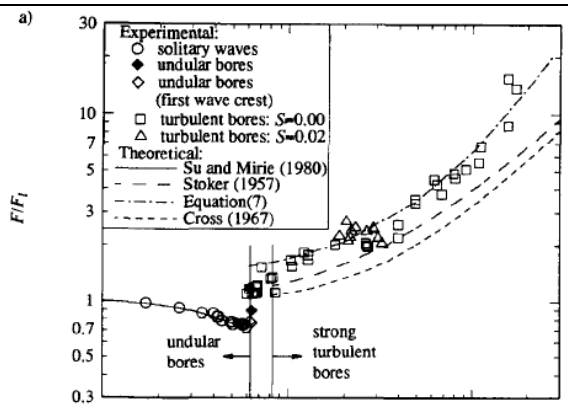

Figure C.6: Maximum (a) Forces; and (b) Moments on Wall due to Solitary-Wave and Bore Impact, where equation 7 refers to the empirical formulation: $\frac{F}{F_I} = 1.325 + 0.347\left(\frac{H}{h}\right) + \frac{1}{58.5}\left(\frac{H}{h}\right)^2 + \frac{1}{7160}\left(\frac{H}{h}\right)^3$ (7) **where F is the force on the wall; Fl is the force on the wall due to a runup equal to twice the wave height, assuming hydrostatic pressure; H is the wave height at the wall; h is still water depth; M is the moment on the wall; and Ml is the moment corresponding to Fl.** (Jerald D Ramsden, 1996)

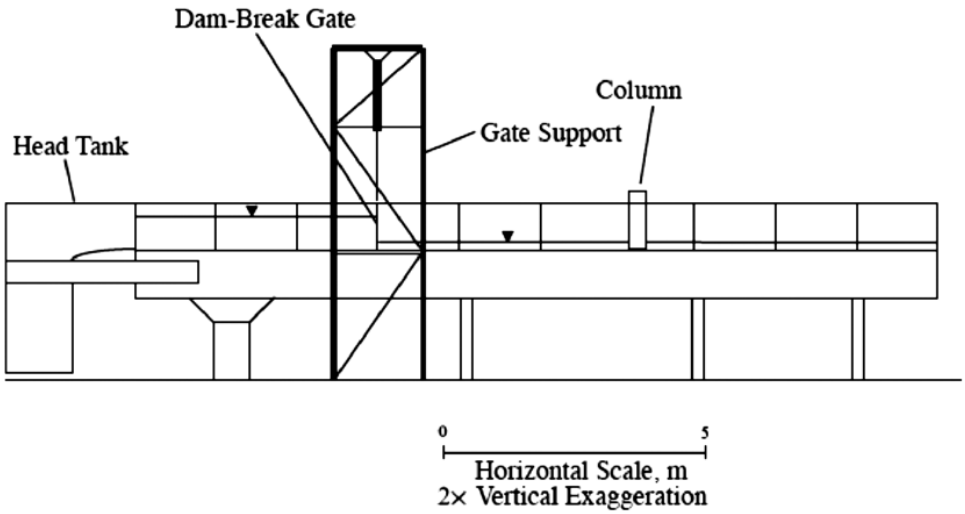

Figure C.7: A schematic view of the experiment apparatus for results below (Arnason et al., 2009; Árnason, 2005)

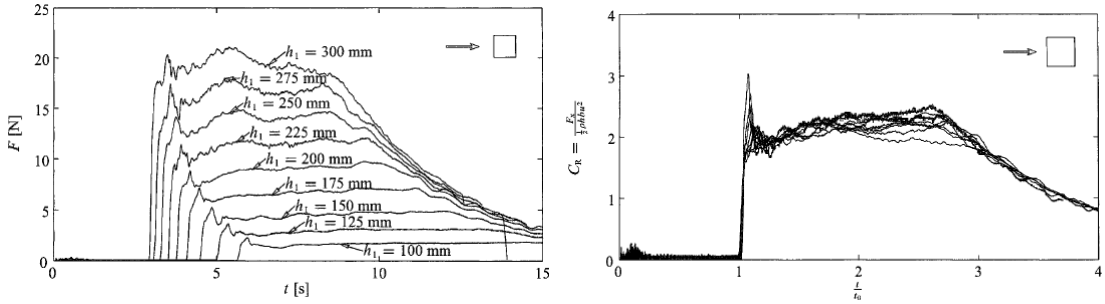

Figure C.8: Short-wave experiment - Measured and non-dimensional force time-histories for a small column (Arnason et al., 2009; Árnason, 2005)**.**

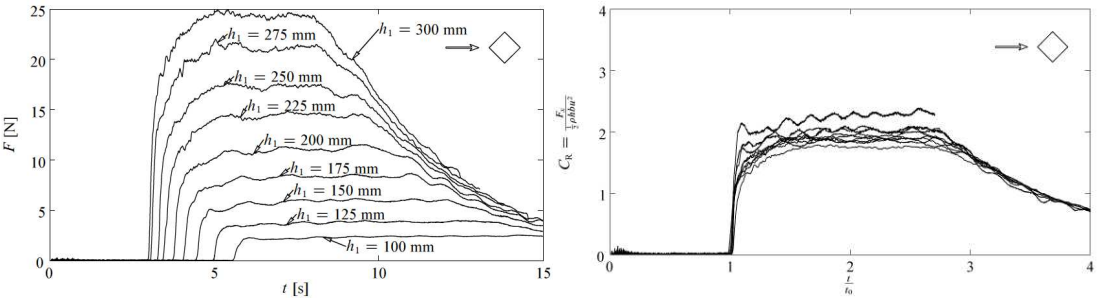

Figure C.9: Non-dimensionalized force histories for the square column with one corner facing the flow (Arnason et al., 2009; Árnason, 2005)

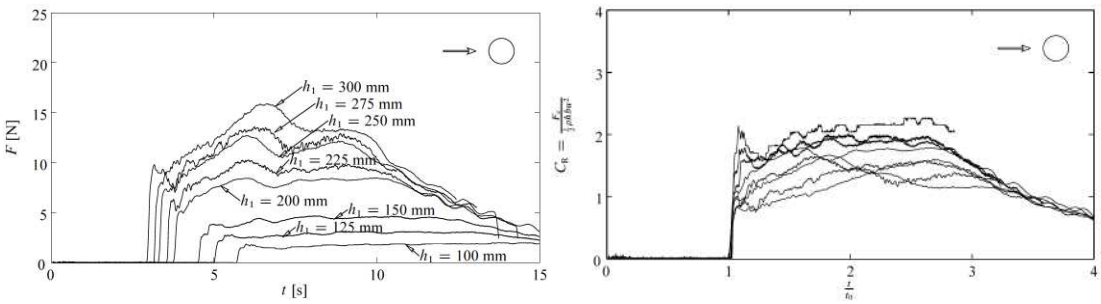

Figure C.10: Non-dimensionalized force histories for the large circular column (Arnason et al., 2009; Árnason, 2005)

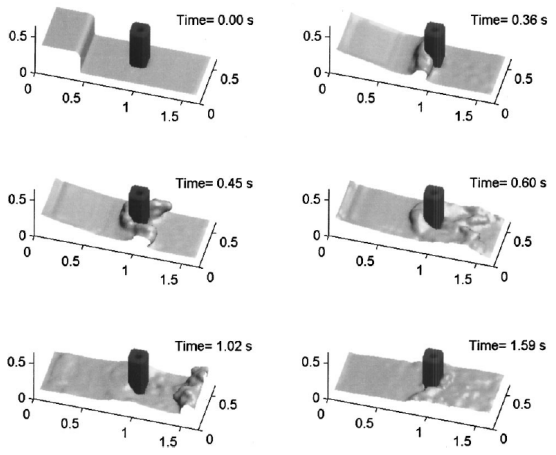

Wave evolution (T50.0 s) initial configuration; (T50.36 s) wave hitting the front of the structure; (T50.45 s) wave wrapping around the structure; (T50.60 s) waves colliding after passing the structure; (T51.02 s) wave colliding with the opposite wall of the tank; (T51.59 s) reflected wave hitting the back of the structure

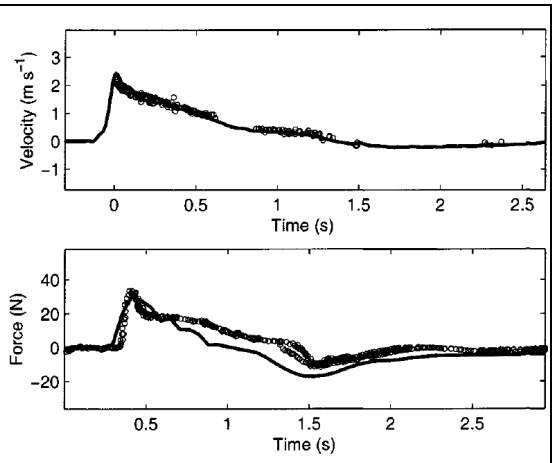

Comparison between numerical ~solid line! and experimental data ~circles!. Both ~a! the velocity at a gauge placed in front of the structure and ~b! the force exerted by the wave on the obstacle are in good agreement numerically and experimentally.

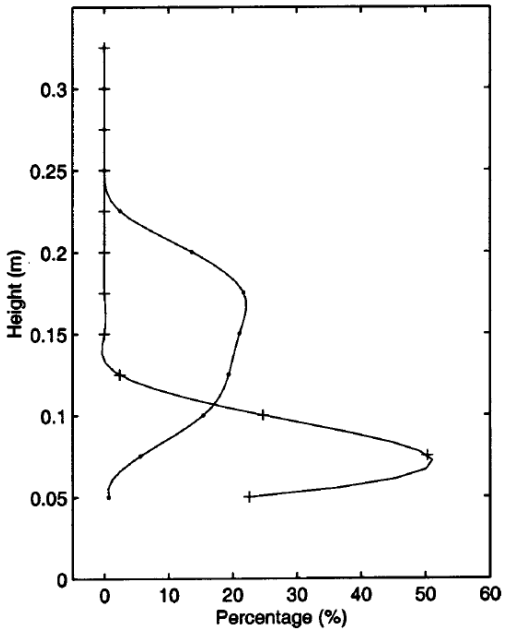

Vertical distribution of force exerted on the front of the structure. Most of the force is exerted on the lower part of the structure when the bottom is dry ~crosses!. This vertical distribution is different when considering a wet bottom ~circles!, since the wave created by the particles initially placed beyond the gate reaches heights close to 0.3 m.

Figure C.11: Study demonstrating the validity of the Smoothed-Particle Hydrnamics method for numerical modelling of 3D wave problems such as collision between waves and structures. In their work, they reproduced a small-scale experiment performed by Yeh and Petroff at the University of Washington referred to as a "bore in a box", where a dam-break wave impacted a free-standing rectangular structure. (Gomez-Gesteira & Dalrymple, 2004)**.**

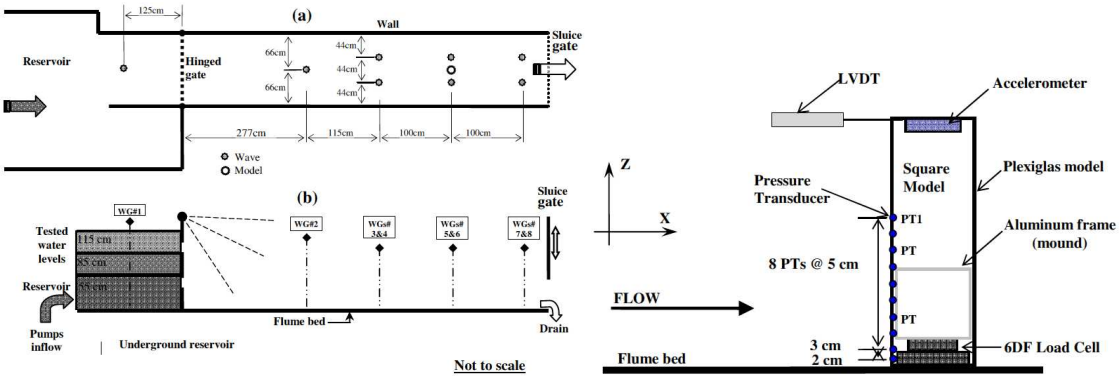

Experimental setup: a) plan view; b) side view.

Instrumentation schema for the square structure.

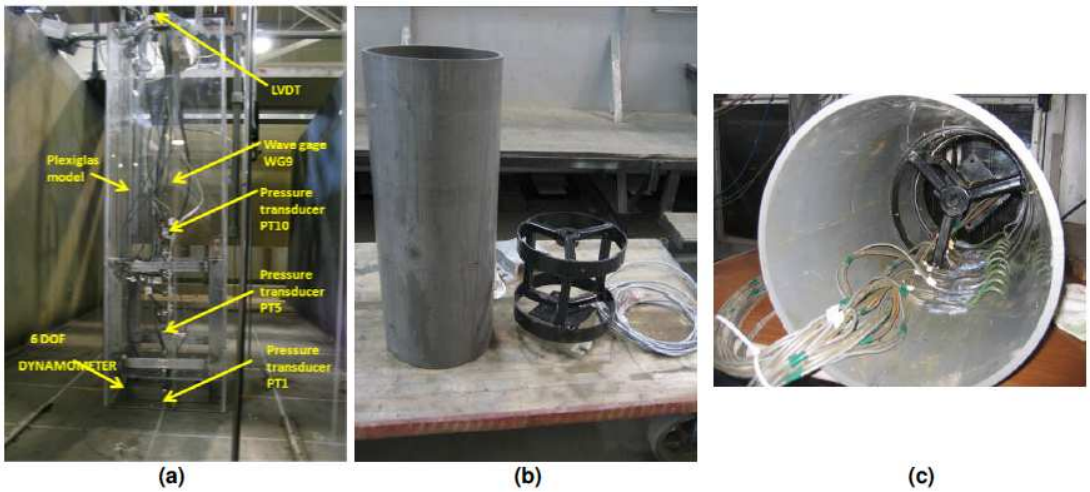

Structural elements and instrumentation: a) square column; b) and c) circular column.

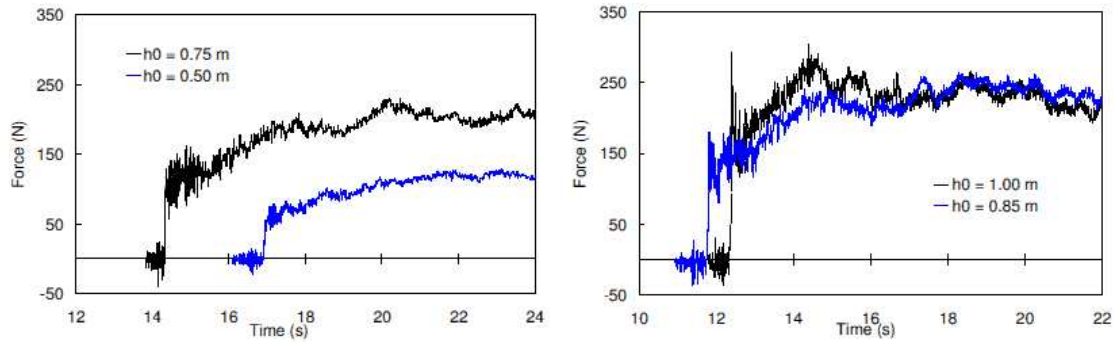

Time history of the total force exerted on the circular structure for various impoundment depths, h0, (Nouri, 2008).

Figure C.12: Physical experiments by (Ioan; Nistor et al., 2010; Younes Nouri et al., 2010; Palermo, Nistor, Nouri, & Cornett, 2009)

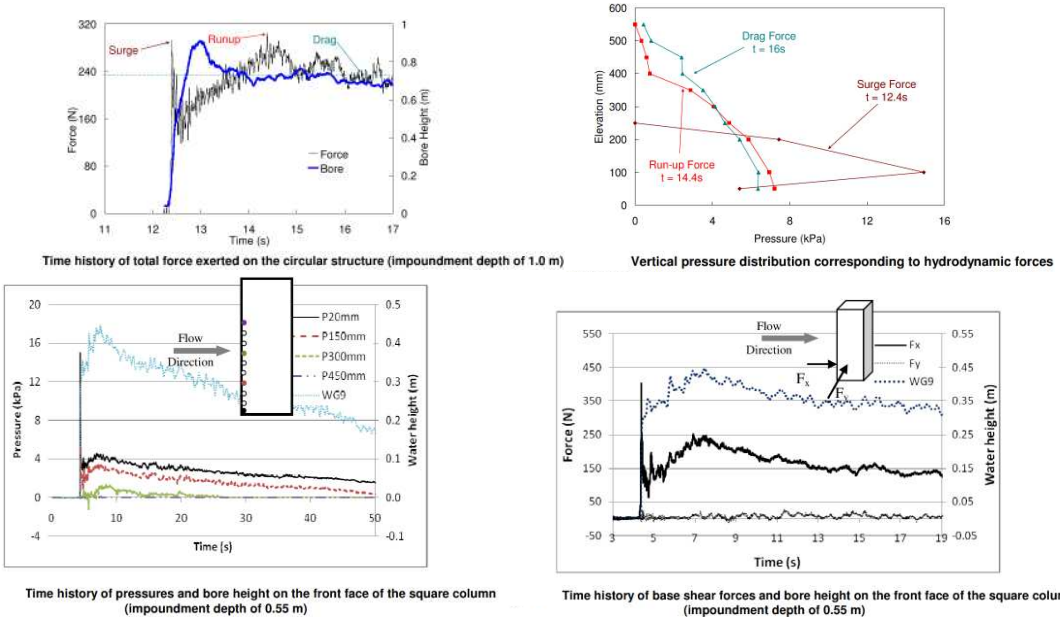

Time history of total force exerted on the circular structure (impoundment depth of 1.0 m)

Vertical pressure distribution corresponding to hydrodynamic forces

Time history of pressures and bore height on the front face of the square column (impoundment depth of 0.55 m)

Time history of base shear forces and bore height on the front face of the square column (impoundment depth of 0.55 m)

Figure C.13: Numerical experiments by (Ioan; Nistor et al., 2010; Younes Nouri et al., 2010)

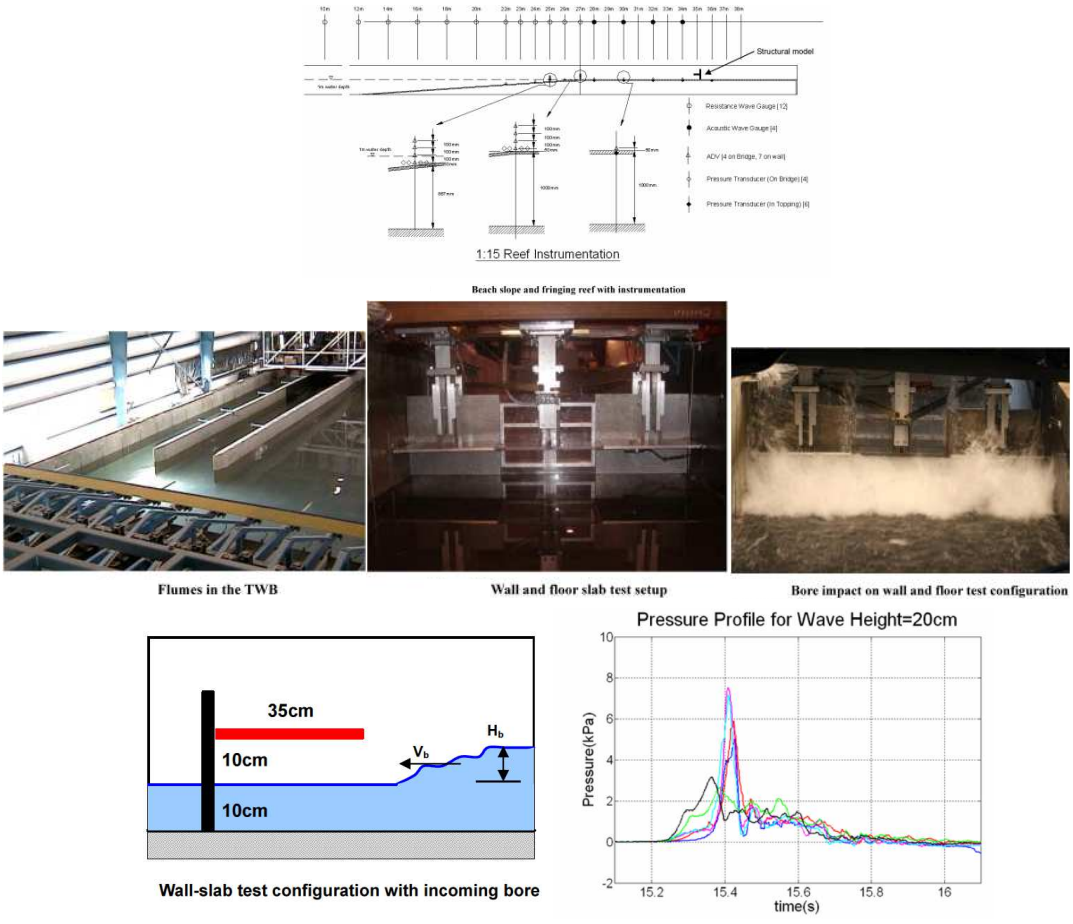

Flumes in the TWB

Wall and floor slab test setup

Bore impact on wall and floor test configuration

Wall-slab test configuration with incoming bore

Figure C.14: Figure F.15: Uplift pressure on floor slab for bores caused by 20, 40 and 60 cm solitary waves with 10 cm water on reef (I N; Robertson et al., 2008)

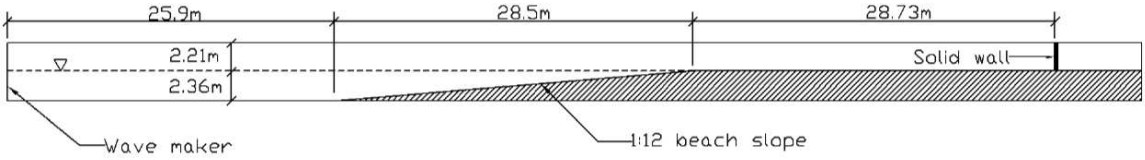

Beach slope and fringing reef with solid wall specimen

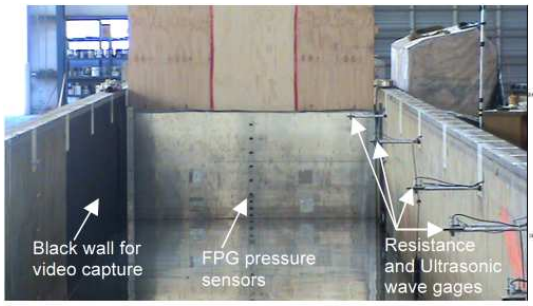

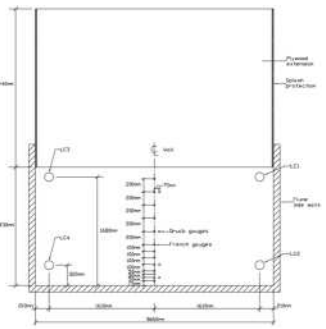

View of instrumented aluminum wall and plywood extension to prevent overtopping

Force time history for 118cm waves on dry reef

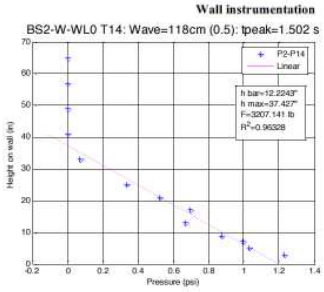

Typical wall pressure distribution at peak lateral load for 118cm wave on dry reef

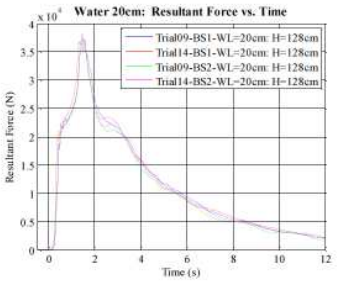

Force time history for 128cm waves with 20cm standing water on reef

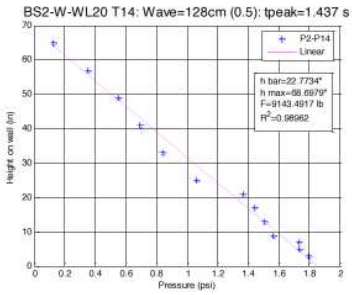

Typical wall pressure distribution at peak lateral load for 128cm wave with 20cm standing water on reef

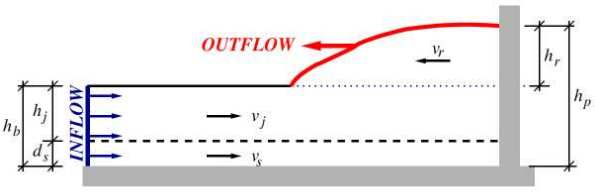

Figure 15. Schematic of bore

$$F = \frac{1}{2}\rho g h_b^2 + \rho h_j v_j^2 + \rho g^{1/3}\left(h_j v_j\right)^{4/3}$$

Comparison of different wall force calculation approaches

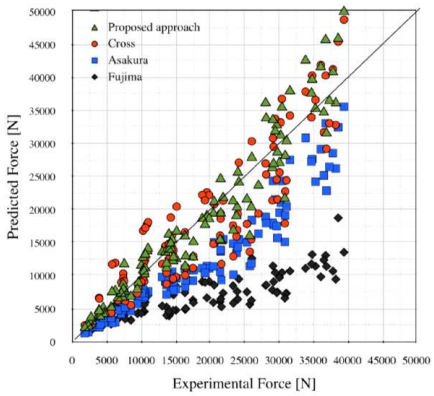

Predicted force versus experimental force.

Figure C.15: Flume experiments by (Ian N Robertson & Riggs, 2011)

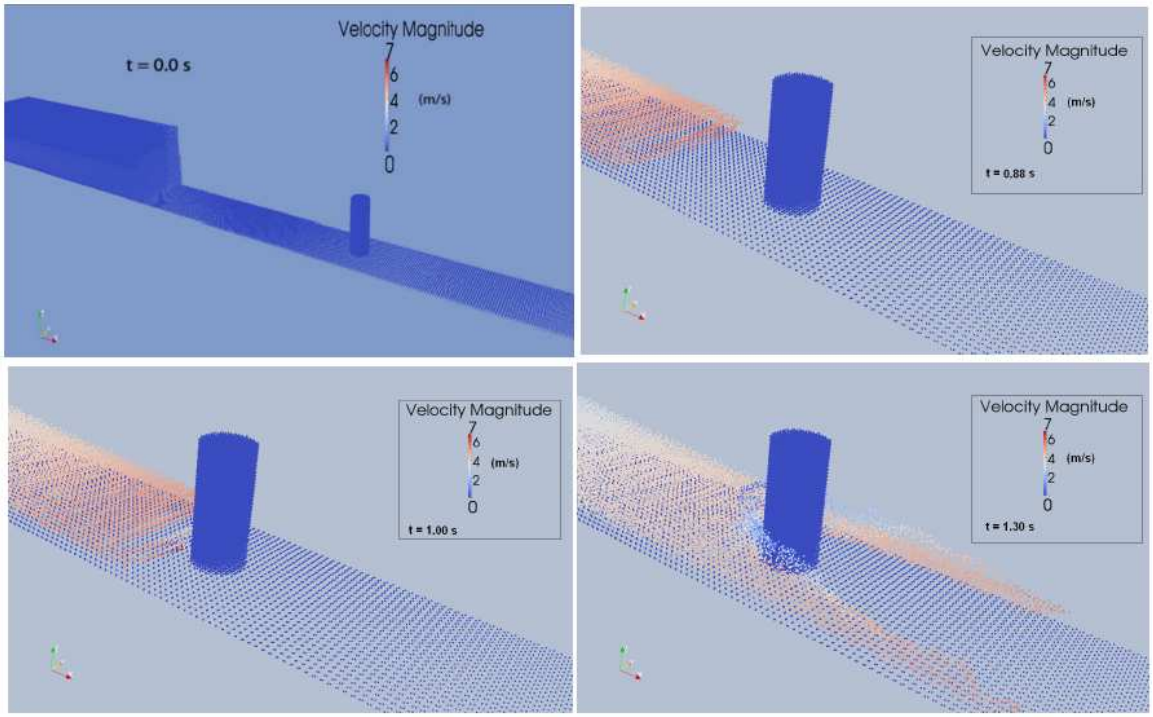

Flow velocity field around the circular column at t = 0.00, 0.88, 1.00, and 1.33 seconds after gate opening.

Figure C.16: (Ioan; Nistor et al., 2010)

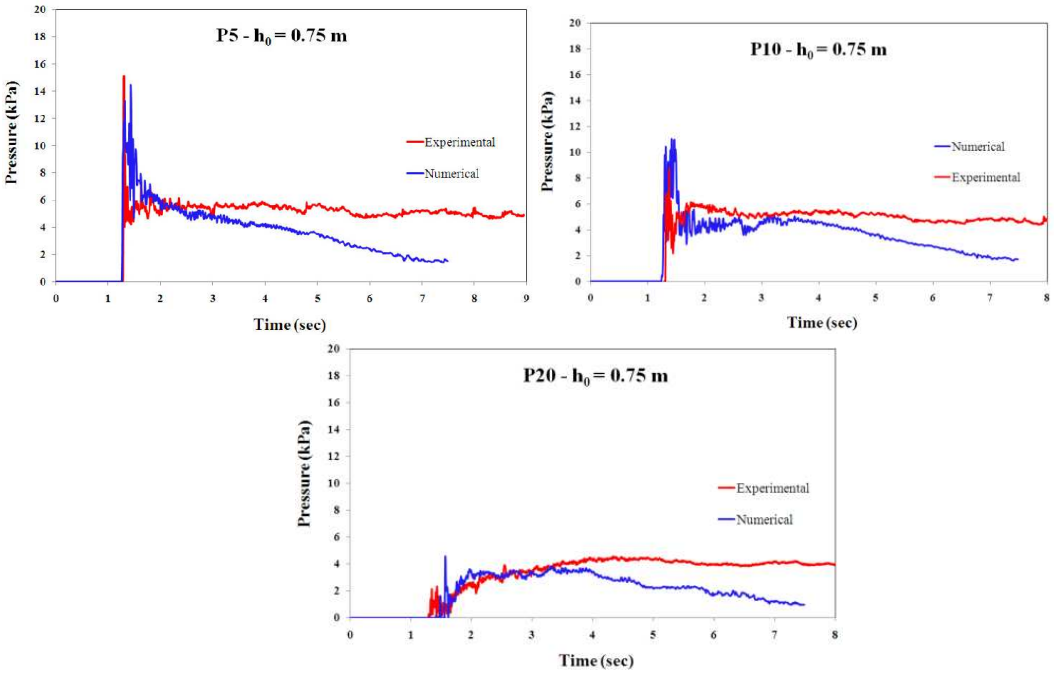

Figure C.17: Comparison of the experimental and numerical pressure time-history for various pressure transducers (circular column with impoundment of 0.75 m, h0 represents the bottom of the flume). The total computational time for duration of simulation of 4.00 seconds was approximately 172 hours (using a 2 GHz Intel Xeon E5405 system with single processor and 16 Gb RAM). (Ioan; Nistor et al., 2010)

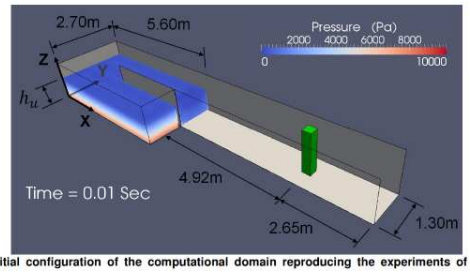

Initial configuration of the computational domain reproducing the experiments of Nistor *et al.* (2010).

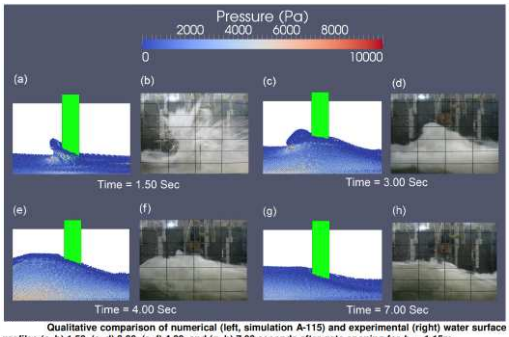

Qualitative comparison of numerical (left, simulation A-115) and experimental (right) water surface profiles (a, b) 1.50, (c, d) 3.00, (e, f) 4.00, and (g, h) 7.00 seconds after gate opening for h_u = 1.15m.

Table 1. Details of numerical simulations corresponding to the experiments of Nistor *et al.* (2010).

Simulation	h_u (m)	c_0 (m/s)	Number of Particles
A-55	0.55	39.42	459,260
A-85	0.85	49.00	654,648
A-85-NC[4]	0.85	49.00	648,060
A-115	1.15	57.00	849,580

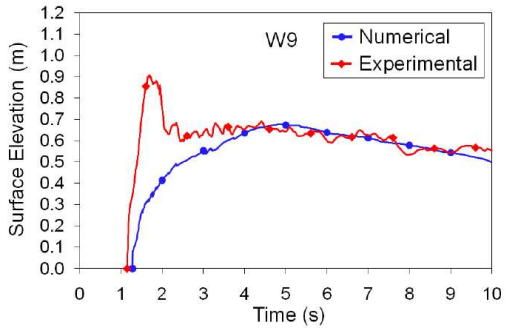

Comparison of numerical (simulation A-85) and experimental time-history of the water surface elevation at wave gauges W9 for h_u = 0.85m.

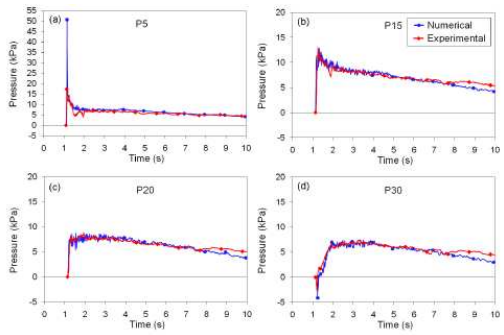

Comparison of numerical (simulation A-115) and experimental time-history of pressures acting on the column at elevations of (a) 0.05, (b) 0.15, (c) 0.20, and (d) 0.30m above the flume's bottom for h_u = 1.15m.

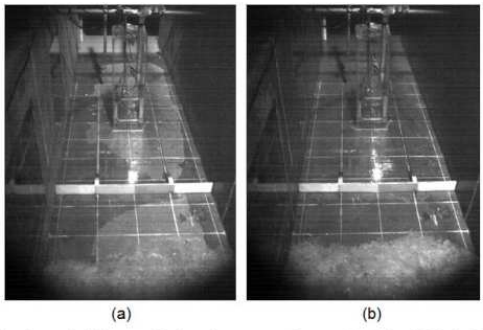

Experimental still frames of the bore-front propagating over (a) a "virtually" dry bed ($h_d \approx 0$) and (b) a wet bed ($h_d \approx 0.005$m) with h_u = 0.55m.

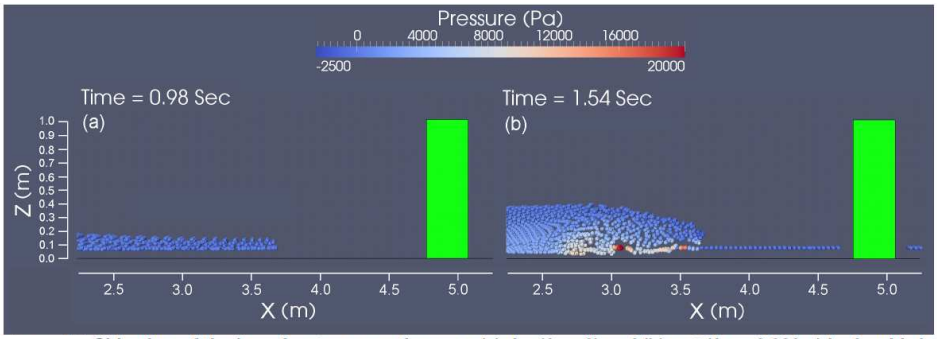

Side view of the bore-front propagating over (a) dry (h_d = 0) and (b) wet ($h_d \approx$ 0.080m) beds with h_u = 0.85m (St-Germain *et al.*, 2012).

Figure C.18: Numerical experiments by (Ioan; Nistor et al., 2010)**.**

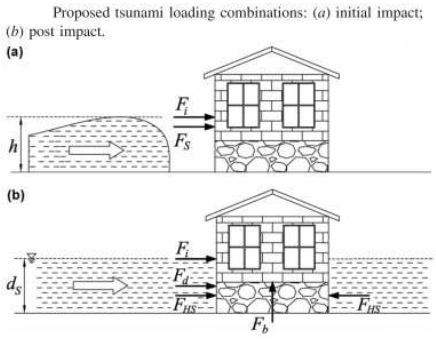

Figure C.19: Proposed tsunami loading combinations: (a) initial impact; (b) post impact.(Palermo et al., 2009)

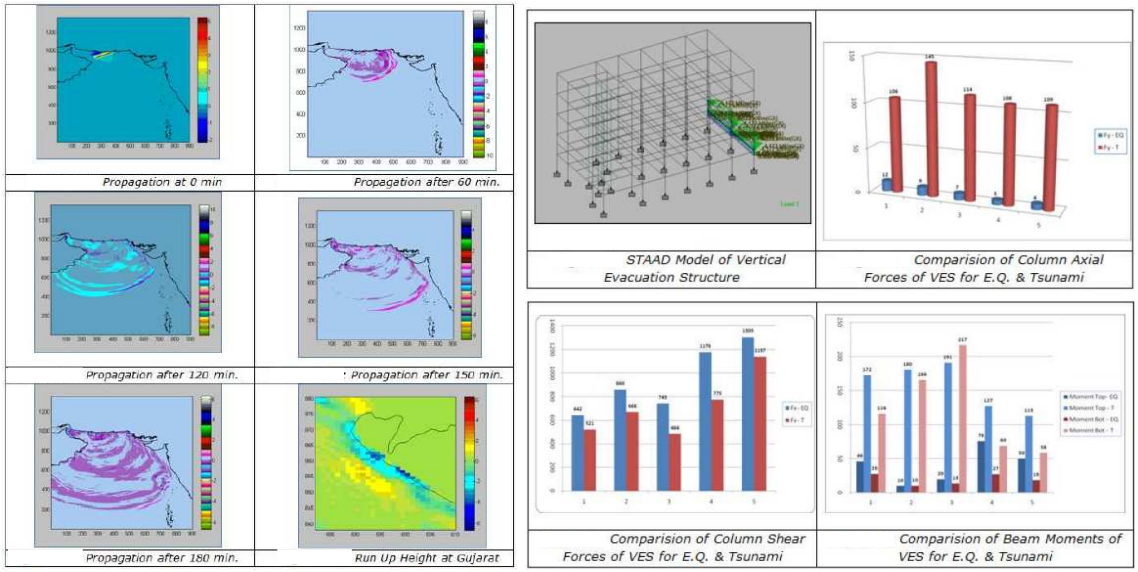

Figure C.20: (Patel, Patel, & Singh, 2011)

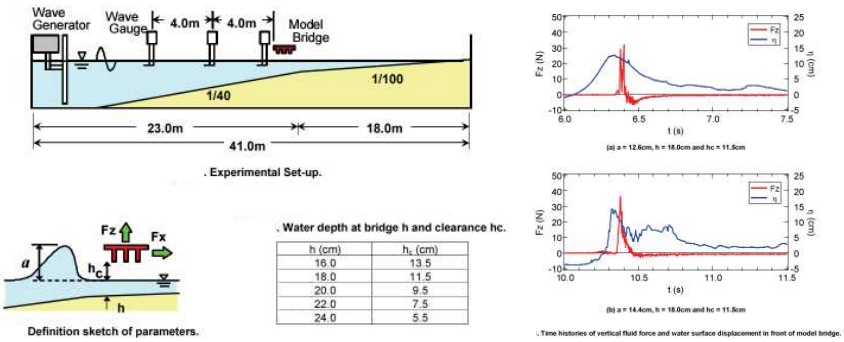

Figure C.21: Girder bridge experiments by Araki et al. (2010)

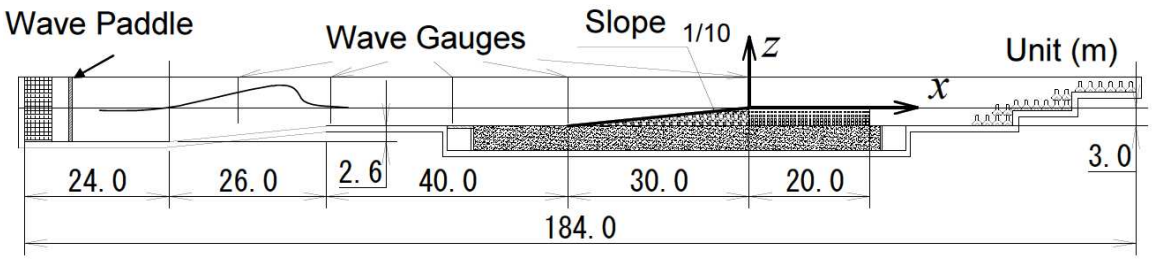

Tsunami wave generator

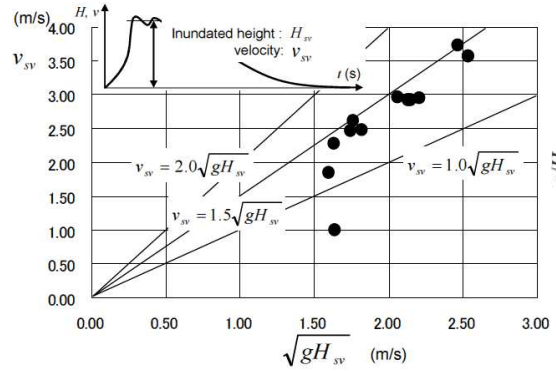

Flow velocity- inundation height relation

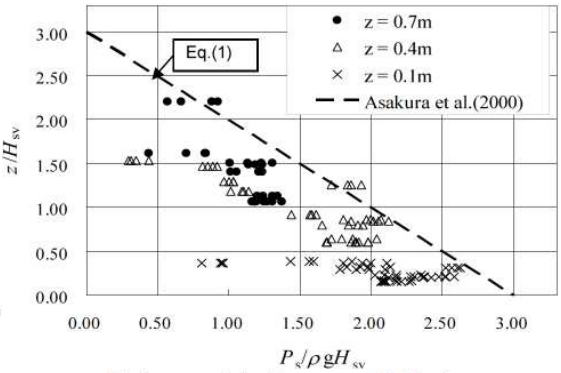

Maximum sustainable pressure distribution

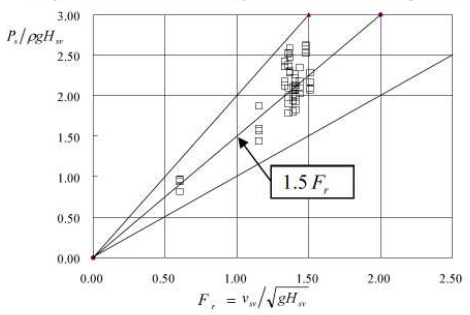

Relationship between $P_s / \rho gH_{sv}$ and Froude number F_r

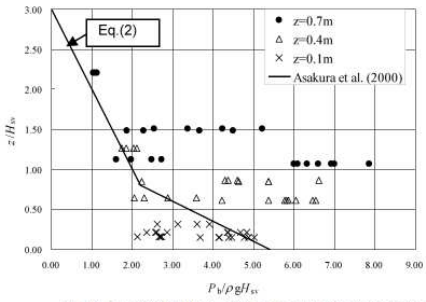

Vertical distribution of the maximum impulsive bore pressure

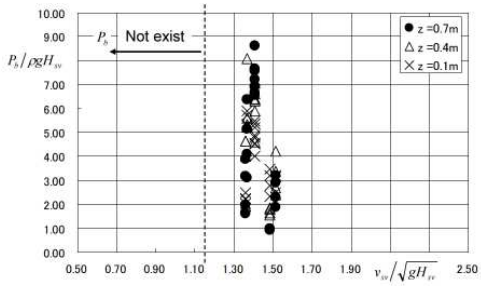

Relationship between maximum impulsive bore pressure P_b and Froude number F_r

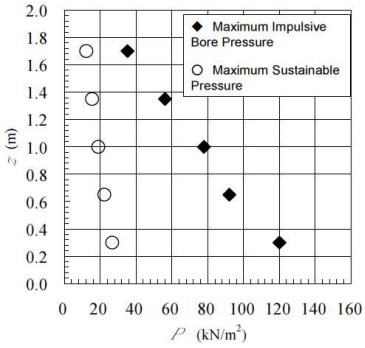

Vertical average pressure distribution

Figure C.22: (Arikawa et al., 2012)

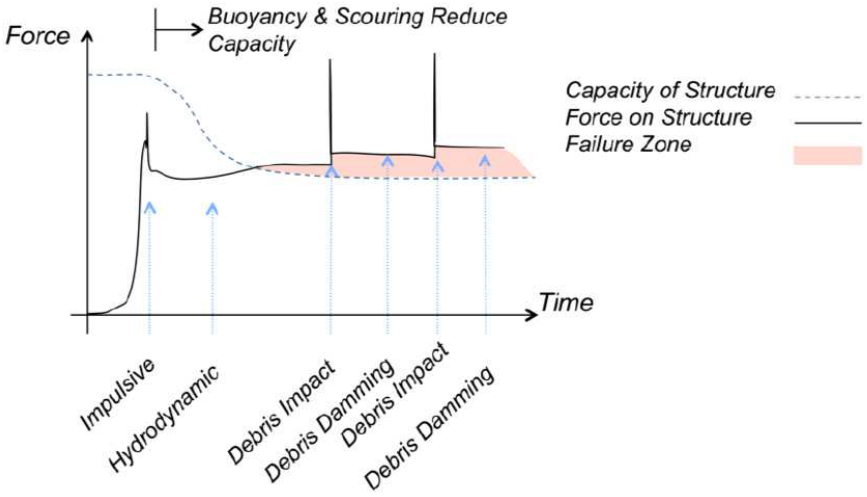

Figure C.23: Typical time series of loading and capacity. An object is assumed inundated initially so that the impulsive force is greater than the subsequent hydrodynamic force, and the structural capacity decreases in time because of the gradual development of buoyancy force and scour action through the surrounding soils (to be discussed in detail later).(Harry; Yeh et al., 2014)

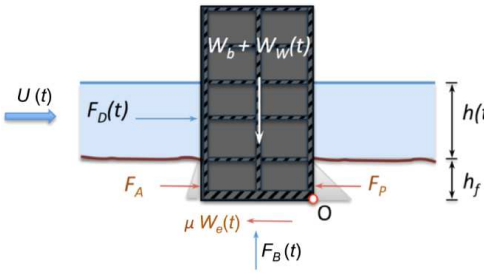

Two stability conditions are considered: (i) incipient sliding and (ii) incipient overturn Incipient sliding occurs when the sum of horizontal forces F_H is greater than zero,:

$$\sum F_H(t) = F_X(t) - R_X(t),$$

where $F_X(t)$ is the sum of the external forces acting on the building (in the present case, this is hydrodynamic force $F_D(t)$), and $R_X(t)$ is the resisting force:

$$R_X(t) = \mu W_e(t) - (F_A - F_P),$$

where F_A and F_P are the active and passive soil pressure forces, respectively, $\mu = \tan\phi$ is the fric coefficient (ϕ is the friction angle). Incipient overturning results when the sum of clockwise mom about a reference point (point O in Fig. 5) becomes greater than zero:

$$\sum M_0(t) = \left(\tfrac{1}{2}h(t) + h_f\right)F_X(t) + \tfrac{1}{3}h_f(F_A - F_P) - \tfrac{1}{2}aW_e(t),$$

Figure C.24: Free body diagram used in global stability analysis. FD is the external hydrodynamic force; Wb is the dry weight of the building; ww is the weight of the flooded water inside of the building; FB is the buoyancy force; FA and FP are active and passive soil pressure forces, respectively; ∝ is the friction coefficient. The moment is computed about the foundation base point "O".(Harry; Yeh et al., 2014)

Standing flume.

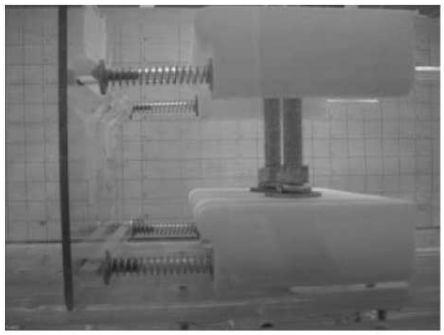

Close up view of spring system with robot-cut plastic plates.

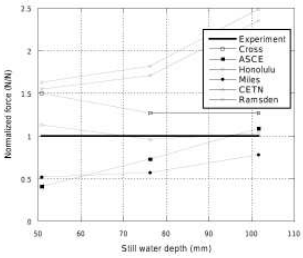

Figure C.25: (Aguíñiga et al., 2013)

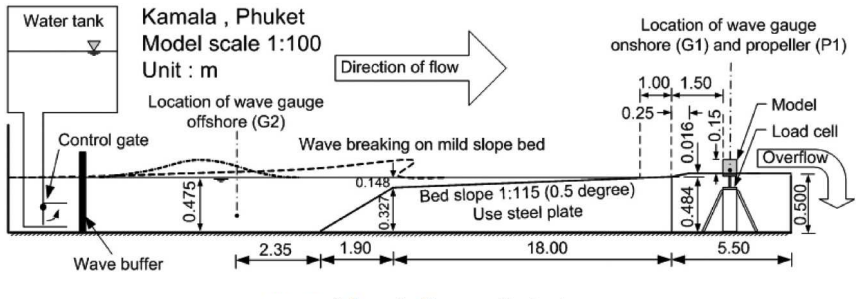

Schematic diagram of test setup.

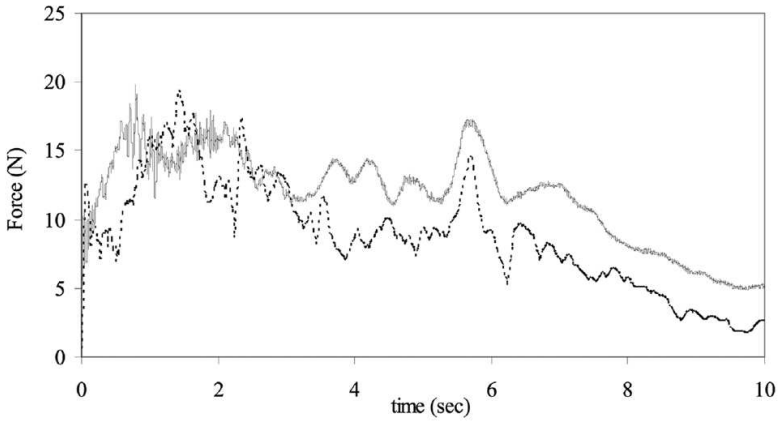

Temporal variations of forces for the case $h_0 =$ 60 mm: solid line, measured; dotted line, prediction by the drag forces Eq. (4).

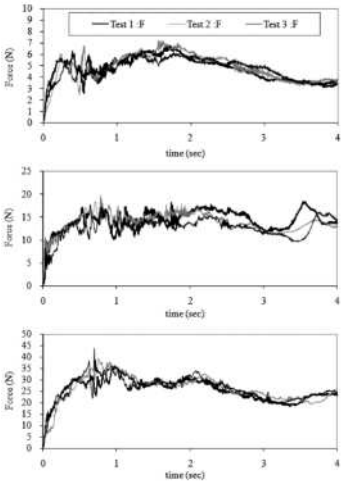

Temporal variations of the wave forces exerted on the model: a) the case with nominal wave of $h_0 = 40$ mm, b) $h_0 = 60$ mm, c) $h_0 = 80$ mm.

Figure C.26: (Panitan Lukkunaprasit et al., 2009)

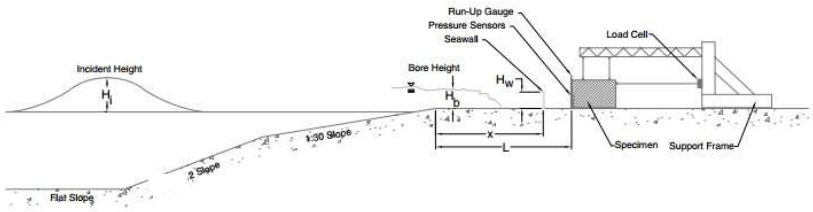

Fig. 3. Schematic of experiment with relative position of slope break, seawall, and specimen (figure not to scale)

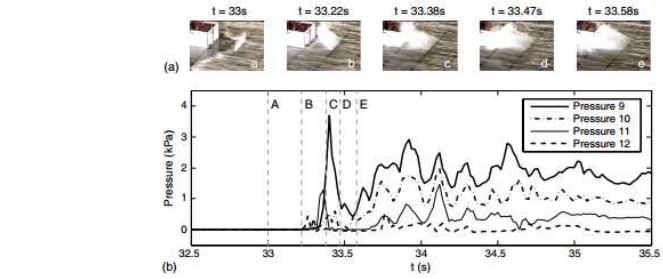

(a) Sequence of images showing initial impact of tsunami on small seawall and "ramp" effect; (b) time series of vertical array pressure array; letters A, B, C, D, and E in Fig. 7(a) correspond to times shown in the pressure time series in Fig. 7(b); images and pressure time histories shown for seawall trial 21, wall 1, position 5 ($x/L = 0.88$) (images by S. Thomas)

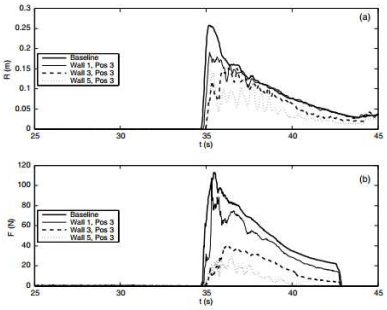

Time series of (a) run-up and (b) force for baseline condition (thick solid) and three wall heights at $x/L = 0.625$ (position 3) for ERF = 7 s; run-up is measured on side of specimen facing the oncoming tsunami (R4)

$$\frac{F_{max}}{(F_b)_{max}} = -0.331\left(\frac{H_w}{H_b}\right) + 0.027\left(\frac{H_w}{H_b}\right)^2 + 0.341\left(\frac{x}{L}\right) - 0.076\left(\frac{x}{L}\right)^2 + 1.109 \quad (1)$$

$$\frac{F_{ave}}{(F_b)_{ave}} = -0.204\left(\frac{H_w}{H_b}\right) - 0.003\left(\frac{H_w}{H_b}\right)^2 + 0.118\left(\frac{x}{L}\right) - 0.500\left(\frac{x}{L}\right)^2 + 0.847 \quad (2)$$

Figure C.27: Influence of Finite-Length Seawalls for Tsunami Loading on Coastal Structure. Thomas, Seth; Asce, M; Cox, Daniel (Thomas et al., 2012)

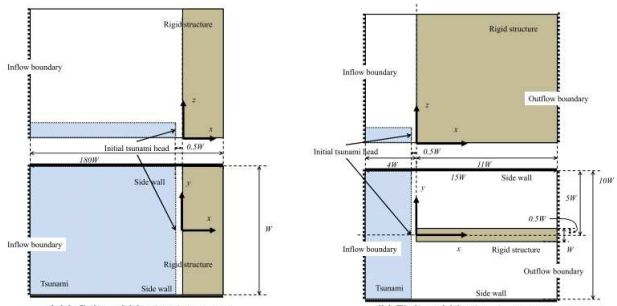

Numerical model

Parameters in numerical simulations		
	Infinite-width structure case	Finite-width structure case
W/h_{in}	Infinite	0.5, 1.0, 2.0, 5.0
F_r	0.8, 1.5, 2.0, 3.0	1.0, 1.5, 2.0, 3.0

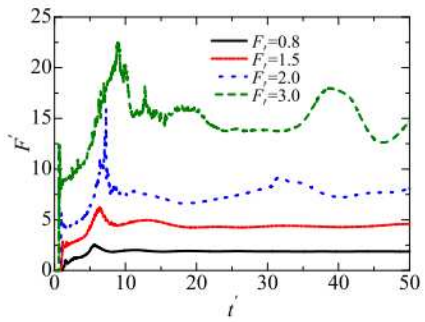

Time-history of the hydrodynamic force acting on the front face of a structure in infinite-width structure case

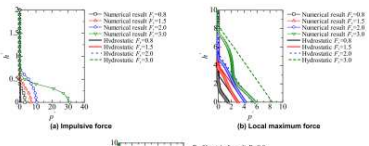

Figure 7. Pressure distribution acting on the front face of a structure in infinite-width structure case

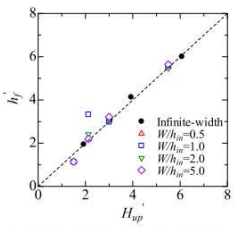

Relationship between the non-dimensional specific energy and the non-dimensional water level in the front of a structure

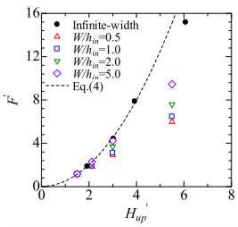

Relationship between the non-dimensional specific energy and the non-dimensional quasi-steady force acting of the front face of a structure

Figure C.28: (Takabatake & Kihara, 2014)

D. Tsunami Design Guidance

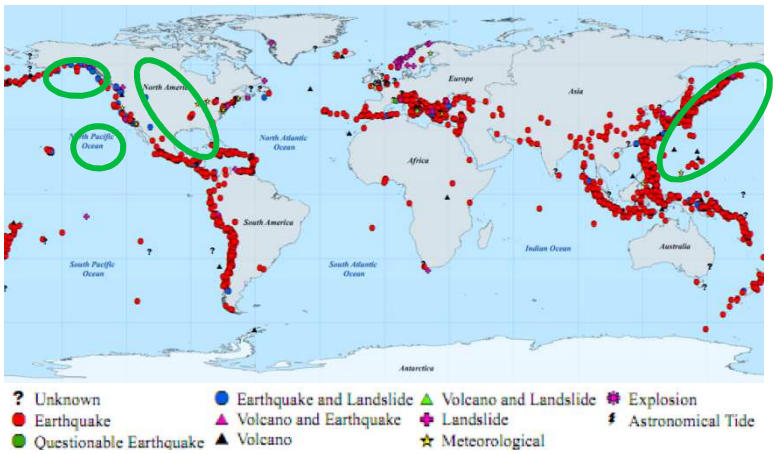

Figure D.1: Historical tsunami events seperated by tsunami cause. Locations currently with tsunami design guidance documents are circled in green, all other locations are without accepted codes of practice for design. <(Nassirpour, 2012)**replace with own figure>**

Table D.1 gives an overview of the comparison between the two sets of design guidance.

	Japanese Guidance (MLIT, 2011a)	US Guidance (ACSE 7-16)
Tsunami Hazard Assessment	Tsunami inundation maps are defined from deterministic Tsunami Hazard Assessments based on source earthquakes with two approximate return periods: Level 1 : 1-in-100yr Level 2 : 1-in-1000yr	Offshore tsunami amplitude maps are defined at a bathymetry contour of 100m depth, determined from Probabilistic Tsunami Hazard Assessment (carried out for five states in the USA, which are deemed to have the greatest tsunami risk). The Maximum Considered Tsunami corresponds to a 1-in-2475yr event.
Sea Defence Design	Sea defence design guidance is developed by the Japan Society of Civil Engineers and other institutions in Japan. The design procedure is to prevent inundation from Level 1 event, and prevent failure (but allow overtopping) for Level 2 event.	There is not currently any accepted code of practice which specifically addresses tsunami design of sea defences in the USA.
Building Design Procedure	Buildings are designed for inundation corresponding to a Level 2 event (as inundation due to a Level 1 event should be prevented by sea defences). Member and structure design is to account for lateral fluid loads, buoyancy, retained water, and secondary effects of debris impact (by prevention of progressive collapse) and scour (by use of deep foundations) though little guidance is given on quantification of these secondary effects.	Performance-based design using tsunami risk categories and performance level objectives based on building function and occupancy. <THIS IS ONE OPTION> Member and structure design is to account for lateral fluid loads, buoyancy, retained water, and secondary effects of debris impact and scour. Guidance is given on quantification of secondary effects of debris impact and estimated scour depth.
Load Assessment for Buildings	Lateral fluid load is calculated as an equivalent hydrostatic load applied to one side of structure. Height of hydrostatic load profile is taken as the design inundation depth multiplied by a factor which accounts for distance from shore and presence/absence of seaward obstacles. Calculations require a design inundation depth, which may be taken directly from tsunami inundation maps, provided by Municipalities.	Lateral fluid load is calculated for hydrostatic, and hydrodynamic force components using calculated inundation depths and velocities. Calculations require design inundation depth and velocity, which are calculated from Offshore Tsunami Amplitude Maps, using either Energy Grade Line Analysis or site-specific numerical inundation modelling.

Table D.1: Comparison of the two main tsunami engineering design guidance documents.

D.1 Design Guidance in Japan

The table below describes the evolution of tsunami-related design guidance in Japan prior to 2011.

Table D.2 Legislation and guidance documents relevant to tsunami design and planning in Japan.

Year	Summary of regulations
1959	**Concerning the Prevention of Disasters to Buildings from Storm and Flood Damage (Housing Bureau Notification No. 42)** Sets out the matters for the designation of disaster risk zones and states that schools, government offices, public halls and other community buildings accommodating large numbers of persons and housing should be sturdy and evacuation areas should be located higher than the predicted inundation depth. In addition, it is stated that the construction of buildings for dwelling purposes in particularly at-risk zones should be prohibited (MLIT, 2011b).
1960	**Building Standard Law of Japan (BSLJ) - Article 39** The 1960 update covers matters including the establishment of tsunami evacuation frameworks and the designation of high-risk areas possibly subjected to tsunami, storm surge, flood, etc. Although BSLJ allows local governments to designate tsunami-prone areas as High Disaster-Risk Area, there were few designated areas prior to 2011. Note that verification of structural safety against tsunami load is not mandatory in the Building Standard Law of Japan (BSLJ) (Hitomitsu, 2011). Note also that this clause is a general one covering floods and other hazards. There are no specific provisions for tsunami loadings (IStructE, 2013).
2004	**Structural Design Method of Buildings for Tsunami Resistance (Okada et al., 2004)** This document (SDMBTR) provides guidance on tsunami forces to be applied to buildings. The prescribed lateral tsunami force is described in Figure D.2 and the document also provides guidance on the effect of buoyancy, as well as load combinations. The document is in two parts: preliminary discussion and proposed design method (Fukuyama et al., 2012; Shibayama et al., 2013).
2005	**Japan Cabinet Office Tsunami Evacuation Building Guidelines** (Japan Cabinet Office, 2005) Gives guidelines aimed at Municipality officers regarding the designation, location and usage of tsunami evacuation buildings. Appendix II ("Basic View on Structural Requirements") provides official design guidelines with reference to SDMBTR (see above) (Fukuyama et al., 2012; MLIT, 2011b).
Mar 2011	**Great East Japan Earthquake and Tsunami**
Nov 2011	**The Design Method of Safe Buildings that are Structurally Resistant to Tsunamis, etc. (MLIT Technical Advice No.2570)** (MLIT, 2011b) Provides provisional amendments to the Japan Cabinet Office Tsunami Evacuation Building Guidelines based on information gathered after the 2011 tsunami.
Dec 2011	**Concerning Setting the Safe Structure Method for Tsunamis which are Presumed when Tsunami Inundation Occurs (MLIT Notification No.1318)** (MLIT, 2011a) Makes several recommendations for design and construction of buildings which are resistant to tsunami loading (Kabeyasawa, 2013).

D.1.1 Design Guidance Prior to the 2011 Japan Tsunami: "Structural Design Method of Buildings for Tsunami Resistance" (SDMBTR) (Okada et al., 2004)

At the time of the 2011 Great East Japan Earthquake and tsunami, Japanese tsunami design guidance took the form of a document titled "Structural Design Method of

Buildings for Tsunami Resistance" (SDMBTR) (Okada et al., 2004), which recommends using an equivalent static pressure distribution over a height three times the tsunami inundation depth (Figure D.2, Eq. (D.1)). Design inundation depth is based on Tsunami Hazard Maps provided by local governments.

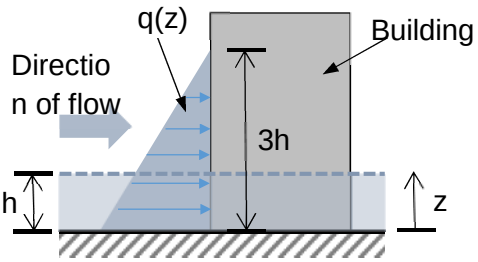

$$q(z) = \rho g(3h - z) \qquad \textbf{(D.1}$$

Where, *q(z)* is the design tsunami wave pressure.

Figure D.2 Tsunami wave-loading for structural design recommended by Japanese guidance.

For structures taller than three times the height of the design inundation depth (3h) Eq. (D.1) gives a total force equal to nine times the hydrostatic force for an equivalent flow depth[1]. A study by Yeh, Robertson, & Preuss (2005) suggested that this approach gives excessive loading estimates.

The SDMBTR guidelines are based on a study by Asakura et al. (2000) which carried out 84 2-dimensional hydraulic model experiments which measured the pressures exerted on structures positioned at various distances from the sea bed for various wave heights, periods and Froude Numbers (a measure of flow velocity non-dimensionalized by the gravitational wave velocity). The effects of sea walls and other protective barriers were not reviewed in these experiments.

D.1.2 Findings From Post-Tsunami Damage Survey

D.1.2.1 Estimating Equivalent Hydrostatic Force Factor

Following the 2011 tsunami an investigative report entitled "A study of Improvement of Building Standards etc. in the tsunami critical areas" was published by the University of Tokyo Institute of Industrial Science and Japan's Building Research Institute (BRI) under the "Building Standards Maintenance Promotion Program" (Tokyo University & BRI, 2011).

The study used several case-study structures which experienced tsunami flow, including 35 buildings (RC structures between 1 and 4 stories) and 42 other structures (free-standing walls and pillars, monuments, bridges and sea defences). For each case-study structure:

- $h_{measured}$ = measured inundation depth at the structure location.
- $h_{capacity}$ = depth at which the structure would be expected to collapse if subjected to a hydrostatic pressure distribution (calculated based on the structural properties of the case study structure).
- α = water depth coefficient ($h_{capacity}$ / $h_{measured}$). (NB/ can also be thought of as an estimated "over-strength coefficient").

[1] $\rho g \int_0^{3h_{max}} (3h_{max} - z)\, dz = 4.5\rho g h^2 \quad \rightarrow \quad \frac{4.5\rho g h^2}{1/2 \rho g h^2} = 9$

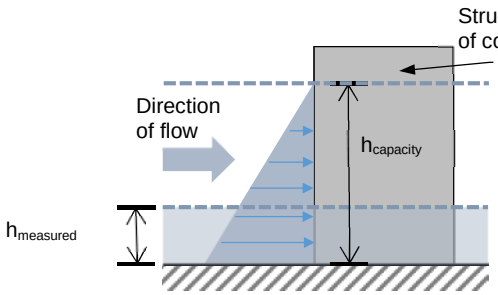

$$\alpha = \frac{h_{capacity}}{h_{measured}} \qquad \text{(D.2)}$$

Figure D.3 Definition of water depth coefficient (*α*). A unique value for each case-study building calculated as the theoretical depth at which hydrostatic pressure on one side of a structure would cause it to collapse, divided by the actual measured inundation depth.

The relationship between $h_{measured}$ and α for all case study structures is shown in Figure D.4, where a high coefficient of water depth ($\alpha > 1$) indicates that the estimated structural strength is *α*-times greater than the equivalent hydrostatic load corresponding to the measured inundation depth. Conversely, a low coefficient of water depth ($\alpha < 1$) indicates that the structure is estimated to be weaker than the measured depth's equivalent hydrostatic load. The case-study structures are separated into 2 groups: those with and without seaward obstructions (i.e. in the case of the latter, no sea defences or buildings between the structure and the sea). Note that many of the case-study structures without obstruction were the sea defences themselves.

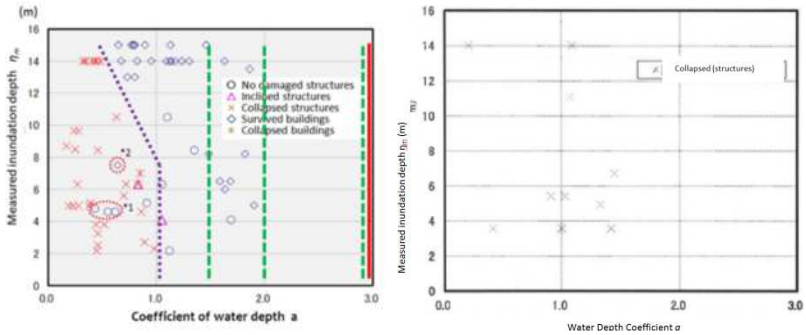

Figure D.4 Water depth coefficient (*α*) vs measured inundation depth, for all case-study buildings and structures. Left-hand graph shows the cases with seaward barriers and the right-hand shows those without (exclusively sea defence structures). Structures with seaward barriers demonstrate a water depth coefficient of around 1, reducing once depths exceed 8m. <and those without barriers…>

Figure D.4 suggests a relationship between the equivalent hydrostatic force (Figure D.3) and the observed collapse of structures, and so for collapse-prevention design purposes (NB, not performance-based design purposes) it was considered that the use of an equivalent hydrostatic force, as per SDMBTR, to estimate tsunami loading was adequate. However, Figure D.4 shows that the design wave pressure in SDMBTR, taken as hydrostatic with $\alpha = 3$ (Figure D.2, Equation (D.1)) overestimated the tsunami loading experienced during the GEJE.

D.1.2.2 Estimating Velocity and Froude Number Based on Drag

To investigate this further, velocity was considered. Equation (D.2) estimates tsunami load based solely on inundation depth, and so to estimate tsunami flow velocities around buildings during the GEJE a hydrodynamic load was instead considered to dominate.

The following was calculated for each case-study structure:

- $\omega_{capacity}$
  - For the measured inundation depth ($h_{measured}$), $\omega_{capacity}$ = the pressure at which the structure would be predicted to collapse if subjected to a uniform (drag) pressure distribution.
  - $\omega_{capacity}$ is therefore a function of the measured inundation depth and the structural properties of the case-study structure.
- $u_{capacity}$
  - At $h_{measured}$, $u_{capacity}$ = the velocity at which the structure would be predicted to collapse due to drag.
- Frcapacity
  - At hmeasured, Frcapacity = the Froude number at which the structure would be predicted to collapse due to drag.
  - o

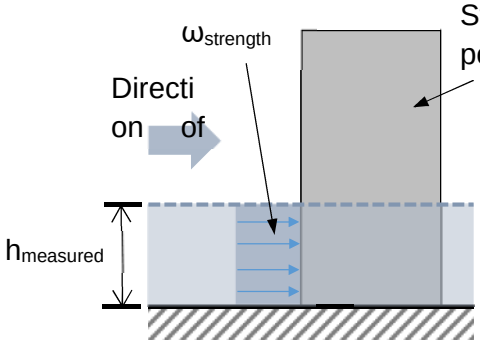

$$\omega_{capacity} = f\left(h_{measured}, \frac{structural}{properties}\right)$$

$$u_{capacity} = \sqrt{\frac{\omega_{capacity}}{\rho}}$$

$$Fr_{capacity} = \frac{u_{capacity}}{\sqrt{g h_{measured}}}$$

  - o

Figure D.5: Calculation of theoretical pressure, velocity and Froude number at which hydrodynamic pressure on one side of a case-study structure would cause it to collapse.[2]

These 3 values ($\omega_{capacity}$, $u_{capacity}$, $Fr_{capacity}$) are plotted for each case-study structure in Figure D.6, Figure D.7 and Figure D.8 respectively. The x-axes give the locations of the case study structures, starting with the southernmost locations on the left of the x-axes. The case-study structures are separated into the same 2 groups as in Figure D.4 (i.e. those with and without seaward obstructions or "barriers"). Those with barriers were further separated into 2 groups: those in mountainous regions (i.e. the rias coastline, "*Sanriku*") and those on coastal plains ("flatland area"). The level of damage experienced by each case-study structure is denoted as in Table D.3. It is assumed that the boundary between collapsed and undamaged structures, indicates the pressures, velocities and Froude Numbers experienced by the case study buildings. These experienced flow conditions vary with location, but their averaged values are summarized in Table D.4.

---

[2] $F_{drag} = \frac{1}{2} C_D \rho u^2 A_D$, $F_{capacity} = \omega_{capacity} A_D$

$C_D = 2$ & at collapse: $F_{drag} = F_{capacity}$ & $u = u_{capacity}$...

Therefore: $u_{capacity} = \sqrt{\frac{\omega_{capacity}}{\rho}}$

Note that structures with significant openings were found to survive when the estimated applied load greatly exceeded their calculated capacity, so they have been omitted from the figures below.

Table D.3: Symbols representing damage level of case-study buildings shown in Figure D.6, Figure D.7 and Figure D.8.

	Structures	Buildings	Interpretation
Undamaged:	○	◇	Force experienced < $F_{capacity}$
Structurally Damaged:	Δ		Force experienced = $F_{capacity}$
Collapsed :	X	*	Force experienced > $F_{capacity}$

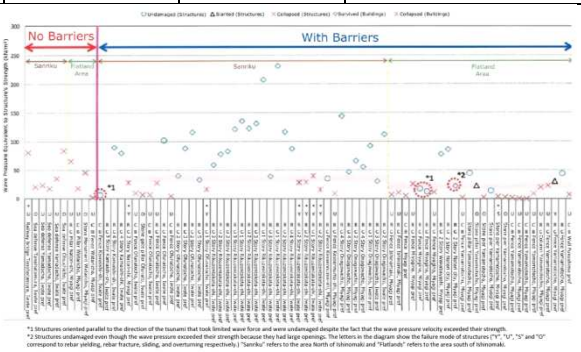

Figure D.6: The pressure ($\omega_{capacity}$) at which the structure would be predicted to collapse if subjected to a uniform (drag) pressure distribution (for the measured inundation depth).

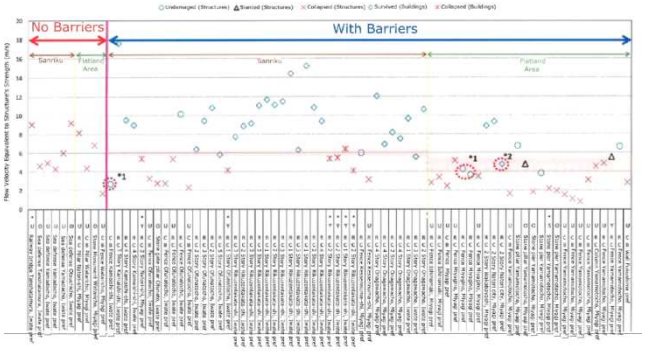

Figure D.7: The velocity ($u_{capacity}$) at which the structure would be predicted to collapse due to drag (at $h_{measured}$).

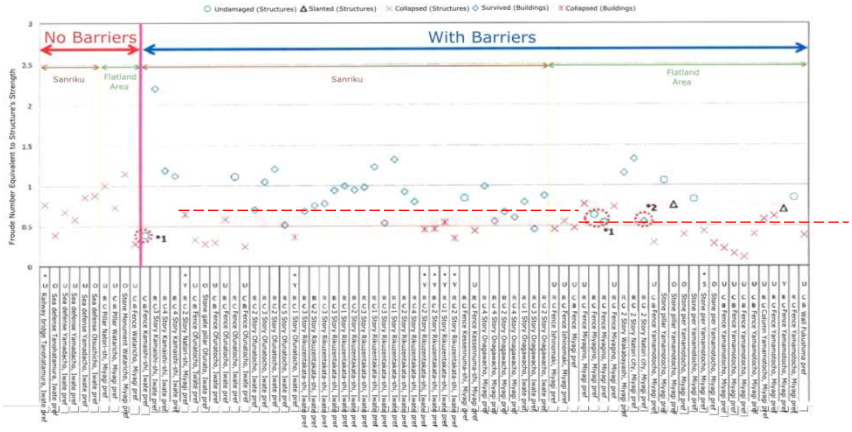

Figure D.8: The Froude number ($Fr_{capacity}$) at which the structure would be expected to fail due to drag (at $h_{measured}$).

Experienced Flow Conditions	Without Seaward Obstructions		With Seaward Obstructions	
	Rias Coastline	Coastal Plains	Rias Coastline	Coastal Plains
Equivalent drag pressure experienced (over the maximum measured inundation depth)	85 kN/m^2		15 – 40 kN/m^2	
Velocity experienced	> 9 m/s		4 – 6 m/s	
Froude number experienced	> 0.9	> 1.2	0.65	0.8

Table D.4: Average approximate flow conditions experienced by the case-study buildings.

The estimated experienced velocities presented in Table D.4 were compared to velocities estimated from survivor videos (generally between 3 – 6 m/s), and from empirical estimates based on inundation and run-up data (between 4 – 6 m/s in areas with barriers, and 6 – 8 m/s in areas without).

D.1.2.3 The Relationship between Froude Number, Velocity and Depth

Note that the estimated experienced velocities were slightly higher in the rias coastline than in the coastal plains (Figure D.7) but the estimated experienced Froude number was slightly lower in the rias coastline than in the coastal plains (Figure D.8, Table D.4). This suggests that funnelling of water in the deep but narrow bays of the rias coastline led to higher maximum velocities, but also greater tsunami depths which resulted in lower Froude numbers.

Figure D.9 shows the relationship between the Froude number, $u_{capacity}$ and $h_{measured}$ and for case-study structures in the rias coastline with seaward obstructions. Here the experienced Froude number can be estimated from the cut-off between destroyed and undamaged structures, which can be seen to occur at Fr = 0.65 for measured inundation depths up to 13m.

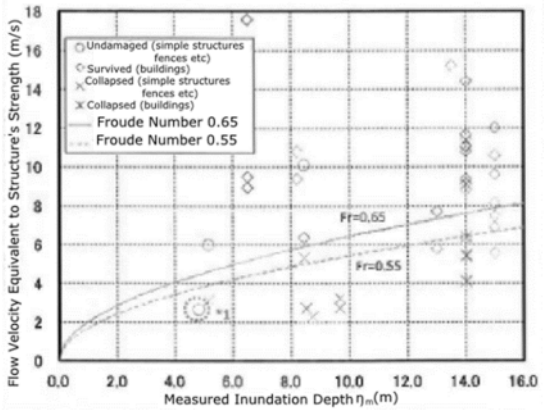

Figure D.9: Relationship between $u_{capacity}$, $h_{measured}$ and $Fr_{capacity}$ for case-study structures in mountainous areas with seaward obstructions.

The estimated experienced Froude number for locations without seaward obstacles was approximately 1.5 times that of locations with obstacles. Furthermore, the estimated experienced Froude number appears to reduce at higher overland flow depths (>13m, Figure D.9), suggesting that as maximum inundation depth increases the maximum experienced velocity does not increase as rapidly, leading to a reduction in the flow's Froude number. Both of these trends are also implicitly present in Figure D.4, relating

the maximum measured inundation depth at each case-study building with the water depth coefficient (*α*), suggesting a link between Fr (derived by assuming a drag force on the case-study structures, Figure D.5) and α (derived from assuming a hydrostatic force, Figure D.3).

D.1.2.4 The Relationship between Froude Number and Depth Coefficient

Assuming both the drag and hydrostatic approximations of the loading are equivalent, then Fr and α can be equated:

$$F_{hydrostatic} = \frac{1}{2} \cdot \alpha h \cdot \rho g(\alpha h) = \frac{\alpha^2}{2}(h^2 \rho g) \quad \textbf{(D.3)}$$

$$F_{drag} = \frac{1}{2} C_D \rho u^2 A_D \quad \textbf{(D.4)}$$

…(where: $C_D = 2$, $A_D = hx1$, $u^2 = Fr^2gh$) …

$$F_{drag} = Fr^2(h^2 \rho g) \quad \textbf{(D.5)}$$

$$F_{hydrostatic} = F_{drag} \rightarrow \frac{\alpha^2}{2} = Fr^2 \quad \textbf{(D.6)}$$

$$\therefore \boldsymbol{\alpha = \mathbf{Fr}\sqrt{2}}$$

The linear relationship proposed by equation (D.6) is evidenced by the experimental data of Asakura et al. (2000), up to the maximum value of *α* = 3 (Figure D.3). The correlation between *Fr* and *α* can also be seen in Figure D.10, which compares tsunami design loads calculated using the drag equation with *Fr* = 0.7, 1.0, 3.0) and equivalent hydrostatic equation (Equation (D.2) with *α* = 1, 1.5, 2, 3, corresponding to *Fr* = 0.71 , 1.06 , 1.41 , 2.12 respectively).

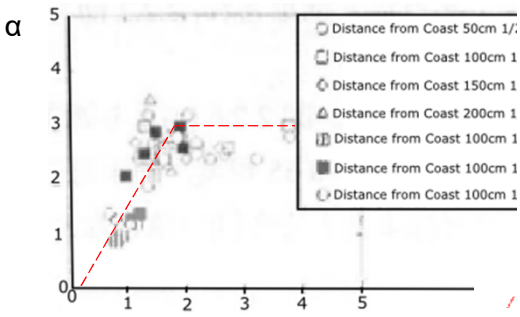

Figure D.10: Relationship between α and Fr for lab experiments by Asakura et al. (2000).

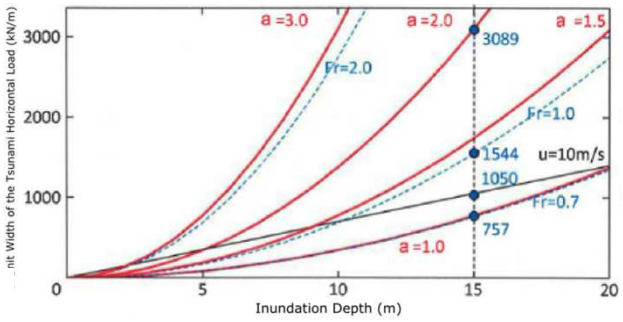

Figure D.11: Comparison of design loads using drag equation (Equation 3 with Fr = 0.7, 1.0, 3.0) and equivalent hydrostatic equation (Equation 2 with α = 1, 1.5, 2, 3).

Therefore the equivalent hydrostatic load (Figure D.3) may be used as an approximation to the hydrodynamic load as long as the load factor (*α*) is chosen so as to represent the Froude number of the experienced flow.

D.1.2.5 Relationship Between Froude Number and Distance from Shore

Figure D.12 shows that the estimated experienced Froude number (at the interface between collapsed and surviving structures) reduces with distance from the shore. This is intuitive as flow velocity is gradually reduced away from the coast as the flow encounters obstacles such as trees, buildings and surface roughness of the ground.

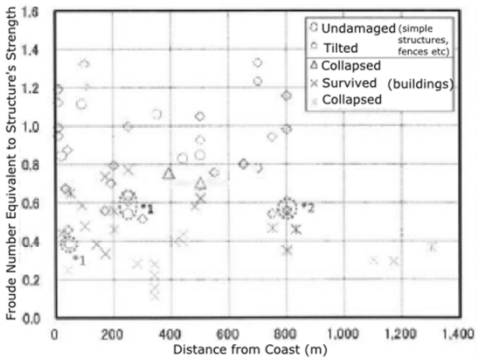

Figure D.12: Relationship between Froude Number and Distance from Shore

Therefore, in the absence of detailed inundation models (which would be required in order to accurately estimate design velocities at building locations), the flow Froude number (and so the load factor α) can be estimated based on distance from the shore and the presence or absence of seaward obstacles.

The new design requirements are therefore to use equivalent hydrostatic load with the load factor α defined based on distance from the shore and the presence or absence of seaward obstacles.

D.1.2.6 Determination of Tsunami Inundation Parameters: New tsunami classifications

Following the 2011 event, Japan has been working towards a tsunami level classification system to inform hazard planning. The process has involved debate between disaster management experts and the government. A consensus on tsunami classification has been achieved and is now implemented in Japan, though it has only recently been conveyed to an international audience (Shibayama et al., 2013).

The definition of tsunami levels is dependent on the frequency of the events: Level 1 corresponds to fairly frequent tsunami occurrence of a relatively modest inundation and Level 2 corresponds to more rare events with extensive inundation. These are described in Table D.5.

Table D.5 Tsunami level descriptors (Shibayama et al., 2013)**.**

Level	Tsunami return period	Inundation depth
1	Several decades to around a hundred or so years	7 – 10m
2	Few hundred to thousands of years	More than 10m

However, Shibayama et al. 2013 explain that the level events are specific to particular locations as the same tsunami source will have different effects depending on proximity to the tsunami source and effect of local bathymetry. Also, what might be a rare level of inundation in one location might be more frequent in another.

Therefore at a particular location it is necessary to investigate historic tsunamis from field data and documentary records and combine these with numerical simulations of past and predicted future tsunamis using seismic data. Using tsunami heights as a function

of date, the levels corresponding to return periods of approximately a hundred and up to a thousand years can be obtained, determining the Level 1 and Level 2 values.

Once a defined level has been set the tsunami defences can be designed. The defences should be built to withstand a Level 1 event, to protect property and help in the protection of life (Shibayama et al., 2013) but the worst-case scenario Level 2 event must also be anticipated. The actual height of the defence to protect against a Level 1 event may be informed by local community considerations, the local topography, bathymetry and further numerical simulations (see for example discussions on the Hamaoka Nuclear Power Plant in EEFIT (2013)). The defence should be able to withstand a Level 2 tsunami but it would not be feasible or desirable to build structures that would not be overtopped at this level, so for these events there must be soft or non-structural measures in place e.g. evacuation areas. Figure D.13 illustrates the design levels.

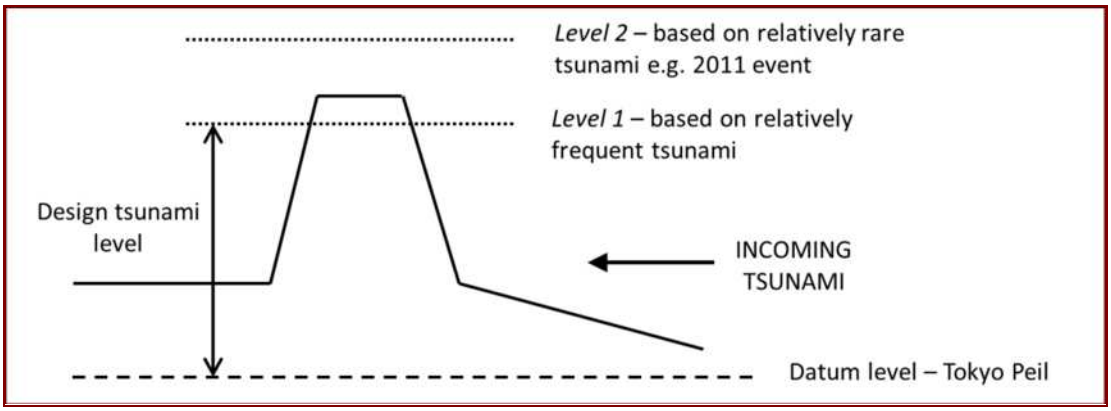

Figure D.13: Illustration of Level 1 and Level 2 tsunami with respect to a coastal defence structure.

This approach gives rise to inundation maps corresponding to L2 tsunamis, provided by Municipalities, from which design inundation depths (but no velocities) may be directly taken.

D.1.3 Load Assessment for Buildings

Recommended changes to design guidance include reduction of the tsunami inundation depth coefficient from 3 to the values given based on distance from the shore and presence of seaward sheltering structures. It is also proposed that wave loading be reduced (by no more than 30 percent) in proportion to openings (e.g. doors and windows) on the pressure-exposed face. Further guidance is also given on the calculation of buoyancy for foundation and superstructure design. Debris and scour are also to be considered, as shown in Figure D.15, though quantification of these effects is still subject to investigation. For debris it is recommended that progressive collapse following the loss of individual load-bearing elements be designed against. Scour is to be combatted primarily by the use of piles.

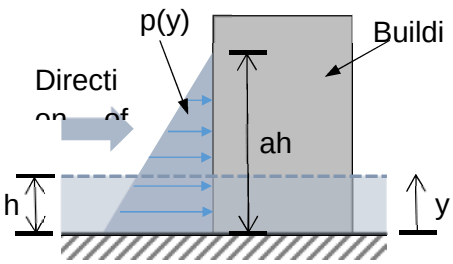

$$p(y) = \rho g(ah - y) \quad \textbf{(D.1)}$$

Figure D.14 Equivalent static loading recommended as design loading in MLIT 2570.

Table D.6: Tsunami loading coefficient (*a*) as a function of distance from water source and presence of sheltering structures (Fukuyama et al., 2012; MLIT, 2011c)**.**

	With shelter between the facility and the incoming wave		*No shelter between the facility and the incoming wave*
Distance from seashore or rivers	> 500m	< 500m	Any distance
Water depth coefficient *a*	1.5	2	3

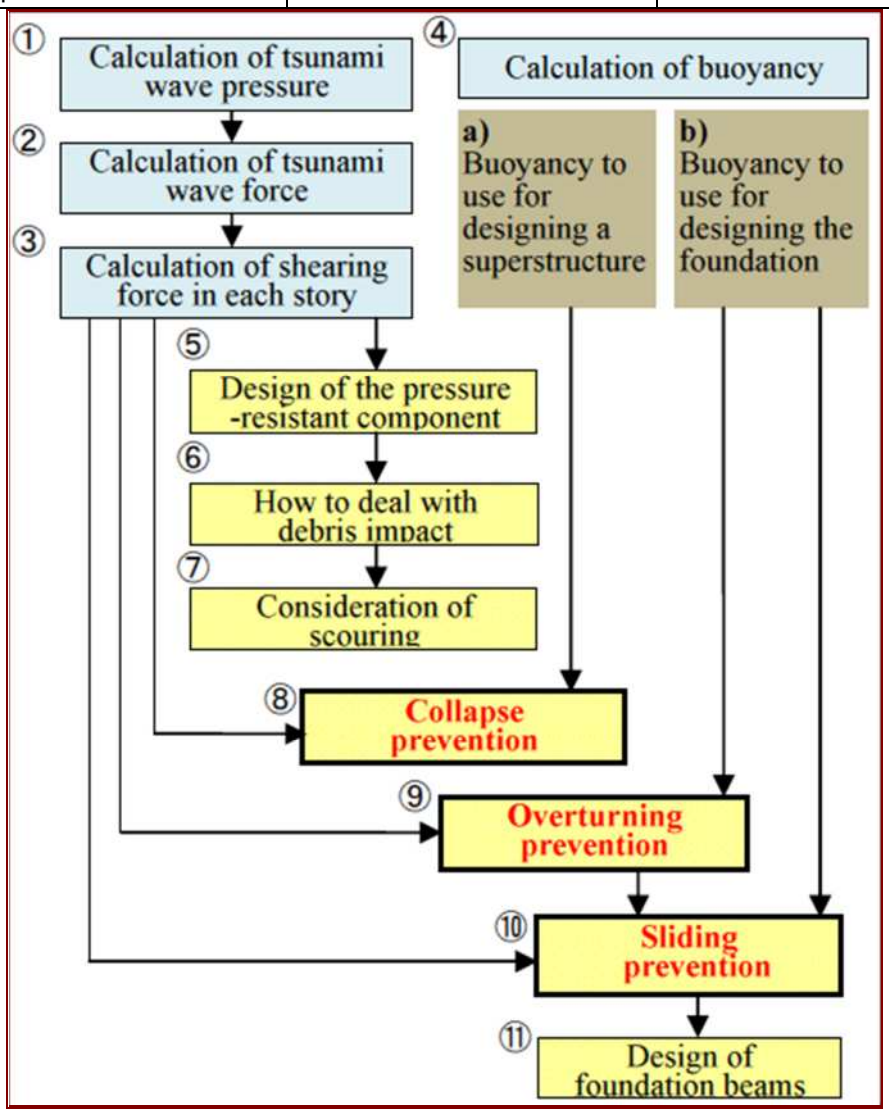

Figure D.15 Japanese proposed design methodology for tsunami evacuation buildings (Fukuyama et al., 2012)

D.2 US Guidance

D.2.1 Determination of Inundation Parameters

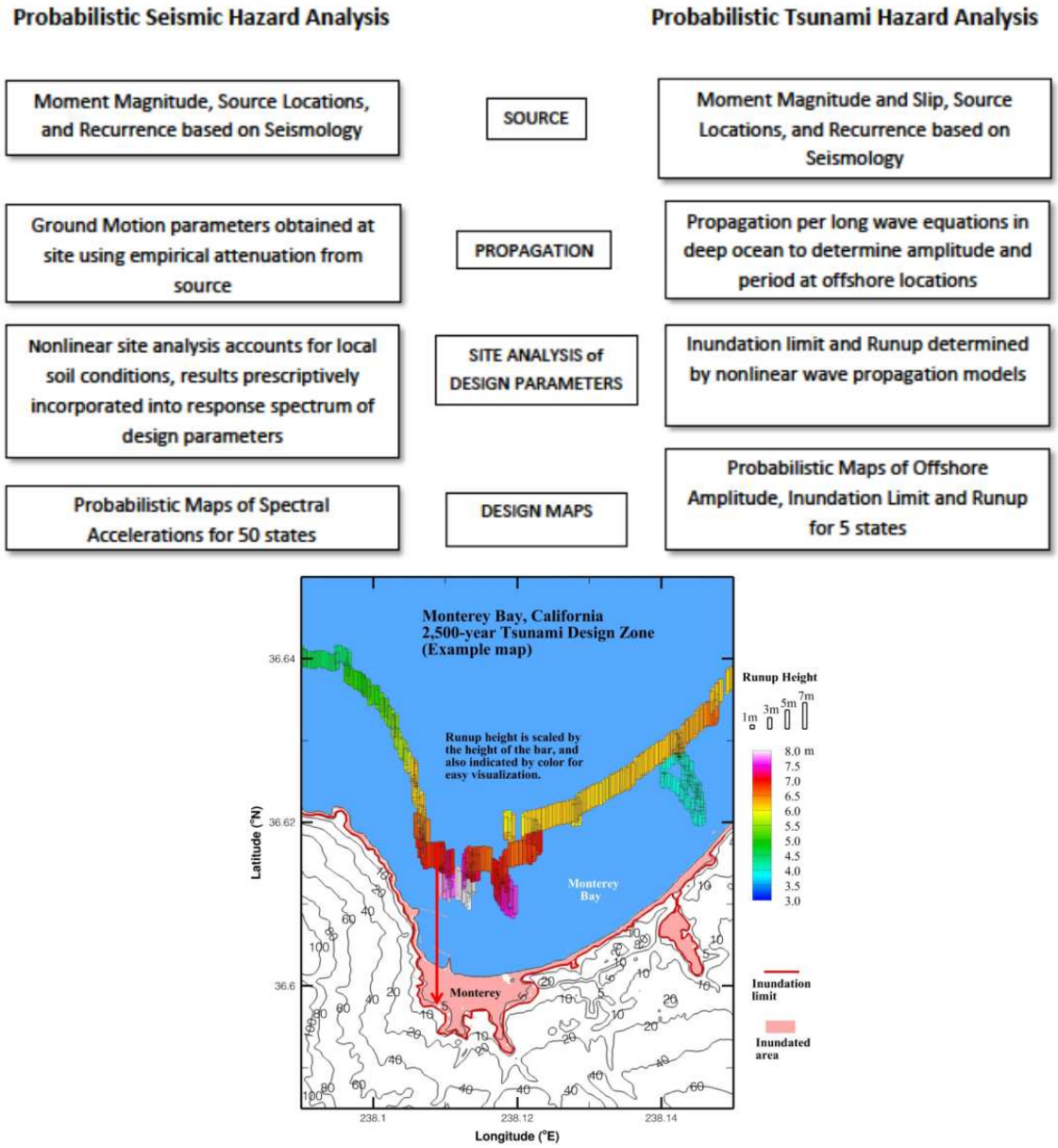

Figure D.16: Comparison of tsunami and seismic probabilistic hazard analysis (top) and examples of a tsunami hazard map (Chock & Robertson, 2013)

Energy grade line analysis is demonstrated below. Here velocity is calculated according to a Froude number assumed to decay with distance inshore as given in equation (D.7), where x is the horizontal distance from the shore, x_R is as defined in Figure D.17, and typically K = 1 (unless bore conditions exist, in which case it is higher).

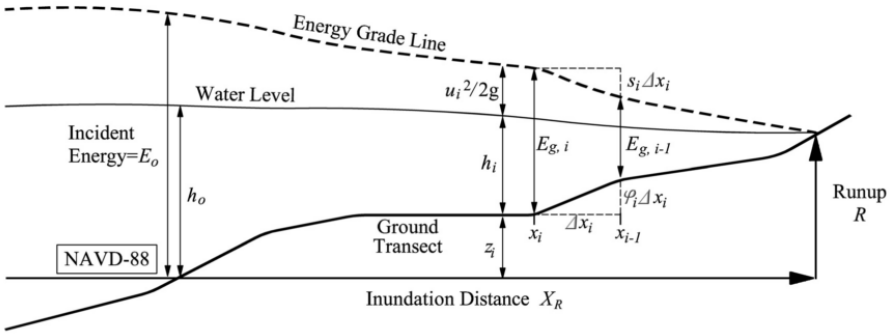

Figure D.17: Energy Grade Line Analysis (Chock, 2014)**. <replace with own figure or place in Appendix>**

$$Fr = K\left(1 - \frac{x}{x_R}\right)^{0.5} \qquad \textbf{(D.7)}$$

D.2.2 Sensitivity Analysis of Bore Impact Forces

In order to calculate example bore impact loads (load cases 8 and 9) the parameters of standing water depth (h_s) and height of hydraulic jump (h_j) (and the combination of these values, the total bore height, h_b) have been estimated as a proportion of the inundation depth (h_i). Figure D.18 shows the effect of varying these assumed proportions.

Figure D.18a shows input loads whereby the bore height (for both dry bed and standing water cases) is taken to be the same as the maximum inundation depth (h_i) at each calculation step, whereas Figure D.18b takes bore height to be 50% of the maximum inundation depth. As expected, it can be seen that increasing bore height (h_b) as a proportion of maximum inundation depth (h_i) greatly increases the load experienced by the structure. For a given bore height (h_b), as relative standing water depth (d_s) increases, the jump height (h_j=h_b-d_s) and so load applied decreases. The bore inundating over standing water is generally more onerous than the dry bed case, except where the standing water depth becomes a significant proportion of the total bore height (such as in Figure D.18b where, the standing water depth is 50% of the total bore height). Determination of realistic values for these parameters will be the subject of further study.

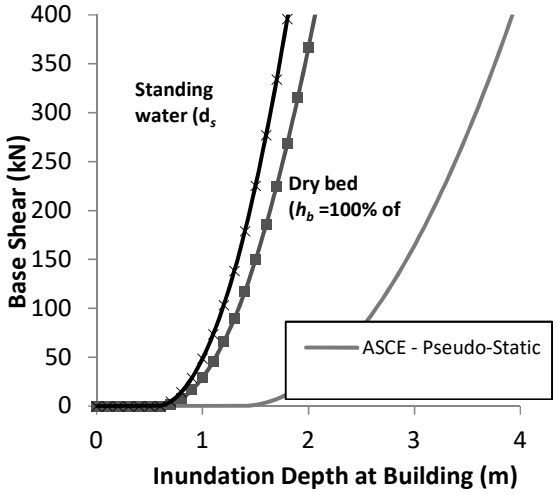

a: Bore height (h_b) = max inundation depth (h_i);

Standing water (h_s) = 15% of bore height.

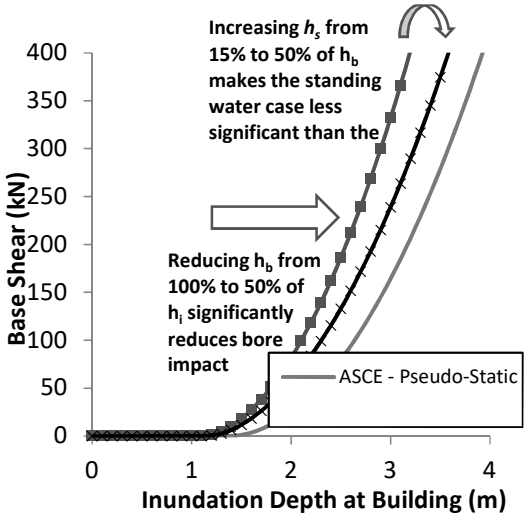

b: Bore height (h_b) = 50% of inundation depth (h_i);

Standing water (h_s) = 50% of bore height.

Figure D.18: ASCE bore impact parameter sensitivity analysis. The ASCE pseudo-static load (load case 7) is included for comparison purposes.

There is currently no single formula for deriving impact forces for a bore propagating over dry land (load case 8). For the calculation of load case 8 assumptions have therefore been made based on expressions in publications by members of the ASCE 7-16 Tsunami Loads and Effect sub-committee. These formulations may be amended in the final issue of ASCE 7-16, but the analysis presented in this paper provides a preliminary comparison with the other load cases. Note also that bore impact experiments (Ian N Robertson & Riggs, 2011) are based on wall impacts where there is no flow around the structure, and where the impacting surface is orthogonal to the direction of the incoming flow. There are currently no expressions for bodies within the flow and for non-bluff bodies.

E. Analytical Fragility Function Derivation

This section presents a preliminary investigation into the generation of analytical fragility functions, using a series of 2D analyses of the central bay of an RC framed structure loaded by tsunamis of various heights. The analysis presented represents an early proof-of-concept study which informed the work within the main body of the thesis.

The technique of tsunami pushover analysis is introduced, and it is shown that damage predictions are very sensitive to the load estimate and pressure distribution employed, and that the definition of TIM, EDP and damage scale play a very important role in fragility function definition. It was also demonstrated that seismic capacity (pushover) curves cannot be used to assess tsunami capacity as proposed by the new HAZUS tsunami methodology (Eguchi et al., 2014; Eguchi, Eguchi, & Graf, 2013; Kircher & Bouabid, 2014). A simple proof-of-concept analysis was conducted to produce analytical fragility curves that are order-of-magnitude comparable to empirical fragility functions from the 2011 Great East Japan Earthquake and Tsunami

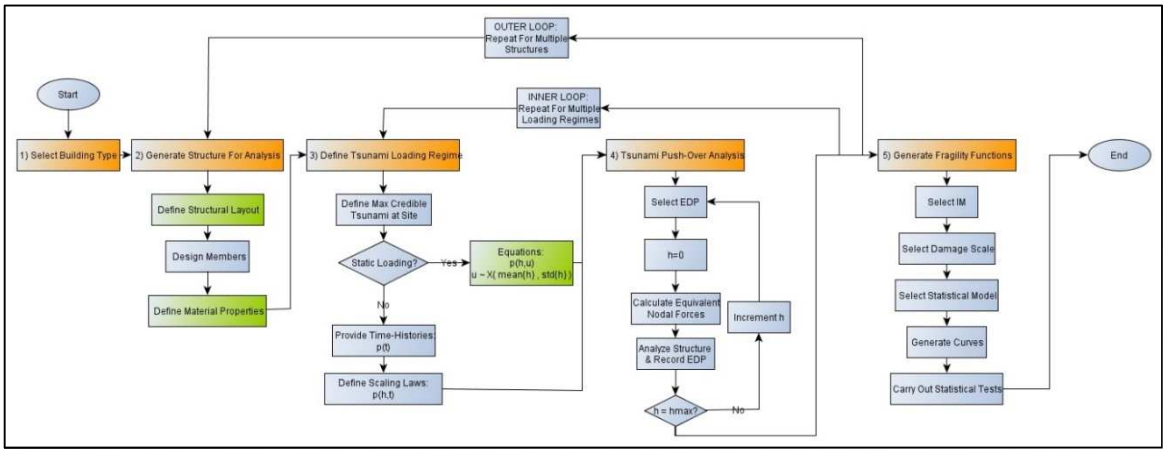

Figure E-1: Proposed method for generating analytical fragility functions

E.1 Introduction

In locations where no damage data is available analytical techniques are required using structural analysis to simulate damage data to form fragility functions. This chapter conducts a preliminary investigation into the generation of analytical fragility functions appropriate for use with inundation model results. This is so as to address the question: *how can tsunami-induced damage be estimated from analysis of structural*

performance? And in doing so an additional question is addressed: how sensitive is structural performance to variations in upstream flow parameters?

Section E.2 outlines the proposed fragility function derivation methodology and presents the structural model (section E.2.2). Section E.3 presents a sensitivity analysis into the effect of different loading scenarios and assumptions on structural response by comparing the displacement response obtained when subjecting a simple structure to a range of tsunami loads. Chapter E.4 presents the first steps towards defining a framework for generating analytical tsunami fragility functions, using structural analysis results and a proposed tsunami damage scale to produce a set of rudimentary fragility functions, which are then compared with empirical functions derived from damage data from the 2011 Japan Tsunami.

This appendix is to be considered a simplified proof-of-concept of more detailed analysis presented in the EngD thesis. The scenario which will be modelled in this study will be a simplified flow applied to an idealised 2D structural model, modelled into the non-linear post-yield range. Uncertainty in the structure will not be considered as part of this study, and uncertainty in loading will be approximated by applying several different loading regimes.

E.2 Mathematical Modelling

This chapter presents the mathematical modelling approaches to be adopted in this analysis. Section E.2.1 outlines the proposed methodology for generating tsunami fragility functions, and the structural model is detailed in section E.2.2.

For tsunamis caused by earthquakes ground shaking damage can be a significant contributor to building damage, as was the case across Japan in 2011. However, for this preliminary study only far-field tsunamis will be considered where the effected structures do not experience preceding seismic damage.

E.2.1 Proposed Method for Deriving Analytical Fragility Functions

Fragility functions are specific to a particular building type and location. After selecting a location and building type, damage data points (also referred to as performance points: the simulated damage state of a structure for a given local tsunami intensity {ds, TIM}) can be obtained. This is achieved by estimating the intensity of the hazard (TIM) for the given location, calculating the forces on a structure representative of the building type being considered, and analysing the structural response to obtain the expected damage state for the given hazard intensity. Multiple data points (i.e. a dataset) are then formed by repeating this procedure for a range of hazard intensities and a range of building configurations within the constraints of the building type being considered. Statistical regression methods are then applied to this damage dataset to generate fragility functions.

Using the results of structural analysis, analytical fragility functions can then be derived (Figure E-3). In order to do this it is necessary to relate the structural response, represented by an Engineering Demand Parameter (EDP) to a Tsunami Intensity Measure (TIM). The majority of existing studies use inundation depth as a TIM, though the quasi-steady force estimate proposed by Qi et al. (2014) is a suitable alternative TIM.

For the preliminary proof-of-concept analysis presented in this appendix, inundation depth is used as the TIM.

Current empirical tsunami fragility functions generally use one of two IMs: flow depth and flow velocity. Tsunami flow depth is the most commonly used TIM to build empirical tsunami fragility curves as it is relatively straightforward to measure in the field. Flow velocities are not usually taken into account as they are hard to determine from observations (EEFIT, 2006), although numerical inundation modelling is beginning to allow for the development of empirical fragility functions which use velocity as their TIM (H Gokon, Koshimura, & Matsuoka, 2010; A. Suppasri et al., 2011; Anawat Suppasri et al., 2009).

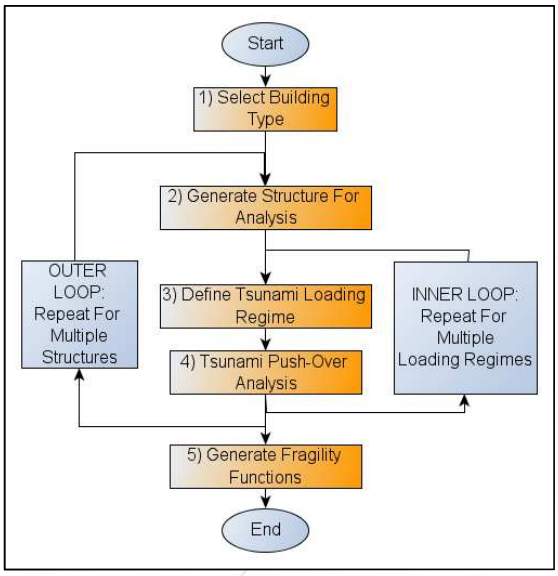

Figure E-2: Proposed procedure for deriving analytical tsunami fragility functions.

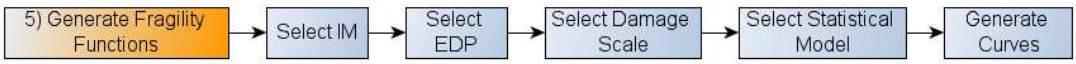

Figure E-3: Procedure for deriving analytical fragility functions from structural analysis data.

Very few analytical tsunami fragility functions have been published and so a suitable EDP has not yet been established in literature. It will therefore be necessary to select an EDP for the purposes of this study. Damage is then to be assessed based on the EDP values. An EDP-based damage scale is therefore required to rank the data into damage classes according to the degree of non-structural and structural damage to the analysed buildings. However, tsunami damage state definitions as a function of EDP have also not yet been developed, and so a suitable damage scale will need to be developed for this study.

Once structural performance has been transformed into damage data, fragility curves can then be fit to that data. Generalized Linear Models (GLMs) will be utilized in this chapter for the reasons outlined previously.

E.2.1.1 Representation of Variability of Structural and Tsunami Parameters

To represent uncertainty in the tsunami loading, for this preliminary investigation, the structure will be analysed under loading from several tsunami design guidance documents. The results from all analyses will then be combined in order to create fragility functions which represent a range of possible loading regimes which can be experienced within the population of buildings. It is noted that this is not proposed as an accurate method for capturing loading variability (the inner loop shown in Figure E-2), but the variation in design-code loading will be used in this example application to demonstrate how fragility functions may be formed.

Only a single building will be analysed, but modelling of variability of structural properties will form part of the focus of the EngD research programme.

E.2.2 Structural Model Formulation

Tsunami pushover analysis is carried out in order to rapidly assess structural performance over a range of tsunami intensities. Tsunami pushover analysis is a novel methodology whereby a structural model is loaded by tsunamis of various heights in order to generate tsunami pushover curves characterizing the structural performance under tsunami loading. The procedure followed is as shown in Figure 6.

The collection of performance points (for tsunamis which give increasing maximum inundation depths) forms the performance curve, or tsunami pushover curve (Figure E-9). This procedure is followed for loading regimes specified in the guidance documents MLIT 2570 (MLIT, 2011c), and FEMA 646 (FEMA, 2012), and proposed for ASCE 7-16 (Gary Y.K. Chock, 2013; Gary Y.K. Chock, Robertson, & Riggs, 2013).

Analytical structural models are required in order to model the population of buildings for which fragility functions are to be derived. Fragility functions are generally derived by building type, where buildings should be classified according to their structural properties, as this will govern their performance under tsunami loading. Empirical tsunami fragility functions exist for several building types, including RC, steel, wood and masonry (Anawat Suppasri et al., 2013). Fragility functions are also specific to a particular location as similar construction types from two different countries or even regions can perform very differently under the same tsunami conditions (EERI & IAEE, n.d.; Anawat Suppasri, Mas, Koshimura, et al., 2012b). Therefore, the analytical model is required to simulate an index building which represents a particular building type in a particular part of the world (step 1 in Figure E-2).

Within a building type (e.g. RC frame structures), there is variation of structural and material parameters (e.g. geometry, material strength, etc.). The range of analytical models used must represent this variability in the building population. For the purposes of this preliminary investigation structural variability will not be considered, only the structural model shown in Figure E-4 will be analysed, variability will still be considered in the loading.

Structural analysis for fragility function derivation must be as simple as possible to allow multiple analyses of various structural configurations and tsunami loading scenarios. Tsunami push over analysis is proposed as a suitable method. Previous studies have used either simplified SDoF systems (S. Park et al., 2013, 2012), simple analytical capacity calculations (Peiris, 2006), or have simply used seismic capacity curves directly

(Kircher & Bouabid, 2014). However, this study extend these methodologies to look at a more detailed non-linear FE model under tsunami loading.

The RC framed structure analysed is a four-story, 2D bare frame used in a series of full-scale shake-table experiments (A. Pinto, Verzeletti, Molina, & Varum, 1999). The RC bare frame was designed to be representative of construction practices used in southern European countries in the 1950's and 1960's. RC details are typical of that time, and lateral resistance is low as no specific seismic provisions were included. The FE model used for analysis is shown in Figure E-4. Inter-story heights are 2.7m and a slab with 2m on each side is cast together with the beams. Beam dimensions, reinforcement details and material properties are as given in (Carvalho et Al, 1999).

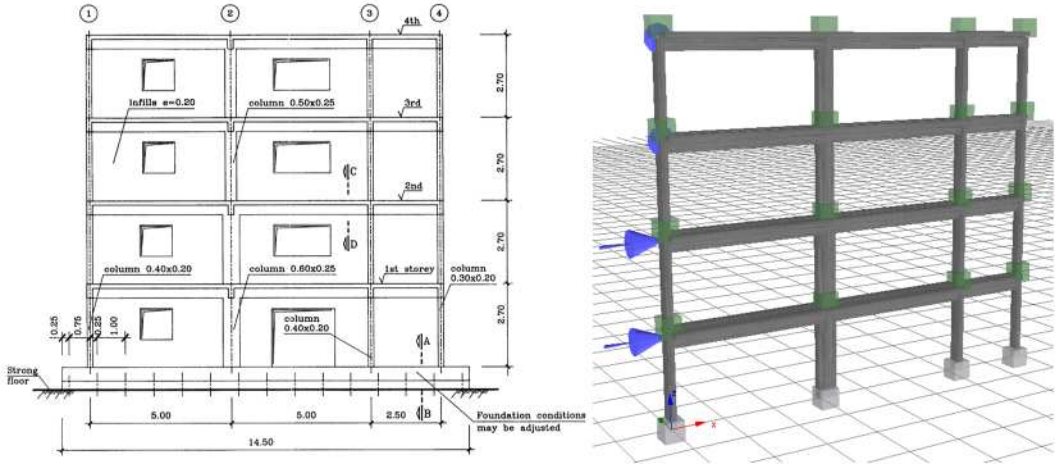

Figure E-4: Structural elevation (left. Source: (Carvalho et Al, 1999)) and FE model (right) with equivalent nodal forces for a tsunami rising above the 2nd floor.

Note that this structure has been selected as it is one of the structures used by Rossetto and Elnashai (2003) to derive the seismic damage state threshold definitions that will be used in this tsunami fragility function investigation (Table E-2). Using the same building under a different loading regime (i.e. tsunami loading) will allow investigation of the appropriateness of using seismic damage scale definitions for tsunami fragility function derivation.

As this preliminary analysis is only concerned with global lateral displacement of the structure (rather than failure of members and infill-panels on the front face) forces are only applied as point loads at each floor (as in (S. Park et al., 2013), Figure E-4), not as distributed loads on the leading column. Therefore, for each tsunami inundation depth being investigated equivalent nodal forces are calculated and applied at each floor. Note also that as foundation failure is not being considered, no load is applied at the base node of the ground floor leading column, so that total applied base-shear can be more readily compared with results from seismic push-over analyses of the same structure.

E.2.2.1 Model Validation

The analysis package chosen for this example application is Seismostruct. This software is chosen due to its ability to simulate large displacement behaviour under static or dynamic loading, considering both geometric and material nonlinearities. Non-linear material behaviour is modelled using the fibre-plasticity approach, whereby each member cross-section is made up of several fibres associated with a uniaxial non-linear stress-strain relationship and the cross-section behaviour is determined by integrating

the fibre responses across the section at each calculation step. Fibre-plasticity was chosen over the lumped-plasticity approach as there is no requirement to pre-define plastic hinge locations.

Validation of the FE model has been carried out for various seismic analyses and verified against results from physical experiments by Rossetto et al. (2014). The results of non-adaptive seismic pushover analysis with uniform loading distribution from Rossetto's study are included below for comparison with tsunami pushover results.

E.2.2.2 Finite Element Analysis Method

The Finite Element (FE) package chosen was Seismostruct due to its ability to simulate large displacement behaviour under static or dynamic loading, considering both geometric and material nonlinearities. Non-linear material behavior is modelled using the fibre-plasticity approach, whereby each member cross-section is made up of several fibres associated with a uniaxial non-linear stress-strain relationship and the cross-section behavior is determined by integrating the fibre responses across the section at each calculation step (Filippou F.C. and Fenves G.L., (2004); Fragiadakis and Papadrakakis (2008)). Fibre-plasticity was chosen over the lumped-plasticity approach as there is no requirement to pre-define plastic hinge locations and so it is not necessary to go thru the usual incremental pushover process of loading until yield, adding plastic hinges, incrementing the load until next yield etc, but instead non-linear behavior is automatically considered across the structure at each calculation step.

The constitutive concrete material model used was a uniaxial nonlinear constant confinement model that follows the constitutive relationship proposed by Mander (1988). The steel material model employed was a uniaxial steel model based on a stress-strain relationship proposed by Menegotto and Pinto (1973) coupled with the isotropic hardening rules proposed by Filippou et al. (1983).

Validation of the FE model is carried out for various seismic analyses verified against results from the physical experiments is presented in Tiziana Rossetto et al. (2014).

E.3 Structural Analysis

There is a high level of uncertainty associated with tsunami loading, as evidenced by the range of tsunami loading definitions presented and analysed. This chapter aims to demonstrate the effect of different loading scenarios and assumptions on structural response by comparing the displacement response obtained when subjecting a simple structure to a range of tsunami loads.

A series of 2D analyses of the central bay of an RC framed structure loaded by tsunamis of various heights. This analysis forms the basis of a novel methodology presented here: tsunami pushover analysis. The results are presented as a series of tsunami pushover curves characterizing the structural performance under these tsunami loadings. In order to demonstrate the effect of different loading assumptions on the resulting structural response, various quasi-static loading regimes will also be considered.

E.3.1 Static loading

Under static loading structural failure occurred via a soft-story mechanism for all loading profiles (Figure E-7), induced by failure of ground-to-1st floor columns due to bending (shear stress at column heads was not significant). Figure E-7 shows an example of the level of structural damage according to the chosen performance criteria (Table E-1), at the calculation step immediately prior to numerical instability of the model. The resulting capacity curves for the structure under the various loading profiles are shown in Figure E-9 below. Note that in Figure E-9 load cases 1, 2, 3, 7, 8 and 9 all lie on the same curve, as do cases 4 and 5. This is addressed in the discussion section at the end of this paper. Figure E-10 shows the Inter-Storey Drift (ISD) ratio vs inundation depth.

In order to best illustrate the tsunami pushover procedure this preliminary study will focus on the simple lateral deflection failure mechanism shown in Figure E-5a. Additional superstructure and substructure failure mechanisms, as well as effects such as debris impact and preceding seismic damage, will be the focus of further studies.

Figure E-5: Global lateral deflection/failure due to lateral fluid load (hydrostatic and hydrodynamic) (EEFIT, 2011a).

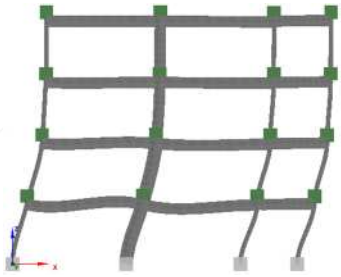

Figure E-6: Structural model under lateral fluid loading.

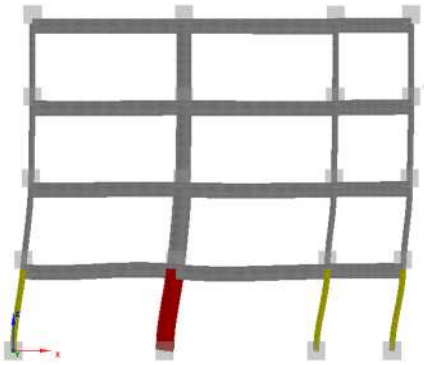

Figure E-7: Structure under FEMA 646 loading (δ_{top}=38mm). Note the second column from the left is larger than the others and so attracts the majority of the load.

Performance Criteria Description	Material Monitored	Strain Criteria	Colour
Yield	Steel reinforcing bars	ε > 0.0013	Yellow
Spall	Concrete cover	ε > -0.0025	Orange
Crush	Core concrete (contained within rebar)	ε > -0.0031	Red

Table E-1: Performance criteria indicated by coloured members in Figure E-7.

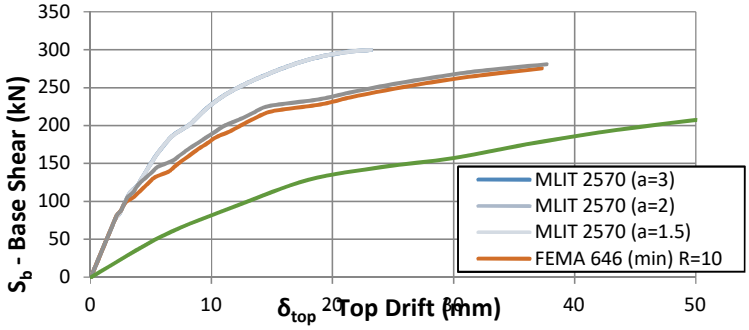

Figure E-8: Applied load vs top drift. Note that the seismic PO continues to a top drift of 300mm.

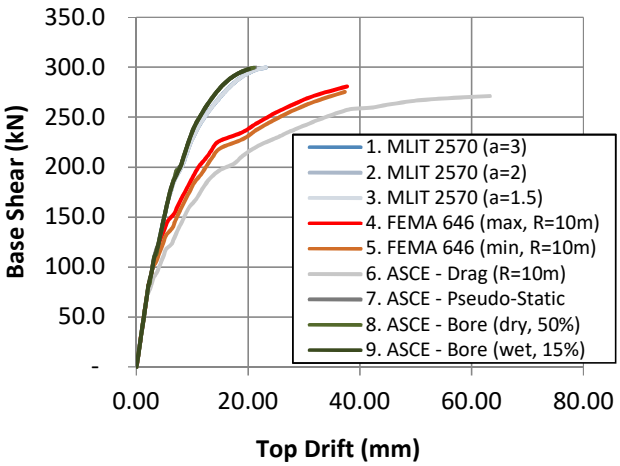

Figure E-9: Applied Load vs Top Drift.

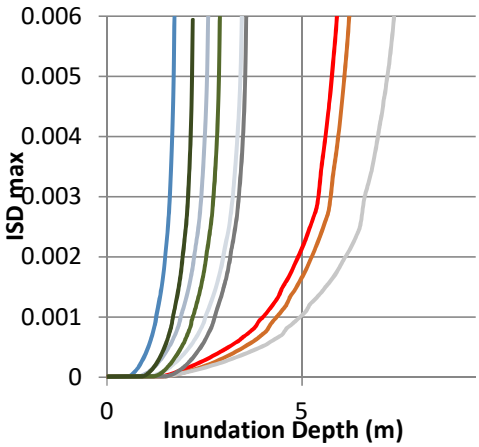

Figure E-10: Maximum Inter-Story Drift Ratio vs inundation depth.

E.3.1.1 The Effect of Load Distribution on Structural Response

The seismic pushover test applied uniform lateral loading over the whole height of the structure (Tiziana Rossetto et al., 2014), FEMA loading applied uniform lateral loading but only over the height of the inundation, and MLIT loading applied a triangular load. Therefore, the height of the centroid of the applied load was greatest for seismic loading, and least for MLIT loading. Considering the structure to deflect approximately as a vertical cantilever fixed at the base, these centroidal loading positions would account for the differences in top drift shown in Figure E-9.

Figure E-9 shows that load cases 1, 2, 3, 7, 8 and 9 (which are all of triangular load distribution) all lie on the same pushover curve, as do cases 4 and 5 (which are of uniform load distribution). Therefore it can be seen that tsunami pushover curves are identical for identical load distributions. However differences become apparent when considering structural deflection as a function inundation depth (Figure E-10) rather than base shear. This is due to the very different magnitude of the forces applied for each inundation depth.

The tsunami pushover curves (Figure E-9) show that for a given level of base shear the structure deflects least under triangular load distributions and most under uniform load distributions. This can be explained by considering the height of the centroid of the applied loading based on the respective loading distributions. The height of the centroid of the applied load was greatest for the uniform load distributions and least for triangular distributions. Considering the structure to deflect approximately as a vertical cantilever fixed at the base, these centroidal loading positions would account for the differences in top drift shown in Figure E-9.

E.3.1.2 Post-peak Behaviour on the Performance Curve

Figure E-8 shows that compared to the tsunami pushover curves, the seismic pushover curve continues over a greater range of displacements and also captures the post-peak

behavior of the structure. For the derivation of seismic analytical fragility functions, high damage states (e.g. heavy damage and collapse) are often defined for deformations corresponding to this post-peak softening branch of the pushover curve (Tiziana Rossetto & Elnashai, 2005). This post-peak behavior is not captured in the presented tsunami pushover analysis method.

The tsunami pushover analysis method presented here is a load-controlled procedure (load is incrementally increased and response recorded at each step). Therefore analysis of the structure cannot continue past the peak of its performance curve, as there is not sufficient structural capacity to resist a further increase in load. Seismically loaded structures can access post-peak deflections because of the dynamic nature of their loading (Tiziana Rossetto et al., 2014), and seismic pushover procedures have adopted several displacement-control methodologies in order to capture this behavior. Therefore, it must be considered how structures responding under tsunami loading might also access this post-peak behavior, and how the post-peak forces can be accurately represented.

Tsunami loading has been applied in this study as static load cases at each inundation depth, which is an accurate representation of an incrementally increasing time-independent load. However, the importance of the time-dependency of real tsunami loading in achieving realistic results for structural response is not clear. Structural response to time-history tsunami forces must therefore be considered in comparison with static pushover curves to investigate the significance of dynamic structural response in defining the behavior of buildings under tsunami loading. This will inform the development of displacement-control pushover techniques in order to capture the post-peak softening branch of the tsunami pushover capacity curve.

E.3.1.3 The Effect of Structural Response Variations on Damage Predictions

The differences shown in Figure E-10 highlight that the resultant damage predictions (if dependent on inter-storey drift) will be different, depending on the loading regime used (Joshua Macabuag & Rossetto, 2014). This highlights that pushover analysis for accurate damage predictions requires the loading applied to be as realistic as possible (in terms of both magnitude and distribution) for each inundation depth, and so simplified and conservative loading defined for design purposes may not provide the required accuracy.

Specific damage state estimation based on the above generated capacity curves will be discussed in Chapter E.4.

E.3.2 Dynamic Loading

To ascertain the validity of using design standard forces for damage predictions it will be necessary to compare these results with those using more detailed time-history forces from physical experiments (Ian N Robertson & Riggs, 2011; Tiziana Rossetto et al., 2011). Work carried out by Lloyd and Rossetto (2012) on laboratory-generated long-wave experiments is producing expressions for tsunami load time-histories based on inundation parameters. However, existing guidance does not discuss how to apply tsunami load time-histories to structures and assess a building's response from the structural analysis. Analysis under dynamic loading forms part of the main EngD study.

E.3.3 Discussion

As expected the pushover curves for the maximum and minimum FEMA loadings are very similar as although their loading magnitudes differ, their load distributions are the same (i.e. uniform vertical distribution). The structural response under the Japanese triangular loading however differs considerable after a top-drift of approximately 4mm. This difference highlights that the tsunami push-over curve of a structure is very sensitive to the load distribution applied. This is analogous to the seismic push-over case whereby the loading distribution (e.g. uniform or triangular) effects the final push-over curve of the structure (Tiziana Rossetto et al., 2014).

Whilst the push-over curves show some difference for different loading definitions, when relating these loadings to inundation depth the differences between the resulting EDP vs TIM curves are far greater (Figure E-10). This is due to the very different magnitude of the forces applied for a given inundation depth (Figure E-9). However, this comparison highlights that unlike design procedures which are looking to create simplified and conservative loads for engineering design, this push-over analysis for analytical fragility function derivation is looking to create accurate damage predictions, and so the loading applied must be as realistic as possible.

In this study a static load has been applied and the maximum displacement measured from non-linear static analysis. However, the applied load represents a peak force that is only applied for a short impulse that may not result in the equivalent static displacement calculated. Therefore it will be key to investigate time history forces as a comparison with these static PO curves.

Figure E-9 shows that under tsunami loading the structure is failing at the peak of its performance curves, at relatively low inter-storey drift ratios. Comparison with seismic push-over of the same structure Figure E-8 shows that the seismic pushover curve continues over a greater range of displacements, and the higher damage states are achieved during these greater deformations, which are not achieved in the presented tsunami push-over analysis. The reason for this is that this preliminary tsunami pushover analysis is a simple load controlled test (load is incrementally increased and response recorded at each step) and so cannot analysis the structure past the peak of its performance curve, as there is not sufficient structural capacity to resist the next load increment. Seismic pushover can adopt several displacement-control methodologies for overcoming this problem in order to also capture the softening post-peak branch of the response (Anthoine 2006; Trueb 1983 and Izzuddin 1991). However, post-peak behaviour can be achieved under seismic loading because peak loads are applied for short durations, and so loads which exceed the ultimate capacity of the structure are not long enough for the structures full deflection response (i.e. collapse) to develop, whereas tsunami loading is quasi-static in nature (initial impulse notwithstanding) and so loads greater than the ultimate strength of the structure are likely to be applied long enough for collapse to occur. Note that this lack of post-peak behaviour, agrees with the experimental observations by van de Lindt et al. (2009)

For comparison with empirical fragility relationships, more complex loading and failure mechanisms will be need to be incorporated into the modelling procedure. The

appropriate choice of TIM, EDP and damage scale for tsunami also play a very important role in fragility function definition and will be the focus of further investigation.

E.3.4 Conclusion

This section has presented a preliminary study into the derivation of tsunami push-over curves for the generation of analytical tsunami fragility functions, and the main findings are summarised as follows:

- The tsunami push-over curve of a structure is very sensitive to the load distribution applied, and so accurate definition of tsunami-induced pressure distribution is crucial to obtaining accurate structural response.
- The definition of load as a function of the tsunami intensity measure (e.g. depth) has a large effect on the resultant damage prediction, and so the loading applied must be as realistic as possible.
- Seismic and tsunami capacity (pushover) curves are very different, due to the different load distributions and points of application. Therefore the method proposed by Kircher & Bouabid (2014) to produce tsunami fragility functions from seismic capacity curves is not justified.
- The definition of TIM, EDP and damage scale for tsunami play a very important role in fragility function definition and will be the focus of further investigation.
- It is not clear the importance of the time-dependency of real tsunami loading in achieving realistic results for tsunami response, and so time history forces must be investigated as a comparison with static pushover curves.

E.4 Statistical Analysis

This section presents the first steps towards defining a framework for generating analytical tsunami fragility functions, using the iterative structural analyses presented in section E.3, for which a set of rudimentary fragility functions are produced in order to illustrate the proposed process. Inter-storey drift is selected as the EDP to enable the use of a seismic damage scale definition. Inundation depth is selected as the TIM to enable comparison with empirical fragility functions.

It is shown that the seismic damage scale selected does not capture an adequate range of structural behaviour under tsunami loading, and so a preliminary tsunami damage scale is proposed. The generated fragility functions are order-of-magnitude comparable with empirical functions derived from damage data from the 2011 Japan Tsunami.

E.4.1 Statistical Analysis

E.4.1.1 Statistical Model Fitting

The pushover curves shown in Figure E-8 represent structural behaviour under tsunami loading. This structural response data must be transformed into EDP-TIM space (Figure E-10). Tsunami loading defined by current Japanese design codes, is defined entirely by inundation depth (Joshua Macabuag et al., 2014a), therefore depth will be used as the TIM in this case. This will also allow for easier comparison with empirical tsunami fragility functions, the majority of which are also based on inundation depth. A common EDP for

seismic analytical fragility functions is inter-story drift ratio (ISDR), which will also be adopted here.

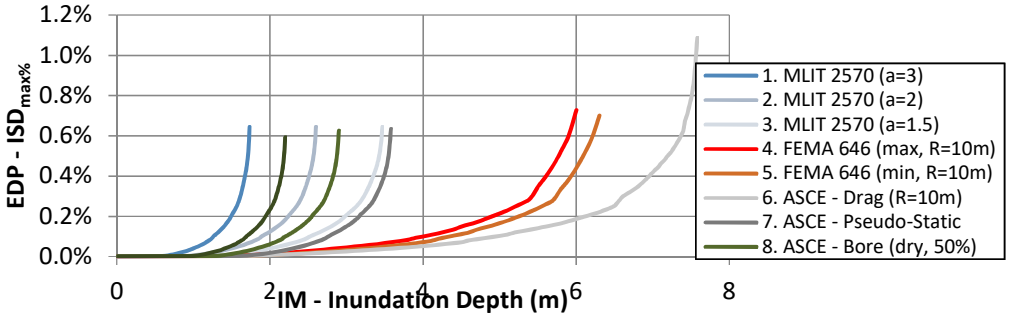

Figure E-11: Maximum Inter-Story Drift Ratio vs inundation depth (i.e. EDP vs TIM). Each curve ends at the point at which numerical instability of the analysis model occurred.

Tsunami damage state definitions as a function of ISDR have also not yet been developed, and so a seismic damage scale will initially be adopted. The selected damage scale (Table E-2) was developed by calibration against several full-scale structural seismic experiments, including the structure used in this tsunami pushover investigation (T. Rossetto & Elnashai, 2003).

Figure E-13 shows fragility functions for the damage states and damage scale defined in Table E-2. The procedure for deriving the fragility functions was to define several statistical models and then select a model based on the Akaike Information Criterion (AIC) relative goodness-of-fit test, which is appropriate for comparing non-nested models as outlined in T Rossetto et al. (2014). The statistical models tested considered transformed (ln|*h*|) and non-transformed IMs, ordered and partially-ordered models, and compared logit, probit, chauchit, loglog and complimentary loglog link functions. This is according to the procedure set out in Charvet et al. (2014). The chosen statistical model is a partially-ordered model regressed on the logarithm of the inundation depths using a probit link function (Figure E-13, Equation (E.1), where Φ^{-1} denotes the inverse cumulative normal distribution).

Damage State	Inter-Storey Drift (ISD) Range
None	0 – 0.32%
Slight	0.04 – 0.43%
Light	0.5% – 1.02%
Moderate	1.02% – 2.41%
Extensive	2.41% – 4.27%
Partial Collapse	4.27% – 5.68%
Collapse	> 5.68%

Table E-2: Seismic Analytical Damage Scale: $ISD_{max\%}$ limit state threshold values for moment-resisting RC frames designed to pre-seismic codes (T. Rossetto & Elnashai, 2003).

$$\Phi^{-1}[P(DS \geq ds_i|h)] = \alpha_i + \beta_i \ln|h| \quad \textbf{(E.1)}$$

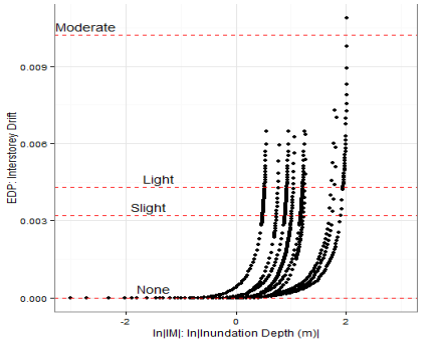

Figure E-12: TIM vs EDP. Performance points from structural analyses. Horizontal lines represent the thresholds defined in Table E-2.

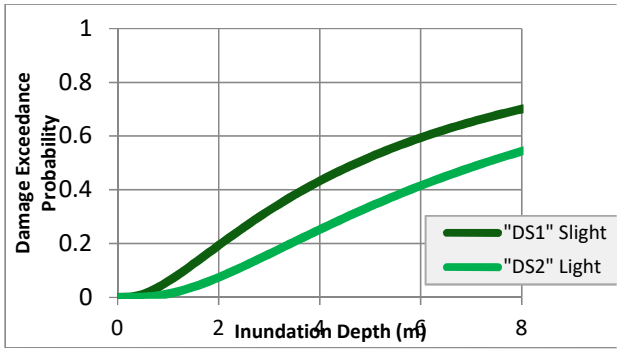

Figure E-13: Fragility functions based on seismic damage state definitions.

Note that although seven damage states (including “no damage”) are defined in Table E-2, only two curves are shown in Figure E-13. This is because only three damage state thresholds are crossed in Figure E-12, and the third threshold (moderate damage) only has one point beyond it, which is not enough data to sensibly form a fragility function.

Figure E-12 and Figure E-13 show that according to the seismic analytical damage scale used, inter-story drift ratios indicating only light or moderate damage can be achieved before instability of the analysis model occurs. This is because for seismic deflection-based damage scales higher damage states defined are often defined on the post-peak softening branch of the seismic pushover curve. The tsunami pushover procedure does not generate a post-peak softening branch (Joshua Macabuag et al., 2014b) and so seismic EDP-based damage scales are not appropriate for defining tsunami damage states as they do not pick up higher damage states induced by tsunami loading. Therefore, the definition of a new EDP-based damage scale for the specific case of tsunamis must be investigated.

E.4.1.2 Towards Defining an Analytical Tsunami Damage Scale

Using seismic EDP and damage state definitions may not be appropriate for the definition of analytical tsunami fragility functions. Therefore, new damage state thresholds will be estimated. The same damage definitions will be used as for an empirical damage scale utilized in Japan following the 2011 Great East Japan Earthquake and Tsunami, so that analytical and empirical curves can be compared. The analytical damage state definitions will be correlated with the empirical damage states via the criteria shown in Table E-4. The criteria used to define yielding, spalling and crushing of columns in the analytical model are shown in Figure E-8. Only structural damage states will be compared, and so minor and moderate damage will be ignored as they define damage to non-structural elements. It is noted that the selected criteria are only a first estimate and further calibration will be required.

Table E-5 shows the interstorey drift ratios for each loadcase at which the criteria given in Figure E-8 are reached. The mean of these values is then taken as an estimate for the new damage state threshold, with the exception of damage state 6, whereby the lowest $ISD_{max\%}$ at which numerical instability of the analysis model occurs is taken as the estimate, so that all loadcases will have at least one instance where they reach damage

state 6. The fragility functions derived from these estimated tsunami damage state thresholds are shown in Figure E-15.

Performance Criteria Description	Material Monitored	Strain Criteria	Colour
Yielding	Steel reinforcing bars	ε > 0.0013	Yellow
Spalling	Concrete cover	ε > -0.0025	Orange
Crushing	Core concrete (contained within rebar)	ε > -0.0031	Red

Table E-3: Performance criteria indicated by coloured members in Table E-4.

Damage State	Classification	Description	Condition	FE Model Definition	Model Image
DS1	Minor damage	No significant structural or non-structural damage, only minor flooding.	Possible to use after minor floor and wall clean up.	Not currently considered in analytical model.	
DS2	Moderate damage	Slight damage to non-structural components.	Possible to use after moderate reparation.		
DS3	Major damage	Heavy damage to some walls but no damage in columns.	Possible to use after major reparations.	1st Yield	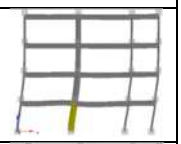
DS4	Complete damage	Heavy damage to several walls and some columns.	Possible to use after complete reparation and retrofitting.	1st Spall	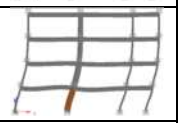
DS5	Collapse	Destructive damage to walls (more than half of wall density) and several columns (bent or destroyed).	Loss of functionality (system collapse). Non-repairable or great cost for retrofitting.	1st Crush	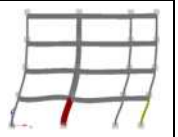
DS6	Washed away	Washed away, only foundations remained, total overturn.	Non-repairable, requires total reconstruction.	Numerical Instability	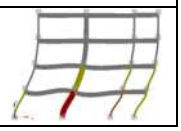

Table E-4: Damage state classification table. Analytical damage state definitions are correlated with an empirical scale used by the Japanese Ministry of Land, Transport and Infrastructure (MLIT) after the 2011 Japan tsunami. The criteria for yielding, spalling and crushing are shown in Figure E-8.

Damage State (survey)	Definition in FE Model	$ISD_{max\%}$ at DS Criteria									
		LC1	LC2	LC3	LC4	LC5	LC6	LC7	LC8	LC9	Estimated Thresholds
DS1		Not currently considered in analytical model.									
DS2											
DS3	1st Yield	0.21%	0.23%	0.23%	0.23%	0.24%	0.24%	0.21%	0.21%	0.23%	0.22%
DS4	1st Spall	0.36%	0.36%	0.36%	0.40%	0.38%	0.43%	0.37%	0.37%	0.37%	0.38%
DS5	1st Crush	0.46%	0.46%	0.46%	0.52%	0.51%	0.50%	0.48%	0.46%	0.48%	0.48%
DS6	Numerical Instability	0.60%	0.65%	0.60%	0.73%	0.70%	1.09%	0.64%	0.63%	0.59%	0.59%

Table E-5: ISD values, by load case, at which the criteria given in Figure E-8 are reached.

E.4.1.3 Comparing Analytical and Empirical Fragility Functions

Figure E-15 shows the derived analytical tsunami fragility functions plotted with empirical curves, for comparison. The empirical curves are derived from building damage survey data from the 2011 Great East Japan Earthquake and Tsunami, based on RC structures greater than 3 floors (Anawat Suppasri et al., 2013).

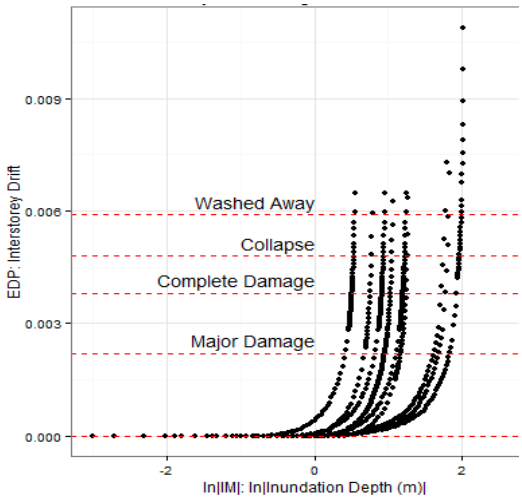

Figure E-14: TIM vs EDP. Note that the same performance points have been used as for Figure E-12. Only the damage state thresholds have been adjusted.

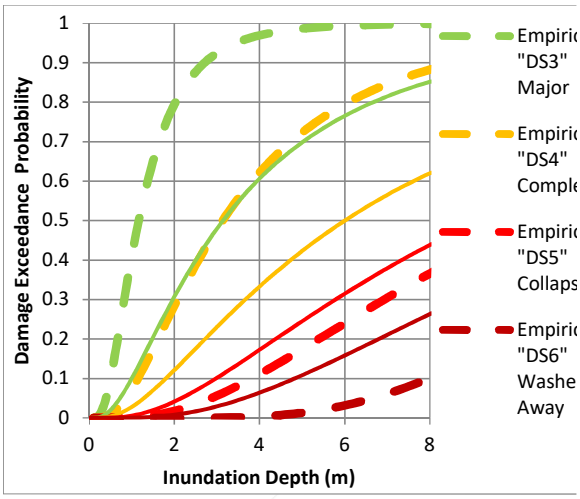

Figure E-15: A comparison between the analytical and empirical fragility functions. The empirical curves are derived from data from the 2011 Great East Japan Earthquake and Tsunami, based on RC structures greater than 3 floors (Anawat Suppasri et al., 2013).

The empirical fragility functions chosen for comparison are for the closest available building type to that used in the structural analysis. However, the damage dataset used to derive these curves will include buildings of different structural properties from that analysed in this preliminary study (e.g. buildings with several floors, designed to seismic codes and of different material and geometric properties). In addition, empirical curves cannot be considered as 'correct' for validation of analytical curves, as they represent many factors that are not picked up in the structural analysis (some of which are biases that distort the empirical data, T Rossetto et al. (2014)). Therefore, it is not possible to make definite conclusions on the accuracy of the analytical fragility functions here, but a preliminary comparison serves to indicate whether the proposed fragility function derivation method may be considered feasible.

Given that the empirical dataset will include buildings that have more floors and are stronger than the structural analysis model, it would be expected that the empirical fragility curves should indicate lower levels of damage. This is true for the "washed away" (DS6) and "collapse" (DS5) damage states, but not the case of "complete damage" (DS4) and "major damage" (DS3).

The empirical curves appear to be spread over a wider range, so that the "major damage" curve (DS3) is higher and the "washed away" curve (DS6) is lower than the analytical curves. The analytical "major damage" curve (DS3) appears to be more closely correlated with the empirical "complete damage" curve (DS4) suggesting that the

analytical criteria of yield first appearing in the loadbearing elements of the structure may be a more suitable definition for DS4, than the currently assigned DS3 (Table E-4). The analytical “collapse” curve (DS5) lies close to the empirical “collapse” curve indicating that column crush may be an adequate indicator of collapse, if also accounting for vertical load redistribution (i.e. the capacity of the structure to survive losing loadbearing elements). The “washed away” curves (DS6) do not show good correlation, possibly indicating that numerical instability is likely not a reliablecriteria, as this can be indicative of a number of features of the analysis and can be affected by altering the calculation parameters so is subjective to the analysis package used.

E.4.2 Discussion

This chapter has presented a proposed method for deriving analytical tsunami fragility functions, demonstrated by a simple example for an RC frame structure using design standard tsunami loadings. The analytical fragility functions produced are order-of-magnitude comparable to empirical fragility functions derived from the 2011 Great East Japan Earthquake and Tsunami. Analysis must be carried out for populations of buildings, and considering more realistic forces and failure mechanisms, to build confidence in the fragility functions produced. However, the comparison serves to demonstrate the viability of the proposed method for generating analytical fragility functions.

The differences in the TIM-EDP relationships shown in Figure E-10 highlight that the resultant damage predictions (i.e. the implementation of the derived fragility functions) will be different, depending on the loading regime used. This highlights that structural analysis for accurate damage predictions requires the loading applied to be as realistic as possible (in terms of both magnitude and distribution) for each inundation depth, and so simplified and conservative loading defined for design purposes may not provide the required accuracy. To ascertain the validity of using design standard forces for fragility function derivation it will be necessary to compare results with those using more detailed time-history forces from physical experiments (Ian N Robertson & Riggs, 2011; Tiziana Rossetto et al., 2011). The distribution of loading parameter variables for a given TIM (e.g. range and probability distribution of loads for a given inundation depth) will also need to be examined in order to perform the inner loop iterations shown in Figure E-2.

Relying on inundation depth as a single parameter to characterise tsunami hazard when other factors are also at play in a tsunami-building interaction scenario is likely to be inaccurate, as shown by (I. Charvet, Ioannou, et al., 2014a). Flow velocity is another major factor, which has the potential to be incorporated in analytical fragility functions. Further considerations which may affect tsunami intensity are: duration of immersion and the total number of waves, the likelihood of debris impacts, and the level of preceding seismic damage.

The preliminary ISD threshold estimates given in Table E-5 are based on analysis of only one building, and so this analysis would have to be extended to populations of buildings to improve accuracy, and provide EDP-based damage scales for multiple building types. However, it should be noted that it is difficult to correlate and validate the resulting damage state thresholds as very limited physical and experimental data exists. In addition, ISD has been assumed as the EDP in this preliminary study, due to its propensity in seismic analytical fragility function derivation. However, this assumption will

need to be examined as alternative EDP.s may be more appropriate for tsunami damage prediction, or it may prove more accurate to define damage states based directly on element performance, such as the criteria shown in Figure E-8.

Whilst the use of the generalized linear model in this preliminary study avoids the discussed pitfalls of linear regression, rigorous statistical modelling will require the use of model diagnostic tools (e.g. absolute goodness-of-fit tests) and quantification of uncertainty (e.g. through confidence intervals, T Rossetto et al. (2014)).

F. Simplified Pushover Numerical Model

This appendix provides additional figures and information related to the structural analysis conducted within the main thesis text.

F.1 OpenSees Model Information

F.1.1 Geometry

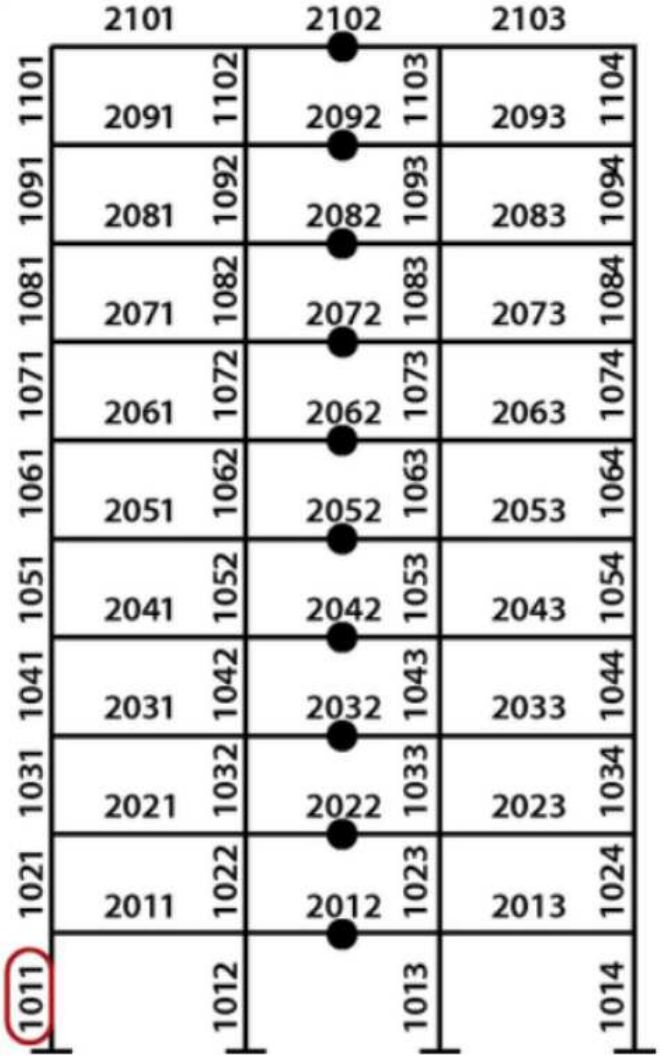

Figure F-1: OpenSees Element numbering from Petrone et. al (2017).

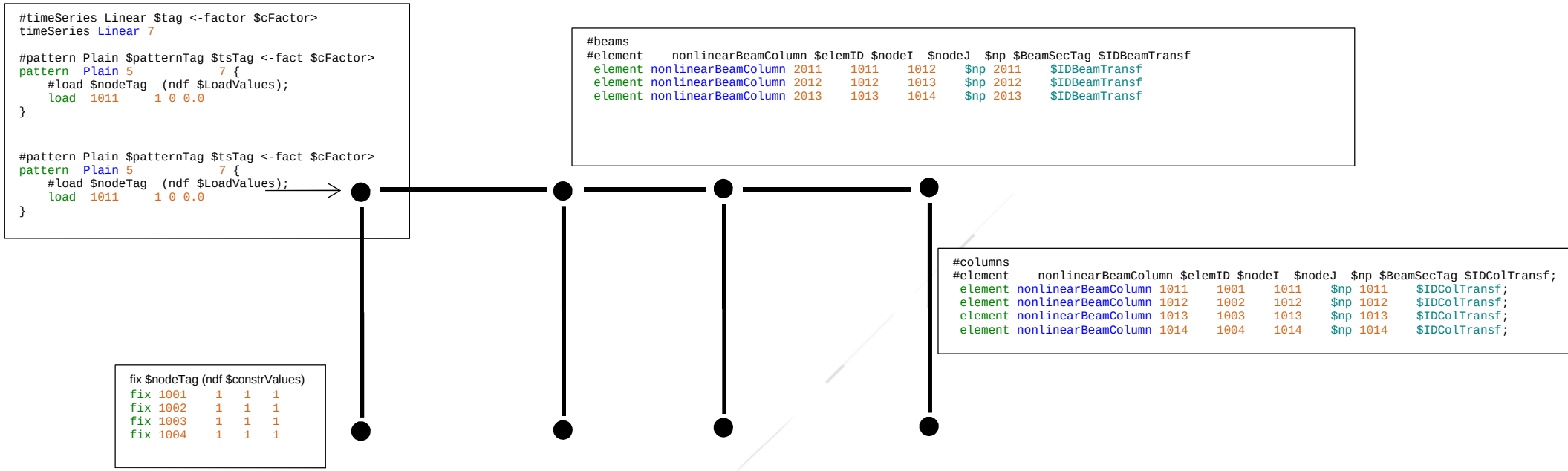

Figure F-2: Ground-1st floor of OpenSees model (other floors omitted for clarity).

```
node $nodeTag (ndm $coords) <-mass (ndf $massValues)>
node    1001    0.00    0.00
node    1002    8.50    0.00
node    1003    14.50   0.00
node    1004    23.00   0.00
node    1011    0.00    4.50
node    1012    8.50    4.50    -mass   141.94  0.000000001 0.000000001
node    1013    14.50   4.50
node    1014    23.00   4.50
```

F.1.2 Cross-sections

```
proc BuildRCrectSection {id HSec BSec coverH coverB coreID coverID steelID numBarsTop barAreaTop numBarsBot barAreaBot
numBarsIntTot barAreaInt nfCoreY nfCoreZ nfCoverY nfCoverZ} {
    # Build fiber rectangular RC section, 1 steel layer top, 1 bot, 1 skin, confined core
    # Define a procedure which generates a rectangular reinforced concrete section
    # with one layer of steel at the top & bottom, skin reinforcement and a
    # confined core.
```

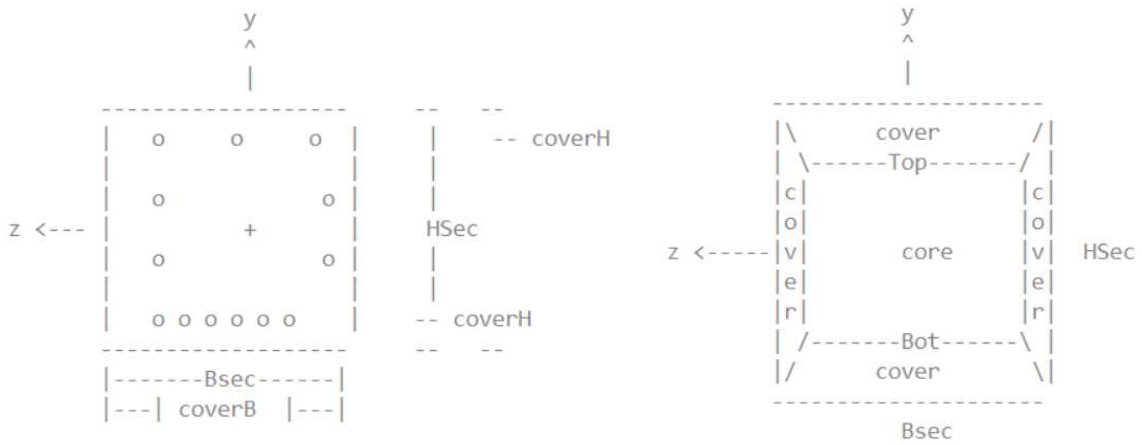

element nonlinearBeamColumn $eleTag $iNode $jNode $numIntgrPts $secTag $transfTag <-mass $massDens> <- iter $maxIters $tol> <-integration $intType>

```
#set    ColTransfType   Linear;     # options, Linear PDelta Corotational
geomTransf  PDelta  $IDColTransf
geomTransf  Linear  $IDBeamTransf
set np  5;  # number of Gauss integration points for nonlinear curvature distribution-- np=2 for linear distribution ok
```

F.1.2.1 Column

```
#BuildRCrectSection $ColSecTag  $HCol   $BCol   $cover  $cover  $IDconcCore $IDconcCover    $IDSteel    $numBarsTopCol  $barAreaTopCol  $numBarsBotCol  $barAreaBotCol  $numBarsIntCol  $barAreaIntCol  $nfCoreY    $nfCoreZ    $nfCoverY
$nfCoverZ
# columns
BuildRCrectSection  1011    [expr 1*$m] [expr 1*$m] [expr 0.05*$m]  [expr 0.05*$m]  1011    1111    2003    7   [expr 3.14*32*$mm*32*$mm/4] 7   [expr 3.14*32*$mm*32*$mm/4] 10  [expr 3.14*32*$mm*32*$mm/4] 20  20  20  20

BuildRCrectSection  1012    [expr 1*$m] [expr 1*$m] [expr 0.05*$m]  [expr 0.05*$m]  1012    1112    2003    8   [expr 3.14*32*$mm*32*$mm/4] 8   [expr 3.14*32*$mm*32*$mm/4] 12  [expr 3.14*32*$mm*32*$mm/4] 20  20  20  20

BuildRCrectSection  1013    [expr 1*$m] [expr 1*$m] [expr 0.05*$m]  [expr 0.05*$m]  1013    1113    2003    8   [expr 3.14*32*$mm*32*$mm/4] 8   [expr 3.14*32*$mm*32*$mm/4] 12  [expr 3.14*32*$mm*32*$mm/4] 20  20  20  20

BuildRCrectSection  1014    [expr 1*$m] [expr 1*$m] [expr 0.05*$m]  [expr 0.05*$m]  1014    1114    2003    7   [expr 3.14*32*$mm*32*$mm/4] 7   [expr 3.14*32*$mm*32*$mm/4] 10  [expr 3.14*32*$mm*32*$mm/4] 20  20  20  20
```

F.1.2.2 Beam

```
#BuildRCrectSection $ColSecTag  $HCol   $BCol   $cover  $cover  $IDconcCore $IDconcCover    $IDSteel    $numBarsTopCol  $barAreaTopCol  $numBarsBotCol  $barAreaBotCol  $numBarsIntCol  $barAreaIntCol  $nfCoreY    $nfCoreZ    $nfCoverY
$nfCoverZ
# beams
BuildRCrectSection  2011    [expr 1.00*$m]  [expr 0.55*$m]  [expr 0.05*$m]  [expr 0.05*$m]  1111    1111    2003    7   [expr 3.14*32*$mm*32*$mm/4] 7   [expr 3.14*32*$mm*32*$mm/4] 4   [expr 3.14*13*$mm*13*$mm/4] 20  20  20  20

BuildRCrectSection  2012    [expr 1.00*$m]  [expr 0.60*$m]  [expr 0.05*$m]  [expr 0.05*$m]  1112    1112    2003    8   [expr 3.14*32*$mm*32*$mm/4] 8   [expr 3.14*32*$mm*32*$mm/4] 4   [expr 3.14*13*$mm*13*$mm/4] 20  20  20  20

BuildRCrectSection  2013    [expr 1.00*$m]  [expr 0.55*$m]  [expr 0.05*$m]  [expr 0.05*$m]  1113    1113    2003    7   [expr 3.14*32*$mm*32*$mm/4] 7   [expr 3.14*32*$mm*32*$mm/4] 4   [expr 3.14*13*$mm*13*$mm/4] 20  20  20  20
```

F.1.3 Material Model

F.1.3.1 Rebar

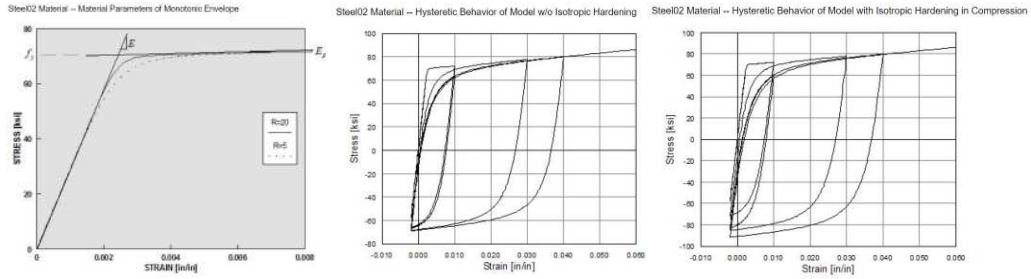

uniaxialMaterial Steel02 $matTag $Fy $E $b $R0 $cR1 $cR2 <$a1 $a2 $a3 $a4 $sigInit>

```
uniaxialMaterial Steel02 2003 424948.94 210000000.00000 0.00340 18 0.925 0.15
```

F.1.3.2 Concrete

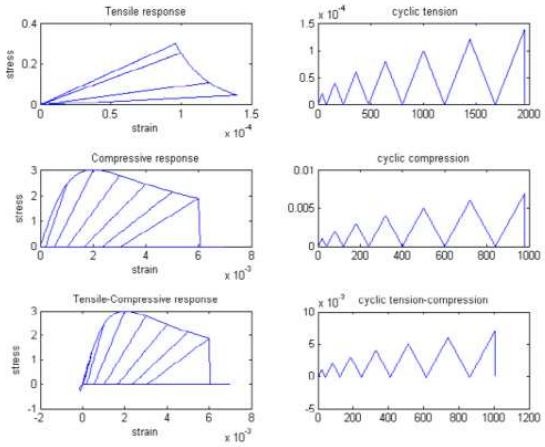

uniaxialMaterial Concrete04 $matTag $fc $ec $ecu $Ec <$fct $et> <$beta>

Column cover & all beam x-section

```
uniaxialMaterial Concrete04 1111 -47874.68 -0.00200 -0.00400 34595767 3501.489 0.00010
uniaxialMaterial Concrete04 1112 -47874.68 -0.00200 -0.00400 34595767 3501.489 0.00010
uniaxialMaterial Concrete04 1113 -47874.68 -0.00200 -0.00400 34595767 3501.489 0.00010
uniaxialMaterial Concrete04 1114 -47874.68 -0.00200 -0.00400 34595767 3501.489 0.00010
```

Column concrete core

```
uniaxialMaterial Concrete04 1011 -54476.01 -0.00338 -0.02625 34595767 3501.489 0.00010
uniaxialMaterial Concrete04 1012 -56782.77 -0.00386 -0.03246 34595767 3501.489 0.00010
uniaxialMaterial Concrete04 1013 -56782.77 -0.00386 -0.03246 34595767 3501.489 0.00010
uniaxialMaterial Concrete04 1014 -54476.01 -0.00338 -0.02625 34595767 3501.489 0.00010
```

F.1.4 Solver

1StoreyPO_170529c01.tcl

```
integrator DisplacementControl  $IDctrlNode   $IDctrlDOF $Dincr;    # use displacement-controlled analysis
analysis Static;                # define type of analysis: static for pushover
set Nsteps [expr int($Dmax/$Dincr)];# number of pushover analysis steps
set ok [analyze $Nsteps];          # this will return zero if no convergence problems were encountered
```

F.1.5 Results

F.1.5.1 Eigenvalue Analysis

Eigen.tcl

```
recorder Node -file Mode_1.out -node 1011 1021 1031 1041 1051 1061 1071 1081 1091 1101 -dof 1 2 6
"eigen 1"
recorder Node -file Mode_2.out -node 1011 1021 1031 1041 1051 1061 1071 1081 1091 1101 -dof 1 2 6
"eigen 2"
recorder Node -file Mode_3.out -node 1011 1021 1031 1041 1051 1061 1071 1081 1091 1101 -dof 1 2 6
"eigen 3"
record
```

T1=0.725296044565688

T2=0.25240152478890193

T3=0.14365286817583045

Therefore, only need to consider overstrength for loads which exceed $F_{capacity}$ for t<3T ≈ 2.2s

F.1.5.2 Gravity Loads

Gravity.tcl

```
pattern Plain 1001 Linear {
eleLoad -ele     2011     -type -beamUniform  [expr -72*$kN/$m]    0
eleLoad -ele     2012     -type -beamUniform  [expr -72*$kN/$m]    0
eleLoad -ele     2013     -type -beamUniform  [expr -72*$kN/$m]    0
recorder Node -file GravityReactions.out -node 1001 1002 1003 1004 -dof 1 2 6 reaction
```

1001			1002			1003			1004		
X	y	z_{rot}	x	y	z_{rot}	x	y	z_{rot}	x	y	z_{rot}
74.5905	3151.56	0	-16.6305	5128.44	0	16.6305	5128.44	0	-74.5905	3151.56	0

Table F-1: Restraint Reactions

```
recorder Element -file ColumnLoads.out -ele 1011 1012 1013 1014 forces
```

$EleTag	x, y, z_{rot}	x, y, z_{rot}
	End1	End2
1011	74.5905 3151.56 -135.304	-74.5905 -3151.56 -200.565
1012	-16.6305 5128.44 25.5841	16.6305 -5128.44 49.2621
1012	16.6305 5128.44 -25.5841	-16.6305 -5128.44 -49.2621
1014	-74.5905 3151.56 135.304	74.5905 -3151.56 200.565

Table F-2: Column forces.

Column loads same as restraint reactions because no load assigned to columns (all lumped at floors).

The above represents the gravity loads to be applied to simplified model.

F.2 Verification Against Seismostruct Model

Opensees results are verified using a second software package, Seismostruct. 1st floor mechanism, so only modelling gound-1st, and applying column axial loads to represent structure weight.

F.2.1 Numerical model

F.2.1.1 Geometry

Node Name	X	Y	Z	Type
n111	0.00	0.00	0.00	structural
n112	0.00	0.00	4.50	structural
n211	8.50	0.00	0.00	structural
n212	8.50	0.00	4.50	structural
n311	14.50	0.00	0.00	structural
n312	14.50	0.00	4.50	structural
n411	23.00	0.00	0.00	structural
n412	23.00	0.00	4.50	structural

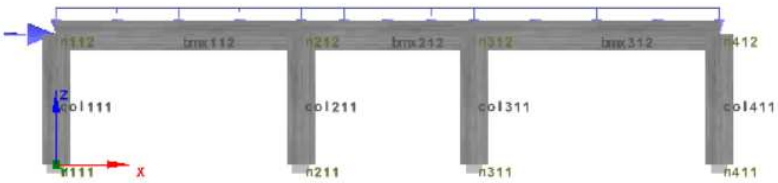

F.2.1.2 Cross-sections

Column

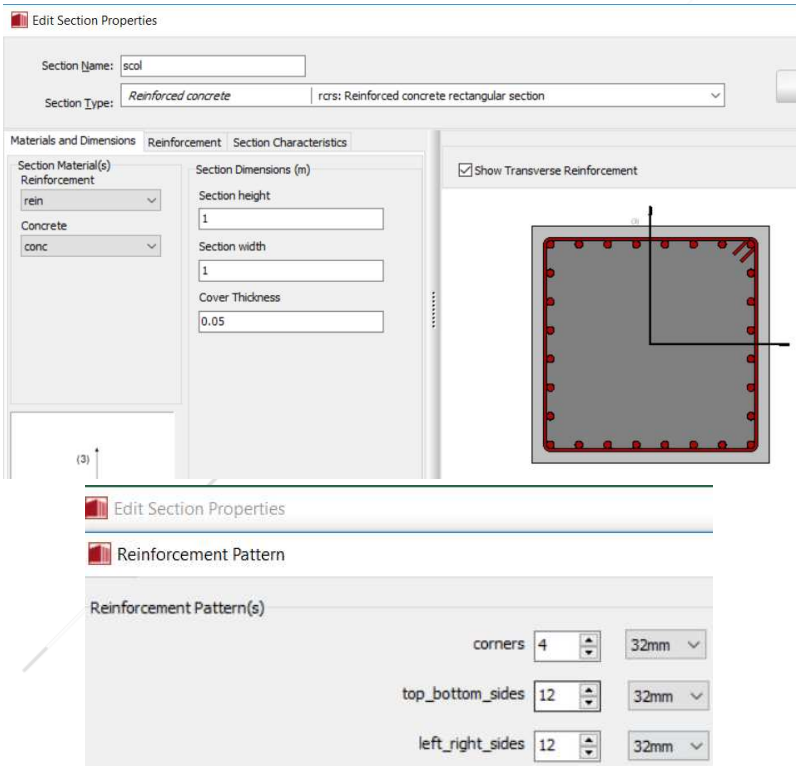

Figure F-3: Rebar material model. Yield at 433N/mm^2. Fracture strain = 0.1.

# bars	bars/side (+ 4 corner bars)	spacing between	A_Σ	$A_{\%}$
2.25%		mm	mm^2	
28	6	128.57	22,518.94	2.25%

Beam

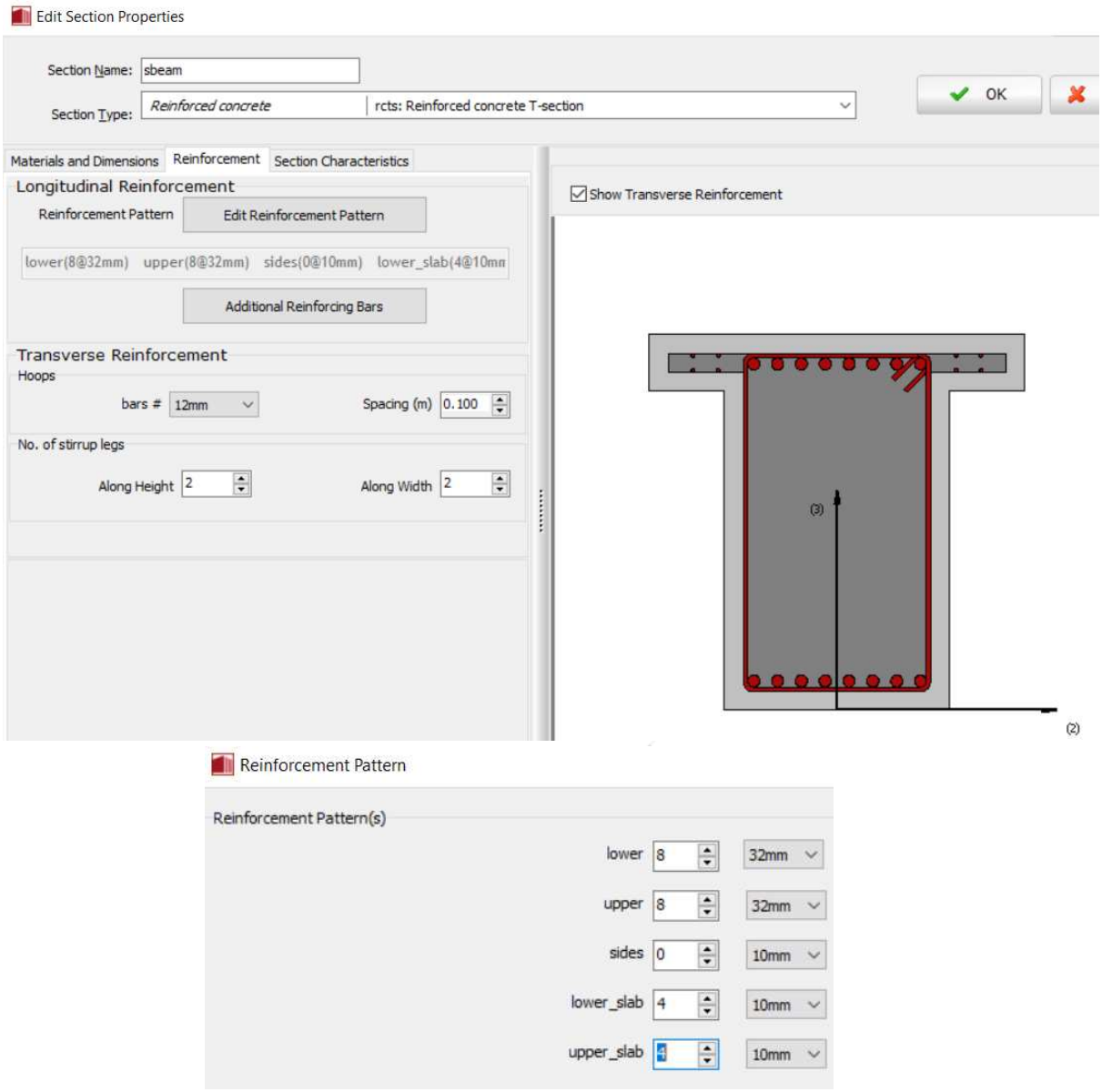

Figure F-4: Beam model.

F.2.1.3 Material model

Rebar

Menegotto-Pinto steel model - stl_mp

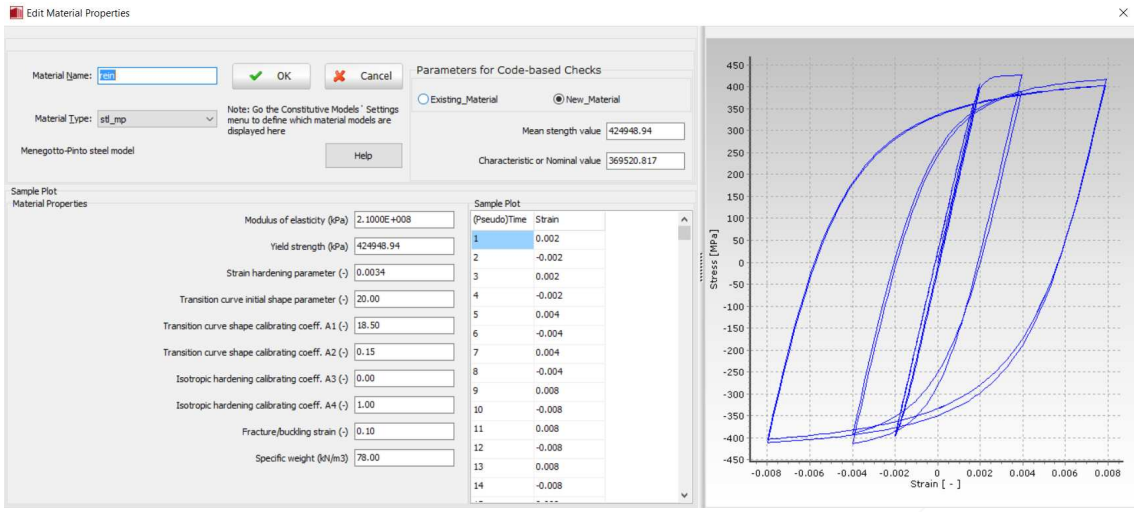

Figure F-5: Rebar material model. Yield at 433N/mm^2. Fracture strain = 0.1.

Concrete

Mander et al. nonlinear concrete model - con_ma

This is a uniaxial nonlinear constant confinement model, initially programmed by Madas [1993], that follows the constitutive relationship proposed by Mander et al. [1988] and the cyclic rules proposed by Martinez-Rueda and Elnashai [1997]. The confinement effects provided by the lateral transverse reinforcement are incorporated through the rules proposed by Mander et al. [1988] whereby constant confining pressure is assumed throughout the entire stress-strain range.

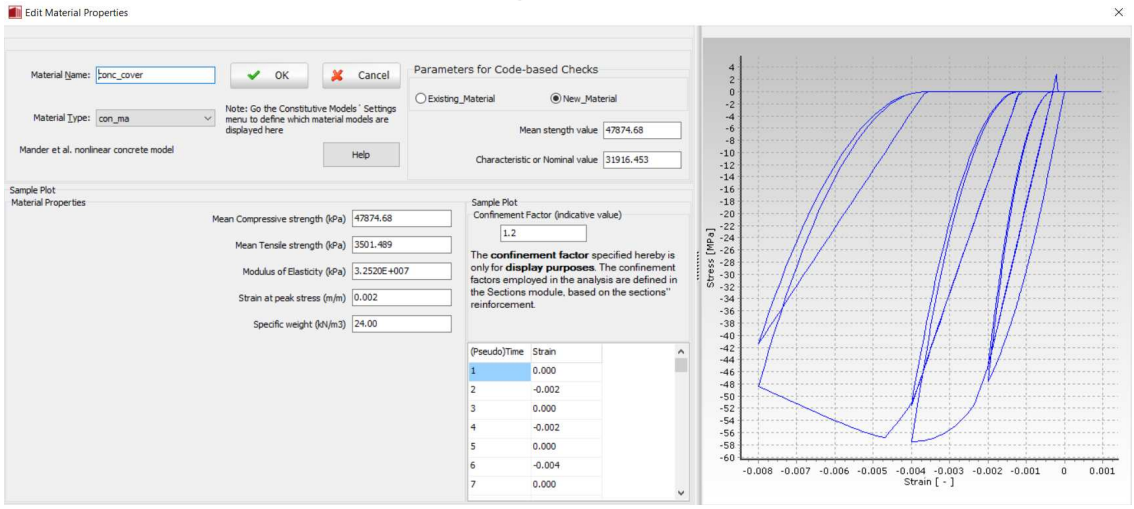

Figure F-6: Concrete material model. Hysteresis loop not defined for σ^{+ve}, indicating that σ^{+ve} corresponds to tension (i.e. ε^{+ve}). Compressive strength = 50N/mm^2. Tensile = 2.2N/mm^2. Strain at peak stress = 0.002.

F.2.1.4 Loads

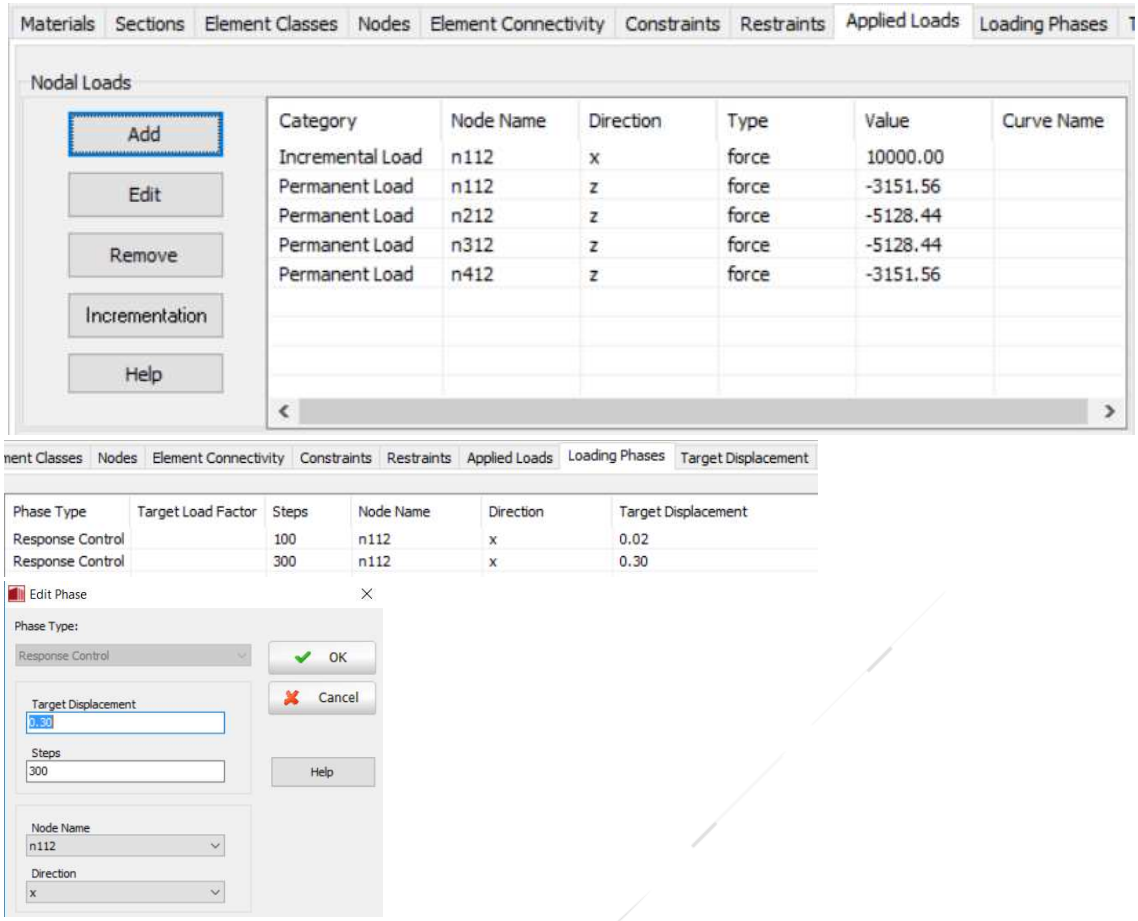

Figure F-7: Applied Loads.

F.2.1.5 Performance Criteria

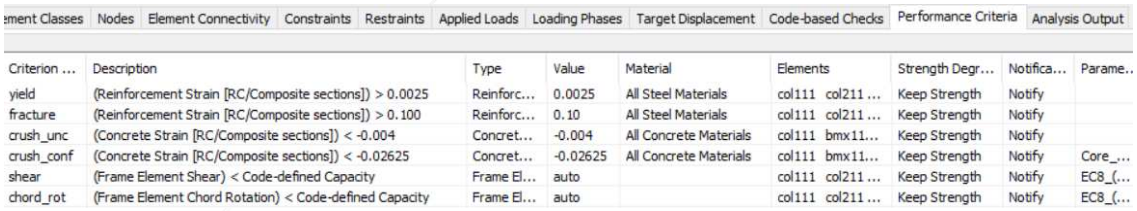

Figure F-8: Performance Criteria.

F.2.2 Results

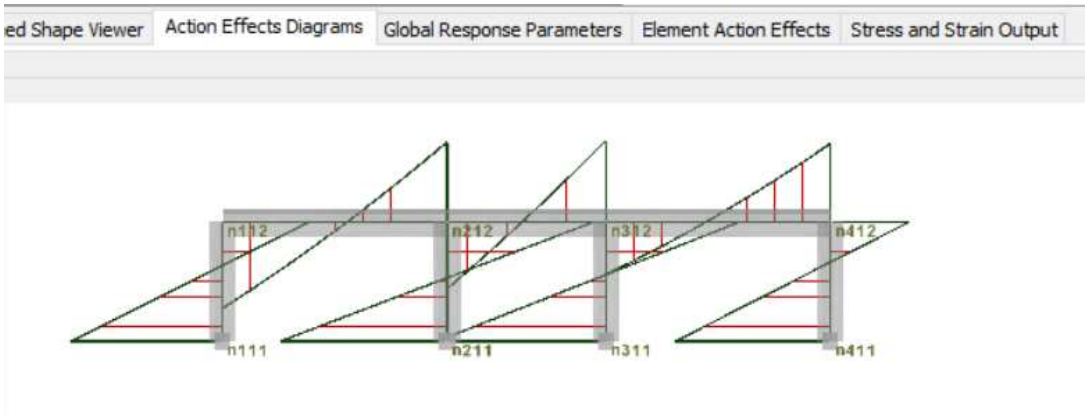

Figure F-9: General BMD prior to structural failure

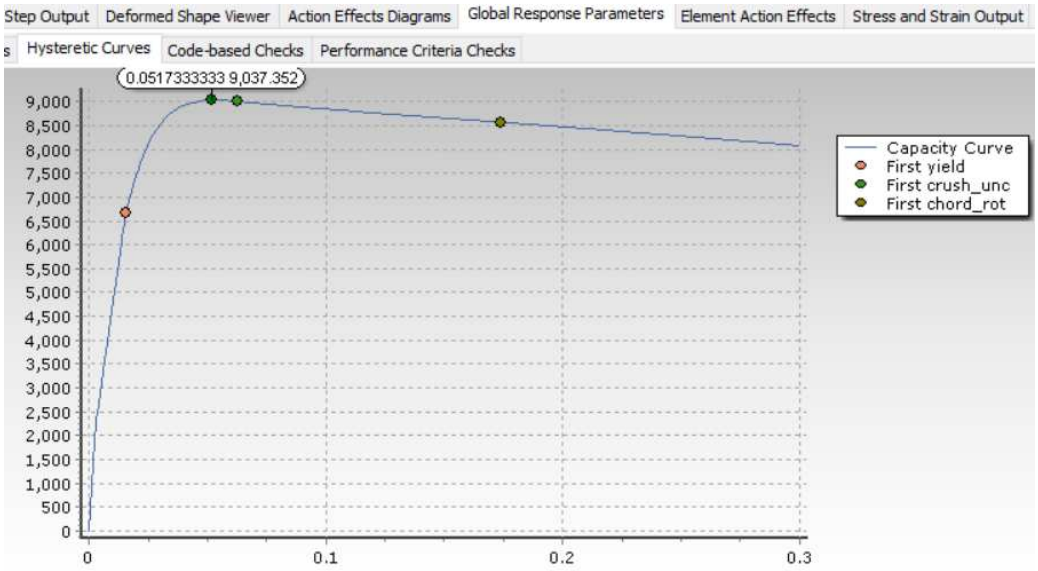

Figure F-10: F vs δ

F.2.2.1 Performance Criteria

Only yield is reached before structural failure (Figure F-10).

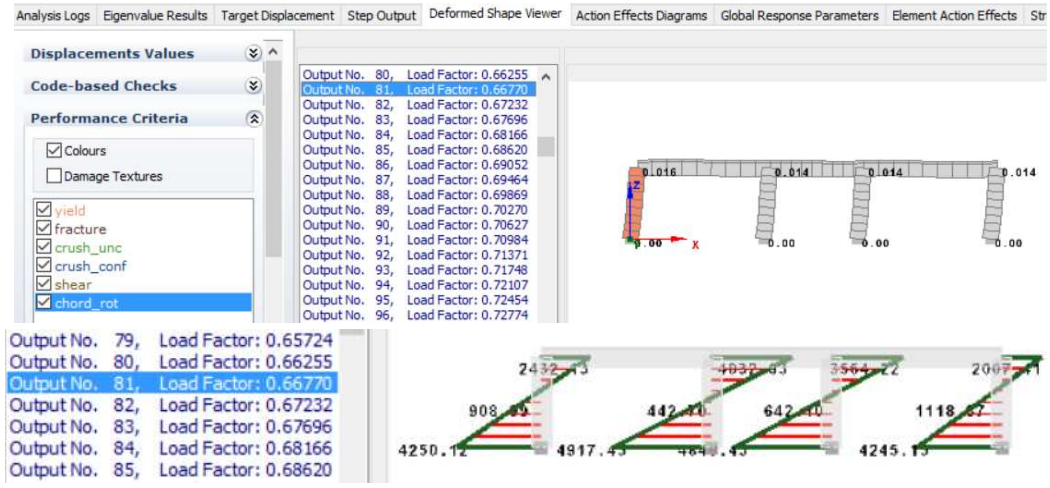

Figure F-11: First Yield

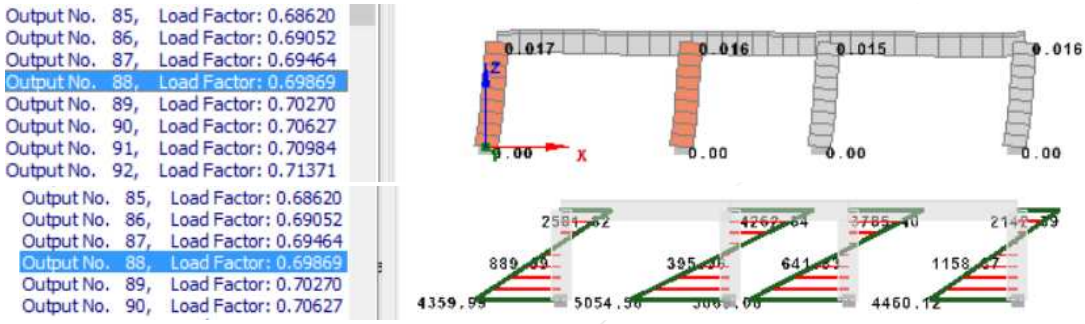

Figure F-12: 2nd Yield

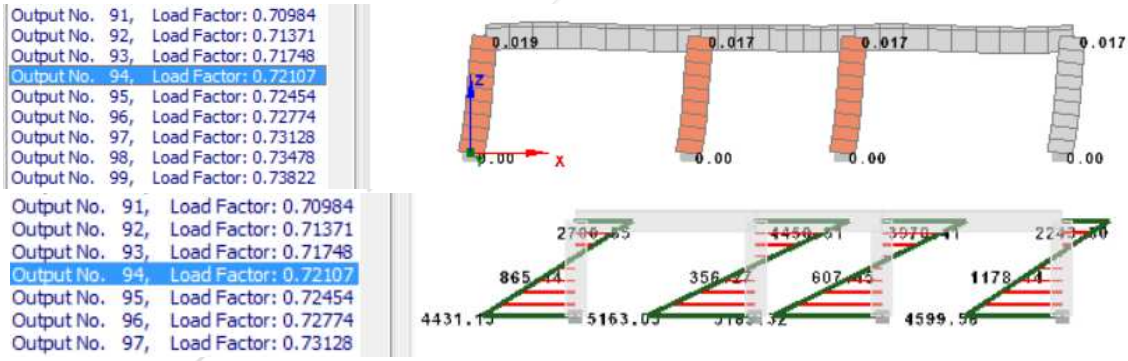

Figure F-13: 3rd Yield

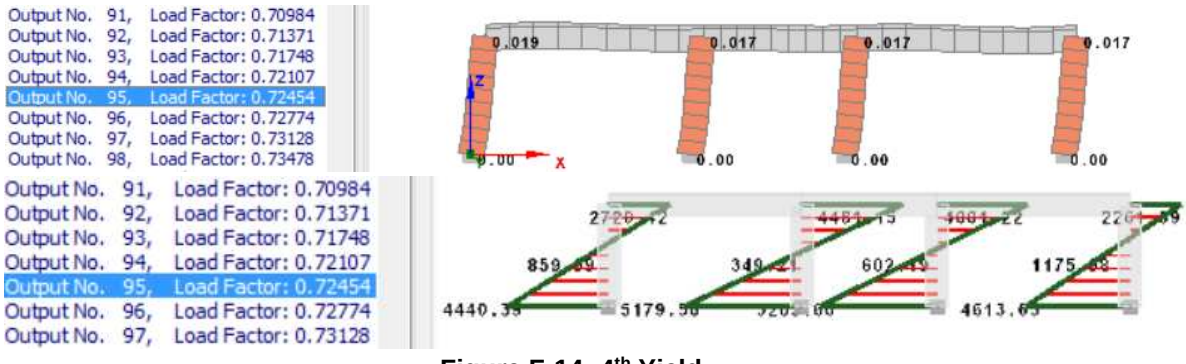

Figure F-14: 4th Yield

F.2.2.2 Bending Moments

Integration section a appears to be at bottom of columns, by comparing the values in Figure F-15 below with values shown in Figure F-11 -Figure F-14.

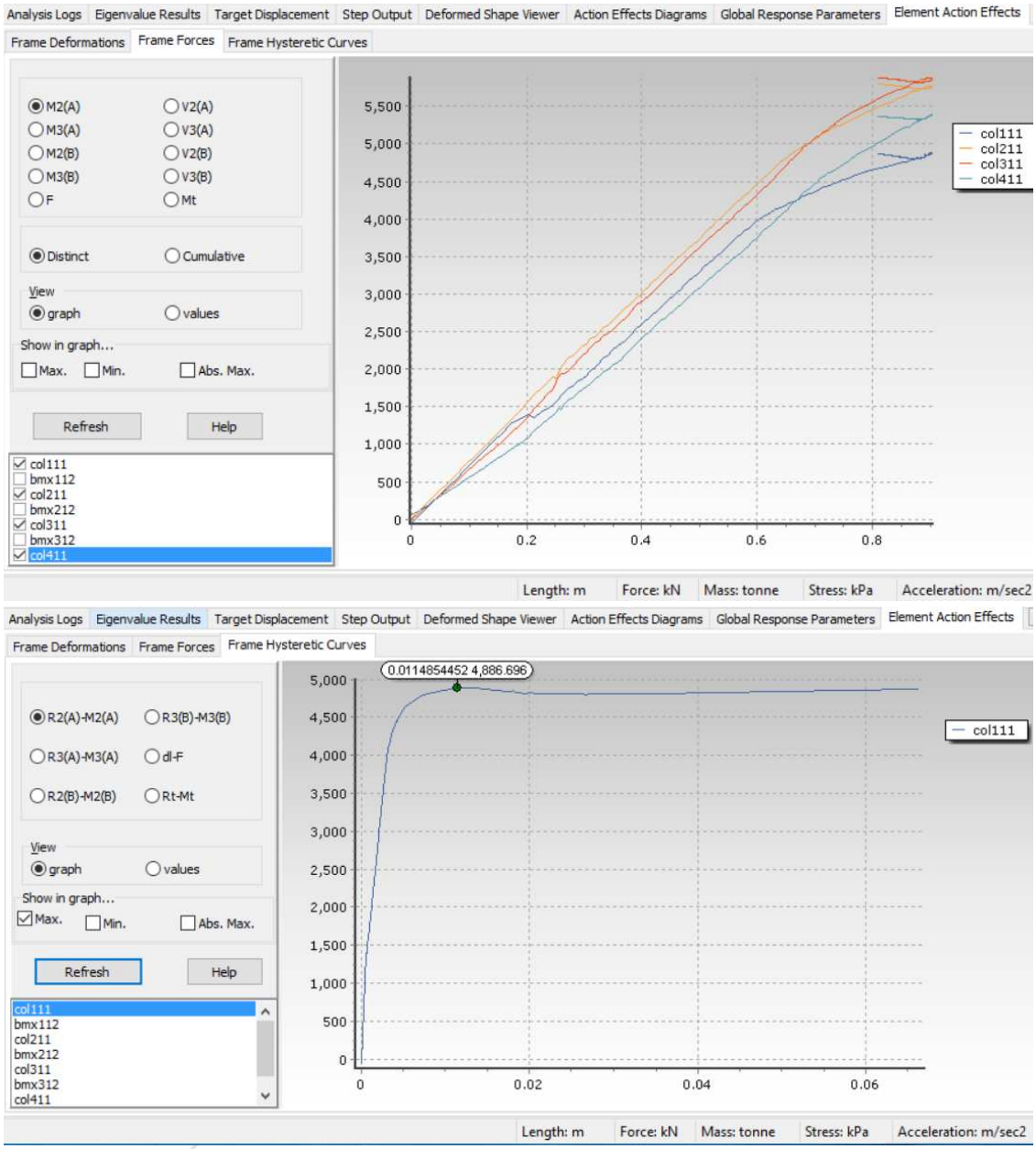

Figure F-15: M vs load factor (top) and M vs rotation (bottom). Peak moments achieved for col111, col211, col311 and col411 are 4887kNm, 5798kNm, 5879kNm, and 5390kNm respectively.

F.2.2.3 Pushover

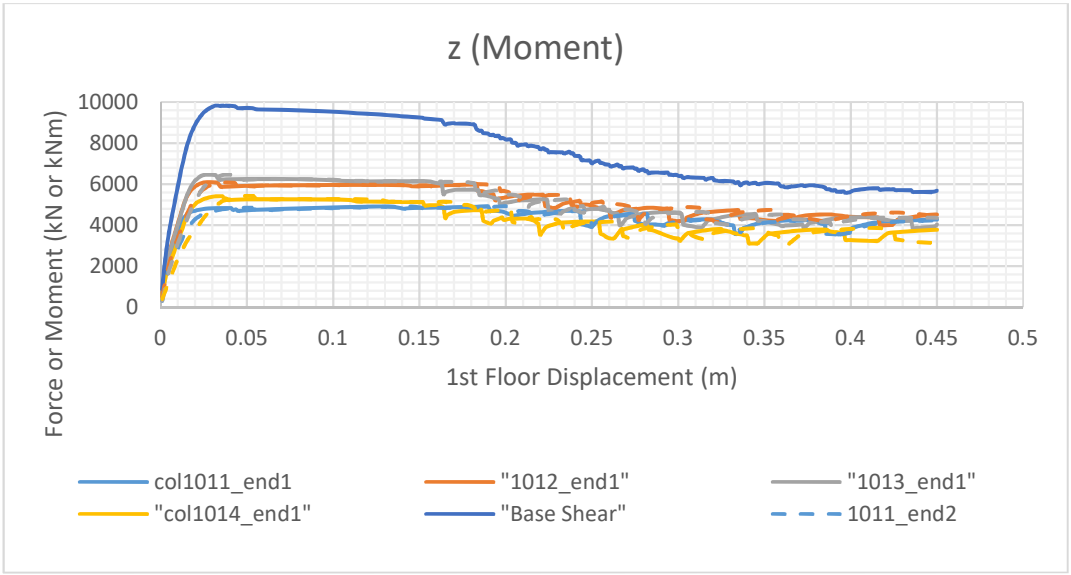

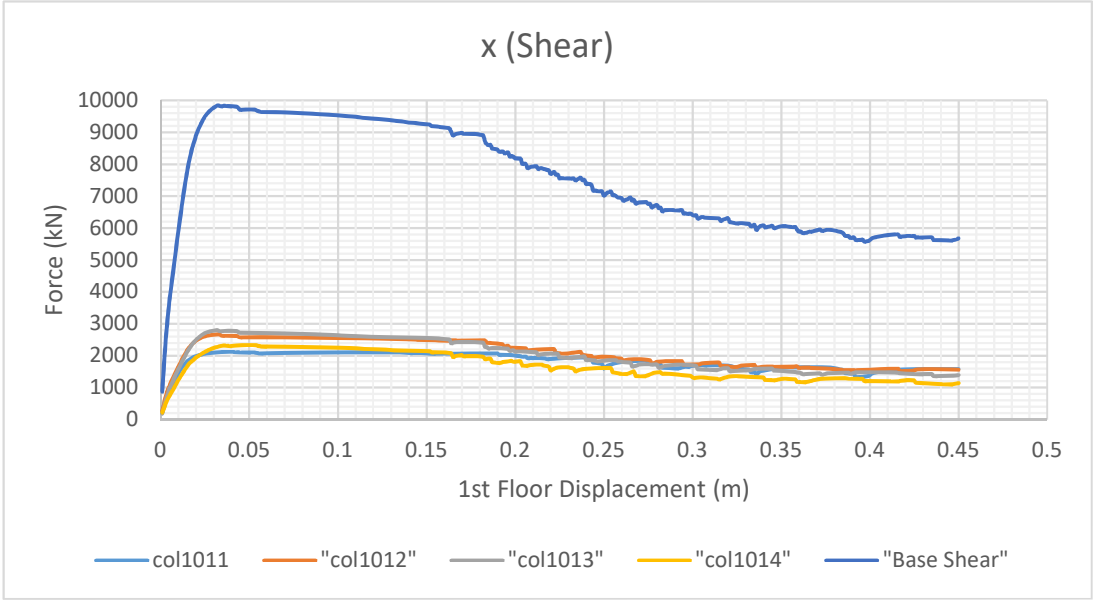

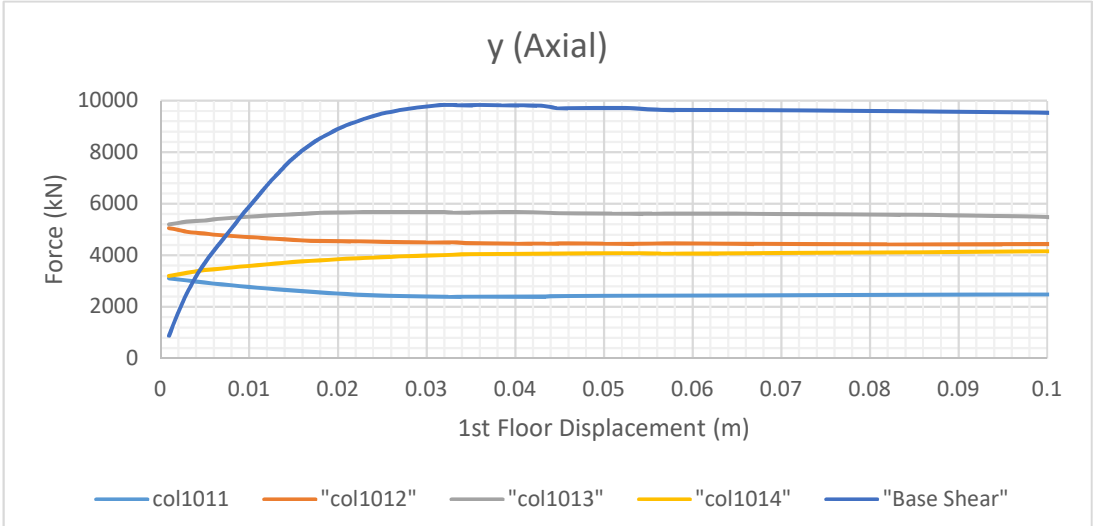

Figure F-16: OpenSees pushover (load applied at 1st floor only)

Peak: 9836.37kN 31.9mm

F.2.2.4 Stress-Strain Relationships

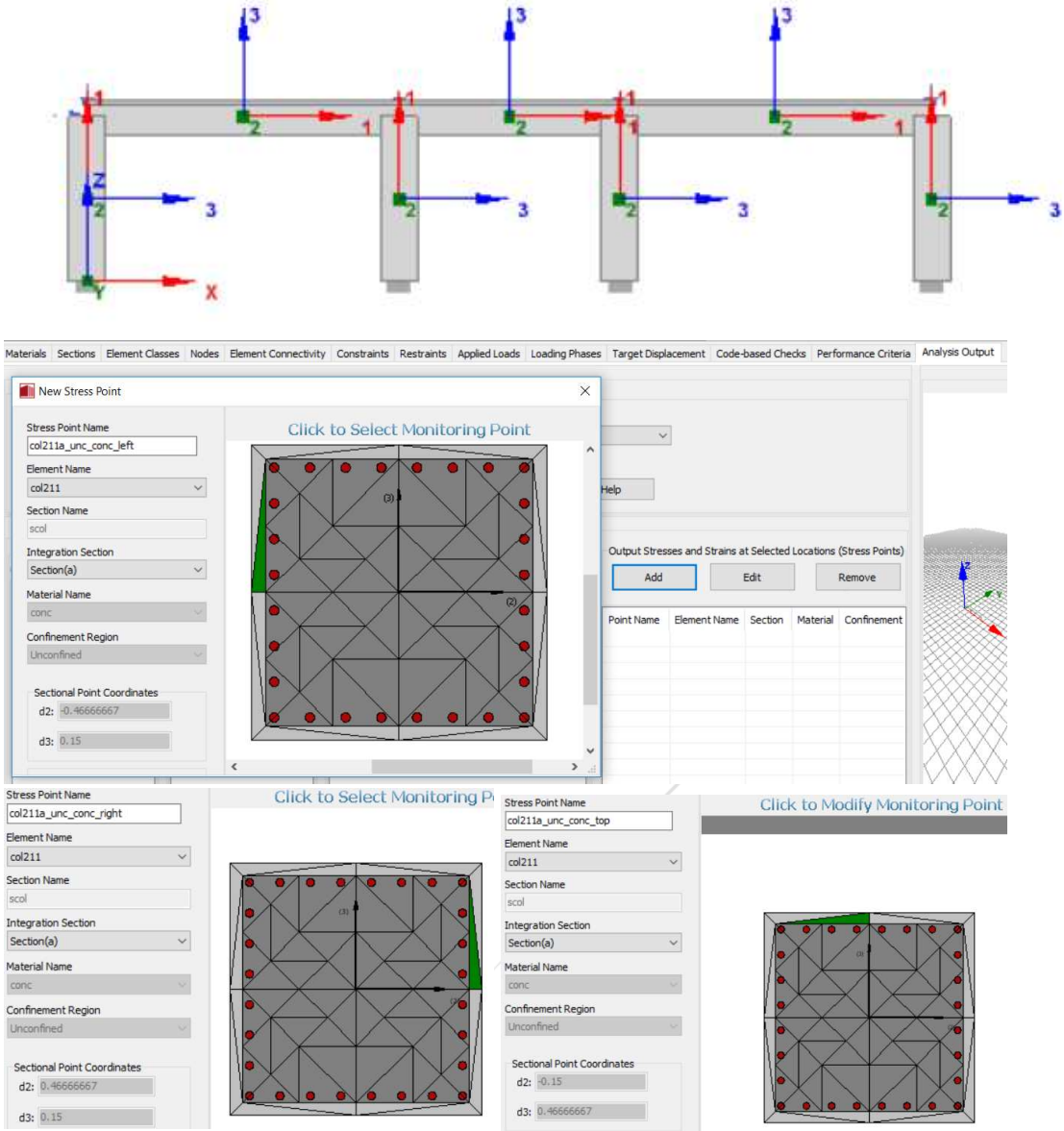

Figure F-17: Local axes (top) and integration sections at <u>bottom</u> of col 211. From local axes diagram: Top of the section indicates tension face, bottom = compression face (appears to be the other way around in Figure F-18 below).

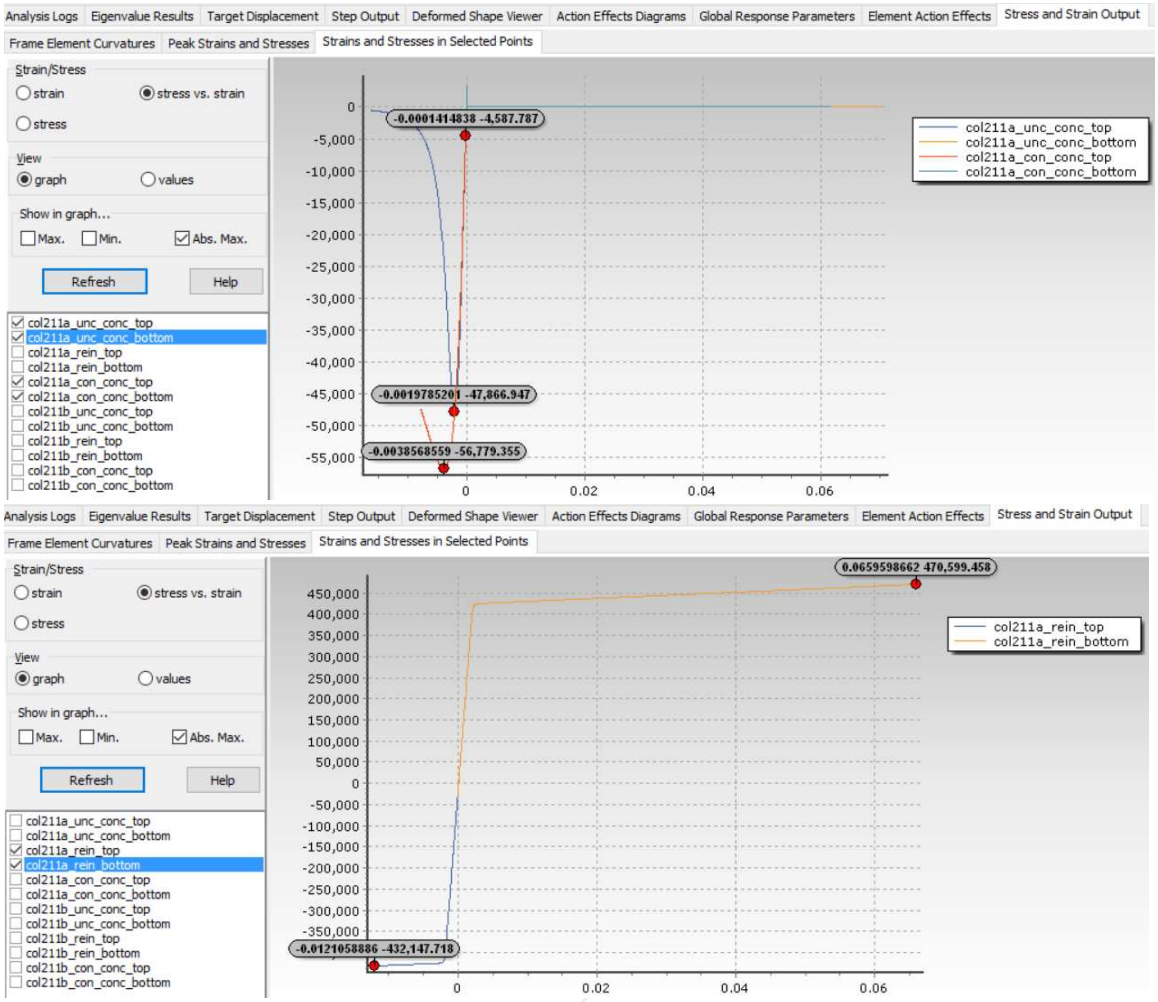

Figure F-18: σ-ε relationship for concrete (top) and rebar (bottom) at <u>bottom</u> of col 211. Tension = +ve, compression = -ve. Top/bottom seems to be opposite of that shown in Figure F-17.

```
recorder Element -file $res/steelStress.out -time -ele 1011 section 1
fiber 0 0 2003 stressStrain; # steel fiber stress-strain, node i
```

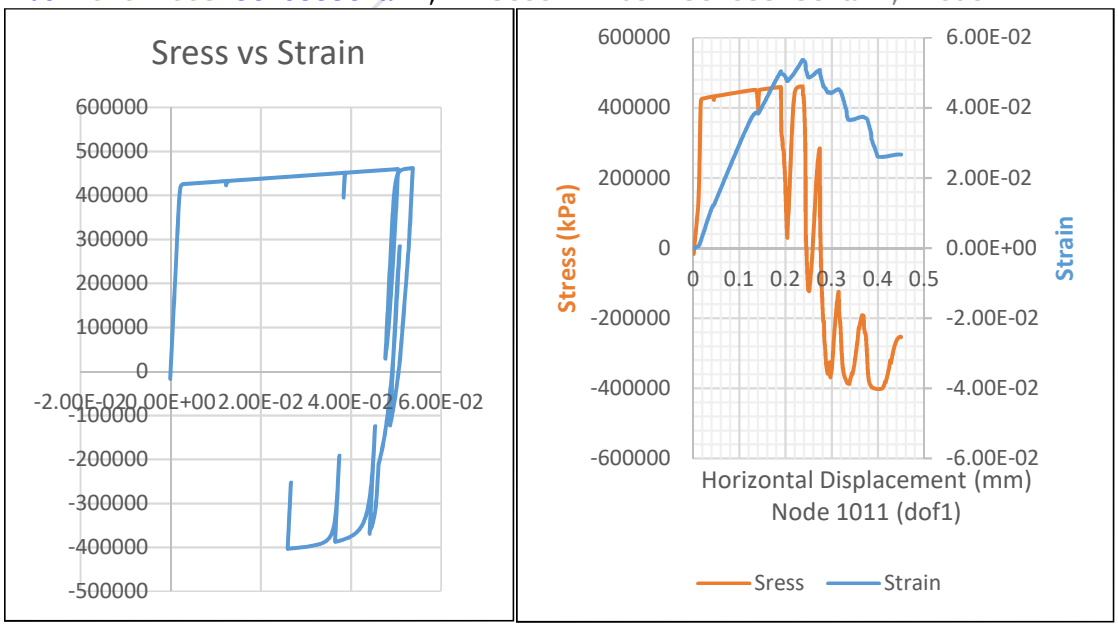

Figure F-19: Rebar stress-strain. Col1011, section 1, fibre 0 0

F.2.2.5 OpenSees/Seismostruct Comparison

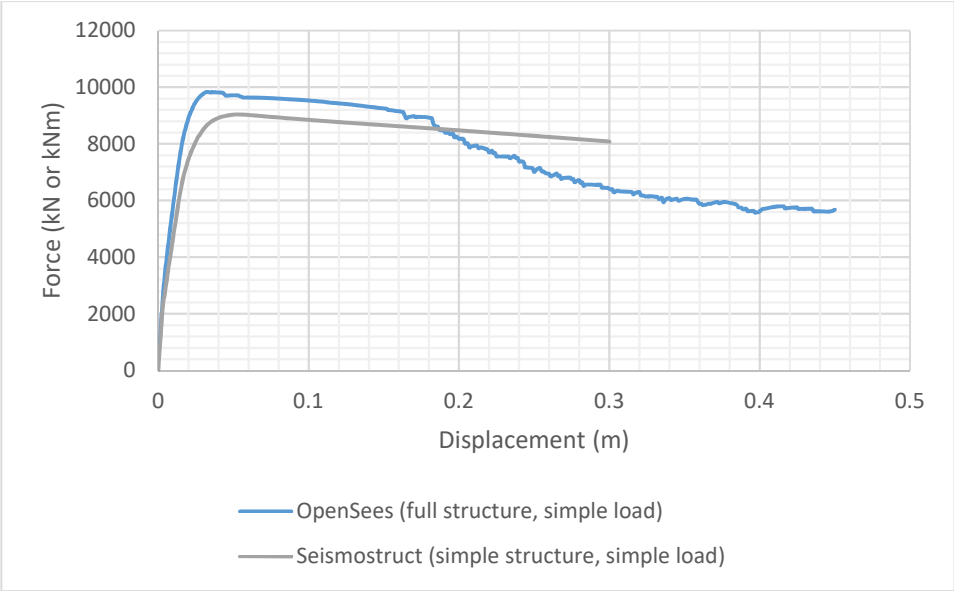

Figure F-20: Comparison of OpenSees Full Structure, Seismostruct Simple Model (both with simplified loading).

F.3 VHPO vs $STPO_1$ comparison

	Column forces (kN)				Column Moments					
	Shear (local x)		Axial (local y)		Moment (local z) (kNm)				(kN)	
					end 1 (bottom)		end 2 (top)		$(z1+z2)/l_{01}$	
	VHPO	SPO	VHPO	SPO	VHPO	SPO	VHPO	SPO	VHPO	SPO
col1011	1,508	2,104	1,085	2,382	4,305	4,825	2,524	4,723	1,517	2,122
col1012	2,338	2,668	4,154	4,505	5,798	6,077	4,893	6,065	2,376	2,698
col1013	2,687	2,775	6,470	5,652	6,474	6,308	5,908	6,347	2,751	2,812
col1014	2,267	2,289	4,850	4,021	5,474	5,408	4,965	5,010	2,320	2,315
sum:	8,800	9,836	16,560	16,560				sum:	8,965	9,947

Table F-3: VHPO & SPO column forces at failure in local axis directions (Fr=0.6, h=19m). The sum of the column shears equates to the total applied lateral load. The sum of the column axial forces equates to the weight of the structure (and so is unchanged at each calculation step)

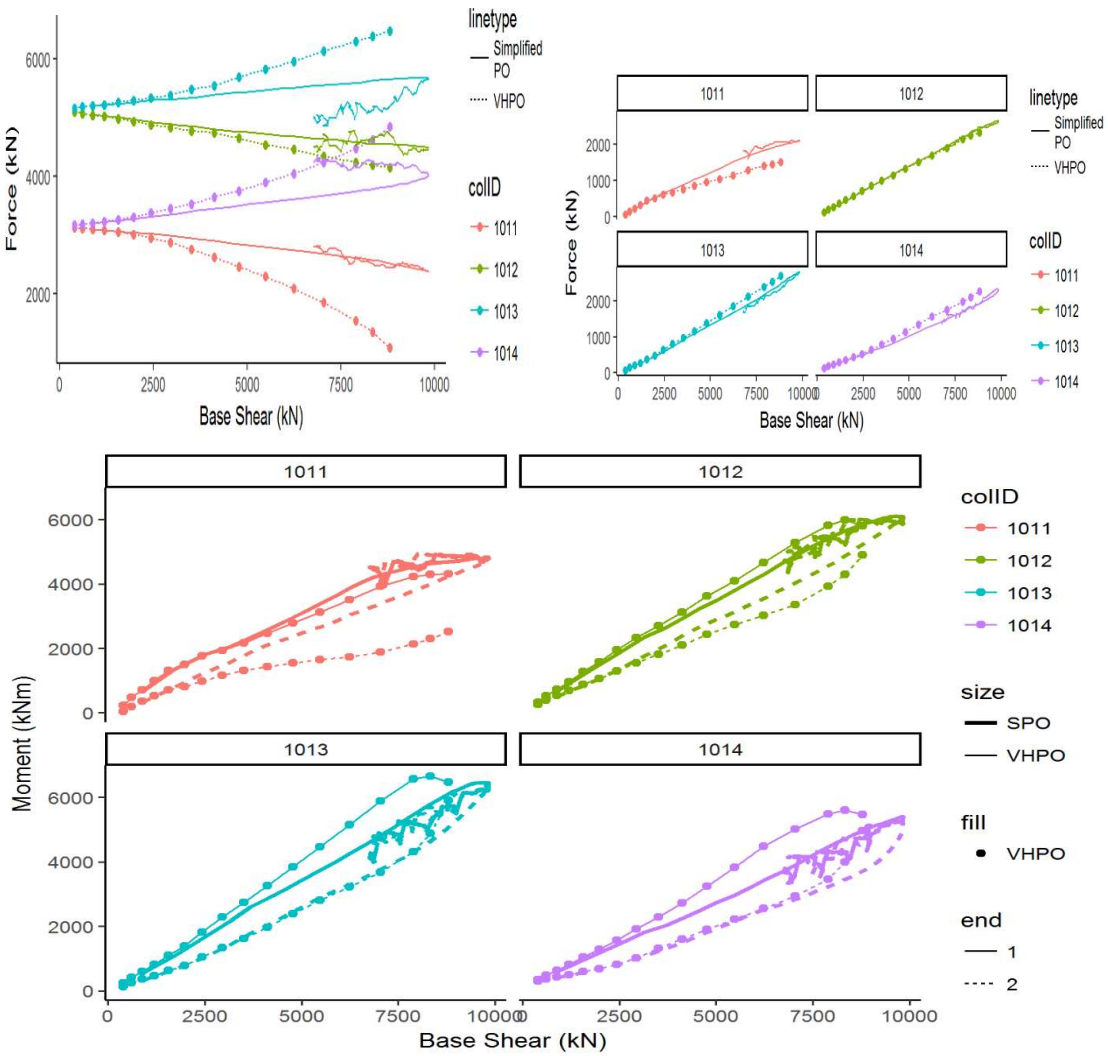

Figure F-21: Ground – 1st Floor Column Forces vs Base Shear, comparison between SPO and VHPO (obtained at CHPO performance points for Fr=0.6). Shear and bending forces are comparable, but axial forces show clear differences between the SPO and HVPO cases. Note, shear and axial loads same at both ends of the columns due to the OpenSees model lumping mass at the column tops.

F.4 VHPO vs STPO$_2$ comparison

Note that CHPO results could be shown as a surface (h,v,F), with the below curves representing sections through the surface at lines of constant Froude Number.

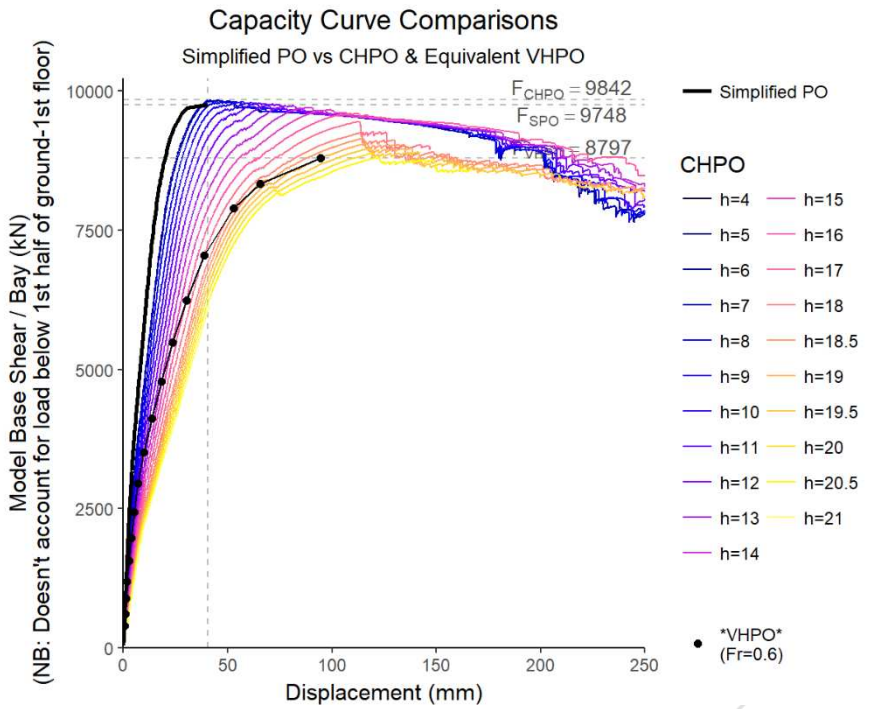

Figure F-22: $STPO_2$ vs VHPO and CHPO

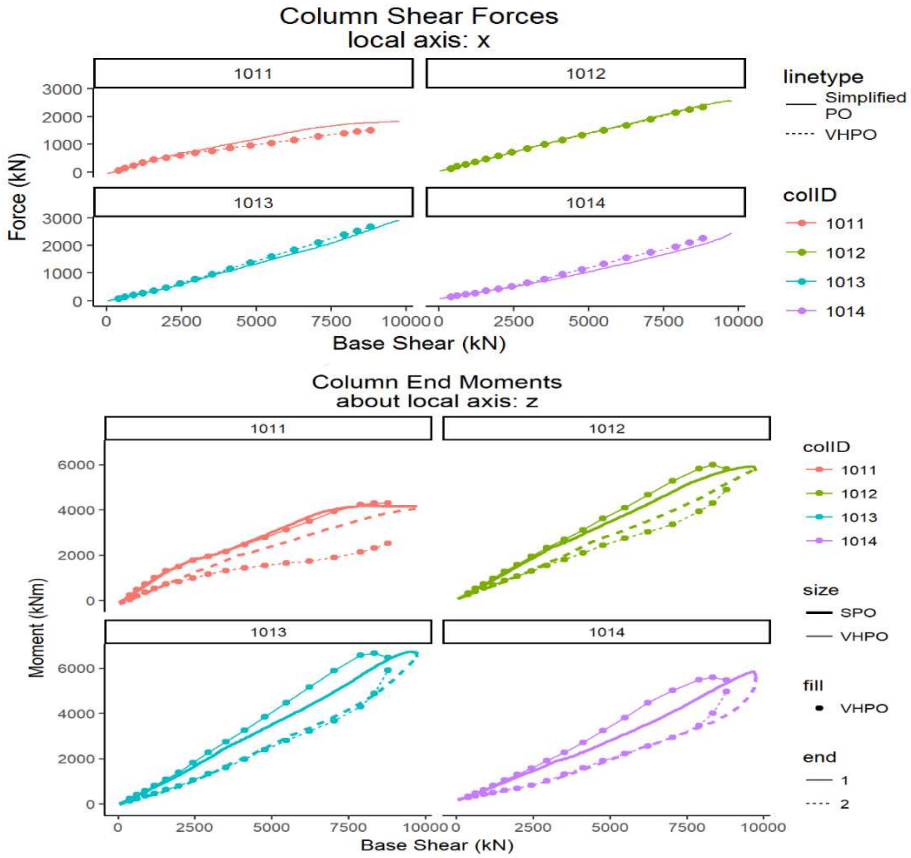

Figure F-23: SPO^+ vs VHPO comparison

F.5 Implications for Structures with more Complex Performance Curves

Real structures should also be considered to have a maximum load capacity (F_{max}), and so dynamic performance of the structure will become a consideration if, before the ductility capacity is reached, the applied load exceeds the maximum load capacity of the structure. In this case the relationships presented in the main text will apply, where t_{dur} is the duration for which the applied load exceeds the ultimate capacity, and T is calculated using the secant stiffness (k_{secant}) as shown in Figure F-24.

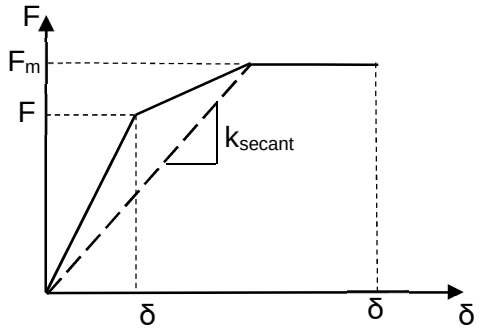

Figure F-24: Definition of maximum force capacity, ultimate ductility capacity, secant stiffness and degradation (both cyclic degradation and in-cycle degradation).

The results imply that, with the exception of global failure due to bore impact, structures must be designed such that their maximum capacity is greater than that applied by the design tsunami, as structural ductility does not allow for the development of overstrength. Strain-hardening may be utilized if requirements are placed on detailing so as to achieve the required maximum load capacity beyond yield. Therefore, for the tsunami design of structures in seismic zones, a preceding earthquake should be assumed and the capacity of the weakened structure governs. For a structure subjected to ground-shaking, the possibility of both cyclic strength degradation and in-cycle strength degradation should be considered in order to determine the suitable residual structural capacity under the subsequent tsunami loading. Note that for structures which are dominated by tsunami loading (e.g. long-period structures), then increasing the yield force of the structure will delay the onset of plastic behavior under ground-shaking, increasing the accelerations (and so inertial forces) experienced by the structure.